UNIVERSITÀ
DEGLI STUDI
FIRENZE

PhD in
Civil and Environmental Engineering

CYCLE XXXII

COORDINATOR Prof. Borri Claudio

Fully automated operational modal analysis for Structural Health Monitoring (SHM) of Heritage Buildings

Academic Discipline (SSD) ICAR/08

Doctoral Candidate
Dr. Zini Giacomo

(signature)

Supervisor
Prof. Bartoli Gianni

(signature)

Supervisor
Prof. Betti Michele

(signature)

Supervisor
Prof. Thiele Klaus

(signature)

Coordinator
Prof. Borri Claudio

(signature)

Years 2016/2019 (*beginning and end of the program*)

Fully automated operational modal analysis for Structural Health Monitoring of Heritage Buildings

To my father

Abstract

The thesis is focused on the definition of an integrated fully automated procedure for the modal identification and tracking in the Cultural Heritage. The established framework aimed to investigate the possibility of a designing an automated procedure for the modal parameters extraction and tracking from long-term monitoring system data minimizing the variance in the estimation.

The proposed flow chart is a self-adaptive algorithm both to the structural dynamics and to the different sources of the unknown dynamic excitation. Firstly, the aim is building an automated procedure for the modal identification able to manage all the sources of uncertainty that affect the problem in every phase. Then, the proposed procedure is used in a wider method for analysing large dataset of long-term dynamic monitoring data aiming to track the modal quantities over the time minimizing the bias. That point is crucial to increase the accuracy in the estimation of the damage sensitive features in a Structural Health Monitoring (SHM) workflow to enable the detection. The work of thesis deepened that aspects investigating the historic masonry towers by means of numerical models and real data.

Lastly, some numerical simulations are performed to investigate the possibility of an integration with global and local dynamic measurements. Despite the application of the method on a specific class the whole framework is conceived to be adapted to different classes of buildings and measuring devices through a data driven process.

Keywords: Structural Health Monitoring, Cultural Heritage, Automated Modal Analysis

Contents

1-Introduction

2-Literature review

3-Automated procedure

4-Cases of study

5-Damage simulations

6-Conclusions

Appendix A1

Appendix A2

References

List of figures

List of tables

Chapter 1

Introduction

1.1 Introduction-1.2 Statement of the problem-1.3 Motivation of the thesis-1.4 Aims of the thesis-1.5 Methodology of the thesis-1.6 Limitation of the method-1.7 Organization of the text

1.1 Introduction

Nowadays, the preservation of the existing structures is one of the greatest challenges for the structural engineers. In the major part of the civilized areas (EU,USA,Japan,etc.) the amount of existing structures that were built in the last centuries is massive. This bulk of different structures is often at the end of their nominal life and in some cases, it is ended many years ago. On the other hand, the loads are even higher due to the increasing intensity of the extreme events.

Moreover, the climate changes lead to harsh environmental conditions that produce a faster decreasing of the construction materials performances. In that scenario, the probability of failure increase and the collapse of the old existing structures become a real menace. Thus, the collapse of the Polcevera viaduct in Genova is the last of a long chain of iconic structures collapses. In that case the decrease of the bridge performances and the simultaneously increase of the loads given by the vehicular traffic lead to the collapse when the structure was on service [1].

Figure 1-I The partial collapse of Polcevera viaduct in the 14th of August 2018, killing 43 people (*source ilpost.it*). The viaduct also known as the Morandi bridge from the name of its designer, the Italian engineer Riccardo Morandi, was built in the 1967 with a system of prestressed cable system innovative for that period. The bridge suffered degradation problems due to the corrosion of the steel cables and rebars.

In other cases [2] [3] [4], the collapses were produced by earthquakes or by designing errors during some intervention on the structure. As well as the Dharahara tower in Katmandu collapsed under the strong shakes of a magnitude 7.8 earthquake and the iconic San Marco bell tower ruined at the beginning of the XXth century after the repair works at the ground level of a building connected with the tower [5]. Even if, in that case the bell tower was seriously damaged in the XVIth century by a lightning storm and it was repaired with an external brick masonry wall connected with the existent. Some other examples are the damages suffered by the cultural heritage [6] [7] [8] [9] [10] during the earthquakes of Accumuli and Emilia Romagna, respectively in the 2016 and 2012.

(a) (b)

(c) (d)

Figure 1-II (a) The Dharahara tower in Katmandu before and after the magnitudo 7.8 earthquake in Nepal in April 2015 (*source nextquotidiano.it*). (b) the collapse of the San Marco bell tower in Venice in July 1902 (illustrated postcard, *source venipedia.it*). (c) The collapse of the clock tower in Finale Emilia after the Emilia Romagna earthquake in the 2012. (d) The sequence of the vault collapse in the San Francesco's church in Assisi during the 1997 earthquake.

From the analysis of the collapses illustrated above (Figure 1-II), the causes can be condensed in two categories:

a) The decay of the structural performances due to the ageing of the materials and to sudden works that change the structural behaviour.
b) The increase of the external loads due to the new performance level needed.

In that scenario the cultural heritage is one of the most exposed categories because of their long nominal life and the low performance level under horizontal loads (Figure 1-III). In particular, the masonry towers seem to be more prone to suffer damages from earthquakes [11], even if, the magnitude is not so high. It is worth to point out that it is impossible to divide the cultural heritage buildings in fixed categories. Because every structure has its own history and every case should be analysed carefully.

The focus of that thesis will be on the cultural heritage both for the cultural and artistic value both for the economic aspect. The first point it is clear, and it is a duty to preserve these iconic structures for the future generations. The second point it is a little bit hidden and material, but the cultural tourism is one of the most important sectors for many countries in the EU, producing a total turnover of 109.532 Million of Euro (*source eurostat*). For some countries represent more than the 10% of the gross domestic product and one of the main economic resources. Hence the preservation of the cultural heritage become a fundamental issue also in the economic life.

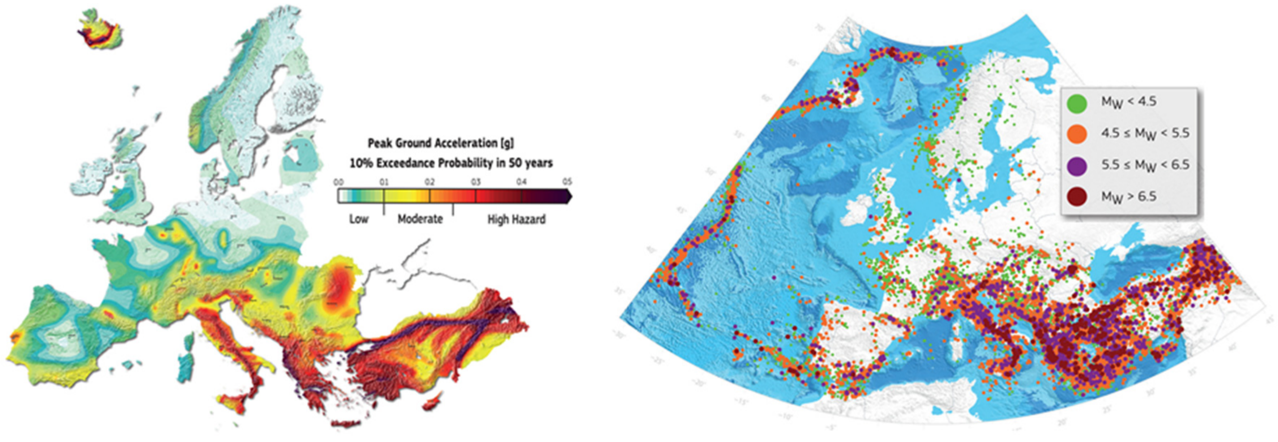

(a) (b)

Figure 1-III (a) Map of the European seismic hazard and (b) Historical earthquake database for the European region [12]

1.2 Statement of the problem

For a long time, the common approach in the civil engineering field has been the design of new constructions. The flow starts from the definition of the loads in a probabilistic manner, satisfying the required performances in the nominal life. Then the design of the structure provides the materials, the geometry, the connectivity etc. ensuring an adequate safety coefficient. At the end the designed structure is verified after the construction phase to check the coherence with the design phase. Performing the standard maintenance, the end of the nominal life can be reached on the safe side. Thus it can be extended by means of refurbishment or strengthening works, that ensure new levels of performances (Figure 1-IV).

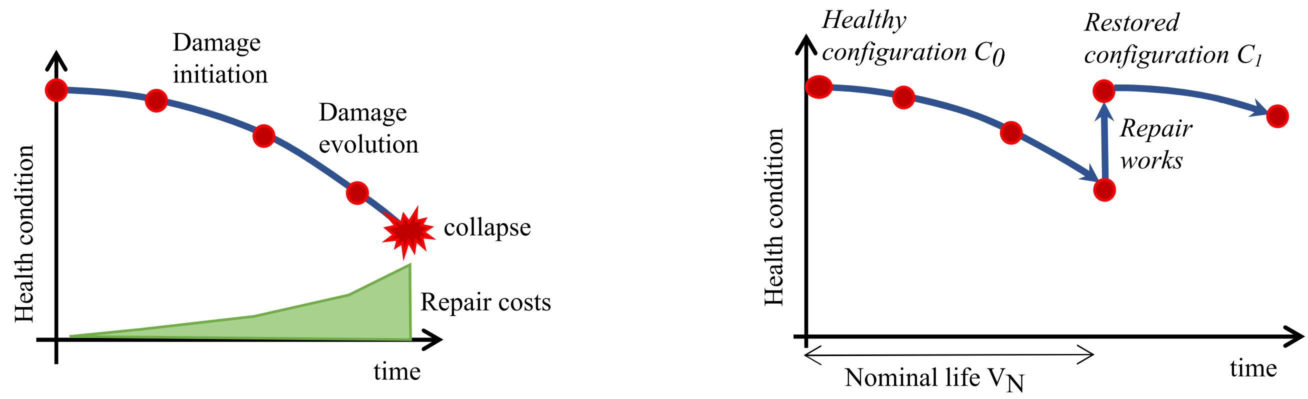

Figure 1-IV On the left, the evolution of the damage related to the decrease of structural performances. The green curve represents the increase of the repair cost to reach again the healthy status. On the right, the time evolution of the structural performances. The repair works shift upper the level of performance.

Dealing with existing structures is more complex, because of the uncertainties that affect the problem. Nonetheless the only available instruments to solve the problem are the data measured on the structure. For that reason, the process should be interdisciplinary, starting with the full knowledge of the structure itself. For this reason, a complete survey of the available information about the construction is needed. Therefore, that requirement could be accomplished directly by the original design drawings or indirectly by means of a comparison with the building techniques used at the time of construction.

Anyway, the only available information are the measurements taken both by the monitoring system both by in situ tests on the materials (sonar tests, flat jack tests, etc.). The first ones can be dynamic or static measurements collected through a time span, called observation period. Instead the second ones are spot measurements that can be performed in different structural elements to increase the structural knowledge. Ideally, the result of the process should be the health assessment of the structure and the definition of the residual life.

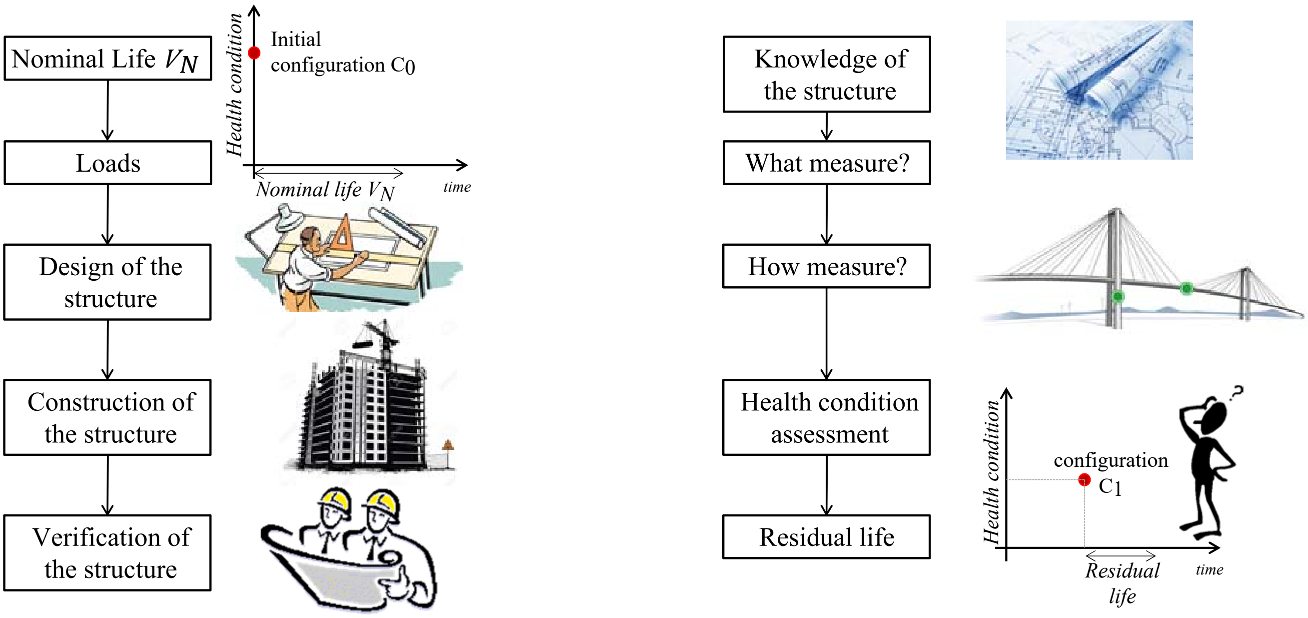

(a) (b)

Figure 1-V On the left the design work-flow starting from the required performance of the structure and the quantification of the nominal life. Consequently, the definition of the loads on the reference period and the design of the structure (materials, geometry etc.). At the end the verification phase of the construction process. On the right, the inverse problem of the existing buildings performance assessment.

Thinking to the uncertainties of the two workflows (Figure 1-V), in the first case, they can be limited to the construction phase. Instead in the second case they are smeared along all the phases leading to a complex problem.

In the case of cultural heritage, the problem is even more complex, because the destructive tests must be avoided to preserve the architectural features of the structures. Thus, the long-term monitoring systems are the only tools available to collect structural data. Now the main questions are the following:

- ➢ *What should be measured to ensure the definition of the current health status?*
- ➢ *Which is the level of damage that can be detected from the measured data?*
- ➢ *Which devices are needed?*

For the first time, it is introduced the definition of damage and it should be explained in detail. Hence the damage should be viewed in wide-spread sense and not only as the appearance of cracks.

From this perspective, the damage can be assumed as a parameter that allows to measure the degree of deviation from the healthy configuration. As shown in [13] the damage can be assumed as the change in the material properties, in the connectivity, in the geometry, in the boundary conditions etc.

The first attempt of correlation between a measured data or a derived property with the evolution of damage was made by Rytter [14]. The Authors established four levels in the damage detection through dynamic signatures:

1) **Detection:** Qualitative indication that damage might be present in the structure.

2) **Localization:** Information about the probable location of damage.
3) **Quantification:** Information about the size of the damage.
4) **Prediction:** Information about the actual safety of the structure and giving a prediction of the residual life.

Every stage adds some information, until the highest level of knowledge is reached. Consequently, the aim of the Author was the definition of a vibration-based inspection (VBI) framework for the large civil structures. Herein, the four level of the Rytter's scale should be interpreted, considering the wide definition of damage adopted above. Thus, answering to the first level (Detection) means that something is changed in the normal operational conditions. For instance, it could be a change in the boundary condition (e.g. the detachment of a masonry wall), or cracks in the bearing walls, or a changing at the foundation level. As a result, the cases could paradoxically be infinite and for the cultural heritage the possible damages change from structure to structure. In that scenario, the knowledge of the structure by means of a deep survey play the major role for the monitoring strategies and the definition of the possible damage scenario.

1.3 Motivation of the thesis

In the section 1.2 it was pointed out the difficulties and the uncertainties in the definition of the performances of the existing buildings. It was pointed out that the degree of uncertainty is even bigger for the cultural heritage buildings, because of the impossibility to have a detailed knowledge of the structure.

In one hand, the challenge is even extreme, and it seems a problem without any solution. On the other hand, the massive number of cultural heritage buildings widespread across the EU need the definition of a suitable framework to answer, at least at the first level in the Rytter's scale. Moreover, as introduced in section 1.1, the economic loss for the ruin of a representative monument will produce an immeasurable impact both in terms of human lives both in terms of damages.

However, the technology advances give us the opportunity of using high-precision measurements instruments and high-speed computers with huge storage capabilities. For these reasons, several Authors [15] [16] [17] [18] have begun to face the problem, even if, a full definition of an integrated framework is still an open issue. Moreover, the damage identification in the case of the large engineering structures is limited by the dimension of the structure itself and the limited number of devices usually available. This issue known as scalability challenge is still a challenge for the scientific community. Hence, the attention on the topic is continuously increasing to overcome these issues and the research is addressed in three main branches:

1) *Development of new sensing technologies:* at the time, the research is mainly focused on the smart materials (smart bricks, concrete etc.). These new materials can reveal the damage itself, without the aid of an external monitoring system. Another area studied in the last years is the employ of fibreoptic sensors for detailed measures that are not sensitive to the environmental effects.
2) *Development of robust and accurate modal parameter identification*: in the last ten years different Authors proposed several automated OMA procedures in order to develop robust and accurate MPI

techniques. In some cases, also the modal tracking (MT) algorithm is deepened to improve the automated SHM framework.

3) *Study on new damage sensitive properties*: The correlation between the damage and the measured properties is still open, even if a lot of efforts in that field were made in the last century. The vibration-based damage detection (VBD) was fully explored with the sensors available at the time but the introduction of new instruments con lead to the definition of new features extracted from the measured data or directly measured.

Each branch is overlapping with others, that is clear for the cases 1) 3) but also the automated extraction of the features deals with the novelties of the other two cases.

1.4 Aims of the thesis

The thesis aims firstly to investigate how the damage detection in the Cultural Heritage structure can be improved by means of a fully automated procedure set with the data collected during some representative observation periods. Then for the historic masonry towers, the enabling of the localization and quantification of damage has been investigated by means of a local and global measurements.

Hence that two main steps can be resumed as follows:

- ➢ Enhancing the feature extraction of the identified Modal Parameters (MP) to minimize the both the external noises and the model bias (STAGE 1)
- ➢ Enabling the damage location and quantification in the case of the historic masonry tower with a local measure (STAGE 2)

Lastly, the damages levels have been qualitatively quantified in terms of reduction of the seismic capacity to give an indication about the level of damage that is supposed to be identified with the proposed algorithm. Hence, the method can be applied partially or totally for different purposes. Firstly, the application of only the first stage can be used in the case of networks of long-term monitoring system to assess the damages in a post-earthquake scenario. Aiming to list the priority of interventions in each monitored structure. Consequently, the long-term monitoring systems should be composed with few devices with a limited cost to build a monitoring network on a territorial level. Thus, the monitored buildings should be a homogeneous group of similar structural type and widespread over the territory. For this reason, the damage detection of the ancient masonry towers with a limited number of accelerometers accomplish all these requirements and it could be enabled with the first stage of the proposed procedure.

Moreover, the second stage based on a local measurement, aims to investigate the capability of localize both the local and the global damages mechanisms that are typical of the CH buildings. Although the procedure workflow aims to be as general as possible to be implemented for others kind of buildings with a carefull selection of the measurements that should be performed to enable the second level of the procedure.

1.5 Methodology of the thesis

The methodology of thesis has been derived from the Structural Health Monitoring (SHM) theory that was firstly formulated by Farrar et al. [19] in the middle nineties. That work has generalized and resumed a lot of disciplines employed in different fields for the damage detection on different structures. For example, the *Condition monitoring* (CM) applied to the rotating machinery and the *Health and usage monitoring system* (HUMSs) applied to rotorcraft drive trains. Nonetheless, some Authors [20] [21], using the machine learning theory, distinguish among two different classes of problems, for the damage identification:

- *The Supervised learning*: When both the data of the undamaged state C_0 and the damaged configuration C* are available.
- *The Unsupervised learning*: When the data from the undamaged configuration C_0 are not available.

Another classification arises again from the machine learning theory, considering if the damage detection performed in the statistical phase is based on a physical model or if it is based only on the data.

- *Data-driven SHM*: The detection of the damage is based only on the data analysis and it is not needed the use of any model as in the inverse or modal based problem.
- *Model-based SHM*: The detection of damage is obtained through the updating of model, usually a FE model update with the measured monitoring data.

Following the data- driven SHM pattern, the thesis aims to develop a framework (Figure 1-VI) to enhance the damage detection and localization for the Cultural Heritage buildings.

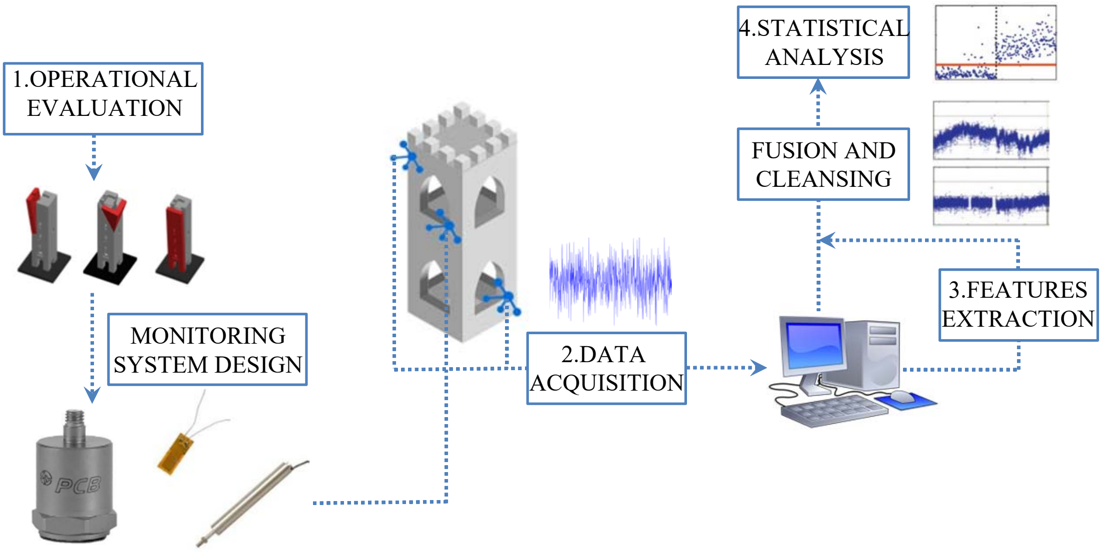

Figure 1-VI The SHM as recognition pattern the four main phases: 1-Operational Evaluation, 2-Data acquisition, 3- Feature extraction and 4- statistical analysis.

Particularly the thesis is focused on the historic masonry towers and the investigations are performed both on real scale tests and on numerical simulated response.

In order to enhance the damage detection, the proposed methodology aims to reduce the variability of the extracted damage sensitive features. For that stage has been considered the frequency as the most reliable damage sensitive feature and it has been investigated how it can be minimized the noise's effects. Hence, the novelties introduced can be resumed as follows:

- Establish a setup procedure to minimize the model bias
- Define some suitable threshold for the input to avoid noisy modes
- Define a parameter to select the extracted damage sensitive features

Then the second stage has been investigated by means of a direct measurement of the modal curvature.

1.6 Limitation of the method

As it has been stated in the previous sections the proposed procedure aims to develop a procedure to improve the damage detection and localization from the analysis of some of the most recurrent damage scenarios that can be observed in the old masonry buildings. The thesis has been focused on the masonry tower to analyse, in one hand a class of structures with a simple dynamic that are prone to earthquakes damages, on the other hand a structure that is very common in the old city centre.

Anyway, the assessment of the feasible damage scenario in the cultural heritage is not so easy and is strictly dependent on the construction techniques and on cracking pattern that can arise from unpredictable causes. Furthermore, the old masonry structures exhibit high level of variability both on the materials both on the structural schemes that should be considered. That problems affect the major part of the structures and could represent a general limitation of the SHM framework to the cultural heritage.

Regarding the work developed on this thesis some specific limitations deal with:

- The environmental effects are neglected
- The validation of the proposed method has been performed on numerical FE models

The first problem has not been faced but there is a wide literature about it and several statistical methods can be applied to clean the extracted modal parameters from that disturbances. However, a complete review about the topic has been written in Section 2.6. but it was not applied because of the limited number of data available from the real long-term monitoring system (Section 4.4).

While the second point was necessary to reproduce simulated response under ambient vibrations of the damaged and undamaged structure. In that way, some other problems dealing with the numerical modelling arise and some others source of errors have been introduced. Furthermore, the quantification of the level of damage and the way of modelling it is not a simple task. Anyway, the thesis attempt to handle that kind of problems giving some indications even qualitative that can be useful for the researchers.

1.7 Organization of the text

The discussion of the topic introduced herein is developed in the following chapters:

- **Chapter 1:** In the first chapter is introduced the problem and the motivation behind the work of thesis. The goal of the thesis is herein described, trying to resume the work in a scientific question. The SHM methodology is introduced with the necessary references for further information. The aim of this chapter is giving a global view of the problem to the reader, introducing the methodology that will be used for answering to the scientific question.

- **Chapter 2:** This chapter deals with the literature survey, that it is split in three different paragraphs. The first deals with the investigation of the dynamic properties more sensitive to damage (*What should be measured?*). The second describes the available sensing instruments (*How should be measured?*), focusing on the new trends. The last is a review of the proposed techniques for the operative modal analysis (OMA).
- **Chapter 3:** In this chapter have been briefly reviewed the available automated procedure for the extraction of the dynamic features proposed by the researchers in the last years. Then has been introduced a new automated procedure capable that minimize the variance of the extracted modal parameters. Moreover, it has been validated through the analysis of simulated response on a FE model of a masonry tower. Lastly an automated procedure to analyse the long-term data has been proposed, aiming the definition of adaptive thresholds defined on a suitable observation period.
- **Chapter 4:** This chapter shows some application to the Cultural Heritage of the automated procedure for the extraction of the modal parameters on some real cases of study. Then the method has been applied to a real ten months dataset collected from the long-term monitoring system installed on an old masonry tower. The obtained results have been discussed and some preliminary conclusions have been drawn.
- **Chapter 5:** In this chapter the feasible earthquake damages for the masonry tower have been described. First of all, the most common damage scenarios have been shown, according with the results available in literature. Then a simplified model representing a confined masonry tower has been analysed and the capability of the most common damage sensitive features have been tested after a simulated earthquake with different intensity and spectral contents. Lastly a 3D FE model of a masonry tower has been tested with a limited number of damage scenarios inferred. Thus, the response under random vibrations are collected and the proposed procedure has been applied before and after the damage.
- **Chapter 6:** The last chapter is the discussion of the results and the analysis of the future developments.
- **Appendix I:** Matlab codes
- **Appendix II:** Tables of the results

In Figure 1-VII the road map of the thesis is described with the contents of each chapter to aid the reader. The second chapter dealing with a wide review of the problem from different perspective, can be partially skipped depending on the reader’s background.

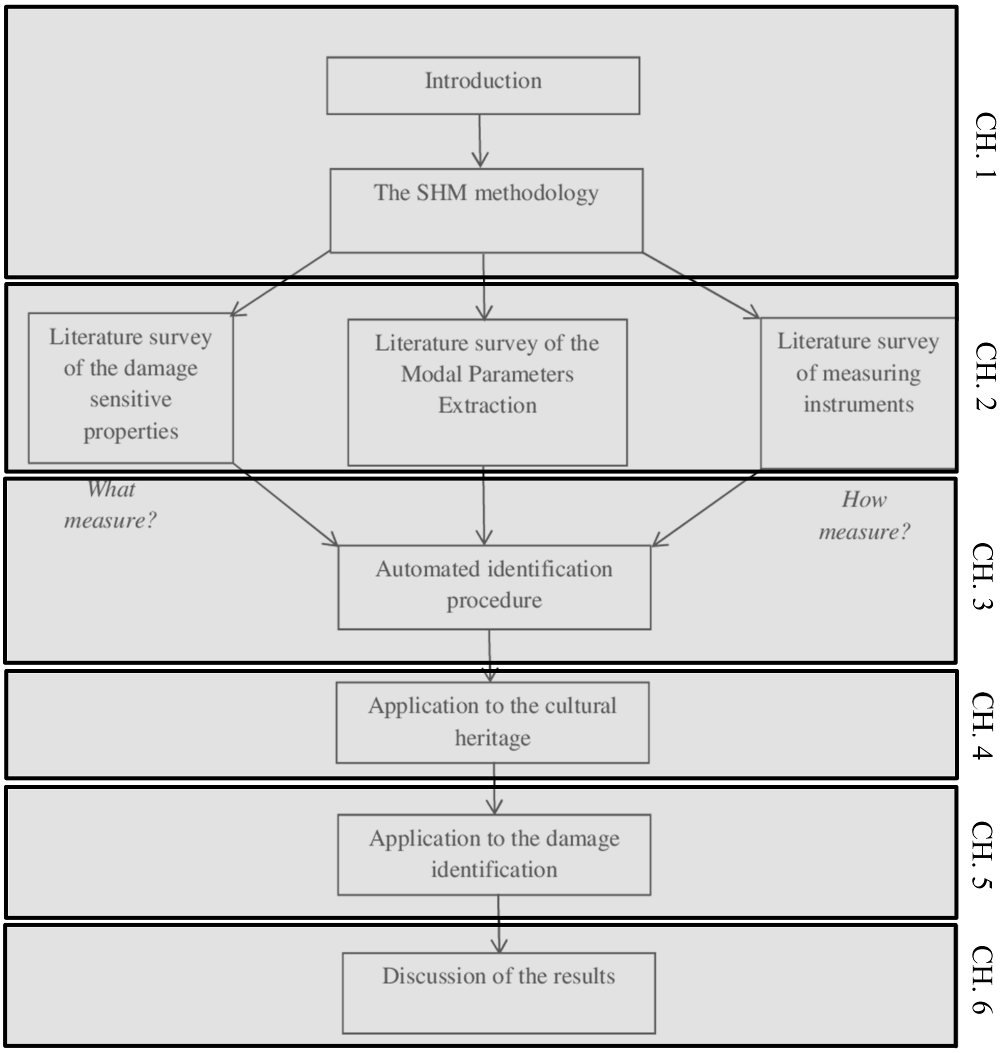

Figure 1-VII Outline of the thesis.

1.8 References

[1] G.M. Calvi, M. Moratti, G.J. O'Reilly, N. Scattarreggia, D. Malomo, R. Monteiro, R. Pinho, Once upon a time in Italy: the tale of the Morandi bridge, Submitt. to Struct. Eng. Int. 8664 (2018).

[2] L. Binda, A. Anzani, A. Saisi, Failures due to long-term behaviour of heavy structures: the Pavia Civic Tower and the Noto Cathedral, Struct. Stud. Repairs, Maint. Herit. Archit. VIII. 66 (2003) 99–108.

[3] V.M. Joshi, Historic Earthquake-Resilient Structures in Nepal and Other Himalayan Regions and Their Seismic Restoration, 33 (2017) 299–319.

[4] D. Sabia, T. Aoki, R.M. Cosentini, R. Lancellotta, Model Updating to Forecast the Dynamic Behavior of the Ghirlandina Tower in Modena, Italy, J. Earthq. Eng. 19 (2015) 1–24.

[5] L. Binda, Learning from Failure Masonry Structures, WITpress, Southampton, n.d.

[6] M. Acito, M. Bocciarelli, C. Chesi, G. Milani, Collapse of the clock tower in Finale Emilia after the May 2012 Emilia Romagna earthquake sequence: Numerical insight, Eng. Struct. 72 (2014) 70–91.

[7] F. Ubertini, N. Cavalagli, G. Comanducci, A.L. Materazzi, A.L. Pisello, F. Cotana, Automated post-earthquake damage detection in a monumental bell tower by continuous dynamic monitoring, in: Struct. Anal. Hist. Constr. Anamn. Diagnosis, Ther. Control. - Proc. 10th Int. Conf. Struct. Anal. Hist. Constr.

SAHC 2016, 2016.

[8] E. Bassoli, L. Vincenzi, A.M. D'Altri, S. de Miranda, M. Forghieri, G. Castellazzi, Ambient vibration-based finite element model updating of an earthquake-damaged masonry tower, Struct. Control Heal. Monit. 25 (2018) 1–15.

[9] G. Castellazzi, A.M. D'Altri, S. de Miranda, F. Ubertini, An innovative numerical modeling strategy for the structural analysis of historical monumental buildings, Eng. Struct. 132 (2017) 229–248.

[10] L. Zanotti Fragonara, G. Boscato, R. Ceravolo, S. Russo, S. Ientile, M.L. Pecorelli, A. Quattrone, Dynamic investigation on the Mirandola bell tower in post-earthquake scenarios, Bull. Earthq. Eng. 15 (2017) 313–337.

[11] A. Preciado, S.T. Sperbeck, A. Ramírez-Gaytán, Seismic vulnerability enhancement of medieval and masonry bell towers externally prestressed with unbonded smart tendons, Eng. Struct. 122 (2016) 50–61.

[12] P.B. Lourenco, G. Karanikoloudis, Seismic behavior and assessment of masonry heritage structures. Needs in engineering judgement and education, RILEM Tech. Lett. 3 (2019) 114–120.

[13] K. Farrar, C. R.;Warden, Structural Health Monitoring: A Machine Learning Perspective, New York, 2013.

[14] A. Rytter, Aalborg Universitet Vibrational Based Inspection of Civil Engineering Structures Rytter , Anders, Aalborg Universitet, 1993.

[15] C. Gentile, M. Guidobaldi, A. Saisi, One-year dynamic monitoring of a historic tower: damage detection under changing environment, Meccanica. 51 (2016) 2873–2889.

[16] M.G. Masciotta, J.C.A. Roque, L.F. Ramos, P.B. Lourenço, A multidisciplinary approach to assess the health state of heritage structures: The case study of the Church of Monastery of Jerónimos in Lisbon, Constr. Build. Mater. 116 (2016) 169–187.

[17] F. Ubertini, G. Comanducci, N. Cavalagli, A.L. Pisello, A.L. Materazzi, F. Cotana, Environmental effects on natural frequencies of the San Pietro bell tower in Perugia, Italy, and their removal for structural performance assessment, Mech. Syst. Signal Process. 82 (2017) 307–322.

[18] R. Ceravolo, G. De Lucia, M.L. Pecorelli, Issues on the modal characterization of large monumental structures with complex dynamic interactions, Procedia Eng. 199 (2017) 3344–3349.

[19] H. Sohn, C.R. Farrar, F.M. Hemez, J.J. Czarnecki, A Review of Structural Health Monitoring Literature : 1996-2001, 2003.

[20] K. Worden, C.R. Farrar, G. Manson, G. Park, The fundamental axioms of structural health monitoring, Proc. R. Soc. A Math. Phys. Eng. Sci. 463 (2007) 1639–1664.

[21] A. Deraemaeker, K. Worden, New trends in vibration based structural health monitoring, Springer Science & Business Media, 2012.

Chapter 2

Literature review

2.1 Introduction

This chapter is a review both of some basic concepts both a literature survey of the main contribution by the Authors in the last years in the damage identification through vibration signatures. The first part (*Section 2.2*) is a brief recall of some background about the dynamics of structures and modal testing, focusing on the random vibration analysis. This part can be skipped by the reader, because of its basic contents of structure dynamics, but in Author's opinion it contains the references for reviewing some background.

Then the major contributes in the modal identification techniques are analysed (*Section 2.3*) introducing the issues dealing with the automatization of the procedure for SHM purposes. A brief section (*Section 2.4*) is devoted to the overview of the most employed sensors and devices for dynamic long-term purposes. Hence a review (*Section 2.5*) of the most investigated damage sensitive features is performed to understand the capability of each in detecting damage. The environmental effects (*Section 2.7*) on the damage sensitive features is analysed furnishing the linear and non-linear multivariate statistical tools able to clean the data and to reduce them in low-dimension vectors. The last section (*Section 2.8*) is focused on the proposed procedures for the damage detection in the SHM framework.

2.2 Review of Dynamics for linear systems

Considering a multi-degree of freedom system (MDOF) represented by *N* generalized coordinates gathered in the vector $u(t)\ \epsilon\mathcal{R}^{Nx1}$, the dynamic equilibrium following the D'Alembert's principle can be expressed as follows:

$$\mathbf{M}\ddot{u}(t) + \mathbf{C}\dot{u}(t) + \mathbf{K}u(t) = \mathbf{B_1}F(t) - \mathbf{M}\mathbf{B_2}\ddot{u}_g(t) \tag{1}$$

Where $\mathbf{M}\epsilon\mathcal{R}^{NxN}$ is the mass matrix, $\mathbf{C}\epsilon\mathcal{R}^{NxN}$ is the damping matrix, $\mathbf{K}\epsilon\mathcal{R}^{NxN}$ is the stiffness matrix, $\mathbf{B_1}\ \epsilon\mathcal{R}^{Nxm}$ and $\mathbf{B_2}\ \epsilon\mathcal{R}^{Nx3}$ are Boolean matrices with all zeros and ones corresponding to the degrees of freedom where the forces are applied, $\ddot{u}_g(t)\epsilon\mathcal{R}^{3x1}$ is the vector containing the ground acceleration and $F(t)\mathcal{R}^{mx1}$ is the applied dynamic force. That representation implies a linearity in the elastic and damping forces, obtaining a linear system. If the properties of the system are not variable during the time, the system is called time-invariant. All the dynamic systems represented by equation (1) faced in that book must be considered as linear-time invariant systems.

The equation (1) represents the dynamic equilibrium at each time instant (Figure 2-I (a)): in one side the inertia, damping and elastic forces should equalize the external dynamic forces at each degree of freedom (DOF). With a linear transformation, under certain hypothesis (*cfr. section 2.2.1*), it is possible to decouple the system of differential equations in *N* differential equations of a Single Degree Of Freedom System (Figure 2-I (b)).

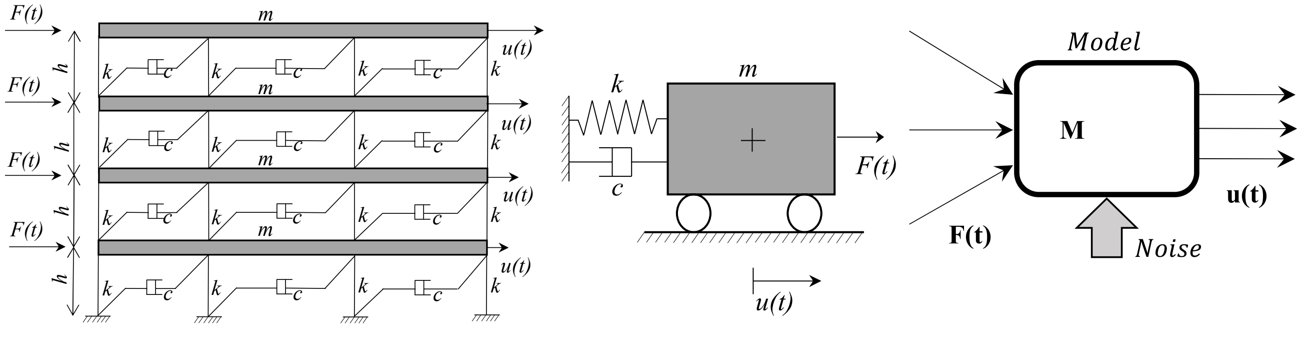

Figure 2-I (a) Multi-Degree of Freedom (MDOF) planar representation of a shear-type building (b) SDOF scheme with lumped mass damping and stiffness (c) Theory of the system representation of a Multiple Input- Multiple Output (MIMO) system.

Some Authors [1] [2] [3] [4] describe the dynamic system as a input-output box scheme (Figure 2-I (c)) derived from the theory of system identification [5]. If the model is calibrated on the physical laws that characterize the phenomenon, it is called *white box model*. On the other hand, if the model is calibrated without knowing any physics of the problem it is called *black box model*, instead if some physics is known it is called *grey box model*. The time-continuous linear invariant physical based systems are typical of the classical dynamics of structure (Figure 2-I (a) (b)). Instead the discrete- time linear invariant systems deal with the modal identification based on the recorded signals.

The dynamic loads that can be applied to a civil structure can have different nature and can be modelled in the following manner:

- *Periodic loads* characterized by the repetition of the signal over a period of vibration. Some examples of periodic forces applied to civil structures can be the transmitted forces from the rotating machinery.
- *Impulsive or step loads* characterized by high intensity over a reduced time of application. Mathematically is expressed as a Dirac's delta function $\delta(t-\tau)$, that is a generalized function with a unitary intensity centred at $t=\tau$. This is the case of the blast or earthquake loads, that excite instantaneously the structures leaving them vibrating on their own after the shock.
- *Pseudo-random periodic loads* are periodic signals randomly mixed. This is the case of the waves loads in the offshore structures.
- *Random vibrations* are described in statistical terms as the result of a stationary stochastic process. The traffic induced vibration, the wind loads, belong to that category of dynamic loads.

The total response of a MDOF system to this kind of loads can be expressed as the sum of the free vibration solution problem (*transient*) and the solution of the forced vibration problem (*steady state*). The full description of the solutions is beyond the aim of this book and it can be found in [6].

2.2.1 Classically Damped Systems

In the case of classical damping systems[1] [7] the equation of motion can be decoupled with the classical modal analysis, the damping matrix become real-valued and the eigenvalues and the eigenvectors are the same of the

---

[1] The Damping matrix of a classically damped system must satisfy the following identity:

$$\mathbf{C}\mathbf{M}^{-1}\mathbf{K}=\mathbf{K}\mathbf{M}^{-1}\mathbf{C}$$

undamped case. The global response can be faced as the linear superposition of the modal coordinates $q_n(t)$ of the *N* modes through the modal matrix $\boldsymbol{\Phi}\epsilon\mathcal{R}^{NxN}$:

$$u(t) = \boldsymbol{\Phi}q(t) = \sum_{n=1}^{N} \phi_n q_n(t) \tag{2}$$

The solution eigenvalue problem (3) allows to evaluate the natural frequencies and the mode shapes.

$$[K - \omega^2 M]\boldsymbol{\Phi}q(t) = \emptyset \tag{3}$$

The mode shapes are real-valued only in the case of classically damped systems anyway they are complex-valued. Once the frequencies and the mode shapes are known, by using the orthogonality property, the equation of motion can be decoupled in a system of homogeneous differential equations describing the motion of a Single Degree of Freedom (SDOF) system.

$$\begin{gathered}\boldsymbol{\Phi}^{\boldsymbol{T}}\mathbf{M}\boldsymbol{\Phi}\ddot{q} + \boldsymbol{\Phi}^{\boldsymbol{T}}\mathbf{C}\boldsymbol{\Phi}\dot{q} + \boldsymbol{\Phi}^{\boldsymbol{T}}\mathbf{K}\boldsymbol{\Phi}q = \boldsymbol{\Phi}^{\boldsymbol{T}}\mathbf{B_1}F(t) - \boldsymbol{\Phi}^{\boldsymbol{T}}\mathbf{M}\mathbf{B_2}\ddot{u}_g(t)\\ \boldsymbol{M_n}\ddot{q}_n + \boldsymbol{C_n}\dot{q}_n + \boldsymbol{K_n}q_n = \boldsymbol{\Phi_n^T B_1}F(t) - \boldsymbol{\Phi_n^T M B_2}\ddot{u}_g(t)\end{gathered} \tag{4}$$

Multiplying the equation (4) for the inverse of the modal mass matrix $\boldsymbol{M_n^{-1}}$ it is possible to derive the following equation:

$$\begin{gathered}\ddot{q}_n + \boldsymbol{C_n}\dot{q}_n + \boldsymbol{K_n}q_n = \boldsymbol{\gamma_{1n}}F(t) - \boldsymbol{\gamma_{2n}}\ddot{u}_g(t)\\ \boldsymbol{\gamma_{1n}} = \boldsymbol{M_n^{-1}\Phi_n^T\, B_1} \quad \boldsymbol{\gamma_{2n}} = \boldsymbol{M_n^{-1}\Phi_n^T\, M\, B_2} \quad \boldsymbol{C_n} = \boldsymbol{diag}(2\xi_n\omega_n) \quad \boldsymbol{K_n} = \boldsymbol{diag}(\omega_n^2)\end{gathered} \tag{5}$$

Where the matrices $\boldsymbol{\gamma_1}$ and $\boldsymbol{\gamma_2}$ represents the modal participating factors respectively for the dynamic forces and the ground motion accelerations. In the case of the general damping the equation of motion will be described in the state space form and the eigenvectors will be expressed in a conjugate complex form.

2.2.2 Non-Classically Damped Systems

In the case of system without classic damping, the damping matrix is not anymore diagonalized by the modal matrix $\boldsymbol{\Phi}$. The problem should be faced with the introduction of the state space formulation [8] and the system of *N* second order differential equations become a 2*N* system of first order differential equations.

$$\begin{gathered}\mathbf{A}\dot{x}(t) + \mathbf{B}x(t) = F(t)\\ u(t) = \mathbf{P}x(t)\end{gathered}$$

Where:

$$x(t) = \begin{pmatrix}\dot{u}(t)\\ u(t)\end{pmatrix} \quad \mathbf{A} = \begin{pmatrix}\emptyset & \mathbf{M}\\ \mathbf{M} & \mathbf{C}\end{pmatrix} \quad \mathbf{B} = \begin{pmatrix}-\mathbf{M} & \emptyset\\ \emptyset & \mathbf{K}\end{pmatrix} \quad F(t) = \begin{pmatrix}\emptyset\\ \mathbf{B_1}F(t) - \mathbf{M}\mathbf{B_2}\ddot{u}_g(t)\end{pmatrix} \tag{6}$$

$$\mathbf{P} = (\emptyset \;\; \mathbf{I})$$

The second of the (6) is the so call observability equation that links the 2N state space with the measured response vector. Expanding the domain to the state space will bring some simplification for the solution of the differential equation that now are of the first order. The solution of the free decay is calculated from the results of the eigenvalue problem in the state space.

$$x(t) = \boldsymbol{\varphi} e^{\lambda t} \rightarrow \ \boldsymbol{\varphi} = \begin{pmatrix} \boldsymbol{\lambda\phi} \\ \boldsymbol{\phi} \end{pmatrix} \tag{7}$$

The upper part of the modal $\boldsymbol{\varphi} \epsilon\ \mathbb{C}^{2Nx2N}$ matrix contains the mode shapes velocities and the lower part the mode shapes. The eigenvalue matrix $\boldsymbol{\lambda} \epsilon\ \mathbb{C}^{2Nx2N}$ is a diagonal matrix with dimension 2N that in the case of underdamped system are complex conjugate, leading to complex conjugate eigenvectors. In the case of a non-classically damped system, the modal mass, modal damping and modal stiffness matrices are no more real diagonal matrices but full complex matrices. The modal expansion became the sum over 2N conjugate complex modal coordinates.

$$x(t) = \boldsymbol{\varphi} q(t) = \sum_{n=1}^{2N} \varphi_n q_n(t) \tag{8}$$

The same calculation made in the previous section can be done considering that the system matrices cannot be diagonalized and the expansion in a doubled dimension considering that the eigenvalue and the eigen matrices are complex conjugate.

2.2.3 Time domain analysis

Considering a classically damped system it is possible to perform the modal decomposition (2) in order to compute the solution for each DOFs. Separating the two right members of equation (1) it is possible to face the periodic forces using the Fourier's series, superposing the solution for different natural frequencies. On the other hand, the non-periodic excitations should be treated as arbitrary forces.

The forced solution of the (1) in the general case of an arbitrary force is force known as the convolution or Duhamel's integer.

$$u(t) = \int_{-\infty}^{+\infty} F(\tau)\, h(t-\tau) d\tau = (F * h)(t) \tag{9}$$

Where $h(t)$ is known as the Impulsive Response Function (IRF) of the system and $F(t)$ is the amplitude of the arbitrary force at the selected time instant. The forced response to an arbitrary force is then the superposition of the IRF multiplied for the force amplitude at the different time.

$$\begin{aligned} h(t-\tau) &= \frac{1}{m\omega_D} e^{-\xi\omega_n(t-\tau)} sin[\omega_D(t-\tau)] \quad t \geq \tau \qquad (a) \\ h(t-\tau) &= -\frac{1}{\omega_D} e^{-\xi\omega_n(t-\tau)} sin[\omega_D(t-\tau)] \quad t \geq \tau \qquad (b) \end{aligned} \tag{10}$$

The equation (10) and (10) describe the impulse response for a SDOF system in the case of a periodic force and a ground motion respectively. In both cases the response is a damped sinusoid starting with initial zero displacements and velocities at the time instant t. The global response of the system will be the superposition of the convolution integrals of each modal coordinate through the modal matrix.

The arbitrary force can be interpreted as the sum of infinite periodic forces with different periods, so this case can be considered an extension of the periodic forces.

2.2.4 Frequency domain analysis

Performing the Fourier transform of both members of equation (5), it is possible to obtain the following relation between the modal forces and coordinates.

$$-\omega^2 Q_n(\omega) + \boldsymbol{C_n} i\,\omega\, Q_n(\omega) + \boldsymbol{K_n}\, Q_n(\omega) = \boldsymbol{\gamma_{1n}} F(\omega) - \boldsymbol{\gamma_{2n}} \ddot{u}_g(\omega) \tag{11}$$

Exploiting the derivation properties of the Fourier's transform the differential problem become algebraic.

$$Q_n(\omega) = \frac{1}{-\omega^2 + \boldsymbol{C_n} i\omega + \boldsymbol{K_n}} \left[\boldsymbol{\gamma_{1n}} F(\omega) - \boldsymbol{\gamma_{2n}} \ddot{u}_g(\omega)\right] \tag{12}$$

The convolution operator in the time domain is then substituted by a simple multiplication between the input and the so called frequency response function (FRF) [9] or mechanical admittance [10] $H_n(\omega)$.

$$H_n(\omega) = \frac{1}{-\omega^2 + \boldsymbol{C_n} i\omega + \boldsymbol{K_n}} = \frac{1}{-\omega^2 + 2\,\xi_n \omega_n \omega\, i + \omega_n^2} \tag{13}$$

This complex function maps the system response based on the system dynamic properties k, m, ξ and the frequency content of the input ω. The transformation consists in a magnification and in a rotation, the first operation is represented by the modulus (or *magnitude spectrum*) $|\, H_n(\omega)|$ and the second by the phase angle (or *phase spectrum*) δ_n.

$$\begin{gathered} |\, H_n(\omega)| = \sqrt{H_n(\omega)\, H_n(\omega)^*} = \frac{1}{\sqrt{(\omega_n^2 - \omega^2)^2 + (2\,\xi_n \omega_n \omega)^2}} \\ \delta_n = \tan^{-1}\left(\frac{Im\{\, H_n(\omega)\}}{Re\{\, H_n(\omega)\}}\right) = \tan^{-1}\left(\frac{2\,\xi_n \omega_n \omega}{(\omega_n^2 - \omega^2)}\right) \end{gathered} \tag{14}$$

In some texts $|\, H_n(\omega)|$ is called dynamic magnification factor [11] or deformation response factor [6] using the ratio between the force and the natural frequency and expressing the magnification as a ratio between the dynamic and the equivalent static displacement.

The IRF and the FRF are a Fourier's pair expressing the relation between the external inputs and the outputs filtered by the dynamic behaviour of the system. For the sake of simplicity in this brief review the classical damping is described, and the modal expansion is performed reducing all the considerations to a simple SDOF system, but all the FRF for each modal coordinate can be gathered together finding the FRF matrix or the IRF matrix.

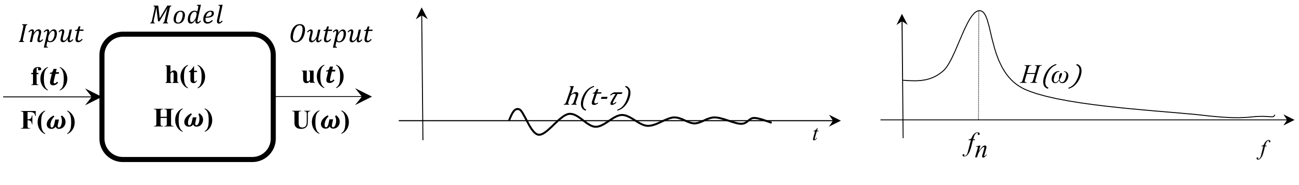

(a) (b) (c)

Figure 2-II (a) The input-output mode of the dynamic system (b) The impulsive response function for a SDOF (c) The Frequency Response Function for a SDOF.

The FRF can be expanded in a sum of functions of the following form with the partial fraction expansion theorem:

$$H_n(\omega) = \sum_{r=1}^{N} \frac{A_r}{(\lambda - \lambda_r)} \tag{15}$$

Where λ_r are the poles of the system and A_r the residues, the representation expressed by the (15) will be crucial in the modal identification techniques in the frequency domain.

2.2.5 Random vibrations

At the contrary of the dynamic deterministic forces, the random vibration signatures are described in probabilistic and statistical terms. Assuming that the time series $x(t)$ is a realization of a random process X, called random if it is impossible to know *a-priori* the values assumed over the time. Anyway, it is possible to characterize the probability density function $p(x)$ expressing the probability that a random variable is contained in the interval $[x; x + dx]$.

Gathering *n* different realization $\{x_1(t), x_2(t), x_3(t), \cdots, x_n(t)\}$ together it is possible to obtain an ensemble. If the mean across the ensemble is constant, implying that the mean value is independent from time the process is called *stationary*. That means that the properties of the random process are constant over the time. The random process is even called *ergodic* if the mean along the realization (or sample) is independent from time. If a random process is ergodic and stationary, then a sample is representative of the random process. If the probability distribution across the ensemble are Gaussian, the process is called *Gaussian random process*.

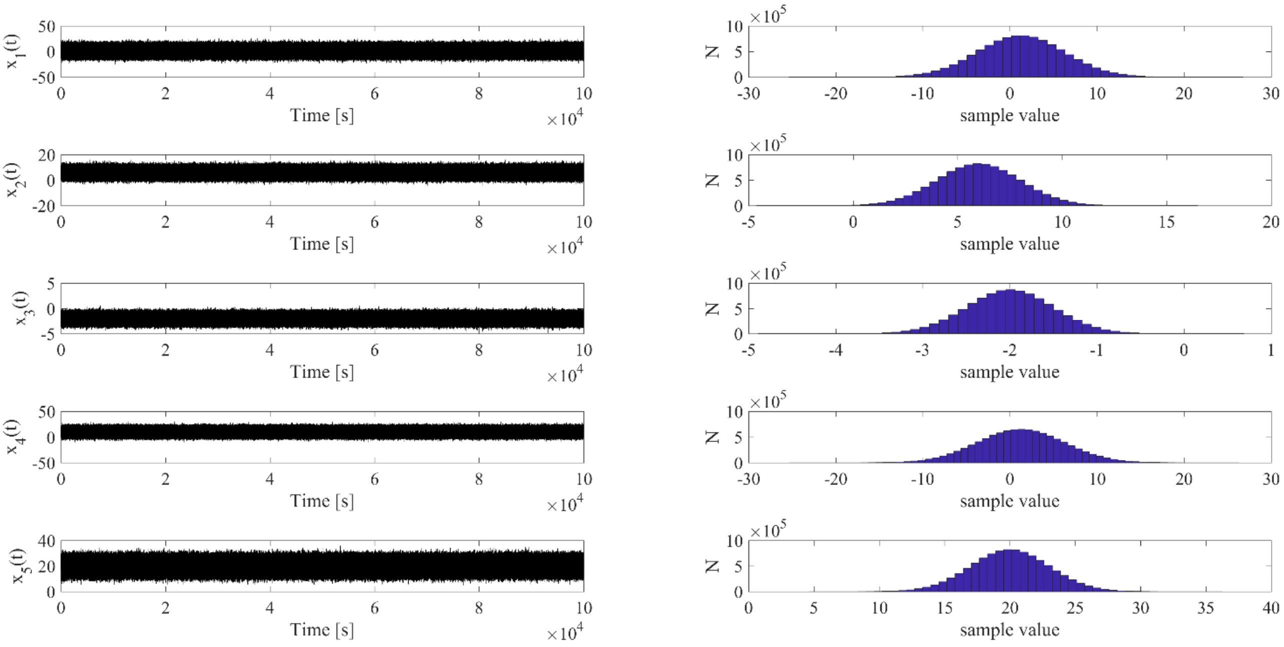

(a) (b)

Figure 2-III (a) An ensemble of five samples. (b) the probability density function along each sample, that is clearly Gaussian

In Figure 2-III is showed a simulated set of random signals gathered in one ensemble they represent a Gaussian random process, because the distribution of the values is clearly Gaussian as shown in the histogram graphs, but the stochastic process is neither stationary neither ergodic (the ensemble mean is dependent with time and the mean along the averages is clearly variable in every sample) . Hence a single sample is not representative of the random process X. It is worth to point it out that an ergodic process is also stationary, but a stationary process does not imply the ergodicity of the process.

A random process is characterized by its statistical properties or moments. The first four order moments are showed herein, it is worth to notice how it is possible to estimate that moments by time averaging, hypothesizing an ergodic random process.

$$\begin{gathered}\mu_x = \boldsymbol{E}[x(t)] = \int_{-\infty}^{+\infty} p(x)x(t)\,dx = \frac{1}{T}\int_0^T x(t)\,dt \\ Var(x(t)) = \boldsymbol{E}[(x(t)-\mu_x)^2] = \int_{-\infty}^{+\infty} p(x)(x(t)-\mu_x)^2\,dx = \frac{1}{T}\int_0^T (x(t)-\mu_x)^2\,dt \\ Skw\,(x(t)) = \boldsymbol{E}[(x(t)-\mu_x)^3] = \int_{-\infty}^{+\infty} p(x)(x(t)-\mu_x)^3\,dx = \frac{1}{T}\int_0^T (x(t)-\mu_x)^3\,dt \\ Kurtosis(x(t)) = \boldsymbol{E}[(x(t)-\mu_x)^4] = \int_{-\infty}^{+\infty} p(x)(x(t)-\mu_x)^4\,dx = \frac{1}{T}\int_0^T (x(t)-\mu_x)^4\,dt\end{gathered} \tag{16}$$

In general, the *k-th* order central moment is given by:

$$\mu_{xk} = \boldsymbol{E}[(x(t)-\mu_x)^k] = \int_{-\infty}^{+\infty} p(x)(x(t)-\mu_x)^k\,dx = \frac{1}{T}\int_0^T (x(t)-\mu_x)^k\,dt \tag{17}$$

It is worth to notice that the third and fourth order give information about the probability density function (pdf) of the process. If the skewness is equal to zero, the pdf is symmetric and if the kurtosis is equal to three the pdf is Gaussian. Values larger than three imply that the tails of the pdf are longer, and the signal is more intermittent, instead values smaller than three means that the signal may contain some sinusoidal fluctuations.

In the spectral analysis a fundamental role is played by the correlation functions expressing the correlation between two points in a sample and in some way the memory of the stochastic process.

For the time span $\tau = 0$ the correlation function reaches the maximum equalizing the variance of the random process. The correlation function tends to the square of the mean for the time span τ approaching to infinite.

$$\begin{gathered}R_{xx}(\tau) = E[x(t)x(t+\tau)] = \frac{1}{T}\int_0^T x(t)x(t+\tau)dt \\ R_{xy}(\tau) = E[x(t)y(t+\tau)] = \frac{1}{T}\int_{-\infty}^{+\infty} x(t)y(t+\tau)dt\end{gathered} \tag{18}$$

Because it is impossible to perform the Fourier's transform of the realization x(t) because the function is not limited and its area is not finite, the only way to characterize the frequency content is to perform the Fourier's transform to the autocorrelation function, that gives indirect information on the periodicity of the signal. Indeed, the auto correlation function and the power spectral density are two Fourier's pair. Considering that the auto correlation function is an odd function ($R_{xx}(\tau) = R_{xx}(-\tau)$) the power spectral density is real and equal to the $A(\omega)$ coefficient of the complex Fourier's transform.

$$\begin{gathered}S_{xx}(\omega) = \mathcal{F}[R_{xx}(\tau)] = \frac{1}{2\pi}\int_{-\infty}^{+\infty} R_{xx}(\tau)\,e^{-i\omega\tau}d\tau = \frac{1}{2\pi}\int_{-\infty}^{+\infty} R_{xx}(\tau)\,\cos\omega t\,d\tau = A(\omega) \\ R_{xx}(\tau) = \mathcal{F}^{-1}[S_{xx}(\omega)] = \int_{-\infty}^{+\infty} S_{xx}(\omega)\,e^{i\omega\tau}d\tau\end{gathered} \tag{19}$$

In the same way the cross correlation and the cross spectral density are two Fourier's pair. In the case of the cross correlation an important property is that $R_{xy}(\tau) = R_{yx}(-\tau)$ which leads to complex conjugate cross spectra ($S_{xy}(\tau) = S_{yx}(\tau)^*$). From that definitions, the area under the auto power spectra will be equal to the variance of the stochastic process.

$$\begin{gathered} S_{xy}(\omega) = \mathcal{F}[R_{xy}(\tau)] = \frac{1}{2\pi}\int_{-\infty}^{+\infty} R_{xy}(\tau)\, e^{-i\omega\tau} d\tau) \\ R_{xy}(\tau) = \mathcal{F}^{-1}[S_{xy}(\omega)] = \int_{-\infty}^{+\infty} S_{xy}(\omega)\, e^{-i\omega\tau} d\tau \end{gathered} \tag{20}$$

It is common to define a stochastic process based the distribution of energy among the frequencies. If the auto spectral density is condensed only in some frequencies the process is called *narrow band*. The auto correlation function of a narrow band process will be the sum of different sinusoids that slightly decreases until reaching the zero value for high time lags. Anyway, if the energy of the process is split over a wide range of frequencies, the process is called *broad band*. The autocorrelation function of a broad band process is a Dirac's delta, as an infinite impulse. If ideally the band of a broad band process spans from minus to plus infinity the process is called *white noise*.

In the real recorded signals, the length it is not infinite so the statistical properties of a random process can be estimated with suitable statistical indicators as the sample mean and the sample variance [12]. The error that is made with the estimated statistical values depends on the bandwidth B and the length of the signal T [13] [2].

$$\begin{gathered} \sigma[\hat{\mu}_x] = \frac{\sigma_x}{\sqrt{BT}} \\ \varepsilon_r[\hat{\sigma}_x^2] = \frac{\sigma_x}{\sqrt{BT}} \end{gathered} \tag{21}$$

For further details it is possible to see the major texts about the random analysis and stochastic dynamics [2,3,14].

2.2.6 Signal analysis

In the reality it is possible to obtain the signals as discrete functions (*discrete time series*) recording with a certain sampling frequency f_s. In one hand, the theory introduced in the previous sections is still valid in the discrete formulation; on the other hand, a source of error id introduced approximating the statistic with a finite number of samples. Hence the length of the signals and the sampling frequency plays an important role in the OMA and their choice should be taken carefully. The choice of a suitable sampling frequency allows to maximize the Signal-to-Noise Ratio (SNR) intended as the ratio between the true signal and the noise present in a record. Considering the noise as a broad band process with a fixed level of energy characterized by its variance σ^2, the spectral value G_w will be lower if the sampling rate f_s increase.

$$\sigma^2 = f_s G_w \;\rightarrow G_w = \frac{\sigma^2}{f_s} \tag{22}$$

The SNR can be formulated as the ratio between the maximum power of the signal G_s and the noise level G_w. Indeed, higher values of the SNR can be obtained using a reasonable sampling frequency that minimize the effects of the noise.

$$SNR = 20log_{10}\left(\frac{G_s}{G_w}\right) \tag{23}$$

The American National Standards (ANSI S2.47 [15]) suggests a minimum level of SNR equal to 5 Db, other Authors [9] fixed a reasonable value to 30-40 dB for the OMA tests. Anyway, a good level for OMA tests should be of 70-80 dB, allowing a correct modal identification of all the modes available in the analysed signals.

The signal should exhibit a suitable length to obtain a good estimation of the auto correlation function of the first mode (lowest frequency). Good results can be obtained when the minimum time series length is equal to:

$$T_{tot} > \frac{10}{\xi f_{min}} \tag{24}$$

It is useful to reduce the band of interest where the structural modes are present by considering a reduced sampling frequency f_c. To avoid the effects of the filter at the extremes of the frequency band of interest it is worth to resample the signals with a Nyquist frequency at least major than the 20% of the maximum values of the frequency band f_{max}.

$$f_c \geq 2.4 f_{max} \tag{25}$$

This operation is called down-sampling or decimation allowing a good compromise between minimizing the effects of noise enhancing a suitable frequency resolution.

The physics inside a signal is buried in the chaos of random noises contained in the signal itself; hence a filtering operation is required to find the interesting part of the signal. Usually a high-pass filter is performed to remove Digital Converter (DC) offsets and the trends due to the temperature effects on the electronic parts. Then a low-pass filter is performed to cut out the effects of the higher frequency outside of the band of interest for the modal identification enhancing the anti-aliasing filtering effects.

In the OMA procedure it is common to operate with digital signals derived from the Analog to Digital Converter (ADC), for that reason the most common filters are digital. Two main kind of digital filters are available: The Finite Impulse Response (FIR) and the Infinite Impulse Response (IIR) filters. The most common digital filters are a combination of FIR and IIR such as the Chebyshev filter, the Elliptical filter, the Bessel filter and the Butterworth filter. The difference among them is the slope of the cut-off branch, the presence of ripples and the phase distortion of the signals.

The entire signal processing theory for discrete signals is a complex topic that is beyond the scope of this thesis, further information can be found in [16].

2.3 Modal testing of civil structures

In the last fifty years a lot of effort were made in the field of the modal identification of large civil structures. The implementation of the Fast Fourier Transform (FFT) algorithm [17] gives a great contribution in the development of the Experimental Modal Analysis (EMA). These techniques are performed by using dynamic testing machines that generate a controllable dynamic input such as harmonic forces (eccentric mass shaker) or Impact (hydraulic shaker, impact hammer). Then the results are analysed in the frequency domain obtaining the Frequency Response Functions (FRFs) or the Impulsive Response Functions (IRFs) for the tested structure. As introduced in the previous section the relation between the dynamic forces and the response is linear through the complex transfer functions (or FRFs). Traditionally the EMA techniques are divided in different categories based on the number of input and measured output in the system: the Single Input- Single Output (SISO), the Single Input- Multiple Output systems (SIMO) and the Multiple Input-Multiple Output (MIMO) systems. Bendat and Piersol [14] introduce the fundamental theorems for the SISO, SIMO, MIMO system that related the spectral density of the output to the spectral density of the input through the FRFs:

$$\mathbf{S}_{\boldsymbol{yy}}(\mathbf{f}) = \mathbf{H}(\mathbf{f})^{*}\mathbf{S}_{\mathbf{xx}}(\mathbf{f})\mathbf{H}(\mathbf{f})^{\boldsymbol{T}} = \mathbf{H}(\mathbf{f})\mathbf{S}_{\mathbf{xx}}(\mathbf{f})\mathbf{H}(\mathbf{f})^{\mathbf{H}} \qquad (26)$$

The (26) expresses in the MIMO case, but for the other cases the formulation is the same with scalar equation instead of matrices.

From the late 90s the researchers spent a lot of effort to identify the structural dynamics under operative conditions without knowing the input force that was modelled as a Gaussian white noise input. The theory of random vibration contributes on the development of the output-only identification techniques, giving the theoretical basis of all the Operative Modal Analysis (OMA) techniques. From that perspective is possible to affirm that the OMA techniques based on the analysis of stochastic inputs are the counterpart of the EMA techniques based on deterministic inputs.

The EMA techniques for modal testing of large structures are almost abandoned because they need the use of heavy machinery to bring in the application point that in many cases is not easily accessible. At least they still in use for the modal tests of laboratory specimens, considering the small dimension and the accessibility of each point to test. Hence, the attention on the OMA techniques grew up and several techniques were proposed by the Authors. They can be split in two different classes base on two distinct classifications. The first deals with the domain of application, indeed it is possible to recognize the frequency domain and the time domain techniques. The second deals with a more specific discrimination based on the needs of setting parameters or not for the identification techniques, indeed two different categories are available: the parametric and non-parametric techniques. In the last decades the main efforts in that research field were made with the introduction of automated or semi-automated techniques that are based on parametric identification algorithm, but they can provide automatically the results with the setting of the minor number of parameters.

Within the context of this thesis, the adopted classification is the first because of its simplicity. In the next section some of the most relevant OMA techniques will be reviewed focusing on those used for the proposed automated identification procedure.

2.3.1 Time domain identification

The time domain identification techniques are based on the modelling of the data or the correlation functions among them with linear time invariant systems derived from the system identification and control theory [5]. This branch of the mathematical engineering is based on deriving numerical models that can be fitted to the measured data. These techniques require the definition of some parameters for the definition of the model that have generated the observations.

This category involves a complex and time-demanding calculations, but it is suitable to be implemented in the

Common languages of programming. Moreover, the equation of motion of a M-DOF system are suitable to be modelled in terms of numerical models. Among all the proposed techniques during the last decades, it is worth to mention the Next-ERA procedure [18,19], the ARMAV modelling [1] and the Stochastic Space Identification (SSI) [20]. In the next subsection a brief review focused on the SSI method is done to introduce some more details about this technique that will be used in this thesis.

2.3.1.1 The Stochastic Subspace Iteration (SSI)

The Stochastic Subspace Iteration methods (SSI) derive from the theory of the system control, referring to the classical input-output box scheme [20]. The discrete time invariant formulation for a linear system excited with ambient vibrations w_k considering a noise that affect the output v_k data can be described as follows:

$$\begin{gathered}\mathbf{x_{k+1}} = \mathbf{A}\,\mathbf{x_k} + \mathbf{w_k} \\ \mathbf{y_k} = \mathbf{C}\,\mathbf{x_k} + \mathbf{v_k}\end{gathered} \tag{27}$$

The state space vector $\mathbf{x_k} \in \mathcal{R}^{2N\text{x}1}$ represents the stochastic model at the discrete time k representing a *N* degree of freedom system with *l* measured DOFs, the vectors $\mathbf{x_{k+1}} \in \mathcal{R}^{2N\text{x}1}$ and $\mathbf{y_{k+1}} \in \mathcal{R}^{l\text{x}1}$ represent respectively the next state space and the observation vectors. The system matrix $\mathbf{A} \in \mathcal{R}^{2N\text{x}2N}$ links the evolution of the next states in the stochastic space, while the controllability matrix $\mathbf{C} \in \mathcal{R}^{l\text{x}2N}$ is the link with the external representation of the stochastic model defined by the *k-th* state space vector $\mathbf{x_k}$. The vectors $\mathbf{w_k} \in \mathcal{R}^{2N\text{x}1}$ and $\mathbf{v_k} \in \mathcal{R}^{l\text{x}1}$ are two white noise modeling the external input and the noise that usually affects the recorded signals. The statistical features of the input process are represented by the mean and the covariance matrix.

$$\mathbf{E}(\mathbf{v_k}) = \mathbf{0} \qquad \mathbf{E}(\mathbf{w_k}) = \mathbf{0} \tag{28}$$

$$\mathbf{E}\left[\begin{pmatrix}\mathbf{v_p} \\ \mathbf{w_p}\end{pmatrix}\begin{pmatrix}\mathbf{v_q^T} & \mathbf{w_q^T}\end{pmatrix}\right] = \begin{pmatrix}\mathbf{Q} & \mathbf{S} \\ \mathbf{S^T} & \mathbf{R}\end{pmatrix}\boldsymbol{\delta}_{\mathbf{pq}} \tag{29}$$

Where $\mathbf{E}(\cdot)$ is the expected value operator and $\boldsymbol{\delta}_{\mathbf{pq}}$ is the Kronecker delta equal to one if p=q anyway is equal to zero. If the process is stationary so that the covariance of the state space vector is independent from the time $\mathbf{E}[\mathbf{x_k}\,\mathbf{x_k^T}] = \boldsymbol{\Sigma}$ and the process is zero mean $\mathbf{E}[\mathbf{x_k}\,] = 0$ and considering the independence from the actual state of the inputs $\mathbf{E}[\mathbf{x_k}\,\mathbf{v_k^T}] = \mathbf{0}$ and $\mathbf{E}[\mathbf{x_k}\,\mathbf{w_k^T}] = \mathbf{0}$. The output covariance matrices of the response can be defined as:

$$\boldsymbol{\Lambda}_{\mathbf{i}} = \mathbf{E}[\mathbf{y_{k+i}}\ \mathbf{y_k^T}] \in \mathcal{R}^{l\text{x}l} \tag{30}$$

And the next state covariance matrix is defined as:

$$\mathbf{G} = \mathbf{E}[\mathbf{x_{k+1}}\ \mathbf{y_k^T}] \in \mathcal{R}^{2N\text{x}l} \tag{31}$$

These observations about the features of the stochastic process lead to the following properties:

$$\begin{gathered}\boldsymbol{\Sigma} = \mathbf{A}\boldsymbol{\Sigma}\mathbf{A^T} + \mathbf{Q} \\ \boldsymbol{\Lambda}_{\mathbf{0}} = \mathbf{C}\boldsymbol{\Sigma}\mathbf{C^T} + \mathbf{R} \\ \mathbf{G} = \mathbf{A}\boldsymbol{\Sigma}\mathbf{C^T} + \mathbf{S} \\ \boldsymbol{\Lambda}_{\mathbf{i}} = \mathbf{C}\,\mathbf{A^{i-1}}\mathbf{G}\end{gathered} \tag{32}$$

Gathering all the recorded signals in a block Henkel matrix $\mathbf{Y} \in \mathcal{R}^{2li\mathrm{x}j}$ is a crucial step in the subspace identification of a system. For definition, it can be split in two different parts one representing the observations of the past ($\mathbf{Y_{past}}$) and the other the predicted values ($\mathbf{Y_{future}}$).

$$\mathbf{Y}=\mathbf{Y}_{\mathbf{0}|\mathbf{2}i}=\frac{1}{\sqrt{j}}\overset{\xleftrightarrow{\qquad\quad j \qquad\quad}}{\left(\begin{array}{cccc} \boldsymbol{Y_0} & \boldsymbol{Y_1} & \cdots & \boldsymbol{Y_{j-1}} \\ \boldsymbol{Y_1} & \boldsymbol{Y_2} & \cdots & \boldsymbol{Y_j} \\ \vdots & \vdots & \ddots & \vdots \\ \boldsymbol{Y_{i-1}} & \boldsymbol{Y_i} & \cdots & \boldsymbol{Y_{i+j-2}} \\ \hline \boldsymbol{Y_i} & \boldsymbol{Y_{i+1}} & \cdots & \boldsymbol{Y_{i+j-1}} \\ \boldsymbol{Y_{i+1}} & \boldsymbol{Y_{i+2}} & \cdots & \boldsymbol{Y_{i+j}} \\ \vdots & \vdots & \ddots & \vdots \\ \boldsymbol{Y_{2i-1}} & \boldsymbol{Y_{2i}} & \cdots & \boldsymbol{Y_{2i+j-2}} \end{array}\right)}\begin{array}{c} \uparrow \\ \\ i \\ \\ \updownarrow \\ \\ i \\ \\ \downarrow \end{array}=\left(\frac{\mathbf{Y_{0|i-1}}}{\mathbf{Y_{i|2i-1}}}\right)=\left(\frac{\mathbf{Y_{past}}}{\mathbf{Y_{future}}}\right) \tag{33}$$

The extended (with *i*>*2N*) observability matrix $\mathbf{O_i} \in \mathcal{R}^{li\mathrm{x}2N}$ is defined as:

$$\mathbf{O_i}=\begin{pmatrix} \mathbf{C} \\ \mathbf{CA} \\ \mathbf{CA^2} \\ \vdots \\ \mathbf{CA^{i-1}} \end{pmatrix} \tag{34}$$

If the pair of matrices $(\mathbf{A}\ \mathbf{C})$ is observable it is possible to derive that $rank\ (\mathbf{O_i})=2N$. The reverse extended controllability matrix $\Delta_\mathbf{i}^\mathbf{c} \in \mathcal{R}^{2N\mathrm{x}li}$ is defined as:

$$\Delta_\mathbf{i}^\mathbf{c}=\begin{pmatrix} \mathbf{A^{i-1}G} \\ \mathbf{A^{i-2}G} \\ \vdots \\ \mathbf{AG} \\ \mathbf{G} \end{pmatrix} \tag{35}$$

If the pair of matrices $(\mathbf{A}\ \mathbf{Q^{1/2}})$ are controllable, all the dynamical modes of the system are excited by the noise process.

The orthogonal projection $\boldsymbol{P_i} \in \mathcal{R}^{li\mathrm{x}j}$ of the raw space generated by the future observations $\mathbf{Y_f} \in \mathcal{R}^{li\mathrm{x}j}$ onto the raw space generated by the past observations $\mathbf{Y_p} \in \mathcal{R}^{li\mathrm{x}j}$ is equal to:

$$\boldsymbol{P_i}=\mathcal{Y}_f/\mathbf{Y_p}=\mathbf{Y_f}\mathbf{Y_p^T}\left(\mathbf{Y_p}\mathbf{Y_p^T}\right)^{\dagger}\mathbf{Y_p} \tag{36}$$

The obtained projection is then weighted with two matrices $\mathbf{W_1} \in \mathcal{R}^{li\mathrm{x}li}$ and $\mathbf{W_2} \in \mathcal{R}^{j\mathrm{x}j}$, then a singular value decomposition is performed obtaining the rank of weighted projection analyzing the singular values matrix.

$$\mathbf{W_1}\boldsymbol{P_i}\mathbf{W_2}=\begin{pmatrix}\mathbf{U_1} & \mathbf{U_2}\end{pmatrix}\begin{pmatrix} \mathbf{S_1} & \mathbf{0} \\ \mathbf{0} & \mathbf{0} \end{pmatrix}\begin{pmatrix} \mathbf{V_1^T} \\ \mathbf{V_2^T} \end{pmatrix}=\mathbf{U_1}\mathbf{S_1}\mathbf{V_1^T} \tag{37}$$

The number of the singular values different from zero is the model order *n* representing the dimension of the projected raw space.

The obtained projection is equal to the extended observability matrix multiplied to the forward Kalman filter state sequence.

$$\boldsymbol{P_i} = \mathbf{O_i}\widehat{\mathbf{X}}_\mathbf{i} \tag{38}$$

Furthermore, the extended controllability matrix can be calculated as follows:

$$\Delta_\mathbf{i}^\mathbf{c} = \mathbf{O}_\mathbf{i}^\dagger \boldsymbol{\Phi}_{[\mathbf{Y_f},\mathbf{Y_p}]} \tag{39}$$

Where $\boldsymbol{\Phi}_{[\mathbf{Y_f},\mathbf{Y_p}]}$ is the covariance between the future and the past observations. It is worth to notice that that covariance is equal to the Toeplitz block matrix $\boldsymbol{\Lambda} \in \mathcal{R}^{lixli}$.

$$\boldsymbol{\Lambda} = \begin{pmatrix} \boldsymbol{\Lambda_i} & \boldsymbol{\Lambda_{i-1}} & \cdots & \boldsymbol{\Lambda_2} & \boldsymbol{\Lambda_1} \\ \boldsymbol{\Lambda_{i+1}} & \boldsymbol{\Lambda_i} & \cdots & \boldsymbol{\Lambda_3} & \boldsymbol{\Lambda_2} \\ \boldsymbol{\Lambda_{i+2}} & \boldsymbol{\Lambda_{i+1}} & \ddots & \boldsymbol{\Lambda_4} & \boldsymbol{\Lambda_3} \\ \vdots & \vdots & \vdots & \vdots & \vdots \\ \boldsymbol{\Lambda_{2i-1}} & \boldsymbol{\Lambda_{2i-2}} & \cdots & \boldsymbol{\Lambda_{i+1}} & \boldsymbol{\Lambda_i} \end{pmatrix} \tag{40}$$

Where each block is the covariance between the signals $\boldsymbol{\Lambda_i} \in \mathcal{R}^{lxl}$.

$$\boldsymbol{\Lambda_i} = \mathbf{E}(\mathbf{Y_i}\,\mathbf{Y^T}) = \frac{1}{j}\sum_{k=0}^{j-1} \mathbf{Y_{k+i}}\,\mathbf{Y_k^T} = \boldsymbol{\Phi}_{[\mathbf{Y_{i|i}},\mathbf{Y_{0|0}}]} \tag{41}$$

Passing from the first formulation to the followings assuming a stationary ergodic stochastic process. Finally, the forward and backward Kalman state sequences $\widehat{\mathbf{X}}_\mathbf{i}$ and $\widehat{\mathbf{Z}}_\mathbf{i}$ are equal to:

$$\begin{gathered} \widehat{\mathbf{X}}_\mathbf{i} = \mathbf{O}_\mathbf{i}^\dagger \boldsymbol{P_i} \\ \widehat{\mathbf{Z}}_\mathbf{i} = \mathbf{O}_\mathbf{i}^\mathbf{T} \boldsymbol{\Phi}_{[\mathbf{Y_f},\mathbf{Y_f}]}^{-1} \mathbf{Y_f} \end{gathered} \tag{42}$$

The stochastic identification show above is exact when the number of measurement approach to infinite *(*$j \to \infty$*)*.

It is now clear the distinction between the data driven (SSI-**data**) and covariance driven (SSI-**cov**) techniques. The first is based on the decomposition of the Hankel matrix (33) and the second on the decomposition of the Toeplitz matrix (40). In both cases perform the SVD allows to define the relation between the elements of the subspace.

$$\begin{gathered} \boldsymbol{P_i} = \mathbf{O_i}\widehat{\mathbf{X}}_\mathbf{i} = \mathbf{US^{1/2}}\ \mathbf{S^{1/2}V^T} \\ \mathbf{O_i} = \mathbf{US^{1/2}}\ \ \widehat{\mathbf{X}}_\mathbf{i} = \ \mathbf{S^{1/2}V^T} \\ \boldsymbol{\Lambda} = \boldsymbol{\Phi}_{[\mathbf{Y_f},\mathbf{Y_p}]} = \mathbf{O_i}\Delta_\mathbf{i}^\mathbf{c} = \mathbf{US^{1/2}}\ \mathbf{S^{1/2}V^T} \\ \mathbf{O_i} = \mathbf{US^{1/2}}\ \ \Delta_\mathbf{i}^\mathbf{c} = \ \mathbf{S^{1/2}V^T} \end{gathered} \tag{43}$$

In literature are available different algorithms that consider different values of the weighted matrices $\mathbf{W_1}$ and $\mathbf{W_2}$ that provide to different flows to estimate the system matrices.

The principal components (PC) considers the following weighting matrices $\mathbf{W_1} = \boldsymbol{I} \in \mathcal{R}^{lixli}$ and $\mathbf{W_2} = \mathbf{Y_p^T} \mathbf{\Phi}^{-1/2}_{[\mathbf{Y_p},\mathbf{Y_p}]} \mathbf{Y_p}\ \mathcal{R}^{jxj}$ obtaining the following projection.

$$\mathbf{W_1}\boldsymbol{P_i}\mathbf{W_2} = \mathbf{\Phi}_{[\mathbf{Y_f},\mathbf{Y_p}]} = \mathbf{\Lambda} \in \mathcal{R}^{lixli} \tag{44}$$

That is the Toeplitz matrix introduced before. From the SVD it is possible to evaluate the extended observability (34) and the controllability (35) matrices.

The Unweighted Principal Components (UPC) considers the following weighting matrices $\mathbf{W_1} = \boldsymbol{I} \in \mathcal{R}^{lixli}$ and $\mathbf{W_2} = \boldsymbol{I} \in \mathcal{R}^{jxj}$, meaning that the projection is not weighted.

$$\mathbf{W_1}\boldsymbol{P_i}\mathbf{W_2} = \boldsymbol{P_i} \in \mathcal{R}^{lixj} \tag{45}$$

The SVD leads to the (37) giving again the extended controllability and observability matrices by the (38)(39). The last is the Canonical Variate Algorithm (CVA) providing $\mathbf{W_1} = \mathbf{\Phi}^{-1/2}_{[\mathbf{Y_f},\mathbf{Y_f}]} \in \mathcal{R}^{lixli}$ and $\mathbf{W_2} = \boldsymbol{I} \in \mathcal{R}^{jxj}$. The operation made by the weighting matrices is equal to write the projection with different basis. The general flow illustrates above leads to different methods for evaluating the system related matrices. As introduced before, it is commonly known as two distinct procedures based on the feeding data (SSI-**data** and SSI-**cov**) but they derive from a common framework.

From the system related matrices $\mathbf{O_i}$ $\Delta_\mathbf{i}^\mathbf{c}$ and the forward Kalman state frequency $\mathbf{\hat{X}_i}$ it is possible to extract the system matrices $\mathbf{A}, \mathbf{G}, \mathbf{C}, \mathbf{\Lambda_0}, \mathbf{Q}, \mathbf{S}, \mathbf{R}$ in the following way.

$$\mathbf{A} = \underline{\mathbf{O_i}}^{\dagger}\overline{\mathbf{O_i}} \tag{46}$$

The symbols mean without the last l-rows if it is under-scored or without the first l-rows if it is over-scored. The matrix $\mathbf{C}$ are the last l-rows of the extended controllability matrix and $\mathbf{G}$ are the last l-columns of the extended controllability matrix $\Delta_\mathbf{i}^\mathbf{c}$.

The initial covariance is calculated as:

$$\mathbf{\Lambda_0} = \mathbf{\Phi}_{[\mathbf{Y_i},\mathbf{Y_i}]} \in \mathcal{R}^{lixli} \tag{47}$$

From the projection of the row space of the future observations without a block row $Y_f^- \in \mathcal{R}^{l(i-1)xj}$ on the past observations adding a block row $Y_p^+ \in \mathcal{R}^{l(i+1)xj}$ is equal to the backward projection.

$$\mathbf{P_{i-1}} = Y_f^- / \mathbf{Y_p^+} = \mathbf{O_{i-1}}\mathbf{\hat{X}_{i+1}} \in \mathcal{R}^{lixli} \tag{48}$$

Thus, the forward Kalman filters sequences can be obtained.

$$\mathbf{\hat{X}_{i+1}} = \underline{\mathbf{O_i}}^{\dagger}\mathbf{P_{i-1}} \tag{49}$$

Substituting on the following equation and solving in a least square sense.

$$\begin{pmatrix} \mathbf{\hat{X}_{i+1}} \\ \mathbf{Y_{i|i}} \end{pmatrix} = \begin{pmatrix} \mathbf{A} \\ \mathbf{C} \end{pmatrix} (\mathbf{\hat{X}_i}) + \begin{pmatrix} \boldsymbol{\rho}_\mathbf{w} \\ \boldsymbol{\rho}_\mathbf{v} \end{pmatrix} \tag{50}$$

With the residues $\boldsymbol{\rho}_\mathbf{w}$ and $\boldsymbol{\rho}_\mathbf{v}$ it is possible to evaluate the input covariances.

$$\begin{pmatrix} \mathbf{Q} & \mathbf{S} \\ \mathbf{S^T} & \mathbf{R} \end{pmatrix} = \mathbf{E}[\begin{pmatrix} \boldsymbol{\rho}_\mathbf{w} \\ \boldsymbol{\rho}_\mathbf{v} \end{pmatrix} (\boldsymbol{\rho}_\mathbf{w}^\mathbf{T} \quad \boldsymbol{\rho}_\mathbf{v}^\mathbf{T})] \tag{51}$$

All the process deals with projection of the observations in different subspaces analyzing the iteration between them.

For the dynamic identification is enough the estimation of the system matrices $\mathbf{A}$, $\mathbf{C}$ governing the model, the discrete poles $\mathbf{\Lambda_d} = diag(\boldsymbol{\lambda_q}) \epsilon\ \mathbb{C}^{nxn}$ and the observed mode shape $\mathbf{V} \epsilon\ \mathbb{C}^{2Nxn}$ can be evaluated as:

$$\begin{gathered}\mathbf{A} = \mathbf{\Psi \Lambda_d \Psi^{-1}} \\ \mathbf{V} = \mathbf{C\Psi}\end{gathered} \tag{52}$$

The discrete state space formulation for the M-DOF dynamic problem leads to the same eigenvalue and eigenvector, then the relationship with the time continue state space model is the following.

$$\begin{gathered}\mathbf{A} = exp(\mathbf{A_c}\Delta t) \\ \boldsymbol{\Psi_c} = \mathbf{\Psi} \qquad \boldsymbol{\lambda_{cq}} = \frac{\boldsymbol{ln(\lambda_q)}}{\boldsymbol{\Delta t}}\end{gathered} \tag{53}$$

Where under-script c refers to the continuous dynamic system [21]. At least the identified modal parameters are equal to:

$$\mathbf{\Phi} = \mathbf{C\Psi} \epsilon\ \mathbb{C}^{2Nxn} \qquad \lambda_{cq}, \lambda_{cq}^{*} = -\xi_q \omega_q \pm i\omega_q \sqrt{1-\xi_q^2} \tag{54}$$

The modal properties associate with the *q-th* mode can be approximated in the following relations.

$$\boldsymbol{\omega_q} = |\boldsymbol{\lambda_{cq}}| \qquad \boldsymbol{\xi_q} = -\frac{\boldsymbol{Re}\{\boldsymbol{\lambda_{cq}}\}}{|\boldsymbol{\lambda_{cq}}|} \qquad \boldsymbol{\phi_q} = \boldsymbol{Re}\{\mathbf{C\Psi_{1:N,q}}\} \tag{55}$$

As it was introduced in the previous section, the identification of the modal model from real data is affected by different source of noise deriving from modelling errors, numerical errors, instruments noise. For that reasons the optimal model order cannot be easily found but it is needed the analysis of the stabilization chart.

2.3.2 Frequency domain identification

The frequency domain identification techniques are based on the definition of the spectral quantities from the collected signals. Theoretically the auto-density power spectra (or simply power spectra) is the Fourier transform of the correlation function as introduced in (19). Considering a simple SDOF system subjected to a Gaussian white noise process which exhibit no correlation at each time lag except for $\tau = 0$. The Fourier transform is a constant value that implies a complete distribution of the energy along every frequency. The problem stand that the Parseval's theorem is violated implying an infinite variance of the process. Anyway, it is possible to overcome this issue introducing the generalized functions, considering a process that exhibit a correlation function as a Dirac's delta function multiplied for a constant value. Thus, the power spectral density is finite, and the energy is equally distributed over a large band of frequencies (broad band process).

From the SISO fundamental theorem (26) it is easy to understand that the auto spectral density is proportional to the modulus of the FRF. In that way it is possible to read the resonant frequencies as the peaks in the power spectral density.

When dealing with the real data the estimation of the correlation functions and consequently of the power spectra or directly the power spectra is not so easy, and a series of operation are required to limit the introduced bias. In the context of this thesis, it is used the Welch method that directly estimated the power spectral density as the mean of the power spectral density of the signals segmented in N window with a certain percentage of overlapping. To limit the bias introduced by the leakage each window is multiplied for a Hanning tapering window. Other methods are the random decrement estimation and the half spectra, for further details the reader can see [2].

2.3.2.1 The Frequency Domain Decomposition (FDD)

The main idea of the FDD [22] is based on the SVD decomposition of the power spectral density matrix (PSD) that is a positive definite Hermitian matrix. The decomposition lead to the diagonal singular value matrix **S**, left multiplied for a matrix **U** and right multiplied for the transpose complex conjugate matrix of **U**:

$$\mathbf{S_y} = \mathbf{USU^H} \tag{56}$$

This decomposition can be interpreted as the multiplication of the mode shape matrix for the auto-spectral density of the modal coordinates:

$$\mathbf{S_y(f)} = \mathbf{\tilde{\Phi} s_n(f) \tilde{\Phi}^H} \tag{57}$$

The FDD is a biased technique because the decomposition (56) is not the exact decomposition of the PSD matrix of a structure excited with a white noise. If the system is light damped and the modes are well separated the decomposition (57) is a good approximation of the modal properties of the system.

Usually the hypothesis of white noise input and low values of damping are satisfied, but the separation between the modes is very often violated. For this reason, the PSD matrix on a certain frequency band can be written as the superposition of the modal auto spectral density of each modal coordinate:

$$\mathbf{S_y(f)} = \mathbf{s_1(f)\tilde{\Phi}_1\tilde{\Phi}_1^H} + \mathbf{s_2(f)\tilde{\Phi}_2\tilde{\Phi}_2^H} + \dots \tag{58}$$

Defining a set of orthogonal vectors $\mathbf{V} = [\mathbf{v_1}, \mathbf{v_2}, \dots]$ such that:

$$\mathbf{V^H\tilde{\Phi}} = \mathbf{I} \tag{59}$$

it is now possible to isolate the spectral density of a single modal coordinate by projecting the PSD matrix in the new reference system **V**, in this way the auto-spectral density is available for each modal coordinate:

$$\mathbf{s_q(f)} = \mathbf{V^H S_y(f) V} \tag{60}$$

This operation is called modal filtering allowing the definition of approximated auto-spectral densities for each modal coordinate of the MDOF system [23].

With the introduction of the Enhanced Frequency Domain Decomposition (EFDD) procedure is now possible taking back the auto-spectral density in the time domain estimating the modal damping ratio as the logarithmic decrement of the autocorrelation function that can be interpreted as free decay. This operation implies the selection of the bell functions or via modal filtering or in terms of MAC index of the mode shapes around the peak, joining the spectral density values that exhibit a high degree of correlation in terms of mode shapes. Once the bells functions are extracted in each frequency band of interest, it is possible to came back in the time domain with the inverse Fourier transform obtaining the autocorrelation function that can be interpreted as the free decays of each mode. Then the damping ratio can be evaluated as the logarithm decrement of the autocorrelation functions through a linear regression [24].

2.3.3 Observations about the modal identification techniques

The frequency domain techniques (FDD, EFDD) have the advantages of being quite simple and immediate but they all introduced a level of bias, both for the approximation in the decompositions, both in the calculation of the spectral densities (leakage). Moreover, they require also the hypothesis of low damping that in the quasi totality of the large civil structures is satisfied.

On the other hand, the time domain techniques (SSI) needs the setting of a high number of parameters depending on the parametric nature of the procedure. As introduced before that kind of techniques exhibit the advantage of being automated and then are more effective in the processing of a huge amount of data such as a long-term monitoring dataset.

Further information about other identification techniques available for the modal testing as the Ibrahim Time Domain, the Maximum Likehood , the polyreference least-squares complex frequency-domain also known as “Polymax” are reviewed and deeply discussed in [25].

2.4 Sensors and measuring devices

There is a wide range of measuring devices for measuring the vibrations of civil structures and the availability is still increasing thanks to the technological developments. The setting up of new devices is strictly connected with the research of new damage sensitive properties or to the definition of higher accuracy devices possibly insensitive to the environmental changes. The choice of the sensors for long-term monitoring purposes should be the conclusion of the operational evaluation phase including all the requirements from an electrotechnical point of view. The aim of this section is not a complete review of all the available devices but only an introduction to the sensors used in the context of this thesis. A complete review can be found in [26–28]. To stress the connection between the employed devices (*How measure?*) and the extraction of the suitable damage sensitive features (*What measure?*) a non-conventional classification is made dividing the sensors in three classes. The first class (*section 2.4.1*) leads to the direct extraction of a dynamic global quantity (frequency, damping and mode shape). The second class (*section 2.4.2*) deals with a local measure (mode shape strains, static displacements across a crack, static deformations) in a certain location. The third class regards the measurements of the environmental effects (temperature, wind, humidity) that can modify the dynamic behaviour.

2.4.1 Sensors measuring the global response

Among all transducers to measuring the global response the accelerometers are still the most effective due to their sensitivity and their cost effectiveness. The most used are the piezoelectric accelerometers thanks to their high accuracy, stability and they don’t require external power source (active transducers). The only disadvantage is that they are not able to measure the DC components (0 Hz), that can be a big issue when measuring very flexible structures with resonant frequencies closed to DC. The device measures the acceleration on an internal mass with an active system made by quartz or ceramics that produce an electric output. They can measure a wide range of acceleration below the resonant frequency of the system (0-2000 Hz).

Others two categories are the piezoresistive and force balanced accelerometers. The first have the advantage of measuring uniform acceleration values but they need an external power source (passive transducers). The second are very often used in the civil engineering modal testing for flexible structures thanks to their accuracy in the low frequency range. The signals acquired by the sensors are then transmitted through a cabled system to the Data AcQuisition system (DAQ) that filters, amplifies and converts the acquisition in discrete time histories with a certain sampling frequency. Usually the signal collected by the sensors cannot be directly processed and a signal conditioning process is needed. The Analog to Digital Converter (ADC) converts the information of the analog signal into a digital signal in the binary system. Higher is capacity of the ADC in terms of binary digits better will be the resolution in the representation of the recorded analog signals.

2.4.2 Sensors measuring the local response

In the case of local measurements, it is possible to use displacements transducers and strain gauges that respectively measures the displacements and the strain from an initial configuration. These devices are usually employed in the static monitoring system due to their limited resolution of capturing rapid varying quantities. Recently for the direct dynamic measurement of the strains the Fiber Optic Sensors (FOS) that have a high precision and they are not sensitive to the environmental effects thanks to the compensation procedures. This kind of sensors can be also split along the whole structure giving information about the global behaviour through local high accuracy measurements.

Different kind of FOS sensors are available and they have been applied for monitoring the construction phase of bridges [29] but not so many cases are available for long-term monitoring of civil structures. Probably the technology is not still mature for the long-term SHM applications and the high costs for the sensors and the acquisition unit have decreased the application to large structures.

2.4.3 Sensors measuring the environmental effects

The most common are the thermocouple to measure the air temperature, the hygrometers to measure the humidity of the air and the anemometers to measure the wind speed or pression and the direction.

2.5 Damage sensitive properties

The definition of the most sensitive damage properties through numerical models and laboratory specimens is a research topic where the scientific community made a lot of efforts from the second half of the last century. The problem with the analysis performed is how the damage is modelled or inferred to the tested specimen. In the case of masonry structures, the major part of the investigations was made with numerical models and in a limited number of cases with scaled models under static horizontal loads or on the shacking table.

In this section are reviewed the major contribution about the definition of the most sensitive damage properties and the indicators defined by the Authors. The complete review it is beyond the aims of that thesis, but different review are available in literature [30–34].

2.5.1 Resonant frequency

From the early years of the damage identification through the vibration-based methods, the frequency was one of the most investigated features. First because the modal frequencies are evaluated from the dynamic identification techniques with the data recorded from few accelerometers.

Cawley and Adams [35] used a perturbation approach neglecting the mass variations, showing that the changes in frequency are proportional to the elements stiffness variation. With a sensitivity analysis the elements that produced the large frequency shift respect to the used mode shape were used as feasible damage locations. By the analysis of the error function that measure the correlation between the measured frequency shift and the damage scenario, it was possible to localize damage in plates using numerical models. Gudmunson [36] consider the shift of the resonance frequency due to damage as a perturbation of the undisturbed geometry. The problem was solved with a first order approximation evaluating the resonance frequency shift as a function of the variation in the modal strain energy. The theory was applied to the Euler-Bernoulli beam formulation and verified by numerical and experimental tests on beam structures. Kim and Stubbs [37] developed a study based on the fractional change in the frequency is equal to the fractional change in the modal strain energy as it was introduced by Gudmunson. Starting from the Euler-Bernoulli formulation for the beam the variation in the modal strain energy is equal to the loss rate due to the crack. The fractional variation of the frequency is proportional to the dimensionless cracking size and to the sensitivity to damage of the *k-th* location in the *i-th* mode shape. The method fits very well for the numerical simulation and the sensitivity for the *k-th* location in the *i-th* mode can be expressed as the ratio of the modal stiffness of the element and of the whole structure.

For this reason, the experimental test was made with the modal identification of the numerical baseline model and the damage locations are found where is equal to zero the localization error. Zhang [38] analysed the change in frequency for a cantilever beam applying the Euler-Bernoulli theory for identifying and localizing multiple cracks. The starting point is the perturbation approach of the previous Authors; the localization and depth of the crack was found solving the non-linear equation with the Newton-Raphson method. For every crack is needed a set of two modal shapes to solve the algebraic system. The method is tested on two different cantilevers with a hammer impulse test. The results are validated with a FE model of the structure that shows a good agreement of the results. The frequencies are evaluated with a processing method based on the Hilbert-Huang transform that allows a high resolution of the obtained frequencies.

2.5.2 Mode shapes

Assuming, that damage at a given section of a structure locally decreases the local stiffness, lowering the frequencies and increasing the periods. It is automatically to investigate about the change in the dynamic motion. The mode shapes represent the decomposition of the motion in the modal components.

For these reasons, the mode shapes were investigated as damage sensitive features in the past decades. Some Authors [39] used the MAC index, as a damage index for localizing damage. The MAC index [40] expresses the correlation between the two different mode shapes j-th and k-th calculated by two different data set of measures (A and B). The MAC values are between 0 and 1 and the 1 value is obtained by the perfect correlation between the two modes shape and the 0 value is obtained when the two mode shapes are independent.

$$(MAC)_{jk} = \frac{\left|\sum_{i=1}^{n}[\phi_A]_i^j\,[\phi_B]_i^k\right|^2}{\sum_{i=1}^{n}\left([\phi_A]_i^j\right)^2\sum_{i=1}^{n}\left([\phi_B]_i^j\right)^2} \tag{61}$$

Where:

$[\phi_A]_i^j$ Are the i-th components of the j-th mode of the A data set of measured mode shapes.

$[\phi_B]_i^k$ Are the i-th components of the k-th mode of the B data set of measured mode shapes.

If the MAC is evaluated with two sets of mode shapes that represent the structural response before and after the damage. It is possible to measure the difference between the two configurations in terms of the MAC index. From the MAC index is defined the COMAC index that express the correlation of the modal displacement in i-th modal coordination of two different data set involving m-th mode shapes.

$$(\mathrm{COMAC})_i = \frac{\left|\sum_{j=1}^{m}[\phi_A]_i^j\,[\phi_B]_i^j\right|^2}{\sum_{j=1}^{m}\left([\phi_A]_i^j\right)^2\sum_{j=1}^{m}\left([\phi_B]_i^j\right)^2} \tag{62}$$

Where:

$[\phi_A]_i^j$ Is the modal contribution, in the i-th modal coordinate, of the j-th mode shape for the A dataset of measurements.

$[\phi_B]_i^j$ Is the modal contribution, in the i-th modal coordinate, of the j-th mode shape for the B dataset of measurements.

Obviously, this index assumes values between zero and one expressing in the first case the independence of the two set of modal shape in the i-th modal coordinate; in the second one the perfect correlation. This means that the values of the modal displacements are almost equal in the i-th modal coordinates for COMAC value near to one. Instead COMAC values far from 1 shows an abnormal behaviour, that means the presence of damage.

2.5.3 Mode shapes curvature

The modal curvature is one of the most investigated damage sensitive properties. The first studies were made by Pandey and Biswas [41] showing that the modal curvature evaluated with the central difference operator is a good damage indicator. They studied a numerical FE model of a beam and the results that they obtained shows a good result in the localization of a single crack. The damage was simulated reducing the Young Elastic Moduli E in one element of the numerical model and the difference in the modal shape curvature was used for localizing the fault. The modal shape curvature exhibits a peak in the section where the damage was introduced.

Wahab et al. [42] introduced the curvature damage factor (CDF) that average the MSC difference of each modes, smoothing the effect of the false positive peaks that were showed in the previous works. In this paper were tested both numerical beam model both a full-scale test on the Z-24 bridge. The method is effective to locate the faults for simple and multiple damages and for simple supported and continuous beam. The full-scale test on the Z24 bridge was made introducing different level of settlement in one pier. The analysed mode shape from the real testing data were not enough smooth for employing the results in the MSC calculation with the central difference operator. For these reasons, the mode shapes were interpolated for every ten measured points with a six-order polynomial. From the fitted mode shapes the MSC were calculated from every mode and then the CDF index was computed. The results show a good resolution of the CDF for the damage assessment, even if the authors underline how the measure of the mode shape should have a high level of resolution and that the high modes could be used with attention because it is possible to find some false positive indication. Vestroni et al.[43] shows with a perturbative approach that the mode shape and the modal curvature of the damaged structure are influenced by the contribution of the higher mode. They evaluated a filtering procedure that allows to avoid the false positive indication pointed out by previous authors.

Roy et al. [44]identify and localize the damage with a perturbation approach on the mode shapes. In that paper is showed how the second derivative of the mode shape is sensitive to damage. It is localized where the variation of the mode shape curvature crosses the zero.

The procedure is tested on a FE model of a representative Californian shear type buildings with twelve stories, designed with the capacity design strategy (strong beam and weak columns). The damage scenario was a reduction of the 20% of the elastic stiffness in the sixth floor. The differences in the mode shape and its derivatives allows to localize the damage in the model.

2.5.4 Flexibility-Based deflections

The dynamically evaluated flexibility matrix $\mathbf{G} \in \mathcal{R}^{MxM}$ for a MDOF system can be written as follows:

$$\mathbf{G} = \mathbf{\Phi}^{\boldsymbol{T}}\mathbf{\Omega}^{-\mathbf{1}}\mathbf{\Phi} \tag{63}$$

Where $\boldsymbol{\Phi} \in \mathcal{R}^{MxN}$ is the mass-normalized mode shapes matrix of the N measured mode shapes and $\mathbf{\Omega}^{-\mathbf{1}} = \operatorname{diag}\left(\frac{1}{\omega_i^2}\right) \in \mathcal{R}^{NxN}$. Bernal [45] proved the good approximation of the obtained dynamic flexibility matrix with only few modes. That implies that a great advantage because usually the first modes can be easily extracted from the Ambient Vibration Tests.

Xiong [46] identified the effects of scouring in the piers on a cable bridge by means of the flexibility deflection calculated from the identified flexibility matrix. Once the flexibility matrix $\mathbf{G}$ is evaluated, it is possible to calculate the static deflections $d \in \mathcal{R}^{Mx1}$multiplying it for a load vector $f \in \mathcal{R}^{Mx1}$.

$$d = \mathbf{G}f \tag{64}$$

Then the effects of scouring on the pier were evaluated in terms of deflection considering a unitary force acting vertically in the middle of the girder. The method was able of capturing the effects of the scouring identifying some potentially dangerous configurations.

2.5.5 Observations about the Damage sensitive properties

The core of the damage identification is the definition of which, among the measured damage sensitive properties, is the most sensitive to the system change (*What measure?*). Despite it is a topic investigated from fifty years, there is not a unique answer to that question that allows the best solution for managing the SHM framework. For the cultural heritage the frequency is still the most used damage sensitive feature even if it is the less sensitive to the damage, that is a local quantity and the frequency is a global measurement. Moreover, this parameter is largely influenced by the environmental effects with a strong correlation with the thermal gradients.

On the other hand, the frequency is the more stable parameter that can be identified through the OMA techniques and it requires a limited number of sensors along the structure. The damping seems the more unstable quantity for its non-linear behaviour that is evaluated from linear models. An accurate estimation of the mode shapes needs a refined grid of sensors that is inconceivable for the long-term monitoring purposes, especially in the cultural heritage field.

Some interesting results can be obtained from the direct measure of the modal curvature and from the modal flexibility evaluation. In the first case, the position of some device across a location potentially interested by the presence of damage can be an attractive solution. Anyway, it is worth to investigate on the precision needed to directly measure the strains in old masonry structures and the extension of the measuring base. In the second case, some hypothesis on the mass matrix should be done and the capability of the method should be investigated in the field of cultural heritage.

2.6 Multivariate statistical tools for the environmental effects removing

The environmental effects lead to changes in the dynamic response of the structures due to changes in the material properties. The most investigated effect is the air temperature that has different effects on the materials. The first investigated structures were the bridges and a strong correlation was found between the air temperature and the resonant frequencies. Several examples can be found in literature for different cases of bridges or buildings [47–51]. In the last years the effects of the environmental effects was exploited by the authors [52–54], showing positive and negative correlation between resonant frequencies and the temperature effects. The variance of frequency due to the environmental effects assumes similar value to the effects due to damage, for that reason the use of multivariate statistical analysis is needed to clean the data from these effects. Further details can be found in the statistics handbooks [4,55,56].

2.6.1 Multiple linear regression

The Multiple Linear Regression (MLR) is a linear multivariate statistical technique, that allows the prediction of one or more dependent variables (observations) from a series of independent parameters (predictors). Mathematically, it can be formulated as a system of linear equations:

$$\begin{cases} y_1 = \beta_0 + \beta_1 z_{11} + \beta_2 z_{12} + \cdots + \beta_n z_{1n} + \varepsilon_1 \\ y_2 = \beta_0 + \beta_1 z_{21} + \beta_2 z_{22} + \cdots + \beta_n z_{2n} + \varepsilon_2 \\ \vdots \\ y_m = \beta_0 + \beta_1 z_{m1} + \beta_2 z_{m2} + \cdots + \beta_n z_{mn} + \varepsilon_m \end{cases} \tag{65}$$

That in the compact matrix formulation leads to the following equation:

$$y = \mathbf{Z}\,\upbeta + \upvarepsilon \tag{66}$$

Where $y \in \mathcal{R}^{mx1}$ is the vector of the dependent variables (observations), $\mathbf{Z} \in \mathcal{R}^{mxn}$ is a matrix gathering in the columns the n sets of independent variables (predictors), $\upbeta \in \mathcal{R}^{nx1}$ is a weighting vector of each independent variables and $\varepsilon \in \mathcal{R}^{mx1}$ of the random errors constituted by independent events with zero mean and a certain variance. That implies the following properties of the random error vector:

$$\mathbf{E}[\varepsilon] = 0 \qquad\qquad cov[\varepsilon] = \mathbf{E}[\varepsilon^T\varepsilon] = \sigma_\varepsilon^2\mathbf{I} \tag{67}$$

In the MLR problem represented by the (65) regarding the SHM the observations are the selected damage sensitive features and the predictors are those parameters that affect the extracted damage sensitive features (temperature, humidity, wind speed, etc.). The problem is usually solved in a least square sense minimizing the square difference between the measures and the predicted values.

$$\mathbf{S}(\beta) = (\mathbf{y} - \mathbf{Z}\,\beta)^{\mathbf{T}}(\boldsymbol{y} - \mathbf{Z}\,\beta) \tag{68}$$

The values of $\hat{\beta}$ that minimize the objective function described by the (68) are the estimators of β. The vector containing the difference among the predicted values $\hat{y} \in \mathcal{R}^{mx1}$ and the observation is the residual vector $\hat{\varepsilon} \in \mathcal{R}^{mx1}$.

$$\hat{\varepsilon} = \mathrm{y} - \hat{y} \tag{69}$$

The same operations can be done when are available M multiple observation gathered together in the observation vector become a matrix $\mathbf{Y} \in \mathcal{R}^{mxM}$, in that case the predictor vector become a matrix $\boldsymbol{\beta} \in \mathcal{R}^{nxM}$ and again the residual vector become a matrix $\boldsymbol{\varepsilon} \in \mathcal{R}^{mxM}$. The equation (66) assumes the following form.

$$\mathbf{Y} = \mathbf{Z}\,\boldsymbol{\beta} + \boldsymbol{\varepsilon} \tag{70}$$

2.6.2 Principal Component Analysis

The Principal Component analysis (PCA) is a statistical multivariate technique based on data reduction and interpretation. The basis of that method stands beside the reduction of a system described by m observation of M independent variables into a system described by k principal components reproducing the entire system variability. From a geometric point of view, the problem can be formulated as the research of a new base where the variance is equal to the maximum. This is equivalent to find the eigenvalue and the eigenvectors of the covariance matrix $\boldsymbol{\Lambda_0} \in \mathcal{R}^{mxm}$ of the observation matrix $\mathbf{Y} \in \mathcal{R}^{mxM}$.

$$\boldsymbol{\Lambda_0} = \mathbf{E}[(\mathbf{Y} - \mu_Y)(\mathbf{Y} - \mu_{\mathrm{Y}})^{\mathbf{T}}] \tag{71}$$

Consequently, the PCA is a linear remapping of the observed data in a new orthogonal system defined by the considered principal components. Calling with $\mathbf{X} \in \mathcal{R}^{mxM}$ the score matrix and $\mathbf{T} \in \mathcal{R}^{mxm}$ the loading matrix, it is possible to formulate the following linear mapping.

$$\mathbf{X} = \mathbf{TY} \tag{72}$$

In some way, $\mathbf{X}$ is the observation matrix written in the new coordinates after the linear transform $\mathbf{T}$. The searched based should maximize the variance along each direction, so that the covariance matrix assume a diagonal form $\boldsymbol{\Sigma}^{\mathbf{2}} = \boldsymbol{diag}(\boldsymbol{\sigma}_{\mathbf{1}}^{\mathbf{2}}, \cdots, \boldsymbol{\sigma}_{\boldsymbol{m}}^{\mathbf{2}})$ with the variance along the diagonal. The simplest way to obtain that result is performing the SVD of the covariance matrix $\boldsymbol{\Lambda_0} \in \mathcal{R}^{mxm}$.

$$\boldsymbol{\Lambda_0} = \mathbf{YY^T} = \mathbf{T\Sigma^2T^T} = (\hat{\mathbf{T}} \quad \tilde{\mathbf{T}})\begin{pmatrix} \hat{\boldsymbol{\Sigma}}^2 & \mathbf{0} \\ \mathbf{0} & \tilde{\boldsymbol{\Sigma}}^2 \end{pmatrix}\begin{pmatrix} \hat{\mathbf{T}} \\ \tilde{\mathbf{T}} \end{pmatrix} \tag{73}$$

The reduction of the system is performed by retaining only the first k-values of the $\boldsymbol{\Sigma}^2$ matrix evaluating the contribution of each component in the following manner.

$$\lambda_i = \frac{\sigma_i^2}{tr(\boldsymbol{\Sigma}^2)} \tag{74}$$

Once the chosen number of components is retained the score matrix can be calculated, and the estimation of the observation matrix will be calculated as follows.

$$\hat{\mathbf{Y}} = \hat{\mathbf{T}}^{\mathrm{T}}\mathbf{X} = \hat{\mathbf{T}}^{\mathrm{T}}\hat{\mathbf{T}}\mathbf{Y} \tag{75}$$

The loss of information after the selection of the retained k values can be evaluated from the norm of the residual error matrix $\mathbf{E} \in \mathcal{R}^{mxM}$.

$$||\mathbf{E}|| = \left\|\mathbf{Y} - \hat{\mathbf{Y}}\right\| \tag{76}$$

Loosely speaking the residual error matrix represents the uncorrelated part of the M-observed features with m-observations without knowing the nature of the correlated parameters. Equation (73) expresses clearly the reduction of dimension operated with the PCA splitting the observation space through the analysis of the singular value matrix $\boldsymbol{\Sigma}^2$.

2.6.3 The Non-Linear Principal Component Analysis

The non-linear PCA is a non-linear mapping of observed data matrix through the functions gathered in the matrix $\mathbf{G} \in \mathcal{R}^{mxk}$.

$$\mathbf{X} = \mathbf{G}(\mathbf{Y}) \tag{77}$$

The inverse transformation to restore the full dimensions of the system will be implemented with another set of non-linear functions $\mathbf{H} \in \mathcal{R}^{mxk}$.

$$\hat{\mathbf{Y}} = \mathbf{H}(\mathbf{X}) \tag{78}$$

The solution of that non-linear problem implies the use of algorithms that provide a numerical solution. Sohn et al. [57] uses Artificial Neural Network (ANN) to reveal the hidden relation between the unmeasured parameters that generate fluctuations on the response and the measured responses. Golinval et al. [58] uses the Local PCA to analyse the non-linear relation among the observed and non-observed parameters. The method is a sort of a local linearization of the non-linear problem. Indeed, the data space is partitioned in k $\mathbf{Y}_{\mathrm{i}}$ subspace and the linear PCA algorithm is performed to the covariance matrix normalized respect to the subspace centroid $\bar{\mathbf{Y}}_{\imath}$.

$$(\mathbf{Y}_{\mathrm{i}} - \bar{\mathbf{Y}}_{\imath})(\mathbf{Y}_{\mathrm{i}} - \bar{\mathbf{Y}}_{\imath})^{\mathrm{T}} = \mathbf{T}_i\hat{\boldsymbol{\Sigma}}_i^2\mathbf{T}_{\mathrm{i}}^{\mathrm{T}} \tag{79}$$

According to (72) the projected data on each subspace can be found as follows.

$$\mathbf{X}_i = \mathbf{T}_i\mathbf{Y}_i \tag{80}$$

The focus of the procedure is then on how should be partitioned the data space, considering the non linear relation. The partition is performed with the Loyd’s algorithm based on the Euclidean distance between each element and the cluster centroid. Kambhatla and Leen [59] modified the Loyd’s algorithm using the projection distance instead of the Euclidean. The projection distance or distortion function is the distance among the projection on each space principal direction. Then Golinval et al. [58] proposed the characteristic distance, that is the linear combination of the Euclidean and projection distance, depending on a scalar parameter.

The non-linear kernel PCA [60] is also an attractive tool for eliminating the non-linear environmental effects, it is based on the suitable definition of two parameters: the standard deviation of the Gaussian kernel and the number of retained PC. This technique can be viewed as a generalization of the PC method hypothesizing a non-linear mapping of the observation in a high dimensional space. The eigenvalue decomposition of the mapped output covariance matrix can be written in the following form:

$$\mathbf{G(Y)G(Y)}^{T} = \mathbf{USU^T} \rightarrow \mathbf{G(Y)G(Y)^T U} = \mathbf{US} \tag{81}$$

Notice that this is the same decomposition of (73) when $\mathbf{G(Y)} = \mathbf{Y}$. For this reason, the kernel PCA is a generalization of the classical local PCA that overcome the non-linear problems using the kernel functions. Thus operating some matrix substitutions, the equation (81) can be written as a generalized eigenvalue problem of the multiplication of the non-linear mapping $\mathbf{K} = \mathbf{G(Y)^T G(Y)} \in \mathcal{R}^{mxm}$.

$$\mathbf{KA} = \mathbf{AS} \tag{82}$$

All these considerations are very important if the non-linear mapping is performing using the kernel functions.

$$\mathbf{k}(\mathrm{y_i}, \mathrm{y_j}) = \mathbf{G(y_i)^T G(y_j)} = \mathbf{exp}\left(-\frac{\left\|\mathrm{y_i} - \mathrm{y_j}\right\|^2}{2\sigma^2}\right) \tag{83}$$

The information loss can be computed from the kernel functions as the space generated by the columns of the matrix $\mathbf{A} \in \mathcal{R}^{mxm}$ that are not retained as principal components.

$$||\mathbf{E}|| = \mathbf{KA_2A_2^TK^T} \tag{84}$$

2.7 Damage detection

The damage detection is the final goal of the whole SHM framework, within the level of detail required respect to the Rytter's scale. The main difference among the proposed methods can be found in how the reference or undamaged configuration is chosen. It is possible to define two classes the inverse problem or model based, that needs the definition of a suitable model based on the physics of the problem. The FE numerical models identified through a model updating approach are the most employed for the definition of the reference configuration in the inverse problem.

The data-based approach is derived from the statistical tools of the machine learning techniques, starting from the definition of a reference model defined through a training period. The potential damage is then recognized with outlier analysis of the Novelty Index (NI), that anomalies relate to an abnormal structural behaviour probably due to the presence of damage. Both methods exhibit some limitations and a level of uncertainty due to the problem itself and to the numerical operations performed.

2.7.1 Inverse problem (model-based approach)

The model-based approach is probably the most attractive tool because it allows to have a physical based model which allows a large set of simulations that can both localize and quantify the extent of damage. The reliability of the procedure depend on the modal updating procedures [61] and to the degree of uncertainties about the structure properties.

In the recent years, the Bayesian updating approach was investigated to reduce the uncertainties effects on the calibration of the model parameters. The application on old masonry towers seems to be promising [62] for defining the confidence interval of the chosen updating parameters. Anyway, the number of parameters and the different levels of uncertainties is still large, and the identification of a reliable FE model is a complex task.

2.7.2 Data-based approach

The approach based on statistical data is capable of detecting abnormal structural conditions from a reference or undamaged condition. The system is trained over the reference period and the structural response can be predicted, then the outliers can be identified, and a different structural condition is detected. That can be associated with the presence of damage and the structural bearing capacity could be decreased. It is clear that, in the major part of the cases only the damage assessment can be enabled and more accurate analysis for the localization and quantification.

The separation among the two categories is indicative for the classification but it is not a clear distinction. Because it is possible to deal also with physical based model set on data or it is possible to interpret the statistical investigation as a sort of numerical model too. Both two approaches exhibit points of strength and of weakness and there is not a universal solution for the analysed problem. In the Author's opinion the data-based approach seems to be more suitable for the cultural heritage because of the high level of uncertainties for defining the numerical model.

2.8 Automated procedures for the damage identification

Even if the OMA procedures are a mature research field that has been transposed to the practical engineering applications. The SHM paradigm needs the definition of suitable automated procedures to extract the damage sensitive properties. One of the most common method [63–65] used for the detect the occurrence of abnormal structural condition is the use of multivariate control charts. One of the most employed control charts used with SHM purposes is the Shewart or T^2 but the framework is the same for the other methods.

For instance, the method deals with the construction of a safety region based on the past observation of the monitored system in the reference or healthy conditions. If the new observations of the monitored system stand inside the safety region built with a certain confidence value on the statistics of the past observations, then the system is considered healthy anyway it should be considered damaged.

The T^2 statistics is calculated as follows

$$T^2 = (x - \bar{x})\boldsymbol{\Sigma}^{-1}(x - \bar{x}) \tag{85}$$

Where $x \in \mathcal{R}^m$ is the observation $\bar{x}$ is the ensemble average of the process and $\boldsymbol{\Sigma}$ is the process covariance matrix. If Lower Control Limit (LCL) is equal to zero is possible to define the Upper Control Limit as the threshold dividing the safety region from the damage zone.

$$UCL = \frac{m\,(s+1)(r-1)}{sr-s-m+1}\,F_{m,s\,r-s-m+1}(\alpha) \tag{86}$$

Where $F_{m,s\,r-s-m+1}(\alpha)$ denotes the percentile of the F distribution with m and sr-s-m+1 degrees of freedom with s is the number of groups collected in the reference state and r is the number of observations. An application to the damage detection in an arch concrete bridge can be found in [63]. Some further information about the statistical theory control charts can be found in [66].

2.9 References

[1] P. Andersen, Identification of Civil Engineering Structures using Vector ARMA Models, Engineering. 37 (1997) 14–21.

[2] A. Brandt, Noise and Vibration Analysis: Signal Analysis and Experimental Procedures, 2011.

[3] D.E. Newland, Random Vibration, in: Handb. Noise Vib. Control, 2008.

[4] G.E.P. Box, G.M. Jenkins, G.C. Reinsel, Time series analysis: Forecasting and control: Fourth edition, 2013.

[5] L. Ljung, System Identification Theory for User.pdf, PTR Prentice Hall Up. Saddle River NJ. (1987).

[6] A.K. Chopra, Dynamics of structures : theory and applications to earthquake engineering, Pearson Educ. (2007) 874.

[7] T.K. Caughey, M.E.J. O'Kelly, General theory of vibration of damped linear dynamic systems, (1963).

[8] W. Heylen, P. Sas, Modal analysis theory and testing, Katholieke Universteit Leuven, Departement Werktuigkunde; Leuven, 2006.

[9] R. Brincker, C.E. Ventura, Introduction to Operational Modal Analysis, 2015.

[10] D.J. Ewins, Modal Testing: Theory, Practice and Application, 2000.

[11] Clough R.W; Penzien J., Dynamics of Structures, 2003.

[12] A. Papoulis, S.-U. Pillai, Probabilities, Random Variables, and Stochastic Processes, 1991.

[13] J.S. Bendat, A.G. Piersol, Random Data: Analysis and Measurement Procedures: Fourth Edition, 2012.

[14] J.S. Bendat, A.G. Piersol, Engineering applications of correlation and spectral analysis, New York, Wiley-Interscience, 1980. 315 P. (1980).

[15] American National Standards Institute (ANSI), "Vibration of buildings—Guidelinesforthe measurement ofvibrationsandevaluation of their effects on buildings." ANSI S2.47-1990, (1990).

[16] A. V Oppenheim, R.W. Schafer, Discrete Time Signal Processing (2nd version), Book. (2009).

[17] J.W. Cooley, P.A.W. Lewis, P.D. Welch, The Fast Fourier Transform and its Applications, IEEE Trans. Educ. (1969).

[18] G.H. James III, T.G. Carne, J.P. Lauffer, The Natural Excitation Technique (NExT) for Modal Parameter Extraction From Operating Wind Turbines, Int. J. Anal. Exp. Modal Anal. 10 (1993) 260–277.

[19] J.-N. JUANG, R.S. PAPPA, An eigensystem realization algorithm for modal parameter identification and model reduction, J. Guid. Control. Dyn. 8 (1985) 620–627.

[20] P. Van Overschee, B. De Moor, Subspace Identification for Linear Systems, Holanda: Kluwer Academic Publishers, Dordrecht, 1996.

[21] B. Peeters, System Identification and Damage Detection in Civil Engineering, KU Leuven, 2000.

[22] R. Brincker, L. Zhang, P. Andersen, Modal identification of output-only systems using frequency domain decomposition, Smart Mater. Struct. 10 (2001) 441–445.

[23] L. Zhang, T. Wang, Y. Tamura, A frequency-spatial domain decomposition (FSDD) method for operational modal analysis, Mech. Syst. Signal Process. 24 (2010) 1227–1239.

[24] R. Brincker, C.E. Ventura, P. Andersen, Damping estimation by frequency domain decomposition, Time. 1 (2001) 698–703.

[25] E. Reynders, System Identification Methods for (Operational) Modal Analysis: Review and Comparison, Arch. Comput. Methods Eng. 19 (2012) 51–124.

[26] L.F. Ramos, Damage identification on masonry structures based on vibration signatures, PhD Thesis. (2007).

[27] A. Barrias, J.R. Casas, S. Villalba, A review of distributed optical fiber sensors for civil engineering applications, Sensors (Switzerland). 16 (2016).

[28] B. Glišić, D. Inaudi, Fibre Optic Methods for Structural Health Monitoring, 2007.

[29] C. Rodrigues, D. Inaudi, B. Glišić, Long-gauge fibre optic sensors: performance comparison and applications, Int. J. Lifecycle Perform. Eng. 1 (2013) 209.

[30] D. Theodossopoulos, B. Sinha, A review of analytical methods in the current design processes and assessment of performance of masonry structures, Constr. Build. Mater. 41 (2013) 990–1001.

[31] J. Sinou, A review of damage detection and health monitoring of mechanical systems from changes in the measurement of linear and non-linear vibrations, 2013. http://hal.archives-ouvertes.fr/docs/00/77/93/22/PDF/Sinou_Chapter_13_review_SHM.pdf.

[32] H. Sohn, C.R. Farrar, F.M. Hemez, J.J. Czarnecki, A Review of Structural Health Monitoring Literature : 1996-2001, 2003.

[33] S.W. Doebling, C.R. Farrar, M.B. Prime, A summary review of vibration-based damage identification methods, Shock Vib. Dig. (1998).

[34] D. Dessi, G. Camerlengo, Damage identification techniques via modal curvature analysis: Overview and comparison, Mech. Syst. Signal Process. 52–53 (2015) 181–205.

[35] P. Cawley, R.D. Adams, The Location of Defects in Structures From Measurements of Natural Frequencies The Journal of Strain Analysis for Engineering Design, J. Strain Anal. Eng. Des. 14 (1979) 49–57.

[36] P. Gudmundson, Eigenfrequency changes of structures due to cracks, notches or other geometrical changes, J. Mech. Phys. Solids. 30 (1982) 339–353.

[37] J.-T. Kim, N. Stubbs, Crack Detection in Beam-Type Structures Using Frequency Data, J. Sound Vib. 259 (2003) 145–160.

[38] K. Zhang, X. Yan, Multi-cracks identification method for cantilever beam structure with variable cross-sections based on measured natural frequency changes, J. Sound Vib. 387 (2017) 53–65.

[39] J.M. Ndambi, J. Vantomme, K. Harri, Damage assessment in reinforced concrete beams using

eigenfrequencies and mode shape derivatives, Eng. Struct. 24 (2002) 501–515.

[40] D. Ewins, Modal Testing Theory and Practice, 1986. http://link.aip.org/link/?JVADDM/108/109/1.

[41] A.K. Pandey, M. Biswas, M.M. Samman, Damage detection from changes in curvature mode shapes, J. Sound Vib. 145 (1991) 321–332.

[42] M.M. Abdel Wahab, G. De Roeck, Damage Detection in Bridges Using Modal Curvatures: Application To a Real Damage Scenario, J. Sound Vib. 226 (1999) 217–235.

[43] J. Ciambella, F. Vestroni, The use of modal curvatures for damage localizationin beam-type structures, J. Sound Vib. 340 (2015) 126–137.

[44] K. Roy, S. Ray-Chaudhuri, Fundamental mode shape and its derivatives in structural damage localization, J. Sound Vib. 332 (2013) 5584–5593.

[45] D. Bernal, B. Gunes, Flexibility Based Approach for Damage Characterization: Benchmark Application, J. Eng. Mech. 130 (2003) 61–70.

[46] W. Xiong, B. Kong, P. Tang, J. Ye, Vibration-Based Identification for the Presence of Scouring of Cable-Stayed Bridges, J. Aerosp. Eng. 31 (2018) 04018007.

[47] V. Meruane, W. Heylen, Structural damage assessment under varying temperature conditions, Struct. Heal. Monit. 11 (2012) 345–357.

[48] C.R. Farrar, S.W. Doebling, P.J. Cornwell, E.G. Straser, Variability of modal parameters measured on the Alamosa Canyon Bridge, 15th Int. Modal Anal. Conf. (1997) 8.

[49] W.S.L. Wah, Y.T. Chen, G.W. Roberts, A. Elamin, Damage Detection of Structures Subject to Nonlinear Effects of Changing Environmental Conditions, Procedia Eng. 188 (2017) 248–255.

[50] E.J. Cross, K.Y. Koo, J.M.W. Brownjohn, K. Worden, Long-term monitoring and data analysis of the Tamar Bridge, Mech. Syst. Signal Process. 35 (2013) 16–34.

[51] W.H. Wu, S.W. Wang, C.C. Chen, G. Lai, Assessment of environmental and nondestructive earthquake effects on modal parameters of an office building based on long-term vibration measurements, Smart Mater. Struct. 26 (2017).

[52] A. Kita, N. Cavalagli, F. Ubertini, Temperature effects on static and dynamic behavior of Consoli Palace in Gubbio, Italy, Mech. Syst. Signal Process. 120 (2019) 180–202.

[53] F. Ubertini, G. Comanducci, N. Cavalagli, A. Laura Pisello, A. Luigi Materazzi, F. Cotana, Environmental effects on natural frequencies of the San Pietro bell tower in Perugia, Italy, and their removal for structural performance assessment, Mech. Syst. Signal Process. 82 (2017) 307–322.

[54] C. Gentile, M. Guidobaldi, A. Saisi, One-year dynamic monitoring of a historic tower: damage detection under changing environment, Meccanica. 51 (2016) 2873–2889.

[55] H.E.A. Tinsley, S.D. Brown, Multivariate Statistics and Mathematical Modeling, in: Handb. Appl. Multivar. Stat. Math. Model., 2007.

[56] B.G. Tabachnick, L.S. Fidell, S.J. Osterlind, Using multivariate statistics, 2001.

[57] H. Sohn, K. Worden, C.R. Farrar, Novelty detection under changing environmental condition, Smart Struct. Mater. 2001 Smart Syst. Bridg. Struct. Highw. 4330 (2003) 108–118.

[58] A.M. Yan, G. Kerschen, P. De Boe, J.C. Golinval, Structural damage diagnosis under varying environmental conditions - Part II: Local PCA for non-linear cases, Mech. Syst. Signal Process. 19 (2005) 865–880.

[59] N. Kambhatla, T. Leen, Dimension Reduction by Local PCA, Neural Comput. 9 (1997) 1493.

[60] E. Reynders, G. Wursten, G. de Roeck, Output-only structural health monitoring in changing environmental conditions by means of nonlinear system identification, Struct. Heal. Monit. 13 (2014) 82–93.

[61] J. Mottershead, M. Friswell, Finite element model updating in structural dynamics, Springer N, Dordrecht, 1995.

[62] S. Monchetti, on the Role of Uncertainties in the seismic assessment of historic masonry towers, Florence/ TU Braunschweig, 2018.

[63] F. Magalhães, A. Cunha, E. Caetano, Vibration based structural health monitoring of an arch bridge: From automated OMA to damage detection, Mech. Syst. Signal Process. 28 (2012) 212–228.

[64] N. Cavalagli, G. Comanducci, F. Ubertini, Earthquake-Induced Damage Detection in a Monumental Masonry Bell-Tower Using Long-Term Dynamic Monitoring Data, J. Earthq. Eng. 22 (2018) 96–119.

[65] J. Kullaa, Damage detection of the Z24 bridge using control charts, Mech. Syst. Signal Process. 17 (2003) 163–170.

[66] K. Farrar, C. R.;Warden, Structural Health Monitoring: A Machine Learning Perspective, New York, 2013.

Chapter 3

Automated procedure

3.1 Introduction-3.2 The Automated Modal Parameters Identification techniques -3.3 Proposed automated system identification procedure-3.4 The Modal EXtractor algorithm-3.5 Validation of the automated system identification procedure -3.6 The proposed long-term monitoring algorithm

3.1 Introduction

This chapter introduces the proposed procedure for the extraction of the dynamic features from the signals collected by the long-term monitoring system. Among all the dynamic identification techniques that are reviewed in the previous chapter (*Section 2.3*) the parametric or time domain techniques are suitable to be implemented in a code. The definition of a robust Automated Modal Parameter Identification (AMPI) technique is the first step for building a SHM framework based on the damage sensitive features introduced in the previous chapter (*Section 2.5*).

The chapter starts with a brief review of the methods proposed by the Authors in the last decades describing the used techniques (*Section 3.2*). Then the problems of the Operative Modal Analysis are faced considering the advantages and the limits of the available procedures. Hence, it is introduced a new procedure AMPI technique that minimize the number of parameters to be set (*Section 3.3*). As well as the AMPI is defined in all the phases the MEX algorithm is created to implement in MATLAB© the instruction flow. Next the MEX algorithm is tested with simulated numerical test on a simplified FE model of a masonry tower (*Section 3.5*). Lastly is introduced an algorithm to process large dataset minimizing the variance of the extracted modal parameters (. *Section 3.6*).

3.2 The Automated Modal Parameters Identification techniques

During the last decades the modal testing of the large civil structures (*cfr Section 2.3*) switched from the EMA techniques to the OMA techniques, thanks to the developments of the mathematical models well established in the system theory. The main advantages are that the unknown input is modelled as a Gaussian white noise enabling the extraction of the modal properties directly from the collected signals. That is the main reason why a renewed interest by the researchers was put on the damage identification through the analysis of the structures during their operational conditions.

The techniques based on the Stochastic Subspace Identification can be considered the most effective identification techniques due to the easy implementation in the common programming codes and the robustness with low computational costs. As fully described in Section 2.3.3.1 the method is based on algebraic operations that can be easily accomplished by the modern computers. The drawbacks of that technique are the high number of parameters must be set and the distinction among the physical and the mathematical or spurious modes in an automated way.

Moreover, the hypothesis at the base of the OMA are often violated (non-stationarity, non-white noise, non-linearity, ground noise, length of the signals, etc.) introducing variance and bias errors that increase the difficulties and the uncertainties of the modal identification. Indeed, the system matrices $(\mathbf{A}, \mathbf{C})$ can only be estimated $(\hat{\mathbf{A}}, \hat{\mathbf{C}})$, introducing a certain level of bias. According to Reynders [1] three types of statistical errors can be defined: the bias of the model, the bias of the modes and the variance of the modes.

The bias of the model produces the so-called spurious modes that can be split in two different categories the noisy and the mathematical modes. The bias of the modes consists in the identification of a single mode that is expressed as the combination of two different modes. The variance of the modes deals with the variability of the identified modal parameters. Some bias of the model can be removed with the stabilization chart, imposing soft criteria on the distances between frequencies, mode shapes and damping ratios across two consecutive modal orders. The noisy modes can be partially eliminated imposing hard criteria on the damping ratio (expected range for the structure) and on the mode shapes (expected complexity). The variance and the bias of the modes should be faced with a proper choice of both the model order and the number of block rows in the Hankel matrix.

From that considerations arise three different order of problems:

- Define a suitable model order and the number of blocks in the Hankel matrix
- Removing the spurious and mathematical poles
- Define the accuracy of the extracted modal parameters.

From all the proposed AMPI algorithm proposed by the Authors during the last decades it is possible to identify four phases (Figure 3-I) that in some cases are not clearly distinguishable.

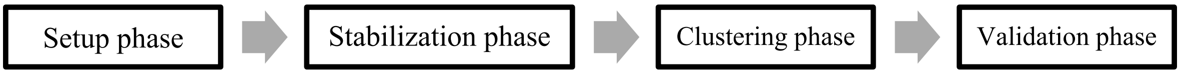

Figure 3-I The identified phases in the AMPI techniques.

For instance, Ubertini [2] proposed an AMPI based on the SSI-data algorithm with a range of variation both on the number of rows in the block Henkel matrix and in the model order. Then a hierarchical clustering approach with a fixed threshold is performed to identify the modes of two complex bridges. The modal properties are identified as the mean within the 95% confidence interval of each cluster. As well, Magalhães [3] has introduced a hierarchical clustering approach with an outlier analysis to extract the modal information. For defining the cutoff distance in the hierarchical tree, the Authors consider as reference the distance used in the stabilization chart. Moreover, for removing the spurious modes clusters it is used a criterion based on a minimum number of elements that belong to the same cluster. The procedure has been improved by Cabboi [4] introducing a self-adaptive threshold value based on the automated interpretation of the stabilization chart. The application to a complex arch iron bridge with SHM purposes has shown good results. In addition, Rainieri [5] has introduced a multi-stage algorithm called ARES, based on the automated definition of the cut-off distance related to the number of rows in the Hankel matrix derived by a sensitivity analysis. Then validation criteria are applied after the clustering stage and a k-mean clustering procedure with k=2 for the refinement of the obtained results.

While, Reynders [6] has proposed a procedure based on a three stages clustering procedure. Firstly, a k-means clustering is performed with k=2 distinguishing between certainly spurious and possibly physical modes using many relevant single-mode validation criteria as possible. The distance between the two clusters is then used as the threshold for the hierarchical clustering algorithm. At the end, for validating the extracted clusters, a set of hard criteria are applied. Similarly, Neu [7] has proposed a multi-stage clustering approach that has been tested to a coupled setup of strain and accelerations measurements used for wind tunnel tests of a wind blade model.

3.2.1 Setup phase

The setup phase is needed because of the stochastic nature of the unknown input leads to the definition of a range of model order. Because the presence of noise in the measurements it is impossible to define an optimal modal order for the subspace reduction. Indeed, the singular values of the projected space will slightly approach to zero and the definition of the optimal model order as a jump among two consecutive singular values is impossible. To tackle this problem the proper selection of a model order range of variation minimizing the bias is needed. In one hand, the under-modelling will lead to high bias in the modes (modal splitting); on the other hand, the over-modelling will lead to model the noise instead of physical modes (introducing spurious modes). Qin [8] analyses the first order perturbation of the system entropy to define the maximum model order but for real cases applications the method seems to be only an indication.

The selection of the number i of blocks in the Hankel matrix is not considered in many cases and it is only fixed a minimum value based on the sampling f_s and the lower expected frequency f_0.

$$i \geq n_c \frac{f_s}{2f_0} \tag{1}$$

Because of i represents the memory of the process, a high value means considering a higher number of past observations. That implies a minimum number of cycles n_c for the lower frequency to identify the first vibration mode. Usually n_c is set equal to one and the equation (1) become function only of the sampling rate and of the lower structural frequency. Brownjhon [9] find the optimal value of i considering a number of 2,33 cycles for the dynamic monitoring of a suspended bridge.

Rainieri [10] observed how the identified modal parameters, especially the damping are sensitive to the increase of the number of block rows in the Hankel matrix. The optimum value of the block rows in the Hankel matrix was found by monitoring the condition number of the projection matrix.

Table 3-I Number of parameters of the setup phase and the possible errors that can arise from an error in the choice.

Parameters in the Setup phase			
	Parameter		*Possible errors*
SU1	Minimum model order	ord_{min}	Bias of the modes
SU2	Maximum model order	ord_{max}	Bias of the model
SU3	Minimum number of block rows in the Hankel matrix	i_{min}	Variance of the modes
SU4	Maximum number of block rows in the Hankel matrix	i_{max}	Variance of the modes
	Total number of parameters		**4**[1]

3.2.2 *Stabilization phase*

Since the first time that the SSI algorithm was proposed to the scientific community, the problem of choosing the optimal model order was tackled by the plot of the stable poles versus the modal order and the frequency (*stabilization chart*). The stable poles are those poles that accomplishes the user defined Soft Criteria (SC) among two consecutive modal order. The aim is to identify the physical modes as those that can be found at

---

[1] Theoretically it should be fixed also the increment in the modal order Δord and the increment in the number of block rows Δi in the Hankel matrix. Moreover, the number of parameters can be reduced to 3 if an optimal value of the rows in the Hankel matrix is found.

every modal order. Ad introduced before, that tool allows to minimize the mathematical modes due to the over-modelling, but it cannot fully discriminate the spurious poles.

Table 3-II Some of the SC proposed by the Authors in the last years.

Soft Criteria (SC)		
S1	Frequency	$\mathbf{d}(\mathrm{f}_1,\mathrm{f}_2)=\frac{\lvert \mathrm{f}_1-\mathrm{f}_2\rvert}{\max(\lvert \mathrm{f}_1\rvert,\lvert \mathrm{f}_2\rvert)}$
S2	Damping	$\mathbf{d}(\xi_1,\xi_2)=\frac{\lvert \xi_1-\xi_2\rvert}{\max(\lvert \xi_1\rvert,\lvert \xi_2\rvert)}$
S3	Mode shape	$\mathbf{d}(\phi_1,\phi_2)=1-\mathrm{MAC}(\phi_1,\phi_2)$
S4	Poles	$\mathbf{d}(\lambda_1,\lambda_2)=\frac{\lvert \lambda_1-\lambda_2\rvert}{\max(\lvert \lambda_1\rvert,\lvert \lambda_2\rvert)}$
S5	Modal Phase Collinearity	$\mathbf{MPC}(\phi_\mathrm{j})=\frac{\left\lVert \mathrm{Re}\left(\tilde{\phi}_j\right)\right\rVert_2^2+\frac{1}{\epsilon_{\mathrm{MPC}}}\mathrm{Re}\left(\tilde{\phi}_j^{\mathrm{T}}\right)\mathrm{Im}\left(\tilde{\phi}_j\right)\left(2\left(\epsilon_{\mathrm{MPC}}^2+1\right)\sin^2(\theta_{\mathrm{MPC}})-1\right)}{\left\lVert \mathrm{Re}\left(\tilde{\phi}_j\right)\right\rVert_2^2+\left\lVert \mathrm{Im}\left(\tilde{\phi}_j\right)\right\rVert_2^2}$
S6	Mean Phase	$\mathbf{MP}(\phi_j)=\mathrm{arg}_\theta\min\frac{\left\lVert \mathrm{Im}\left(\phi_j\right)\tan(\theta)\mathrm{Re}\left(\phi_j\right)\right\rVert_2^2}{1+\tan\theta}$
S7	Modal Phase Deviation	$\mathbf{MPD}(\phi_j)=\frac{\sum_{\mathrm{o}=1}^{\mathrm{N}}\mathrm{w}_\mathrm{o}\arccos\left\lvert\frac{\mathrm{Re}(\phi_{\mathrm{jo}})\mathrm{V}_{22}-\mathrm{Im}(\phi_{\mathrm{jo}})\mathrm{V}_{12}}{\sqrt{\mathrm{V}_{11}^2+\mathrm{V}_{22}^2}\lvert\phi_{jo}\rvert}\right\rvert}{\sum_{\mathrm{o}=1}^{N}\mathrm{w}_\mathrm{o}}$
S8	Modal Transfer Norm	$\mathbf{d}(\mathrm{MTN}_{\infty,1},\mathrm{MTN}_{\infty,2})=\frac{\left\lvert\mathrm{MTN}_{\infty,1}-\mathrm{MTN}_{\infty,2}\right\rvert}{\max\left(\left\lvert\mathrm{MTN}_{\infty,1}\right\rvert,\left\lvert\mathrm{MTN}_{\infty,2}\right\rvert\right)}$
S9	Standard deviation	$\sigma(\mathrm{f}_j),\sigma(\xi_j),\sigma(\phi_j)$

In Table 3-II, are listed the most relevant SC proposed by the Authors that furnish an indication of the physics in the identified mode. The first three SC have been proposed from the introduction of the stabilization diagram, fixing suitable distance thresholds. According to the variance of each parameter the distances among the frequencies and the mode shapes exhibit lower threshold than those in terms of modal damping.

Table 3-III Values adopted by the Authors for building the stabilization chart

Author	$\mathbf{d}(\mathbf{f}_1,\mathbf{f}_2)$	$\mathbf{d}(\boldsymbol{\xi}_1,\boldsymbol{\xi}_2)$	$\mathbf{d}(\boldsymbol{\phi}_1,\boldsymbol{\phi}_2)$
De Roeck [11]	0,01	0,05	0,01
Magalhães [3]	0,01	0,02	0,01
Ubertini [2]	0,01	0,03-0,04	0,01
Peeters [12]	0,01	0,05	0,02

The other criteria show some others properties of the poles based on some assumptions about the mode shape complexity (MPC,MPD,MP) and on the variance $(\sigma(\mathrm{f}),\sigma(\xi),\sigma(\phi))$.

The SC illustrated herein can be split in other two categories: the first need the calculation of some distances among the system poles identified in two consecutive model order and the second that gives indication about the nature of each modes. This last class of single mode validation criteria is more similar to the hard criteria but giving a range of results and not a binary answer (yes/no).

Table 3-IV Some of the HC proposed by the Authors in the last years.

Hard Criteria (HC)		
H1	Damping ratio interval	$\xi \in [\xi_{\mathrm{min}}, \xi_{\mathrm{max}}]$
H2	Complex conjugate mode is present?	Yes/No

For reducing the spurious poles some Hard Criteria (HC) should be selected based on the expected dynamics of the structure. The poles that do not satisfy that criteria are rejected because they clearly don't represent a slightly damped vibration system.

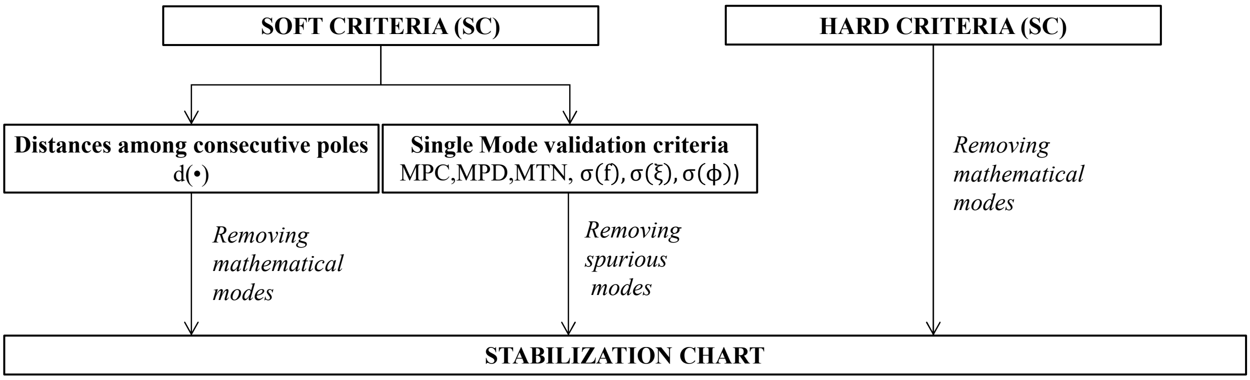

Figure 3-II Classification of the SC and HC used by the Authors in the AMPI.

The effects of each applied criteria are different ways of managing the bias. For removing the mathematical modes is needed only the classical SC limiting the distances among two different consecutive poles and the HC. The spurious poles can be reduced with the single mode validation criteria that furnishes a range of results that allows the discrimination of the spurious poles. The result is an improved stabilization chart with only candidates that exhibit a physic behaviour.

Table 3-V Number of parameters of the setup phase and the possible errors that can arise from an error in the choice.

Parameters in the stabilization phase	
Parameters	*Possible errors*
Soft Criteria (SC)	Missing some stable poles
Hard Criteria (HC)	Missing some low damping modes
Total number of parameters	**5-13**[2]

3.2.3 Clustering phase

The clustering phase is introduced for an automated interpretation of the stabilization diagram, taking all the stable poles and merging them in cluster with homogeneous dynamic features. The most effective technique is the hierarchical clustering based on the classification of the poles distance. The distances among all the elements

---

[2] The range identify a minimum and a maximum number of parameters used by the Authors in the proposed AMPI.

are represented in a sort of tree (called dendrogram) where each branch is the distance between the elements. Then a suitable cut off distance should be decided for cutting the tree joining together the elements that at this point are forming a cluster.

The most reliable distance for grouping together similar elements is a linear combination of the distances in terms of frequency and mode shapes.

$$d_{ij} = \frac{|f_i - f_j|}{\max(|f_i|, |f_j|)} + 1 - \mathrm{MAC}_{ij} \tag{2}$$

That arise from the observation that the frequencies and the mode shapes exhibit lower levels of variance than the modal damping ratio. A key aspect is the selection of a reliable threshold for cutting the dendrogram and defining the clusters. Higher levels of the threshold will group together elements that represents different modes, but low levels can mean exclude some poles that belong to the same mode. Magalhães [3] proposed a suitable threshold of 0,02 for the automated interpretation of the stabilization chart of the "Infante D. Henrique" bridge in Porto. Ubertini [2] extended the threshold to 0,02-0,04 to identify two bridges with a complex dynamic. Both the Authors underlines how the threshold depends on the data quality and on the dynamics of the structure. Indeed, the proposed values are tuned on the obtained stabilization charts from the available dynamic tests.

Recently, several Authors have tried different techniques for the clustering of the stable poles from the algorithms derived by the data mining and the machine learning techniques. The application of multistage clustering procedures seems to be very attractive, but the main drawback is that there is no more links with the stabilization chart that can give some indications on the effectiveness of the procedure. Moreover, in many cases the number of modes is unknown in advance and the k-means clustering algorithms or the partition methods cannot be used without some other operations.

Table 3-VI Number of parameters of the clustering phase and the possible errors that can arise from an error in the choice.

Parameters in the clustering phase			
	Parameter		*Possible errors*
C1	Cutoff distance	d_{max}	Grouping poles representing different modes
C2	Minimum number of elements for cluster	N_{cl}	Avoid the low excited modes
	Total number of parameters		**2**

3.2.4 Validation phase

The validation phase is not explicitly shown in the AMPI, but some indications about the estimated modal parameters are performed by the Authors. Magalhães [3] performs an outlier analysis after the hierarchical clustering stage to exclude some poles that can exhibit some anomalies, then the modal properties are represented by the cluster mean. Ubertini [2] represents the modal properties as the mean within the 95% of confidence interval. In both the cases the variances are linked to the selection of the tuning parameters in the setup phase. Hence low variances in the cluster population means that the selection of the initial tuning parameters is good enough.

Döhler [13] and Pintelon [14] define the uncertainties bounds of the estimated modal parameters performing a first order perturbation analysis. In other cases [5] the variance of the extracted modal parameters calculated over the cluster population is used as an indicator of the quality of the results.

3.3 Proposed automated system identification procedure

Among all the proposed AMPI techniques in the last decades not all the procedures are really fully-automated, but they need some tuning procedure that have to be made in advance. In many cases the influence of the number of block rows in the Henkel matrix is not considered at all or partially with a sensitivity analysis of the obtained results. Sometimes the threshold in the hierarchical clustering phase is fixed but it should depend on the configuration of the identified poles I the stabilization chart. Moreover, the major part of the work in literature don't consider a validation phase to confirm or not the quality of the obtained results.

On the other hand, the operative conditions can be heterogeneous leading to higher uncertainty bounds in the identified modal parameters and some misleading result can be obtained. This is a crucial point, because of the damage assessment based on the measurement of the frequencies require a high precision in the extracted modal parameters.

In that scenario there are still some gap to fill, that should be carefully analysed:

- Reduce as much as possible the parameters that must be chosen
- Validate the results through different strategies
- Define a simple and controllable procedure

The first point is needed to reduce as much as possible the interaction with the analyst, furnishing algorithms capable to learn from the available data. Then in some way the procedure should give some outputs easy to be controlled by the user to understand if everything is working in the right way. At the same time the outputs should be stored in clear way for the Modal tracking.

For each of the phases introduced in the previous section will be explained in detail which are the applied methods and the novelties introduced.

3.3.1 Setup phase

As a matter of fact, the setup phase is not largely discussed by the Authors, even if the proper choice of the modelling parameters of the Stochastic space are relevant in the modal identification results (cfr. Section 3.2.1). The proposed approach discussed herein is based on the selection of the optimal model parameters with a visual inspection of the variation in the matrices condition number and the entropy variation.

The approach joins together the procedures defined in [2,8,10], starting from the definition of the number of modes that can be identified N_m from the analysis of the frequency content in the PSD. That allows the definition of the minimum order needed to represent the N_m identified peaks.

$$ord_{min} = 2k_1\mathrm{N_m} \tag{3}$$

The coefficient k_1 is a coefficient higher than one that considers some modes buried in the peak analysis of the singular values. The maximum model order can be found increasing the minimum model order, without increasing it so much to tap into the over-modelling phenomenon.

$$ord_{max} = 2k_1k_2\mathrm{N_m} \tag{4}$$

The choice of the constants should be a trade-off between a lower computational cost and a high reliability in the modal identification. In some cases, the minimum order starts from the value of 2 implying only one identified mode and with the increase of the modal order the other modes can be identified. This strategy is to avoid with the automated procedure described herein because some mode can be excluded because its low numerosity respect to the maximum reachable. Indeed, it is suitable to fix a minimum model order as defined in (3) allowing the theorical detection of all the expected modes with the maximum number of elements per cluster. In that way the condition C2 should be a useful tool for a first selection of the feasible natural modes.

Table 3-VII Range of variation of the setup parameters chosen by the Authors.

Author	$\boldsymbol{k_1}$	$\boldsymbol{k_2}$	$\boldsymbol{n_c}$	*Structure*
Cabboi [4]	[1-1,36][3]	4,66	[7,92-10,24]	Arch iron bridge
Magalhães [3]	1	5	6,4	Precast concrete arch bridge
Reynders [6]	1	5,33	4	Precast concrete box bridge
Brownjhon [9]	1	7,35	2,33	Suspension Bridge
Ubertini [2]	2,2	1,75	[3,6-5,6][4]	Arch iron bridge-Steel footbridge

Once the range of variation of the modal order is selected, the minimum value of the number of block rows in the Hankel matrix can be found as the minimum number of block that allows the identification of a number of modes equal to the half of ord_{max}.

$$i_{min} = \frac{ord_{max}}{l} = \frac{2k_1k_2\mathrm{N_m}}{l} \tag{5}$$

Where *l* is the number of sensors and ord_{max} is the maximum value reachable by the model order. The equation (5) must satisfy the condition expressed in (1), anyway the minimum value satisfying this condition can be taken as lower bound in the range of variation of *i*.

The maximum value of *i* can be defined as a constant value k_3 multiplied for the minimum value obtained by the (5) satisfying the condition (1).

$$i_{max} = k_3 i_{min} \tag{6}$$

In [2] a reference value for k_3 is assumed equal to 1,5 and it seems a good compromise without increasing too much the computational cost. Once the boundary conditions are selected, the increments Δord, Δi respectively on the modal order and the number of block rows should be defined. To handle this problem, it is possible to

---

[3] The settings are different for the horizontal and vertical modes.

[4] In the proposed AMPI both i and the modal order values are varying the results reported herein corresponds to the boundaries of the chosen interval of variation.

consider a certain number of values related to the maximum number N_{SSI} of SSI analysis to perform in the setup phase.

$$\Delta ord = \frac{ord_{max} - ord_{min}}{\sqrt{N_{SSI}} - 1}$$
$$\Delta i = \frac{i_{max} - i_{min}}{\sqrt{N_{SSI}} - 1} \qquad (7)$$

This approach was introduced in [2] and it is a good compromise to control the computational cost. It should be notice that that approach was introduced to be performed at the beginning of every modal identification. In the procedure introduced herein, this operation is performed only in the setup phase to define the optimal number of *i* and the maximum modal order $\overline{ord}$.

Once the grid of *i* and *ord* is defined through the (2) (3) (4) (5) (6) (7), the proposed procedure is organized into three stages:

- For each value of $i \in [i_{min}: \Delta i: i_{max}]$ a SSI analysis is performed and the condition number of the weighted projection matrix is calculated for each model ordered belonging to the grid.
- The optimal value of i is selected from the optimization of the condition number surface. Then the optimal model order is selected from an analysis of the system entropy.
- Validation of the selected result through the analysis of the coefficient of variation of the frequency and the damping for every identified mode.

The condition number of a matrix **A** indicates when the problem is an ill-conditioned problem amplifying the numerical errors on the input data. It can be calculated as the ratio between the maximum and the minimum over the set of singular values λ_i [10]:

$$k(\mathbf{A}) = \frac{max|\lambda_i|}{min|\lambda_i|} \qquad (8)$$

In the SSI algorithm, both for the covariance and data driven, the SVD of the projection matrix is calculated and the model order is equal to the number of singular values retained. Indeed, for each value of i the condition number can be calculated by the (7). It is impossible to define a-priori the limit of $k(\mathbf{A})$, but from a visual inspection of the condition number plot at the varying of *i*, for a fixed model order it is possible to find the value of i where $k(\mathbf{A})$ is stable.

Hence to define the optimal modal order is checked the singular value entropy ΔE_i at each model order. When it approaches zero no other information can be obtained from the weighted projection matrix of the signals.

$$\Delta E_i = -\left(\frac{\lambda_i}{\sum_1^{ord} \lambda_i}\right) ln\left(\frac{\lambda_i}{\sum_1^{ord} \lambda_i}\right) \qquad (9)$$

In [8] the method is applied for a numerical simulation and for the modal identification of a suspended footbridge. In the first case the jump of ΔE_i is clearer, while in the second case it is hidden by the noise contained in the signals. Indeed, the equation (9) furnish an idea for the reduction of the modal order and the selection of $\overline{ord}$.

3.3.2 Stabilization phase

The stabilization phase is developed as mentioned in the previous section, choosing as SC the one in terms of frequency, damping ratio and mode shape. The HC are the one described on Table 3-IV. The proposed algorithm allowed the automated definition of the distance (*cfr. Section 3.3.3*) among the consecutive poles representing the same mode.

3.3.3 Clustering phase

Starting from the classical definition of the stable poles, the procedure defines an automated reading of the stabilization chart allowing the definition of the cutoff value in the hierarchical clustering analysis.

In the proposed method the cut-off value is chosen according to the automated analysis of the stabilization chart with a two steps procedure:

1. From the highest model order results each identified poles is considered a single element cluster. Then is evaluated the distance from the analysed cluster and each identified cluster in the lower model order. The minimum distance value $\mathrm{d}_i^{(k)}$ among the *i-th* pole at the *k-th* model order and the *j-th* pole at the *(k-1)-th* model order is saved at each step.

$$\mathrm{d}_i^{(k)} = \arg_i\left(\frac{\left|f_{\lambda_i^{(k)}} - f_{\lambda_j^{(k-1)}}\right|}{f_{\lambda_j^{(k-1)}}} + 1 - \mathrm{MAC}\left(\phi_{\lambda_i^{(k)}}, \phi_{\lambda_j^{(k-1)}}\right)\right) \tag{10}$$

   Hence the results of equation (10) represent the component of the distance vector $\mathbf{d}^{(\mathbf{k})} \in \mathcal{R}^i$ calculated as the minimum distance among the i poles of the *k-th* model order and the j poles of *(k-1)-th* model

2. Once the minimum values are calculated for each cluster, then the distance value d_k among all the n_k poles is evaluated at each k-step and is saved in the vector $\mathbf{d} \in \mathcal{R}^{1xN_p}$. The dimension of the vector is equal to the total number of poles N_p that can be found across the different model orders.

$$\mathbf{d} = \left\{\mathrm{d}_1^{(1)} \cdots \mathrm{d}_i^{(k)}\right\} \qquad with\ k = 1 \cdots \frac{ord_{max} - ord_{min}}{\Delta ord} \quad i = 1 \cdots n_k \tag{11}$$

3. The median value of the vector **d** representing all the distances between two consecutive modal orders stable poles is calculated and it is assumed as the cut-off threshold.

$$d_{max} = median(\mathbf{d}) \tag{12}$$

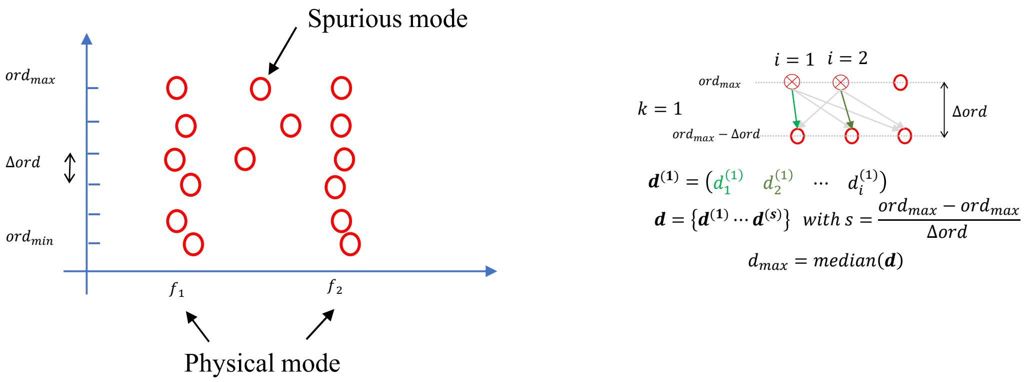

Figure 3-III The automated reading of the stabilization chart procedure. The grey arrows represent all the evaluated distances and the green arrows represent the minimum value.

In that way it is possible to evaluate a cut-off distance considering the main principle of the stabilization chart, that consider a physical mode when the pole is repeated in the higher model order. However, in some cases the median value can be substituted with the third quartile value to consider more candidates mode that will be discarded or not in the validation phase (*cfr. Section 3.2.4*).

This procedure is straightforward as showed in Figure 3-III, and it is a clear automatization of the three stages that are developed for the manual analysis of the stabilization chart. Hence, the choice of the possible physical mode is related to the repetition at different model orders of the same pole, corresponding to the vertical lines in the stabilization chart.

3.3.4 Validation phase

The introduction of a validation phase that must control the quality of the obtained results in a straightforward manner is a novelty in the research field. The proposed approach aims not only to validate the results, but it labels each candidate mode with a value expressing in some way the quality of the identified modes.

The requirements to achieve the aims of this new established phase are the following:

- Define the most effective single mode validation criteria, preferably arising both from time and frequency domain.
- Grouping together the results to obtain a unique value that can be easily compared through the identified sets of modal parameters.

A simple way to perform that requirements is to validate each identified cluster with as much as possible of the single modes validation criteria introduced by the Authors (Table 3-II) and eventually introduce some new criteria. The normalization of each criteria is obtained as the ratio between the considered validation result and to the maximum obtained among all the candidate modes. In such way as to obtain the best validation results are unitary values and zero if the candidate mode does not satisfy the chosen criterion. In some case the use of the reciprocal is needed to achieve the desired result. Furthermore, not all the single mode validation criteria have the same relevance for each case, indeed it is suitable to perform a weighting of the obtained results. That fact can arise from the selected validation criteria or for the structural dynamics itself.

Hence it is introduced the Modal Quality Index (MQI), consisting in the weighted mean of the normalized quality tests (QT) results.

$$(\mathrm{MQI})_{\mathrm{j}} = \frac{\sum_{i=1}^{n} \alpha_{\mathrm{i}} I_i}{\sum_{i=1}^{n} \alpha_{\mathrm{i}}} \qquad with\ \alpha_{\mathrm{i}}, \mathrm{I}_{\mathrm{i}} \in [0,1] \tag{13}$$

Where $(\mathrm{MQI})_{\mathrm{j}}$ is the *j-th* mode quality index, *n* is the number of chosen single mode validation tests, α_i is the *i-th* weighting constant and I_i is the *i-th* test normalized Index result.

The most common single validation criteria will be briefly shown in that paragraph to underline what they are indicating and what can imply a higher value of a certain indicator.

3.3.4.1 Variance of the identified Modal Parameters

The standard deviation of each cluster modal parameter is a strong indicator to detect the mathematical modes. Large deviation from the mean in terms of frequency and damping ratio implies the presence of a mathematical mode. The coefficient of variation of each candidate mode is the most efficient parameters to understand how much the values are deviating from the mean. The reason why high values of deviation among the elements of a cluster means a high probability of a mathematical mode stand beside the meaning of the stabilization chart. A certain physical mode will be identified at the same frequency value or with a little deviation among the poles identified at each modal order. The mathematical modes instead are modelled by the stochastic model to identify the required number of modes equal to the modal order. Thus, the deviation from the mean values are larger than the modes that represent the structural dynamics.

The frequency values are more stable than the damping ratio to the initial tuning in the setup phase, representing a more reliable parameter. The indicators about the level of variance of the *j-th* cluster in terms of frequency and damping are the following:

$$\begin{aligned} \boldsymbol{I_{f,j}} &= 1 - \big(\boldsymbol{cov}(\boldsymbol{f_i})\big)_{\boldsymbol{j}} \\ \boldsymbol{I_{\xi,j}} &= 1 - \big(\boldsymbol{cov}(\xi_i)\big)_{\boldsymbol{j}} \end{aligned} \tag{14}$$

Where $\boldsymbol{I_{\bullet}} \in [\mathbf{0}, \mathbf{1}]$ is the result of the normalized single mode validation criterion and $cov(\bullet)$ represents the cluster Coefficient Of Variation (COV).

3.3.4.2 Modal Transfer Norm

The Modal Transfer Norm (MTN) is the norm infinity of the contribution of each mode to the PSD $\mathbf{S}^{+}_{\mathbf{yy}}(\boldsymbol{\omega}) \in \mathbb{C}^{lxl}$ calculated from the covariance matrix of the reduced state space dimension. Applying the z-transform and using the properties of the stochastic subsystem, it is possible to obtain the PSD matrix:

$$\mathbf{S}^{+}_{\mathbf{yy}}(\mathbf{z}) = \mathbf{C}(z\mathbf{I} - \mathbf{A})^{-1}\mathbf{G} + \frac{1}{2}\boldsymbol{\Lambda}_{\mathbf{0}} \quad \text{with} \quad z = e^{i\omega\Delta t} \tag{15}$$

The contribution $\mathbf{S}^{+}_{\mathbf{yy,i}}(\boldsymbol{\omega}) \in \mathbb{C}^{lxl}$ of each single mode to the modal transfer norm can be written as follows:

$$\mathbf{S}^{+}_{\mathbf{yy,i}}(\mathbf{z}) = \phi_{\mathrm{i}}(z - \lambda_i)^{-1} g_i + \frac{1}{2}\boldsymbol{\Lambda}_{\mathbf{0i}} \tag{16}$$

Where λ_i is the discrete pole and the vector $\boldsymbol{g_i}$ and the covariance matrix $\boldsymbol{\Lambda}_{\mathbf{0i}}$ can be calculated as follows:

$$\begin{aligned} \boldsymbol{g_i} &= (\Psi^{-1})_i\mathbf{G} \\ \boldsymbol{\Lambda_{0i}} &= \phi_{\mathrm{i}}(\Psi^{-1})_i\boldsymbol{\Sigma}^s\Psi_i^T\ \phi_i^T \end{aligned} \tag{17}$$

Loosely speaking, the PSD calculated with the identified system matrices is expanded in the sum (2), projecting $\mathbf{S}^{+}_{\mathbf{yy}}(\boldsymbol{\omega})$ in a new reference system expressed by the eigenvector matrix $\boldsymbol{\Psi}$.

$$\mathbf{S}^{+}_{\mathbf{yy}}(\boldsymbol{\omega}) = \sum_{\boldsymbol{i=1}}^{\boldsymbol{N}} \mathbf{S}^{+}_{\mathbf{yy,i}}(\boldsymbol{\omega}) \tag{18}$$

In [1] it is shown how the MTN is a good indicator for detecting the spurious poles that exhibit lower values.

$$\boldsymbol{n_i} = \left\|\mathbf{S}^{+}_{\mathbf{yy,i}}(\boldsymbol{\omega})\right\|_{\infty} = \overset{max}{\omega}\sigma\left(\mathbf{S}^{+}_{\mathbf{yy,i}}(\boldsymbol{\omega})\right) \tag{19}$$

Where $\sigma(\bullet)$ denotes the set of singular values.

The MTN is the error that is made if a certain mode is excluded from the dynamic response of the system. It estimates the modal participation factor of each mode, implying that large values mean certain physic mode. Lower values mean probably a spurious or mathematical mode with less relevance in the global dynamic response. The indicator can be evaluated as follows:

$$\boldsymbol{I_{MTN,j}} = \frac{\boldsymbol{MTN_j}}{max\left(\boldsymbol{MTN_j}\right)} \tag{20}$$

Where $\boldsymbol{I_{MTN,j}} \in [\mathbf{0},\mathbf{1}]$ is the result of the normalized single mode validation criterion based on the MTN.

3.3.4.3 Modal Phase Collinearity (MPC)

For proportionally damped system the mode shape components plotted in the complex plane are almost aligned on a straight line. In particular, each real mode exhibits a monophase behaviour with almost real components. That means in phase or out of phase components of each mode shape implying a phase angle of zero or hundred eighty degrees. The formula in Table 3-I, firstly proposed in [15] gives values between 0 indicating no collinearity and 1 indicating perfect collinearity.

$$\mathbf{MPC}(\phi_{\mathrm{j}}) = \frac{\left\|\mathrm{Re}\left(\tilde{\phi}_j\right)\right\|_2^2 + \frac{1}{\epsilon_{\mathrm{MPC}}}\mathrm{Re}\left(\tilde{\phi}_j^{\mathrm{T}}\right)\mathrm{Im}\left(\tilde{\phi}_j\right)\left(2\left(\epsilon_{\mathrm{MPC}}^2+1\right)\sin^2(\theta_{\mathrm{MPC}})-1\right)}{\left\|\mathrm{Re}\left(\tilde{\phi}_j\right)\right\|_2^2 + \left\|\mathrm{Im}\left(\tilde{\phi}_j\right)\right\|_2^2} \tag{21}$$

Where $Re(\bullet)$ is the real and $Im(\bullet)$ is the imaginary part, $\|\bullet\|_2$ is the Euclidean norm of the vector and $\tilde{\phi}_{\mathrm{j}} \in \mathbb{C}^N$ represents the mode shape deviation from the mean value.

$$\tilde{\phi}_{ij} = \phi_{\mathrm{ij}} - \frac{\sum_{i=1}^{N}\phi_{\mathrm{ij}}}{N} \tag{22}$$

The degree of correlation of each components of the mode shape can be analysed through ϵ_{MPC} and θ_{MPC}

$$\epsilon_{MPC} = \frac{\left\|\mathrm{Im}\left(\tilde{\phi}_j\right)\right\|_2^2 - \left\|\mathrm{Re}\left(\tilde{\phi}_j\right)\right\|_2^2}{2\mathrm{Im}\left(\tilde{\phi}_j\right)\mathrm{Re}\left(\tilde{\phi}_j\right)} \tag{23}$$

$$\theta_{MPC} = arctan\left(|\epsilon_{MPC}| + sign(\epsilon_{MPC})\sqrt{1+\epsilon_{MPC}^2}\right)$$

The result is unitary if the correlation of each modal component is perfect or zero for completely uncorrelated components. Then the MPC is itself a robust indicator for the physic modes, for the j-th candidate mode the indicator can be written as follows:

$$\boldsymbol{I_{MPC,j}} = \mathbf{MPC}(\phi_j) \tag{24}$$

3.3.4.4 Mean Phase Deviation (MPD)

The MPD represents the mean deviation from the angle in the complex plane representing the best linear fit of the modal shape components. As the MPC represent the common behaviour of the mode shapes in a proportional damped system, but in that case the zero value represents no deviation from the alignment among each component and one value represents a complete deviation from the straight line. Considering a mode shape with N degree of freedom $\phi_j \in \mathbb{C}^N$

$$\mathbf{MPD}(\phi_j) = \frac{\sum_{o=1}^{N} w_o \arccos\left|\frac{\mathrm{Re}(\phi_{jo})V_{22} - \mathrm{Im}(\phi_{jo})V_{12}}{\sqrt{V_{11}^2 + V_{22}^2}|\phi_{jo}|}\right|}{\sum_{o=1}^{N} w_o} \tag{25}$$

Where V_{11}, V_{22}, V_{12} are the components of the singular value matrix in the decomposition of the matrix composed by the real and the imaginary part of the mode shape vector ϕ_j representing the j-th candidate mode. The vector $w \in \mathcal{R}^N$ is a weighting vector to increase the influence of each components, to give more importance to the higher components in the mode shape is usually equal to $|\phi_j|$. Then the MPD is itself a robust indicator for the physic modes, for the j-th candidate mode the indicator can be written as follows:

$$\boldsymbol{I_{MPD,j}} = 1 - \mathbf{MPD}(\phi_j) \tag{26}$$

3.3.4.5 Frequency Rating (FR)

This new indicator is the ratio between the ordinates of the first singular value of the PSD at the frequency of interest and the maximum value. The first singular value is calculated with the FDD technique, using the p-Welch method. This is a rough indicator, but it can give some information derived by the analysis in the frequency domain without considering the results of the stochastic model identification.

$$\boldsymbol{I_{FR,j}} = \frac{\sigma\left(\mathbf{S}_{yy}^{+}(\boldsymbol{\omega_j})\right)}{\underset{\omega}{max}\,\sigma\left(\mathbf{S}_{yy}^{+}(\boldsymbol{\omega})\right)} \tag{27}$$

Where $\boldsymbol{I_{FR,j}} \in [\mathbf{0}, \mathbf{1}]$ is the result of the normalized single mode validation criterion based on the values of the first singular values of the positive PSD $\mathbf{S}_{yy}^{+}(\boldsymbol{\omega})$.

Obviously, the peaks in the spectral density do not automatically mean the presence of physical mode and the amplitude depends on how the much the modes are excited. Indeed, the weighting coefficient α should be chosen carefully to avoid misleading modal identification.

3.4 The Modal EXtractor algorithm

The **M**odal **EX**tractor (MEX) algorithm is the script implemented on MATLAB© that follows the phases described in the previous sections for the automated identification of the modal parameters. Before the operations of the system identification phase (Figure 3-I) a signal pre-processing phase is needed to reduce the noise effects. The number l of collected signals with n samples, are gathered together in the signal matrix $\mathbf{A} \in \mathcal{R}^{nxl}$ and the time vector $\mathbf{t} \in \mathcal{R}^{nx1}$ is calculated from the sampling frequency f_s. Then the signals are reduced to avoid the tails values and the spike are removed fixing a feasible cut-off value in terms of acceleration. The mean is removed from every signal and a battery of two *n-th* order Butterworth[5] filters is applied.

The first provide a high pass filter, reducing the measuring errors at low frequencies produced by the accelerometers. Then a second low pass filter is applied to isolate the frequency band of interest in the signals where the first resonant frequencies are supposed to be. The filtered signals are down sampled[6] to a lower frequency range to minimize the contribution of the background noise. The resampling frequency should be chosen carefully, both considering the effects of the digital filtering both to maximize the SNR. Some Authors [16] suggest that the Nyquist resampling frequency is at least equal to 1,2 times the low pass cut off frequency avoiding the aliasing effects.

As all the blocks of the algorithm, the outputs are both in terms of MATLAB© files (.m) and images (.fig) both to save the obtained results and to have a visual check of the performed operations. At the end of signal pre-processing the outputs are the matrix of the resampled signals matrix ($\mathbf{A_{rf}}$) and the time resampled vector ($\mathbf{t_{rf}}$) and the figures about the raw and processed signals. Also, the number of signals (l) is stored with the RMS and the Kurtosis of each signals collected in two vectors $RMS, KURT \in \mathcal{R}^{l}$.

With the output file of the pre-processing phase is fed the system identification phase that concerns the operations introduced in section 3.3. The parameters that have to be set are only six: the three SC (S1,S2,S3), the two HC (H1,H2) and the minimum number of elements for each cluster (N_{cl}). For the SC there is a wide literature that suggests very close value (*cfr.Table 3-II*), for the HC the only doubt is on the lower bound of the damping ratio. A lower limit is fixed to avoid the identification of harmonic responses to some coloured noise that usually exhibits low damping ratio. Therefore, it is possible to fix that limit once the structural damping can be evaluated in advance. Anyway, it is possible to perform a modal identification with the lower bound equal to zero checking the damping range for every identified mode.

The clustering phase is performed with a single linkage algorithm [7]based on the average distance between two clusters with a threshold distance expressed as in equation (2). The automated interpretation of the stabilization diagram is performed with the procedure described in section 3.3.3. The formed clusters are all candidates'

---

[5] The Butterworth filtering coefficients are found with the function available on MATLAB© *butter.m* and the filtering with the function *filtfilt.m* that produces filtered signals with zero phase distortion (*https://it.mathworks.com/*).

[6] The down sample is performed with the function *resample.m* which allows the downsampling avoiding aliasing phenomena and delay phenomena (*https://it.mathworks.com/*).

[7] This algorithm is implemented on MATLAB© with the function *linkage.m* and also the dendrogram plot can be represented through the function *dendrogram.m*.

modes and a first selection can be done defining a minimum value of the of elements for each cluster. That value can be fixed as a constant k_{cl} multiplied for the maximum number of elements available for each cluster.

$$N_{cl} = k_{cl} \frac{ord_{max} - ord_{min}}{\Delta ord} \tag{28}$$

In my experience this constant can be set equal to 0,33 that is a compromise between the exclusion of the mathematical poles that can arise in case of over-modelling and the possible identification of a low excited mode. Nevertheless, this parameter can be avoided, and all the cluster dimension are considered, and their consistence is then evaluated in the validation phase. Another solution that can be found in [2] is to consider the minimum number of elements in a cluster equal to three. In my experience if the parameters during the set-up phase are well set the value can be set lower than one third, but if the procedure is performed for long term monitoring the value can be set higher. Indeed, the proposed value is a good compromise to have a clearer set of clusters without excluding some low excited mode.

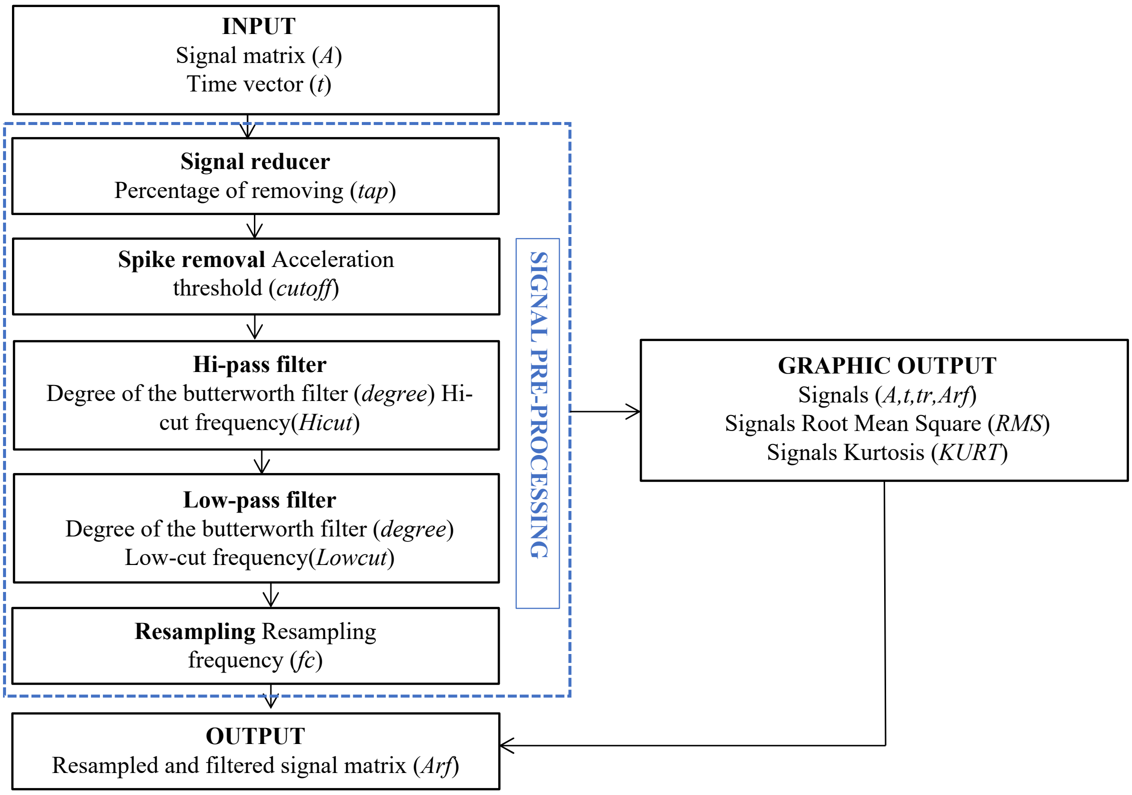

Figure 3-IV The flow chart of the signal pre-processing phase in the MEX algorithm.

In the validation phase for each cluster are calculated the chosen single mode validation criteria (*cfr. Section 3.3.4*) and each weighting coefficients α_i must be carefully decided for a proper calculation of the MQI.

It is impossible to define a priori the optimal value of the coefficients because the results of the modal identification depend both on the structural dynamics both on the ambient excitation (*cfr. Section 3.3.4.1*).

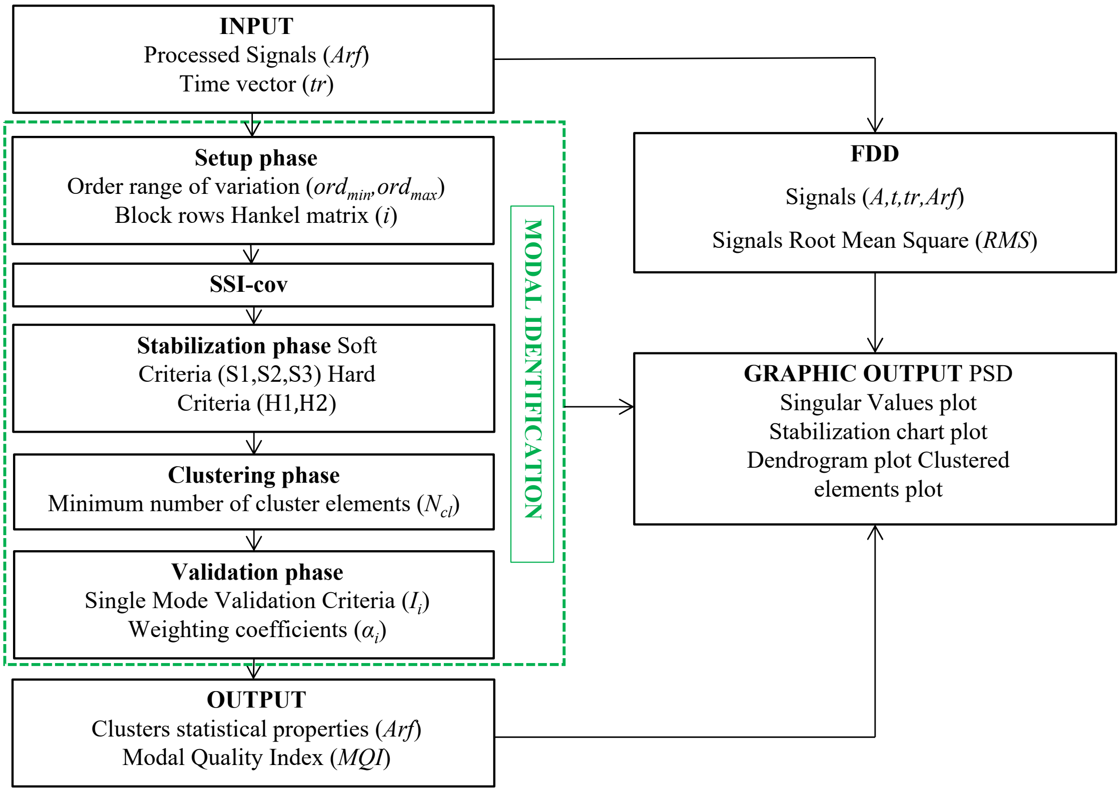

Figure 3-V The flow chart of the signal modal identification phase in the MEX algorithm.

Some recommendations can be given about the feasible range of the weighting coefficients, but every case should be carefully analysed. The standard deviation of the frequency and the modal transfer norm are the most reliable indicators and they need higher weighting values. The indicators about the mode complexity are also very powerful and reliable indicators but, in some case, the real modes could exhibit high level of complexity. Hence, it should be checked the nature of the modes before considering the MPC and MPD as reliable indicators and giving to them high weighting coefficient. Anyway, in the major part of the cases the modes exhibit low levels of complexity and those indicators are very effective.

The indicator about the damping variance is less reliable than the others because this value is very sensitive to the violation of the hypothesis at the base of the SSI identification technique [5]. Actually, it is impossible to check the hypothesis and the set-up phase gives only an idea of the optimal values to set in the SSI procedure.

The frequency rating indicator as it is formulated cannot be consider with a very high weight because the peaks in the PSD singular value decomposition can exhibit different level of intensity for several facts. First, the input energy can be condensed on a limited frequency band exciting more the nearby modes. That does not necessary mean that these are the only modes present in the signals. Second the criterion can give false indications also when harmonic responses are in the signals, exhibiting very high narrow band peaks in the frequency domain. Anyway, this indicator with the MTN is the only arising from the frequency domain technique and it can give a contribution to confirm the obtained identification results.

The parameters used by the algorithm are listed in Table 3-VIII with an indication about the ranges of the established weighting coefficients (V1-V6).

Table 3-VIII Number of parameters in the MEX algorithm and an indicative range of variation of each.

Parameters in the MEX algorithm				
	Parameter		*Range of variation*	*Phase*
S1	SC in terms of frequency	df	[0-0,01]	Stabilization Phase
S2	SC in terms of damping	$d\xi$	[0-0,05]	Stabilization Phase
S3	SC in terms of mode shapes	$d\phi$	[0-0,02]	Stabilization Phase
H1	HC on the damping range	$\Delta\xi$	[0,005-0,1]	Stabilization Phase
H2	HC on the nature of the modes (complex conjugate)	-	-	Stabilization Phase
C2	Minimum number of elements for cluster	k_{cl}	[0-0,5]	Clustering Phase
V1	Weighting coefficients on the frequency variance	α_f	[0,75-1]	Validation Phase
V2	Weighting coefficients on the damping variance	α_ξ	[0,5-1]	Validation Phase
V3	Weighting coefficients on the Modal Transfer Norm	α_{MTN}	[0,5-1]	Validation Phase
V4	Weighting coefficients on the Modal Phase Collinearity	α_{MPC}	[0,75-1]	Validation Phase
V5	Weighting coefficients on the Mean Phase Deviation	α_{MPD}	[0,75-1]	Validation Phase
V6	Weighting coefficients on the Mean Frequency Rating	α_{FR}	[0-0,3]	Validation Phase
	Total number of parameters		**9-15**	

3.5 Validation of the automated system identification procedure

The validation of the procedure is performed through a numerical simulation of a classically damped system. The tested structure is a simplified FE model of the "Torre Grossa". For the sake of simplicity, the lateral buildings are neglected, and the geometry is simplified to avoid computational problems. The modelling strategy of the historic masonry follows the homogenisation approach proposed by Zucchini [17], by the use of 8-nodes iso-parametric elements (SOLID 185) with the commercial software ANSYS.

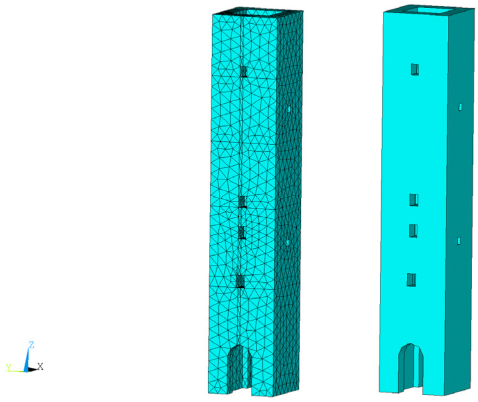

FE model properties				
Young's moduli [MPa]	υ	γ *[kg/m^3]*	*B [m]*	*H [m]*
4500	0,2	1600	9,5×9,5	52

Figure 3-VI View of the FE model developed with the commercial software ANSYS 19.0 and the mechanical properties of the material adopted.

The solid model is composed by 8559 elements and 2671 nodes guaranteeing a good compromise between the computational effort and the obtained results. The geometric and mechanical properties of the elastic analysis are summarized in Figure 3-VI.

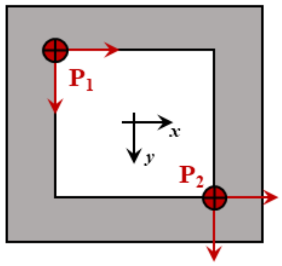

	FE model measured points				
Direction	*Sect. 1 (z=20,5 m)*	*Sect. 2 (z=24,8 m)*	*Sect. 3 (z=30 m)*	*Sect. 4 (z=37,3 m)*	*Sect. 5 (z=42,9 m)*
P1x	A1	A5	A9	A13	A17
P1y	A2	A6	A10	A14	A18
P2x	A3	A7	A11	A15	A19
P2y	A4	A8	A12	A16	A20

Figure 3-VII The measured points of the model represented in the figure on the left. On the right the table with the name of each measurements in each section (Sect. 1-5).

The “experimental” results are calculated with the simulated accelerations recorded in the two directions at two distinct point for each monitored section (Figure 3-VII). That signals are calculated through a linear dynamic analysis with the direct integration of the equation of motion an artificially generated input is with random values extracted from a normal distribution, obtaining a broadband process over the investigated frequency range.

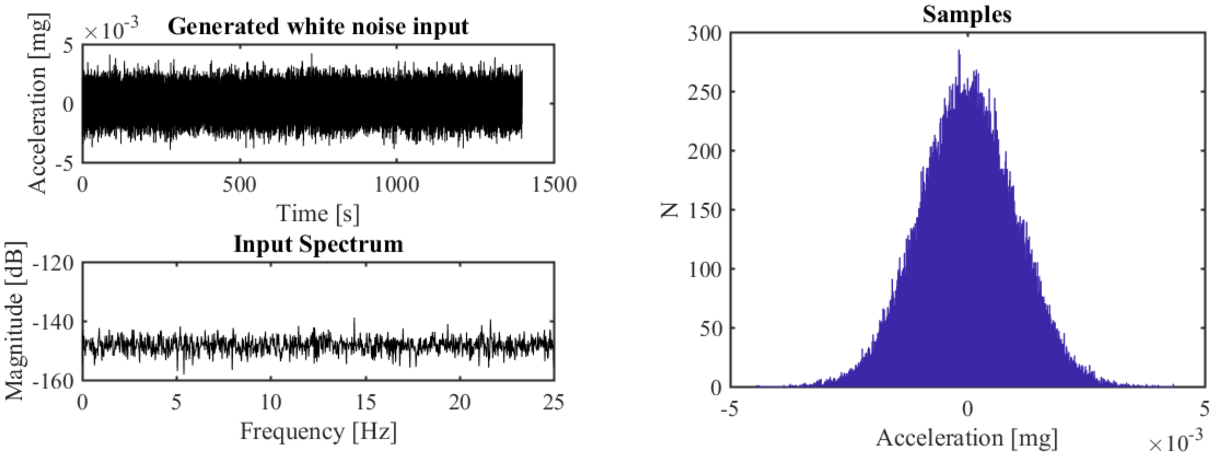

Figure 3-VIII The White noise input used as input in the #TEST (Table 3-X).

The generated white noises are applied both in the x and y directions simultaneously. Hence the FE model is excited through random vibrations acting in the two principal directions to simulate the response under unknown dynamic loads. The effective damping of the model has been checked by an impulsive test with displacements proportional to each mode shape. In order to obtain the free vibration response of each mode as a SDOF (Figure 3-IX). Then the damping has been calculated as the logarithmic decrement at each measured section. Hence the mean value is considered as the effective damping on the simulated response.

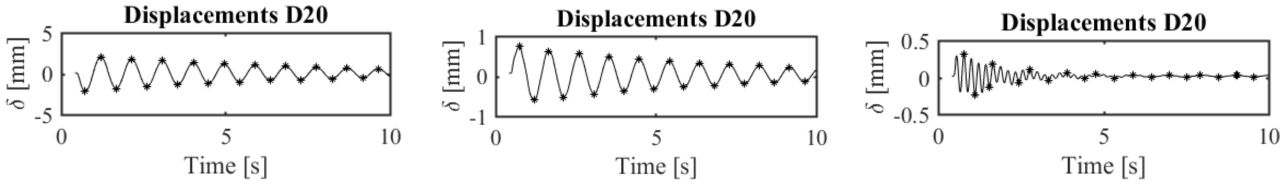

(a) (b) (c)

Figure 3-IX The free vibration of the impulsive tests of the first three modes: (a) first (b) second (c) third mode measured at the last level.

In Figure 3-X are showed in blue the first nine mode shapes for the built FE model that are considered as reference values to validate the results obtained through the MEX algorithm in red. That result is obtained considering the signals recording during the #TEST 1 (Table 3-IX).

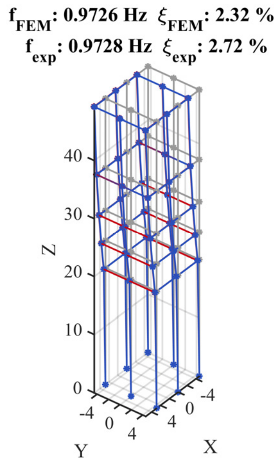

First bending x-x

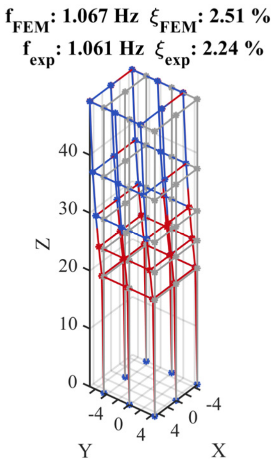

First bending y-y

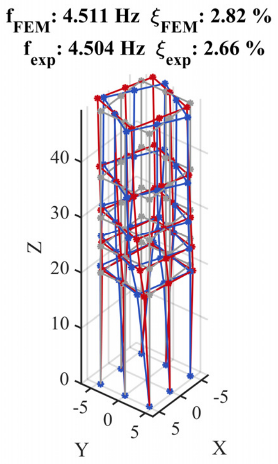

First torsional

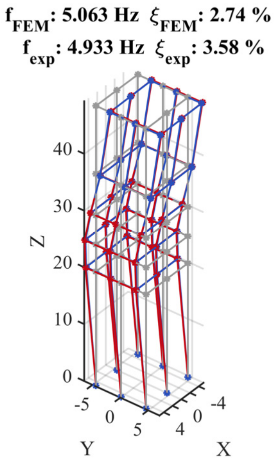

Second bending y-y

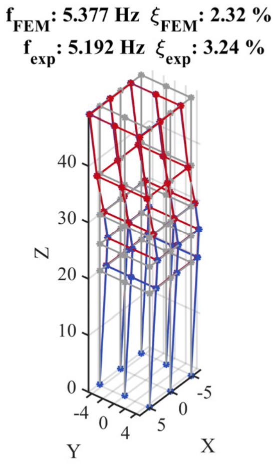

Second bending x-x

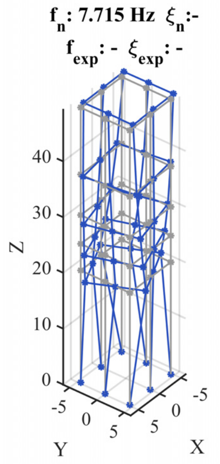

Vertical-torsional

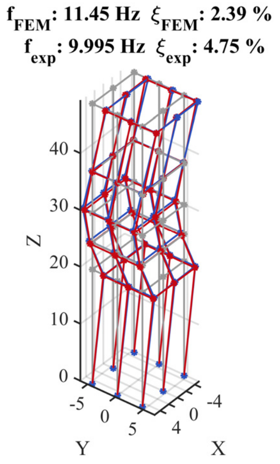

Third bending y-y

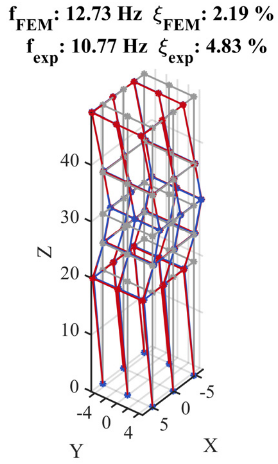

Third bending x-x

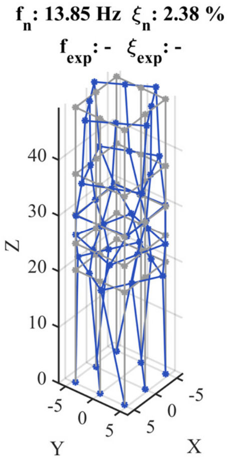

Third torsional

Figure 3-X The mode shapes from the FE model, considered as reference values in blue and in red the mode shapes identified from the simulated white noise responses (#TEST 1).

In Figure 3-XIThe differences between the identified modal parameters and the reference values obtained from the FE model considered as the reference values. The MQI reflects the quality of the modes showing a good agreement with the distances of each modal parameter. For instance, the second mode that collects a value of 0,99 for the minimum cumulative distance equal to 11,36%. Then the first mode exhibits a cumulative distance equal to 17,29% for a MQI value equal to 0,91. Lastly, for the third and fourth mode the MQI falls down to about the 0,83 for a cumulative distance respectively of 19,72% and 34,08%. Even if the cumulative distance of the third mode is not so far from the second it is worth to underline that the most relevant difference is in terms of mode shape that is a more reliable output of the model than the damping. Hence a lower quality in the MQI states that phenomenon.

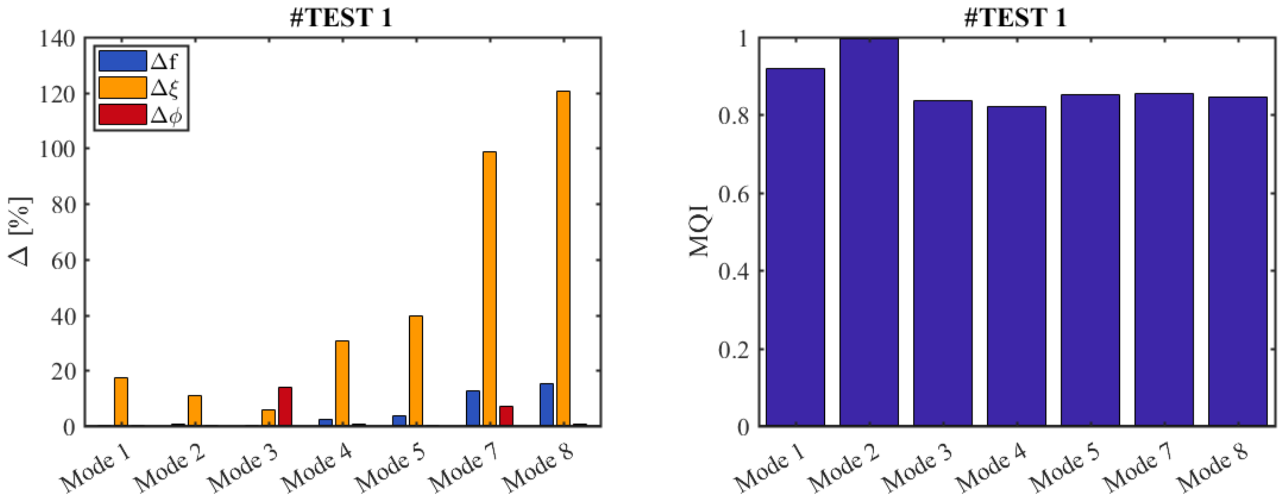

(a) (b)

Figure 3-XI The #TEST 1 results: (a) the distance between the identified and the reference modal parameters (b) the results in terms of MQI.

After the validation of the procedure some of the source of variability are investigated, manipulating the input white noise; in particularly these effects are analysed:

- The presence of some coloured noise
- The effect of the sampling rate
- The effect of limited signals length
- The effects of the SNR

Thus, the tests show in Table 3-IX are performed to the FE model introduced above. Aiming to capture the influence of each single parameter on the identification results by the comparison between the reference values and those calculated with the MEX algorithm. Furthermore, it is investigated the effectiveness of the MQI to characterize the quality of the modes and the capability of rejecting the noisy or spurious mode.

Table 3-IX The test campaign performed on the FE model varying the length, the sampling rate, the level of ground noise and the dynamic input.

FE model input			
Test number #TEST	*Length [s]*	*Sampling rate [Hz]*	*Input*
1	1400	50	White noise input
2a	700	50	White noise input
2b	700	50	White noise input
3	350	50	White noise input
4	175	50	White noise input
5	700	100	White noise input
6	700	50	White noise input and noise in the output (LV 1)
7	700	50	White noise input and noise in the output (LV 2)
8	700	50	White noise input and noise in the output (LV 3)
9	700	50	White noise input and noise in the output (LV 4)
10	700	100	White noise input and noise in the output (LV 1)
11	700	100	White noise input and noise in the output (LV 2)
12	700	100	White noise input and noise in the output (LV 3)
13	700	100	White noise input and noise in the output (LV 4)
14	700	50	White noise input and Harmonic forces

Firstly, is tested the effects due to some coloured noise on the identified modal parameters. The noises are two sinusoidal with two distinct frequencies at 1 and 2,5 Hz (Figure 3-XII). Aiming the simulation of two cases: a narrow band process near to a peak in the frequency response function (1 Hz) and far away from the resonant frequencies (2,5 Hz).

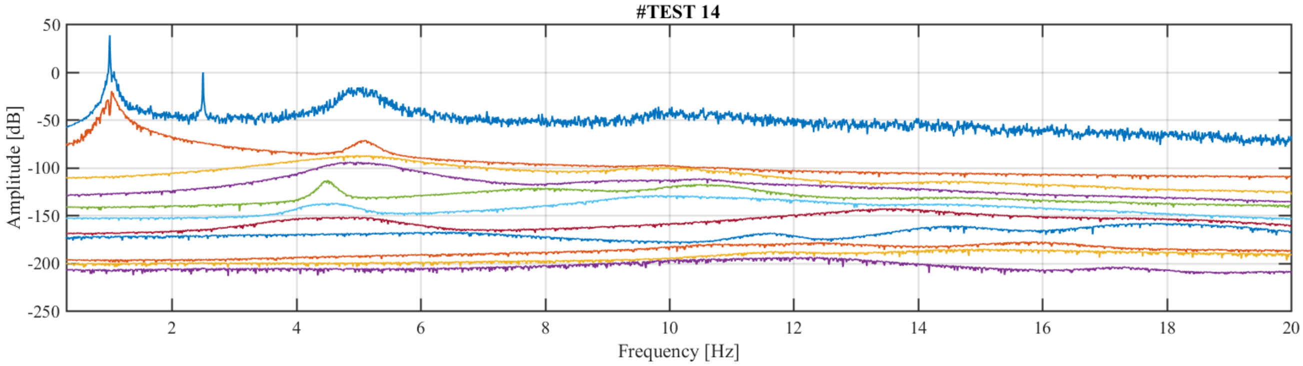

Figure 3-XII The singular values plot of the PSD matrix in the #TEST 14 the two harmonic components are visible at 1 Hz and 2,5 Hz.

To detect the nature of that peaks were performed two tests: the first considering an adequate lower bound for the condition H1 and the second removing that limit. In the first case the peaks at 2,5 Hz is excluded with the H1 criterion by the procedure (Figure 3-XIII (b)) and the first mode is identified with a MQI of 0,62. In the second case both the harmonic components can be found with low MQI values: 0,62 for the peak at 1 Hz and 0,72 for the peak at 2,5 Hz.

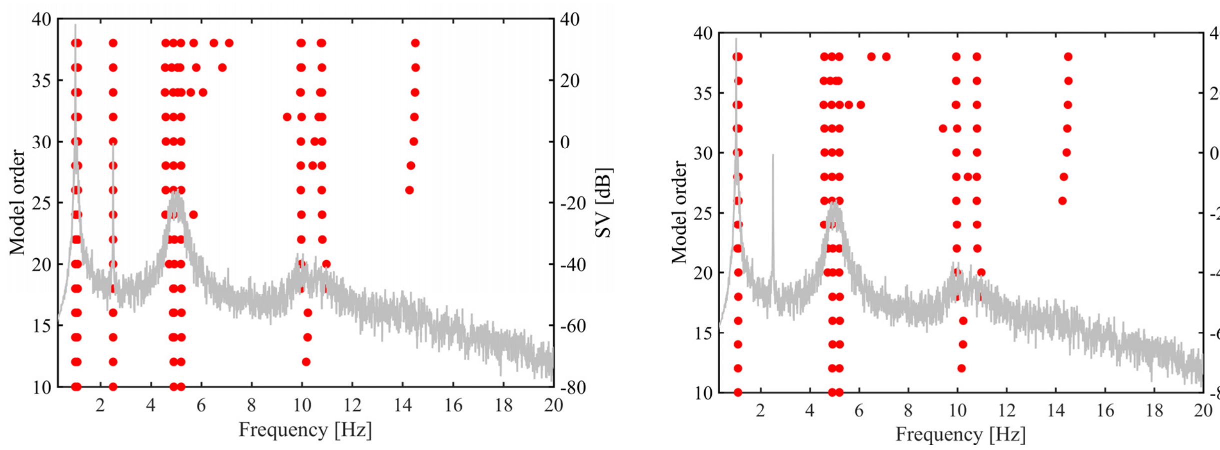

(a) (b)

Figure 3-XIII The stabilization chart obtained for the #TEST 14 (a) with the H1 criterion [0-10%] and (b) with a lower bound fixed at the 0,5% [0,5%-10%].

The influence of the sampling rate is tested both with or without the presence of an external noise modelled as a broadband process affecting the signals with different levels of energy (Table 3-X). Firstly, the influence of the sampling rate is tested without noise using the #TEST 2 and #TEST 5 that have the same length of 700 s. The sampling frequency is reduced by means of two procedures: the first aiming to investigate only the influence of the higher sampling rate decimating the signal by a factor 2 (#TEST 2b) and the second generating a new white noise input with a higher sampling frequency (#TEST 2a) and performing again the numerical analysis. Then the modal parameters are extracted again through the automated algorithm. Hence, the first case gives a feedback on MEX algorithm and the second on the influence of the accuracy in the numerical integration performed by the FE software depending on the integration step length.

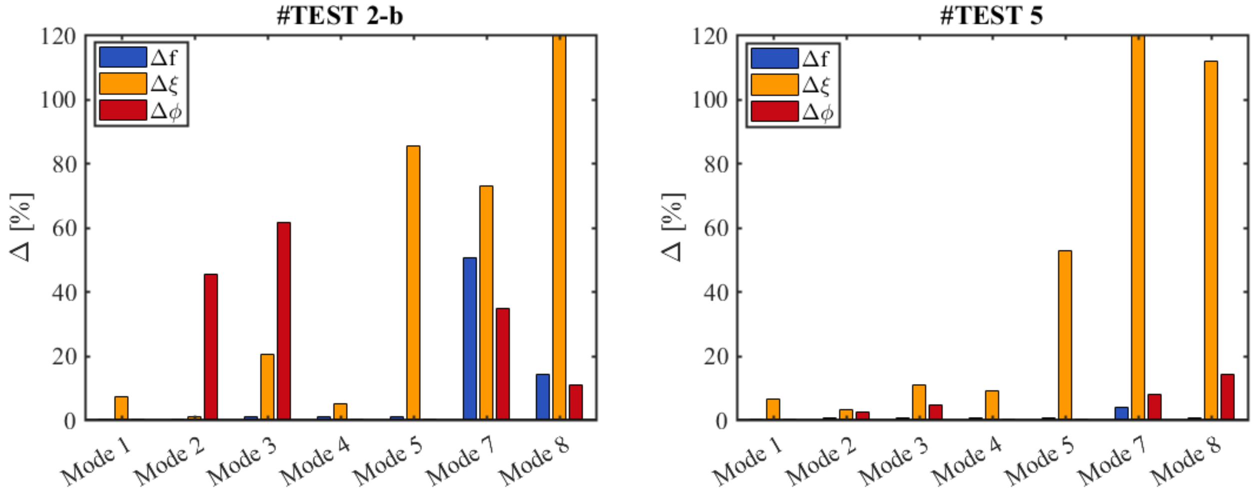

(a) (b)

Figure 3-XIV The tests performed without noise with the same signals length L=700 s with different sampling rates: (a) 50 Hz (b) 100 Hz.

Then the effect of the sampling rate on the modal identification has been investigated by adding a white noise in the signals. The levels of noise are selected from the maximum energy of all the signals during a test scaled by the coefficients in Table 3-X.

Table 3-X The four level of noise considered in the FE analysis; RMS_{max} represents the highest value of the RMS recorded by the accelerometers during the simulated ambient vibrations.

Level of noise introduced on the signals			
Noise Level #LV	*Length [s]*	*Energy*	*Input*
1	700	0,1 RMS_{max}	White noise input
2	700	0,5 RMS_{max}	White noise input
3	700	1 RMS_{max}	White noise input
4	700	3 RMS_{max}	White noise input

To avoid numerical effects due to different time steps the signals with a sampling frequency of 50 Hz are obtained decimating by a factor 2 the results obtained for a sample rate of 100 Hz. Theoretically the noise effect should be reduced increasing the SNR leading to more accurate results.

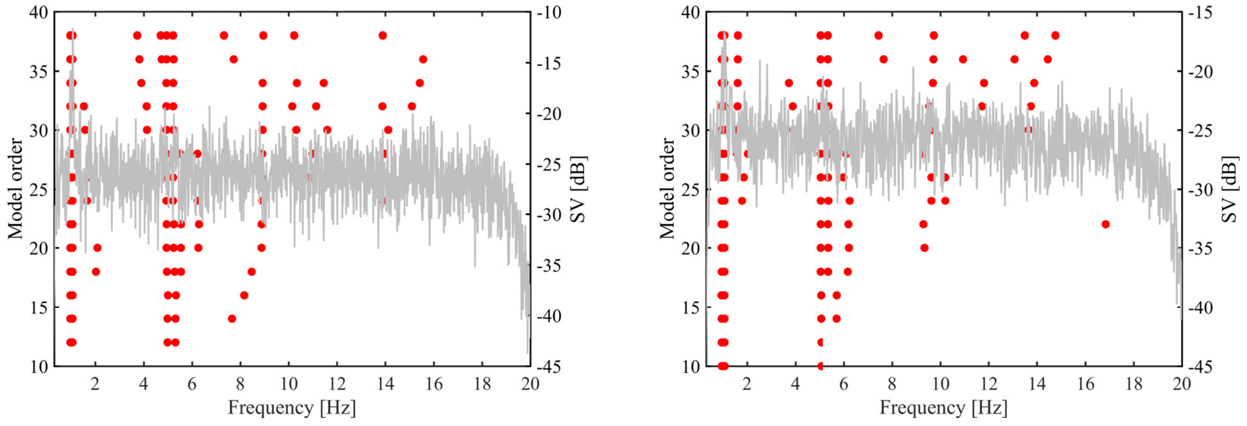

(a) (b)

Figure 3-XV The stabilization chart for the highest level of noise (#LV 4) with a sampling rate of 50 Hz (a) and 100 Hz (b).

Actually, the results of the stabilization chart in Figure 3-XV show similar results and the same number of modes can be identified. In one hand that result is influenced by the extreme value of noise applied. On the other hand, Figure 3-XVI show how the distances between the identified and the reference values is definitively low if the sampling rate is doubled. Mainly the MAC values are affected by the noise level and the average distances values are rising. In both cases it is observable a drop between LV2 and LV3 depending on the reduction in the number of modes identified that stabilize for a value equal to four. Not only the mode shapes exhibit that trend but also the frequency with a limited range of variation reaching about the 2,5 % (50 Hz) and the 1% (100 Hz) in the worst case. Despite that clear behaviour both in terms of frequency and mode shapes, the damping ratio seems to be more stable.

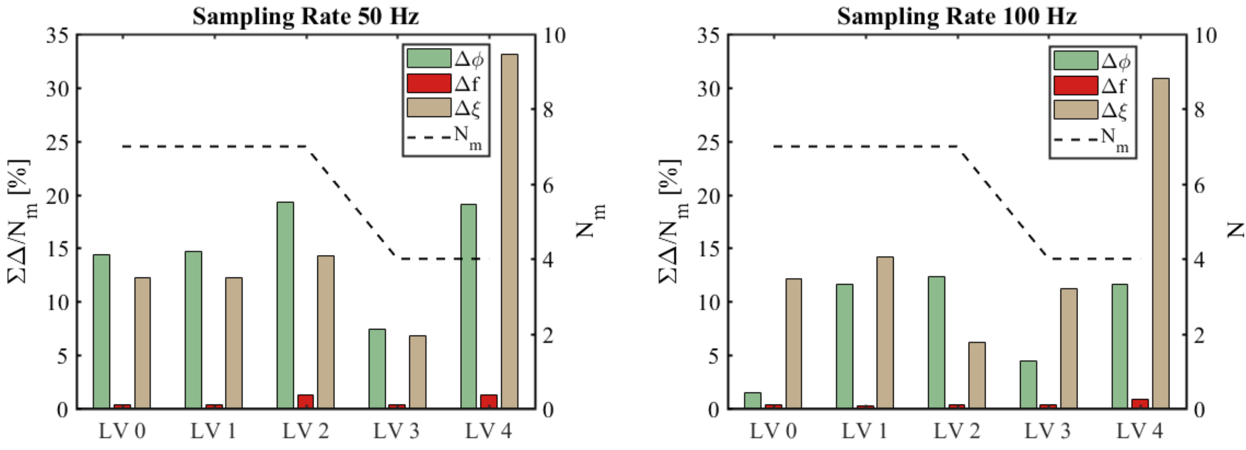

(a) (b)

Figure 3-XVI The relative distances values of the identified modal parameters from the reference values, averaged on the number of identified modes. (a) with a sampling rate of 50 Hz and (b) with a sampling rate of 100 Hz.

The effects of the signal lengths are tested from a 50 Hz sampled signal with a length of 1400 s (#TEST 1), its length is halved until 175 s (#TEST 4). The influence of the signal lengths is more relevant in the identified modal damping than in the frequencies.

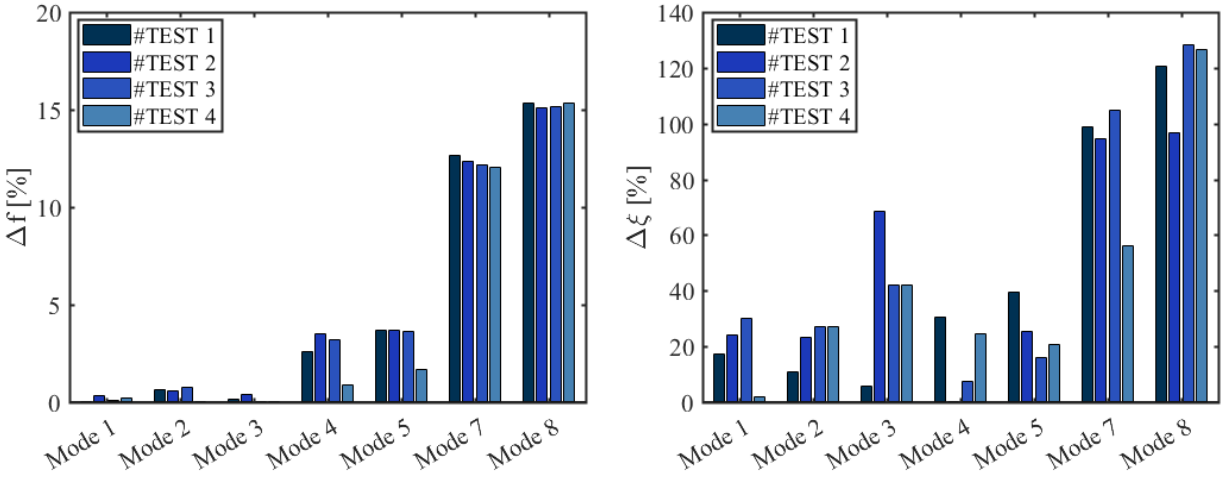

(a) (b)

Figure 3-XVII The results in terms of frequency (a) and damping ratio (b) for the tests considering a decreasing length (#TEST1-#TEST4) with a sampling rate of 50 Hz.

For example, in Figure 3-XVII is showed both the behaviour of the frequency and the damping ratio. The relative distance in terms of frequency is flattened out without any dependence on the signal time length for each mode. However, a growth in the distance values can be detected considering the higher modes. Especially from the first three modes the distance jumps from about the 0,5 % to the 3% and it is stabilized until the mode five. Then soars in the mode seven reaching a value of the 12 %.

While the frequency seems not strongly related to the signal lengths, the damping distances exhibits an increasing trend especially for the first two frequencies. Lastly it should be underlined that an increasing numerical error is introduced dependent on the time step integration that require a smaller interval to identify the higher frequency modes. Thus, the results of that experiments should be considered accurate for the first three modes. While a higher error is expected between the references and the identified values for the higher modes.

3.6 The proposed long-term monitoring algorithm

In section 3.3 it was introduced a robust AMPI allowing the labelling of the obtained candidate modes with a quality index. This allows to have more information about the performed MI in order to retain all the values that exhibit a higher level of accuracy.

In a Continuous Structural Health Monitoring approach (C-SHM) it is fundamental to retain the most significative modal parameters to assess the health status of the monitored structure. Indeed, all the phases required for the extraction of the damage sensitive features are calibrated on the operative condition to extract the highest number of information, avoiding misleading data. In that scenario the algorithm starts with the selection of the inputs (saving time for the MI from low intensity signals), identifies the modal properties and automatically track each mode.

The result is a dataset of modal parameters defined with dynamic threshold on all the phases of the process, aiming to minimize the uncertainties in the extraction of the identification of the modal parameters. Hence the definition of a preliminary observation period (calibration phase) of the structure in its operative conditions is mandatory for succeeding in a proper definition of the thresholds in a statistical way. Once that values are defined the algorithm is fully automated and it does not require the interaction with the user. Moreover, it is capable to perform the analysis even if the number of the signals is reduced for some malfunctioning of the acquiring devices or some missing acquisitions. In the next sections every phase will be fully described, explaining the selection of the threshold parameters.

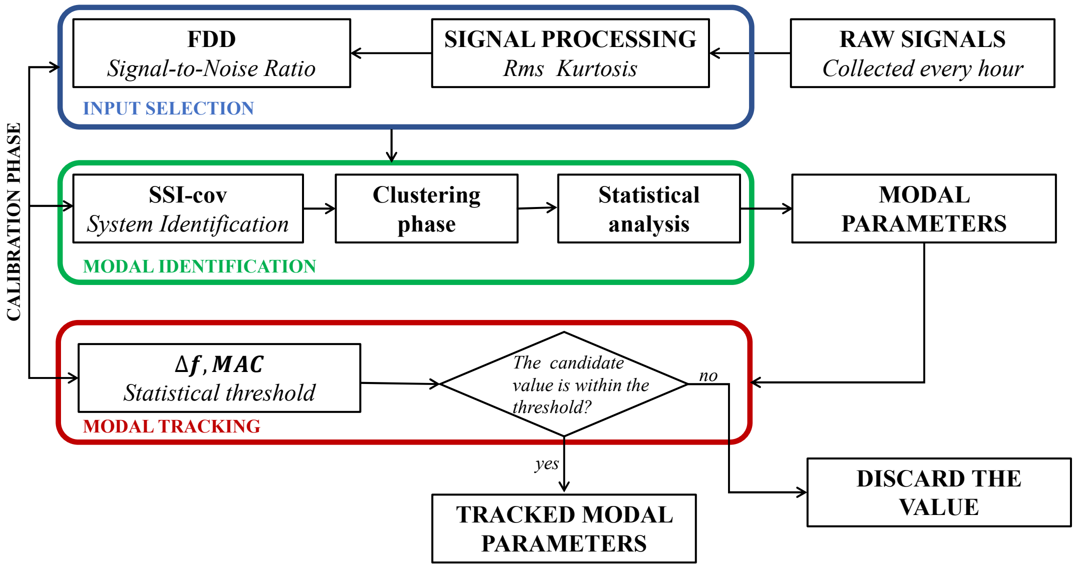

Figure 3-XVIII Block scheme of the proposed long-term monitoring algorithm.

3.6.1 Input selection

For having results good enough in the modal identification, the quality of the input should reach a minimum level of consistence. Considering a C-SHM system with a high rate of acquisition per day, it is possible to discard some values that do not reach the desired level without missing too much information about the structural dynamics of that day. In some case there are some source of random excitations that mainly act during a certain period of the day, leading to a better identification of the modes. This is the case of the vehicular traffic that stresses heavily the structure during the daily peak hours or some other anthropic activities that exhibit a certain frequency. In some other cases the input could be totally random, and it is not possible to make previsions in advance (wind, earthquakes, etc.).

The C-SHM with a proper selection of the inputs try to fill the gap about the basis hypothesis about the white noise behaviour of the inputs in the modal identification phase. Moreover, it can provide a wide information about the higher modes that can be activate only with higher energy power in the signals. It is clear that a blind processing of all the acquired data could be a waste of time and resources and consequently a smart reduction of the input data should be provided.

Moreover, the increasing of the acquisition rate brings also to an increase of the probability of some missing data from the sensor or, in the worst case of all the acquisition. Indeed, the algorithm should be able to consider that eventualities without stopping and furnishing some error flags that the user could read at the end of the process.

Table 3-XI Fixed threshold in the input selection phase.

Input Selection		
Parameter		*Description*
Minimum number of signals	$N_{sig,min}$	Defines a minimum number of signals to describe the structural dynamic
Minimum length of the signals	$L_{sig,min}$	Minimum length of the signals for a satisfactory modal identification
Minimum RMS	RMS_{min}	Minimum level of energy power in the signals
Kurtosis range	$Kurt_{min} - Kurt_{max}$	Allows to get more information about the pdf of the random signals
Minimum SNR	SNR_{min}	Minimum value of the Signal-to-Noise Ratio to identify the modal properties

The first two parameters allow to fix a lower bound to continue in the algorithm flow; the last three parameters aim to focus on the signal quality. The RMS is the second order statistical moment and it is commonly used in the definition of the signal intensity, higher values mean a signal with large deviation from the mean value. The Kurtosis is even more sensitive to abrupt changes in the signal because it is the fourth order statistical moment of the distribution. Higher value of the Kurtosis means large tails in the probability density function of the random signals. It can be proven that values of the Kurtosis equal to 3 means a Gaussian distribution and a value of 1,5 the probability density function corresponds to a harmonic signal. Another parameter that allows a better definition of the ratio between the true signal and the background noise is the SNR. Lower values of that parameter mean that the signal is buried over the ground noise and it cannot be useful for the modal identification. Instead higher values mean a strong signal that stand out from the background noise level allowing a clearer modal identification.

3.6.2 Modal identification

Since the initial parameters of the *SSI-cov* are chosen according to section 3.3.1, the operative conditions can change and some source of errors can arise, decreasing the modal identification accuracy. Indeed, the results of the Modal Identification are continuously monitored in terms of MQI, allowing the selection of the highest quality modes. On the basis of the structure dynamics, the weighting coefficients can be selected in a proper way, maximizing the results of each single mode validation criteria.

The selection can be interpreted based on the MQI values can be interpreted as a-posteriori validation criteria of the parameters chosen at the beginning through the sensitivity analysis. Moreover, it furnishes an indication about the results of the identification process allowing to exclude automatically the modes which exhibit a high variability or complexity.

3.6.3 Modal tracking

The Modal Tracking of the modal properties is a crucial step for the succeeding in the whole procedure. Despite that not so many Authors deepen the algorithm used for performing this task. Indeed, a clustering procedure was setup to initially aggregate the elements with similar properties based on a fixed threshold in terms of frequency and MAC. These initial thresholds should be carefully selected, but only some Authors [3,4] explicitly show the assumed threshold values for the MT.

Table 3-XII Thresholds adopted by the Authors for the MT

Author	df	MAC	*Structure*
Magalhães [3]	0,15	0,80	Pre-stressed concrete arch bridge
Cabboi [4][8]	0,15	0,80	Arch-iron bridge

Despite the lack of values for the CH buildings, it is possible to calculate the range of variation in terms of frequency of each tracked mode available in literature. In Table 3-XIII are reported the range of variation in terms of frequency in the most relevant works about the long-term monitoring of the CH.

Table 3-XIII Frequency range of variation of the tracked modes of the CH.

Author	Δf	*Monitoring period*	*Structure*
Ramos [18]	0,07-0,12	18 Months	Stone masonry tower
Gentile [19]	0,08-0,18	12 Months	Brick masonry tower
Ubertini [20]	0,04-0,12	10 Months	Hollow masonry tower

---

[8] As starting values of an adaptive procedure to define the suitable MAC thresholds.

Kita [21]	0,05-0,15	12 Months	Calcareous stone masonry palace
Azzara [22]	0,05-0,085	12 Months	Stone masonry tower

Instead the MAC is more stable exhibiting a low variability respect to the variations in the environmental conditions. Hence the distance in terms of frequency should be assumed large enough to consider the seasonal fluctuations of the environmental parameters. Usually a reference or baseline modal model is chosen by a previous dynamic campaign with a refined grid of sensors. The drawback of this approach stands beside the nature of the unknown stochastic input that is not controllable at all. Indeed, it may happen that during the preliminary identification campaign not all the modes are well excited and the baseline model results of a poor quality even if the number and the accuracy of the sensors is higher.

For that reason, in the proposed methodology the baseline model is selected through a suitable observation period that can be subjected to different levels of the stochastic input.

The approach consists in a clustering procedure with an initial threshold and each distance from the centroid of each cluster is saved for each element. That data can be used to calculate a statistic threshold based on the observations during the calibration period and to establish a baseline model which exhibits the higher values of the MQI for each mode.

3.7 Conclusions

In this chapter is introduced a new automated procedure for the modal identification that minimize the number of tuning parameters needed. The approach follows the path proposed by the researchers in the last decades, but it proposes three novelties (one for each phase):

- The definition of a setup procedure that minimize the bias arising by the model
- The definition of a threshold in the clustering phase based on the automated interpretation of the stabilization chart
- The definition of a unique parameter (MQI) that can be useful both in detecting the mathematical or spurious poles both for giving an information about the quality of the identified modes

The last point is crucial for selecting or discarding some modes that can be identified but with a high deviance from the real results. Thus, the results of the damage detection can be improved avoiding some misleading information. Then the procedure is tested on simulated responses under random vibrations generated by a simplified FE model of a tower built with the commercial software ANSYS. The effectiveness of the MQI for giving information about the quality of the identified modal parameters has been checked comparing the results obtained from the FE model and those estimated through the automated procedure. In addition, the effects of the signal length, the frequency ratio and SNR have been checked (*cfr. Section 3.5*). Lastly it has been shown how the method is able to automatically detect the presence of harmonic force both near the mode's frequency content both far away from the resonant frequencies.

Once the defined automated procedure has been defined and tested a more general algorithm has been developed to allow the extraction of the modal parameters from large dataset of measurements (*cfr. Section 3.6*). The algorithm selects the input and establish a MQI threshold of the identified modal parameters, monitoring the dynamic behaviour of the structure on one or more significant calibration periods. In the Author opinion the calibration periods should be selected to cover the variability of the main dynamic excitation that is observable in the common operational conditions. Lastly an adaptive threshold for the modal tracking threshold is proposed to enhance the identification of the modes even with low excitation.

3.8 References

[1] E. Reynders, R. Pintelon, G. De Roeck, Uncertainty bounds on modal parameters obtained from stochastic subspace identification, Mech. Syst. Signal Process. 22 (2008) 948–969.

[2] F. Ubertini, C. Gentile, A.L. Materazzi, Automated modal identification in operational conditions and its application to bridges, Eng. Struct. 46 (2013) 264–278.

[3] F. Magalhães, Á. Cunha, E. Caetano, Online automatic identification of the modal parameters of a long span arch bridge, Mech. Syst. Signal Process. 23 (2009) 316–329.

[4] A. Cabboi, F. Magalhães, C. Gentile, Á. Cunha, Automated modal identification and tracking: Application to an iron arch bridge, Struct. Control Heal. Monit. 24 (2017).

[5] C. Rainieri, G. Fabbrocino, Development and validation of an automated operational modal analysis algorithm for vibration-based monitoring and tensile load estimation, Mech. Syst. Signal Process. 60 (2015) 512–534.

[6] E. Reynders, J. Houbrechts, G. De Roeck, Fully automated (operational) modal analysis, Mech. Syst. Signal Process. 29 (2012) 228–250.

[7] E. Neu, F. Janser, A.A. Khatibi, A.C. Orifici, Fully Automated Operational Modal Analysis using multi-stage clustering, Mech. Syst. Signal Process. 84 (2017) 308–323.

[8] S. Qin, J. Kang, Q. Wang, Operational Modal Analysis Based on Subspace Algorithm with an Improved Stabilization Diagram Method, Shock Vib. (2016).

[9] J.M.W. Brownjohn, F. Magalhaes, E. Caetano, A. Cunha, Ambient vibration re-testing and operational modal analysis of the Humber Bridge, Eng. Struct. 32 (2010) 2003–2018.

[10] C. Rainieri, G. Fabbrocino, Influence of model order and number of block rows on accuracy and precision of modal parameter estimates in stochastic subspace identification, Int. J. Lifecycle Perform. Eng. 1 (2014) 317.

[11] B. Peeters, G. De Roeck, Reference-based stochastic subspace identification for output-only modal analysis, Mech. Syst. Signal Process. 13 (1999) 855–878.

[12] B. Peeters, System Identification and Damage Detection in Civil Engineering, KU Leuven, 2000.

[13] M. Döhler, F. Hille, L. Mevel, W. Rücker, Structural health monitoring with statistical methods during progressive damage test of S101 Bridge, Eng. Struct. 69 (2014) 183–193.

[14] R. Pintelon, P. Guillaume, J. Schoukens, Uncertainty calculation in (operational) modal analysis, Mech. Syst. Signal Process. 21 (2007) 2359–2373.

[15] R.S. Pappa, K.B. Elliott, A. Schenk, Consistent-mode indicator for the eigensystem realization algorithm,

J. Guid. Control. Dyn. 16 (1993) 852–858.

[16] R. Brincker, C.E. Ventura, Introduction to Operational Modal Analysis, 2015.

[17] A. Zucchini, P.B. Lourenço, A micro-mechanical model for the homogenisation of masonry, Int. J. Solids Struct. 39 (2002) 3233–3255.

[18] L.F. Lourenco, Paulo B and Ramos, Dynamic Identification and Monitoring of Cultural Heritage Buildings, (2011) 55–78.

[19] C. Gentile, M. Guidobaldi, A. Saisi, One-year dynamic monitoring of a historic tower: damage detection under changing environment, Meccanica. 51 (2016) 2873–2889.

[20] F. Ubertini, G. Comanducci, N. Cavalagli, A. Laura Pisello, A. Luigi Materazzi, F. Cotana, Environmental effects on natural frequencies of the San Pietro bell tower in Perugia, Italy, and their removal for structural performance assessment, Mech. Syst. Signal Process. 82 (2017) 307–322.

[21] A. Kita, N. Cavalagli, F. Ubertini, Temperature effects on static and dynamic behavior of Consoli Palace in Gubbio, Italy, Mech. Syst. Signal Process. 120 (2019) 180–202.

[22] R.M. Azzara, G. De Roeck, M. Girardi, C. Padovani, D. Pellegrini, E. Reynders, The influence of environmental parameters on the dynamic behaviour of the San Frediano bell tower in Lucca, Eng. Struct. 156 (2018) 175–187.

Chapter 4

Cases of Study

4.1 Introduction-4.2 Dynamic testing of historic masonry structures-4.3 Comparison with other techniques-4.4-Long-term monitoring application to the CH4.5-Discussion of the results-4.6 Conclusions-4.7 References

4.1 Introduction

This Chapter deals with the validation of the MEX algorithm through the application to real cases of study. First of all, the algorithm is tested on the data collected in single day dynamic test campaigns (*Section 4.2*) on Cultural Heritage buildings. Each case of study has presented some peculiarities that could be faced in the modal testing of CH. In addition, the results are validated with other techniques developed in the frequency domain (FDD, EFDD, ANPSD). Thus, the obtained results are compared with the available automated procedure for the modal identification focusing on some critical aspects (*Section 4.3*). Then the results obtained from a long-term monitoring system of a masonry tower (*Section 4.4*) have been analysed with the procedure presented in Section 4.6.

The results and the drawbacks in the application of the established procedure has been discussed (*Section 4.5*) deeply and some conclusions (*Section 4.6*) have been drawn from the first nine months of monitoring.

4.2 Dynamic testing of historic masonry structures

The MEX algorithm has been used for the modal testing in operative conditions of several heritage buildings and structures. The dynamic campaigns were developed during my Phd period (2016-2019) with the collaboration of the DICEA-UNIFI-Lab. The first two cases of study were analysed within the MOSCARDO Project aimed to provide a pilot test to establish a long-term monitoring system for the CH.

The obtained results are then compared with the established modal identification procedures available in literature, both in the frequency and in the time domain. The cases of study have been selected to represent different kind of CH, such as masonry towers and arch bridges, in different operational conditions. For example, have been analysed structures with very low levels of vibrations and others with higher values with some coloured noise disturbance. Hence that situations have furnished a wide range of factors that can influence the variance of the identified MP. Along with large range of external noises the problems related to the real scale measurement tests, such as the electrical noise in the measurement chain and some others noise that can arise during the dynamic test.

Therefore, such kind of tests is required to obtain some more details about the performance of the proposed AMPI after the preliminary validation that has been conducted by the numerical analysis in Section 4.5.

4.2.1 The Matilde Tower

The Matilde Tower in Livorno (Italy) has been the case study selected to test the efficiency of the designed Wireless Sensor Networks. The case study is a historic masonry tower built in Livorno harbour, which belongs to a complex architectonical site called “*Fortezza Vecchia*” (Old Fortress).

(a) (b)

Figure 4-I (a) The Matilde Tower and the (b) Old Fortress in the Livorno's harbour.

The Matilde Tower was built in the XIII century as a stand-alone structure that has been modified through the time. Nowadays it appears as a massive tower bounded by the fortress walls and by several small buildings. The structure is a circular tower with an external diameter of about 12 m and a total height of about 29 m (Figure 4-I). The walls width is of 2.5 m and a helicoidal stair is embedded in the walls to reach the different levels. The slabs are built by masonry vaults and concrete, giving a rigid-plane behaviour to the structure. The masonry vaults at the level 0 were retrofitted in the past with four tie rods to get a higher level of confinement.

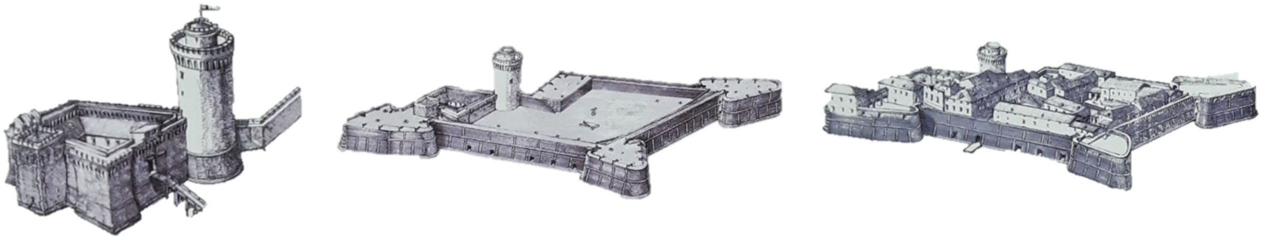

XIII century XVI century XX century

Figure 4-II The changes during the century of the entire architectonical complex.

The tower is surrounded by the walls of the fortress and other buildings reaching different heights. The South-West corner is bounded by the original block of the fortress called "*Quadratura dei Pisani*", and the East side is confined by the ruins of the Cosimo dei Medici palace (Figure 4-II).

The entire architectonical complex suffered several damages, probably due to foundations settlements and to erosion phenomena. The harsh environmental conditions of the seaside, the exposition to thermal effects and the strong wind cyclic loads are the causes of the crack propagation.

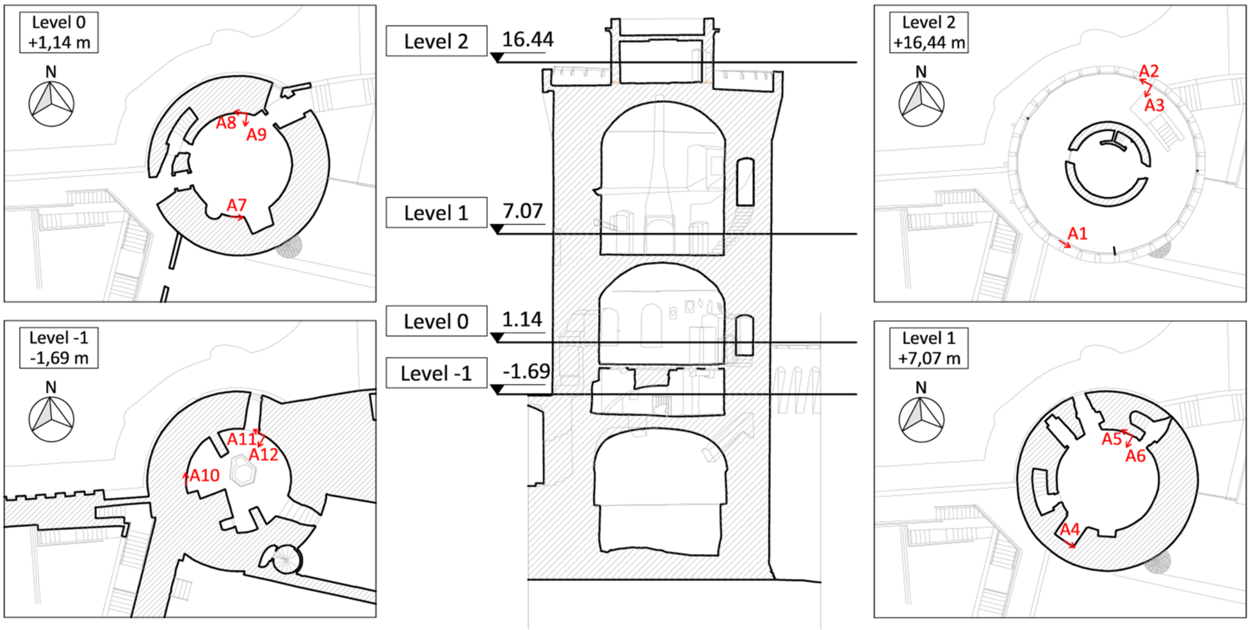

Figure 4-III The position of the accelerometers (red arrows) during the dynamic tests in the Matilde Tower.

The dynamic tests (MM 1) were performed the 23th January 2017 by the DICEA-UNIFI Lab, employing 12 piezoelectric accelerometers (Figure 4-III): eight PCB-393C (A1,A2,A3,A4,A5,A6,A7,A8) with a range of 2,5 g and a sensitivity of 1V/g and four PCB-393B31 (A9,A10,A11,A12) with a range of 0,5 g and a sensitivity of 10V/g. The sensors layout allows the identification of the rigid body movement at each section to fully characterize the mode shapes.

Table 4-I The acquisitions made during the dynamic testing campaign (#MM 1) and the supposed dynamic loads.

Dynamic tests (MM 1)					
Test number MM#	Length [s]	Sampling rate [Hz]	Loads	Day	Time
1	3380	400	Wind	23/01/2017	13:07
2	2460	400	Wind	23/01/2017	14:11
3	2430	400	Wind	23/01/2017	14:58
4	3285	400	Wind	23/01/2017	15:52

The presented case study can be considered an interesting application since it is subjected to a wide spectrum of dynamic excitations caused by the traffic, remarkable wind speeds, and the harmonic forced vibrations generated by the engines of the ferry boats docked in the harbour. That offers the possibility of checking the robustness of the algorithm in a real case of study where the basic hypothesis of white noise decays.

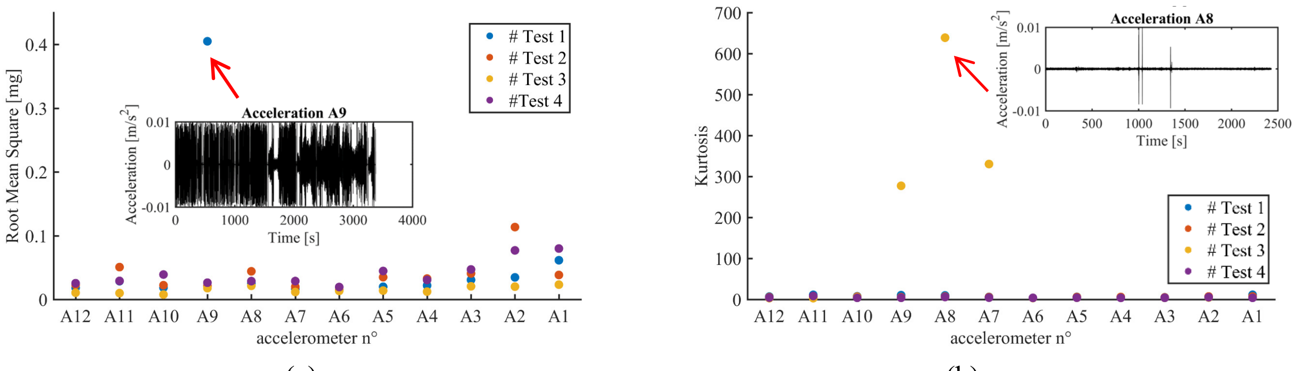

(a) (b)

Figure 4-IV (a) The RMS and (b) the Kurtosis for the tests performed during the first dynamic campaign (#MM 1). During the #TEST 3 the people were inside the tower.

In Figure 4-IV are shown the statistical properties of the recorded signals: in one hand the RMS represents the power of the signals, on the other hand the Kurtosis can detect large deviation from the hypothesized normal distribution. Outliers values can arise from some disturbances (electrical, magnetic, etc) and clear indicate an anomaly in the signals (cfr. Figure 4-IV-a/b). Join that results with some other unknown source of coloured noise gives an important test case on a real structure to test the effectiveness and the drawbacks of the MEX algorithm. The points discussed herein are the following:

- Analyse the effect of the outliers in the signals (spike, dropout, etc.)
- Analyse the effect of the coloured noises
- Analyse the effect of a higher sampling rating and of the signal lengths

The first and the second points will be tackled analysing the effects in the frequency domain both with the classical techniques (ANPSD, FDD, EFDD), both with a time frequency transform (SFT). Then the MEX algorithm is tested to verify, if it is possible to identify automatically the frequencies discarding the spurious modes. The last point is tackled with the results of another test (#MM 2) performed the 3rd of April 2019 with a sampling rate of 1200 Hz and 2400 Hz (cfr. Table 4-IV).

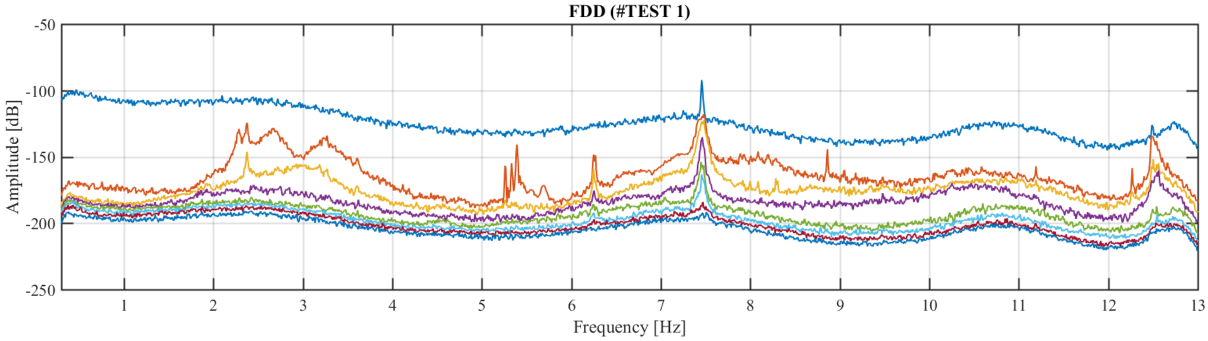

(a)

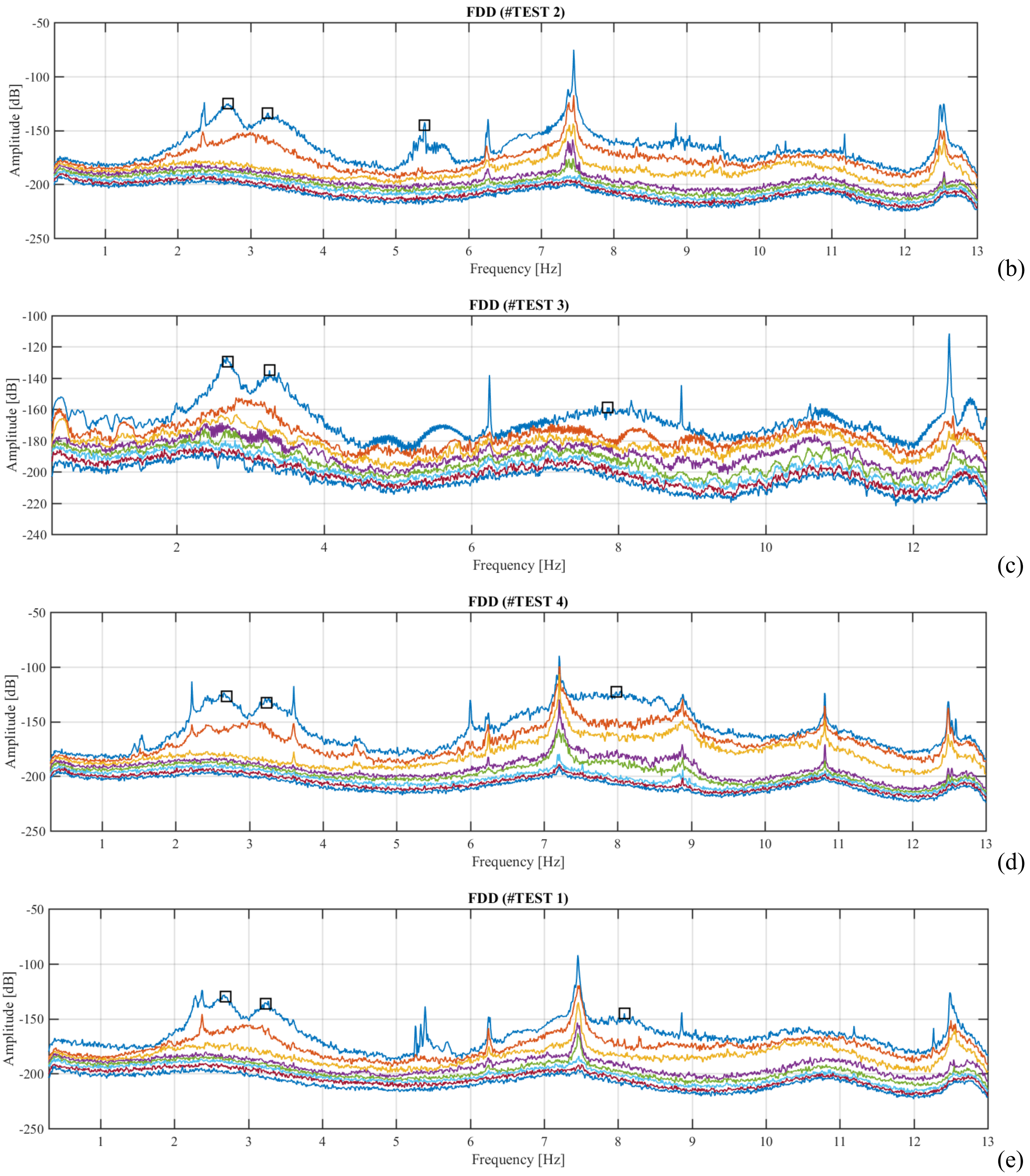

Figure 4-V Singular values plot obtained by the FDD technique for each tested performed in the testing campaign (#MM1), the squares represent the identified frequency that allows to estimate the auto spectral density through the EFDD. (a) #TEST 1 (b) #TEST 2 (c) #TEST 3 (d) #TEST 4 (e) #TEST 1 without the signal recorded by the device A9.

The analysis in the frequency domain shows several peaks that in many cases are not representing the structural modes. Some narrow band process, corresponding to a local increase of the PSD matrix rank can be detected in every dynamic test (Figure 4-V). In the #TEST 1 (Figure 4-V-a), the noise level stand above the other singular values compromising the dynamic identification. Excluding the signal recorded by the accelerometer A9 (Figure 4-V-e) the noise level is below the values containing the structural dynamics.

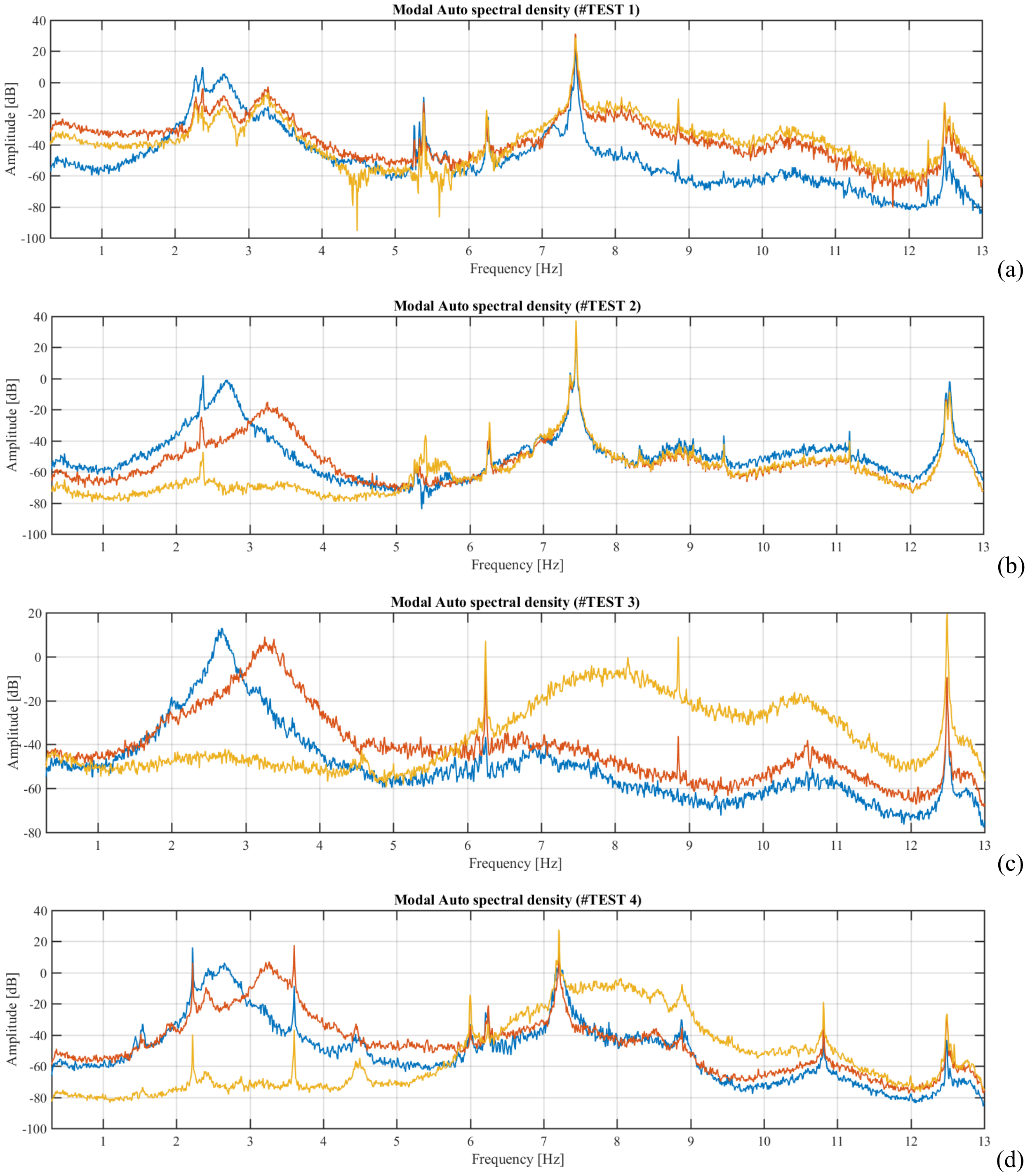

Figure 4-VI The approximated auto spectral density calculated through the EFDD. (a) #TEST 1 without the signal A9 (b) #TEST 2 (c) #TEST 3 (d) #TEST 4.

Projecting the PSD in the basis of the estimated mode shapes through the selection of the peaks in the first singular values (black squares in Figure 4-V (b)(c)(d)(e)), the auto spectral density of each mode (Figure 4-VI). All the plotted auto spectral densities clearly exhibit two peaks corresponding to the first two modes in the frequency band [2-4 Hz]. The third mode can be identified in the frequency band [7,5-8,5 Hz] (Figure 4-VI (c) (d)). Other narrow band peaks can be identified around 2-3,5-5,3-6-7,5-8,8-12,5 Hz.

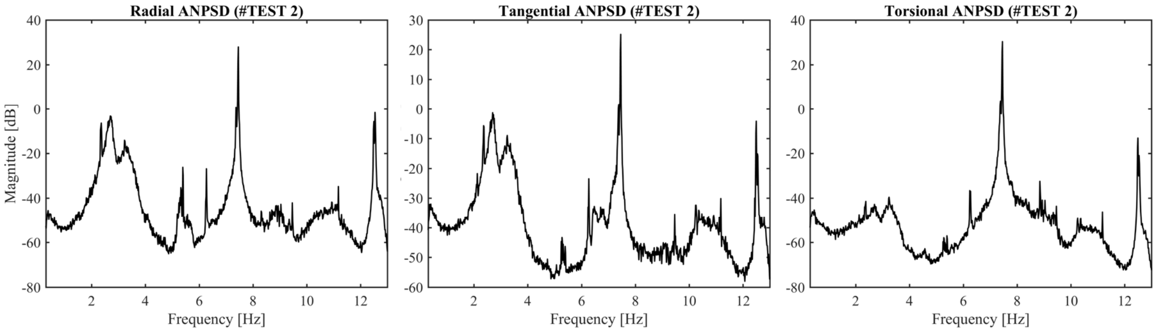

Figure 4-VII Average Normalized Spectral Density (ANSPD) for the three directions that characterize the rigid body motion of each section for the TEST 2.

The peak at 7,5 Hz that can be identified in the #TEST 1 and #TEST 2 seems the forced response to some harmonic force and it can be identified in every direction (Figure 4-VII). The shape of this peak is larger than the narrow band process that can be found in the ANPSD for each direction. This can be explained with the Short Fourier Transform (SFT) that is a time frequency transform that allows to analyse the frequency content in the signal over the time. In Figure 4-VIII the SFT is shown for the #TEST 2 and a lot of energy is condensed on a narrow band process with a linear increasing of the frequency from 5 Hz to 7,5 Hz. At 1600 s the first frequency at 5 Hz appears then the frequency increases linearly until 7,5 Hz until the end of the signals. That behaviour is typical of the rotating machinery that are pushed to the regime frequency from the initial value.

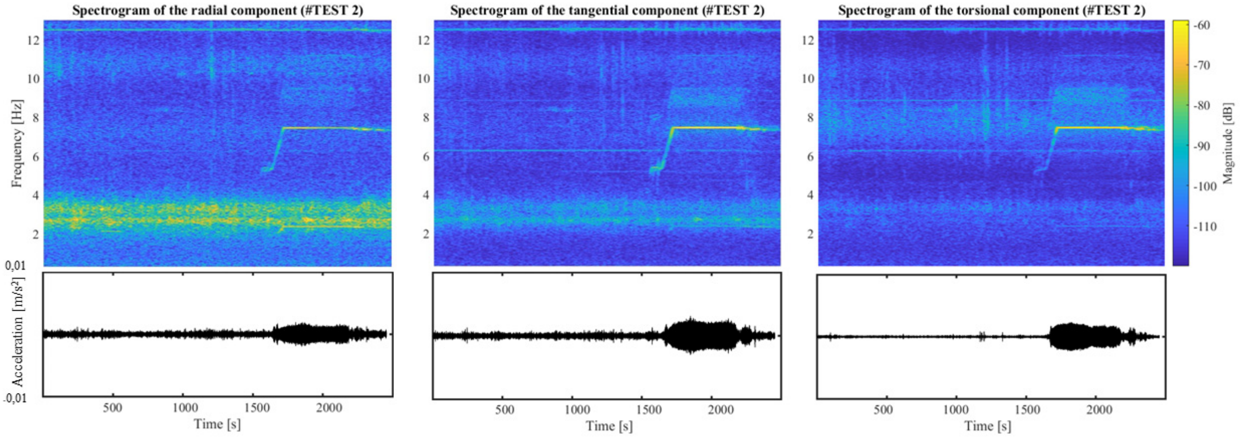

Figure 4-VIII The Short Fourier Transform (SFT) of the mean values of each direction and the corresponding signals recorded at the last level of the tower.

That dynamic test is a suitable case of study for testing the MEX algorithm in particular dynamic conditions tackling these problems and finding a solution for the automated procedure.

Table 4-II The selected parameters for the modal identification of the Matilde Tower.

Parameters selection in the Setup phase					
	Parameter		*Range of variation*	*Selected value*	*Phase*
SU1	Over-modelling coefficient to adjust the number of modes identifiable in the signals	k_1	[1-1,3]	1,15	Setup Phase
SU2	Over-modelling coefficient for the maximum model order	k_2	[5-15]	8	Setup Phase
SU3	Over-modelling coefficient for the maximum number of block rows	k_3	-	10	Setup Phase
SU4	Number of cycles of the lowest frequency	n_c	[1-11]	[1,12-11,21]	Setup Phase
SU5	Variation in the modal order	Δord	-	10	Setup Phase
SU6	Variation in the number of block rows	Δi	-	10	Setup Phase

Through a preliminary inspection of the condition number surface (Figure 4-IX (a)) it is possible to select a first approximation of the optimal number of block rows. Then a proper modal order can be selected, investigating the normalized singular values (Figure 4-IX (b)) plot and the entropy plot (Figure 4-IX (c)).

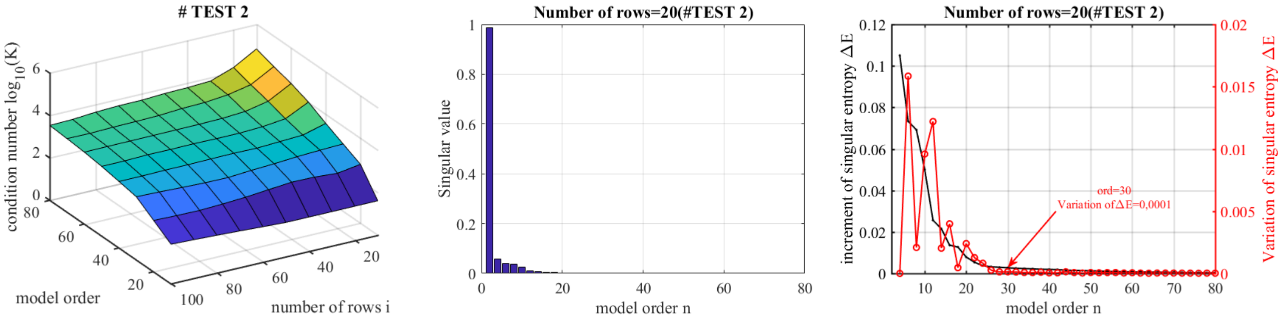

(a) (b) (c)

Figure 4-IX (a)The condition number surface (b) The normalized singular values plot (c) The entropy variation of the #TEST 2.

The selected values are validated analysing the COV of the identified modal properties (Figure 4-X). Hence the selection of the proper number of block rows can be confirmed analysing both the variance of the identified modal parameters both the number of candidate modes and the average value of the MQI.

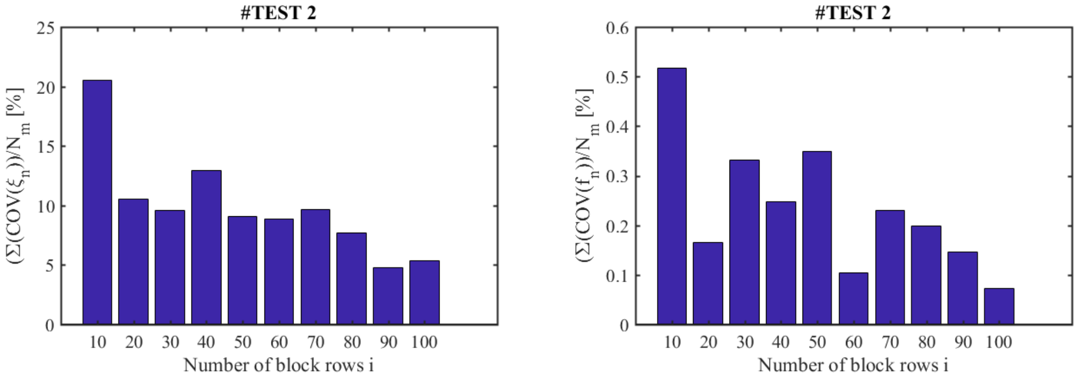

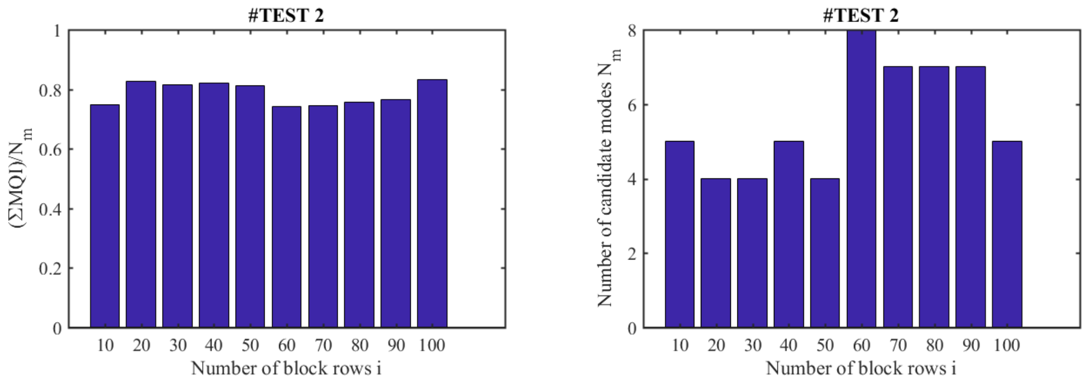

Figure 4-X The variance of the estimated parameters through the variation of the block number of rows selected in the model.

The number of block rows is chosen equal to 20 as a good compromise of all the considered parameters, allowing a lower computational effort too. The maximum model order is selected equal to 30 assuring small perturbation in the first order evaluation of the entropy (Figure 4-IX (c)).

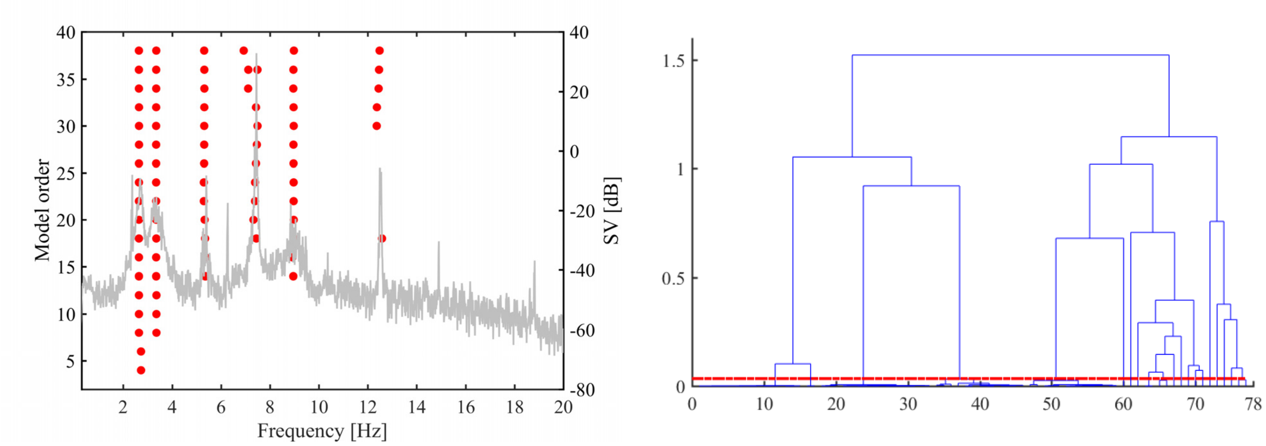

(a) (b)

Figure 4-XI The stabilization chart (a) plot and the dendrogram (b) for the #TEST 2.

At a first glance, the alignments in the stabilization chart plot (Figure 4-XI (a)) can lead to the identification of six modes. But from the time-frequency domain analysis is known that there are two frequencies at 5 and 7,5 Hz that are forced responses to a rotating machinery operating with an initial and a regime frequency (Figure 4-VIII). Moreover both the frequencies at 8,7 and 12,5 Hz seems to be the results of some narrow band process (Figure 4-VII,Figure 4-VIII).

The MEX algorithm identified four modes: the first two at 2,6 and 3,3 Hz and the last two at 5,3 and 8,7 Hz (Figure 4-XII). The group of stable poles at a frequency of 7,3 Hz and 12,5 Hz are excluded from the analysis because their population is not large enough from the imposed threshold (0,33 $N_{cl,max}$). The validation phase give some other information and the MQI (Figure 4-XIII) shows how the first two modes are effectively physical (MQI>0,9) and the other two can be associated with some spurious modes (MQI<0,7).

This test proves how the algorithm van be able to discriminate the automated identified modes in the validation phase. The high number of selected validation tests arising from different approaches, shall give a powerful tool to classify the identified modes.

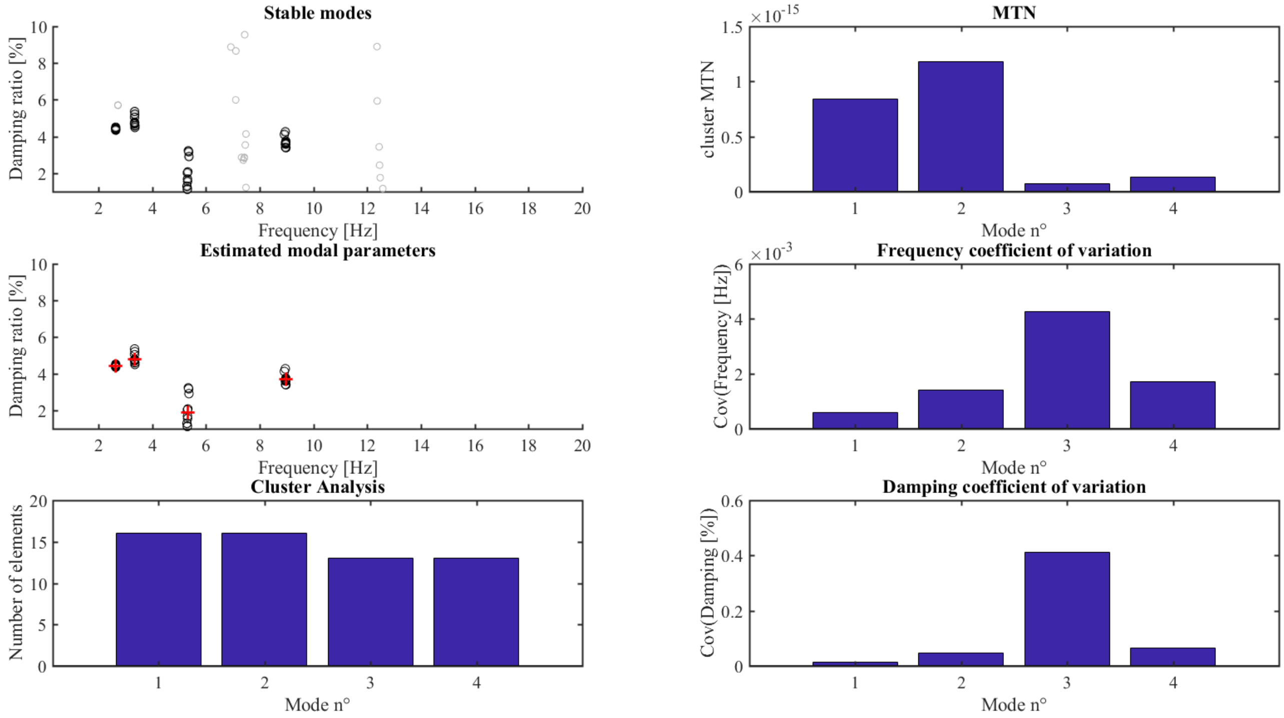

Figure 4-XII Results from the MEX algorithm in the clustering phase for the #TEST 2.

Hence it is needed to define a suitable threshold for the automated discrimination of the identified modes through an observation period. That is one of the points that will be analysed in the next sections when the procedure for the automated tracking of the modal properties will be introduced.

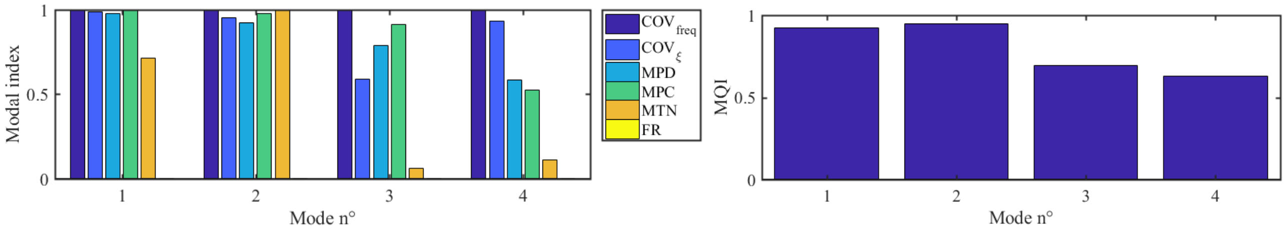

Figure 4-XIII Results from the MEX algorithm in the validation phase for the #TEST 2.

Table 4-III The results of the identified modal parameters of the #TEST 2 during the first dynamic campaign (MM 1)

Estimated Modal Parameters (#TEST 2)						
Mode n°	$\mu(f_n)\ [Hz]$	$\mu(\xi_n)$ [%]	$cov(f_n)$ [%]	$cov(\xi_n)$ [%]	N_{cl}	MQI
1	2,643	4,402	0,0573	1,347	16	0,924
2	3,349	4,797	0,1416	4,732	16	0,948
3	5,321	1,868	0,4270	41,272	13	0,692
4	8,962	3,696	0,1702	6,579	13	0,629

The identified mode shapes that exhibit a consistence in terms of MQI are represented in Figure 4-XIV. In that conditions it is possible only to clearly identify the first two modes (Table 4-III), corresponding to the first bending moment along the two main axes (N-S and E-W).

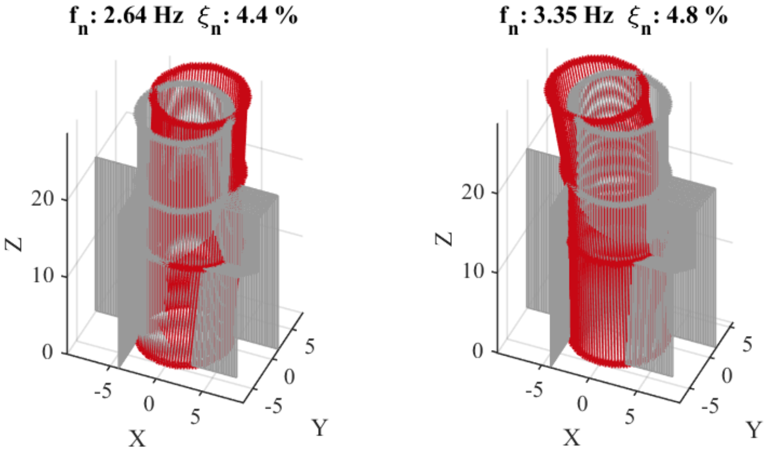

First Bending N-S First Bending E-W

Figure 4-XIV The first two modes identified in the #TEST 2 of the first identification campaign (MM 1)

The effect of a higher sampling rate in the extraction of the modal parameters will be tackled through the analysis of another dynamic campaign (Table 4-IV).

Table 4-IV The dynamic test campaign performed the 3rd of April 2019 (MM 2)

Dynamic tests (MM 2)					
Test number MM 2#	*Length [s]*	*Sampling rate [Hz]*	*Loads*	*Day*	*Time*
1	1482	1200	wind	03/04/19	11:42
2	2634	1200	wind	03/04/19	12:49
3	2207	1200	wind	03/04/19	13:31
4	696	1200	wind	03/04/19	13:59
5	1730	1200	wind	03/04/19	15:26
6	2387	1200	wind	03/04/19	14:40
7	1203	1200	wind	03/04/19	15:35
8	1218	1200	wind	03/04/19	15:45
9	146	1200	wind	03/04/19	16:27
10	1681	1200	wind	03/04/19	16:33
11	514	1200	wind	03/04/19	17:06
12	1061	2400	wind	03/04/19	17:13
13	782	2400	wind	03/04/19	17:33

The environmental conditions of the second test were slightly different, even if the average wind speed is similar 7 m/s (MM 1) and 9 m/s (MM 2), but the harmonic forces cannot be detected in the second dynamic campaign (MM 2). The analysed session is the #TEST 11 that is sampled at 2400 Hz, then down sampled and filtered in the frequency band [0,3-20 Hz].

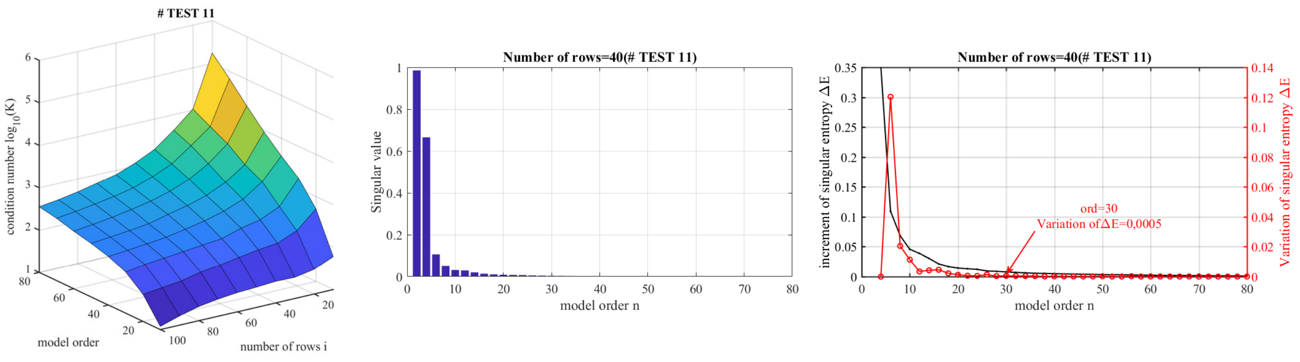

(a) (b) (c)

Figure 4-XV (a) The condition number surface of the projection matrix (b) The normalized singular values plot (c) The variation of the singular entropy in the #TEST 11 of the second dynamic campaign (MM 2).

The setup phase gives the preliminary information for the selection of the modal order and the block rows in the Henkel matrix (Figure 4-XV (a)). The normalized singular values decrease very fast (Figure 4-XV (b)) and just for a value equal to 20 reaches at least the zero value. That means the presence of a few predominant modes with low levels of noise in the analysed signals. This is confirmed by the entropy plot (Figure 4-XV (c)) where the first order perturbation reaches small values since the model order is equal to 20.

The modal order is set equal to 30, implying a little bit of over-modelling to include also the low excited modes. The mathematical modes that can arise are then discarded through the validation phase.

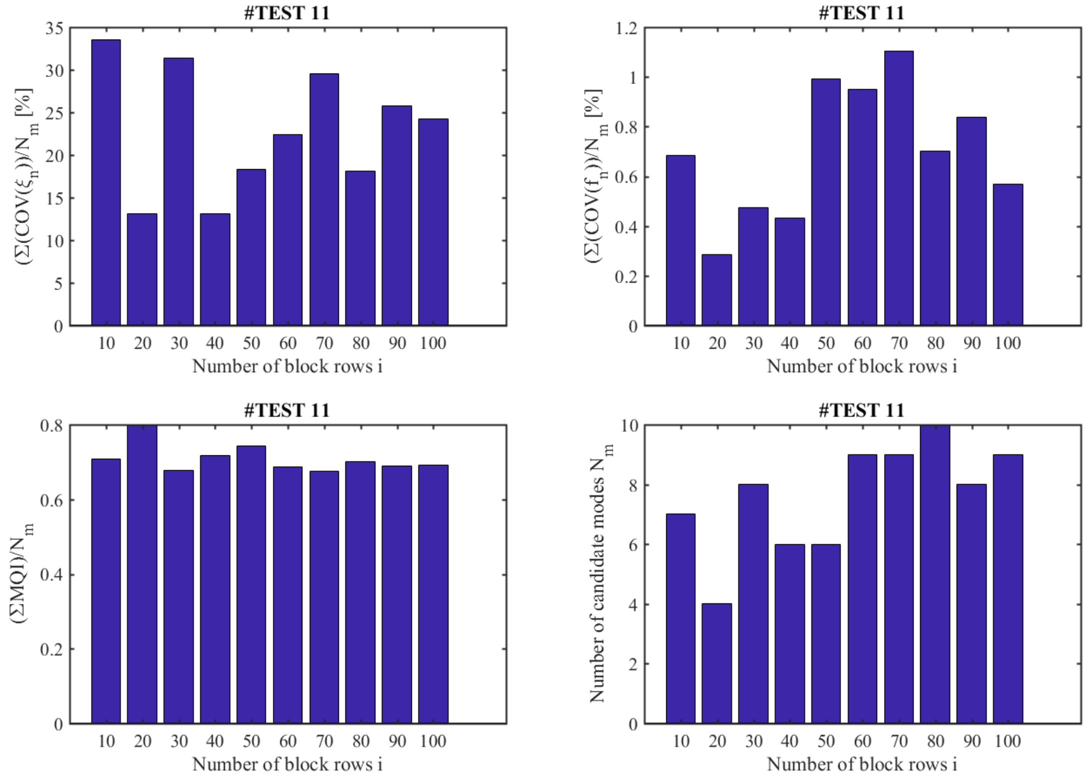

Figure 4-XVI The averaged variance of the modal parameters through the changes of the block Henkel matrix blocks.

Hence the results of the setup phase are checked by the variance of the identified modal parameters with different values of block rows in the Henkel matrix once the modal order is selected. In Figure 4-XVI are showed the results confirming that a value equal to 40 minimize the variance of the identified modal parameters.

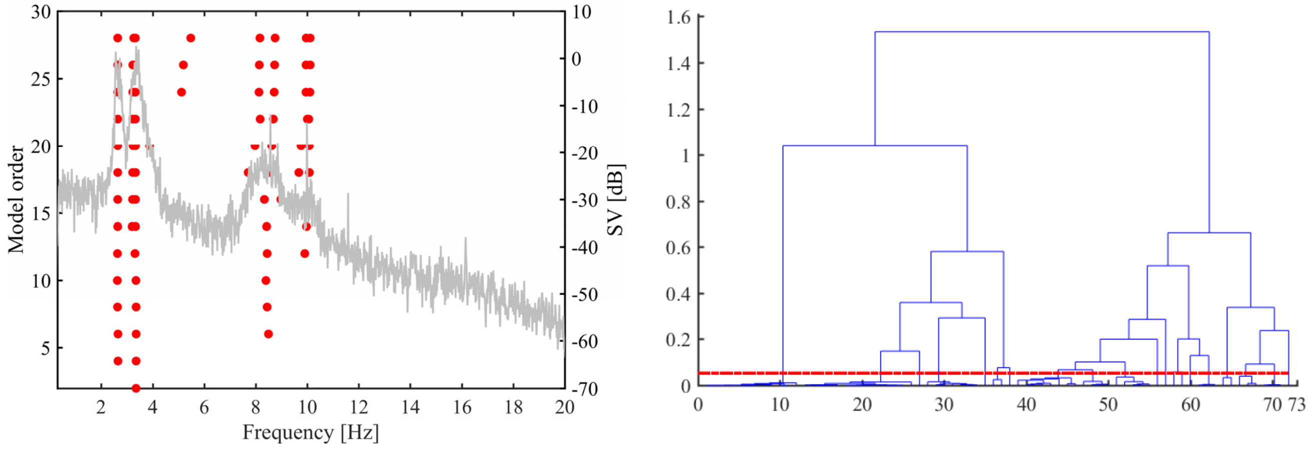

(a) (b)

Figure 4-XVII (a) Stabilization chart and (b) dendrogram of the hierarchical clustering phase for the #TEST 11 of the second dynamic campaign (MM 2)

From a visual inspection of the stabilization chart (Figure 4-XVII (a)) are clearly visible four alignments in the frequency band from 0,3-12 Hz. From the model order equal to 15 the second and third modes seems to split in two modes exhibiting the so called "modal splitting" phenomenon [1]. Consisting in the splitting of a column in two from a certain modal order representing the mode as the combination of two distinct modes that can be real or noisy.

Aiming to establish a completely fully automated procedure that shall work in different operative conditions, the selection of the modes in the validation phase allows to keep some more information before discarding a candidate mode.

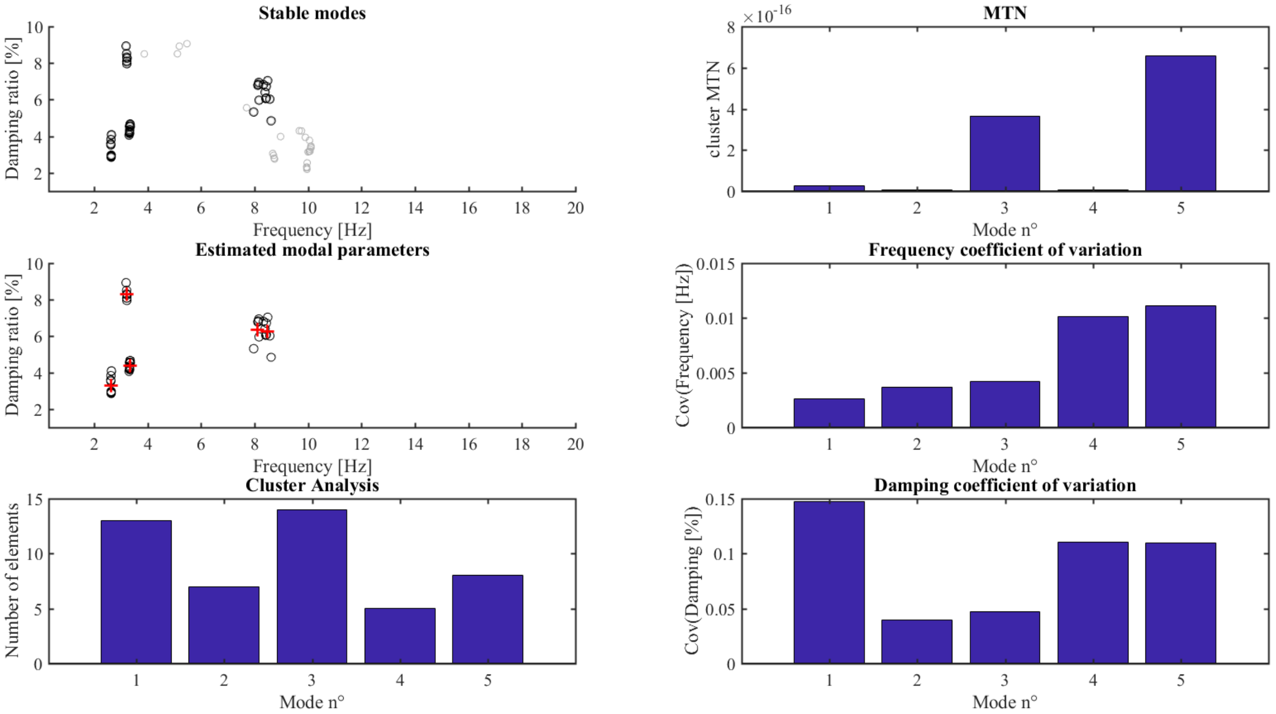

Figure 4-XVIII Results of the clustering phase in the MEX algorithm for the #TEST 11 in the second dynamic testing campaign (MM2).

The first two modes exhibit the highest number of elements per cluster (Figure 4-XVIII), reaching the maximum (N_{cl}=14) in the second mode. The others identified modes can be spurious or low excited, some further information are added in the validation phase (Figure 4-XIX). The results to the selected single mode validation criteria and consequently to the MQI shows that three modes can be retained (1,3,5 in Figure 4-XIX) exhibiting values higher than 0,80 (Table 4-V). Some doubts still remain on the mode number 4 that exhibit a value equal to 0,78 and it should be kept in the future analysis to recognize if it appears or not.

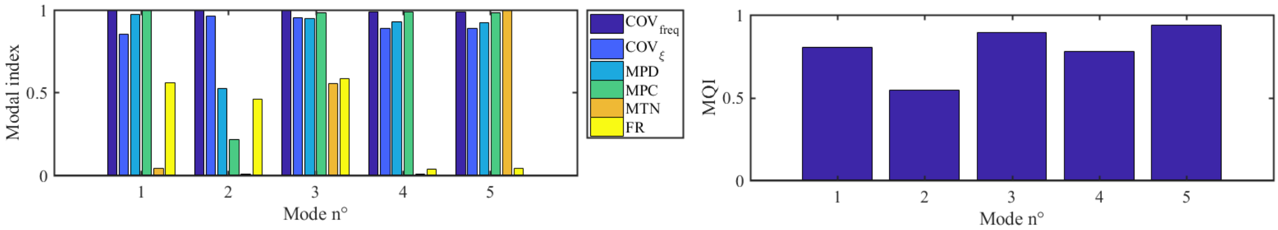

Figure 4-XIX Results of the validation phase in the MEX algorithm for the #TEST 11 in the second dynamic testing campaign (MM2).

Table 4-V The results of the identified modal parameters of the #TEST 11 during the first dynamic campaign (MM 2)

Estimated Modal Parameters (#TEST 11)						
Mode n°	$\mu(f_n)$ [Hz]	$\mu(\xi_n)$ [%]	$cov(f_n)$ [%]	$cov(\xi_n)$ [%]	N_{cl}	*MQI*
1	2,638	3,265	0,2574	14,753	13	0,803
2	3,220	8,313	0,3671	3,929	7	0,546
3	3,335	4,369	0,4168	4,723	14	0,894
4	8,112	6,374	1,0113	11,012	5	0,779
5	8,465	6,251	1,1147	10,958	8	0,938

The plot of the identified mode shapes (Figure 4-XX) gives an idea of the directions, because of the limited number of sensors used in the second dynamic campaign (MM 2). However, the first two modes are coherent with those identified during the first dynamic campaign (Figure 4-XIV).

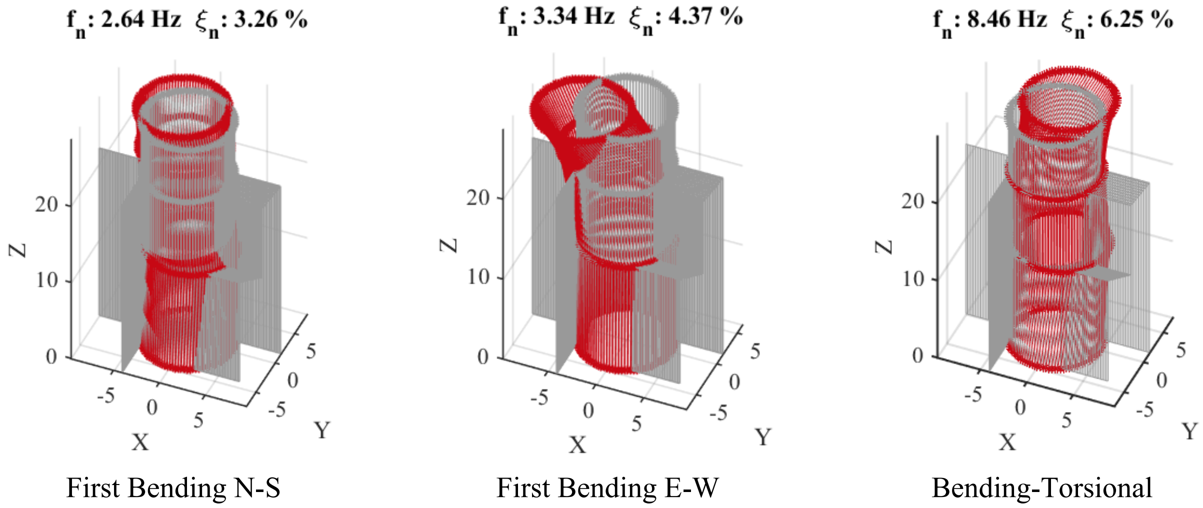

First Bending N-S First Bending E-W Bending-Torsional

Figure 4-XX The identified mode shapes in the #TEST 11 during the second dynamic tests campaign (MM 2).

4.2.2 Torre Grossa

The Torre Grossa is the tallest of the survived towers in the city centre of San Gimignano (Italy). The tower was built in the thirteenth century with a square cross section of about 9.5×9.5 m with an overall height of about 55 m. The sustaining walls, with variable thickness from 2.6 m at the base until 1.6 m at the top, are built with the multilayer technique: two external layers (travertine stones and brick masonry) and a cohesive internal filling.


(a) (b) (c)

Figure 4-XXI (a) Water painting (c) Picture of the Torre Grossa and the Town hall on the left. (b) picture shot from the S-E direction.

Up to 20 meters the tower is confined in the East direction by the “Palazzo Comunale” (Town Hall), and on the West direction by a masonry building until the height of 10 meters. The slabs of the first two levels are built by masonry vaults, while in the last level there is a concrete slab. Internally, the levels of the tower are connected by a steel stair that arrive until the top level where is located a big bell. The tower was repaired in the past with two steel chains in the SW corner that was collapsed during a thunderstorm.

Figure 4-XXII A view of the San Gimignano’s old town with the medieval towers that have been added from the 1990 in the UNESCO list of the World Cultural Heritage.

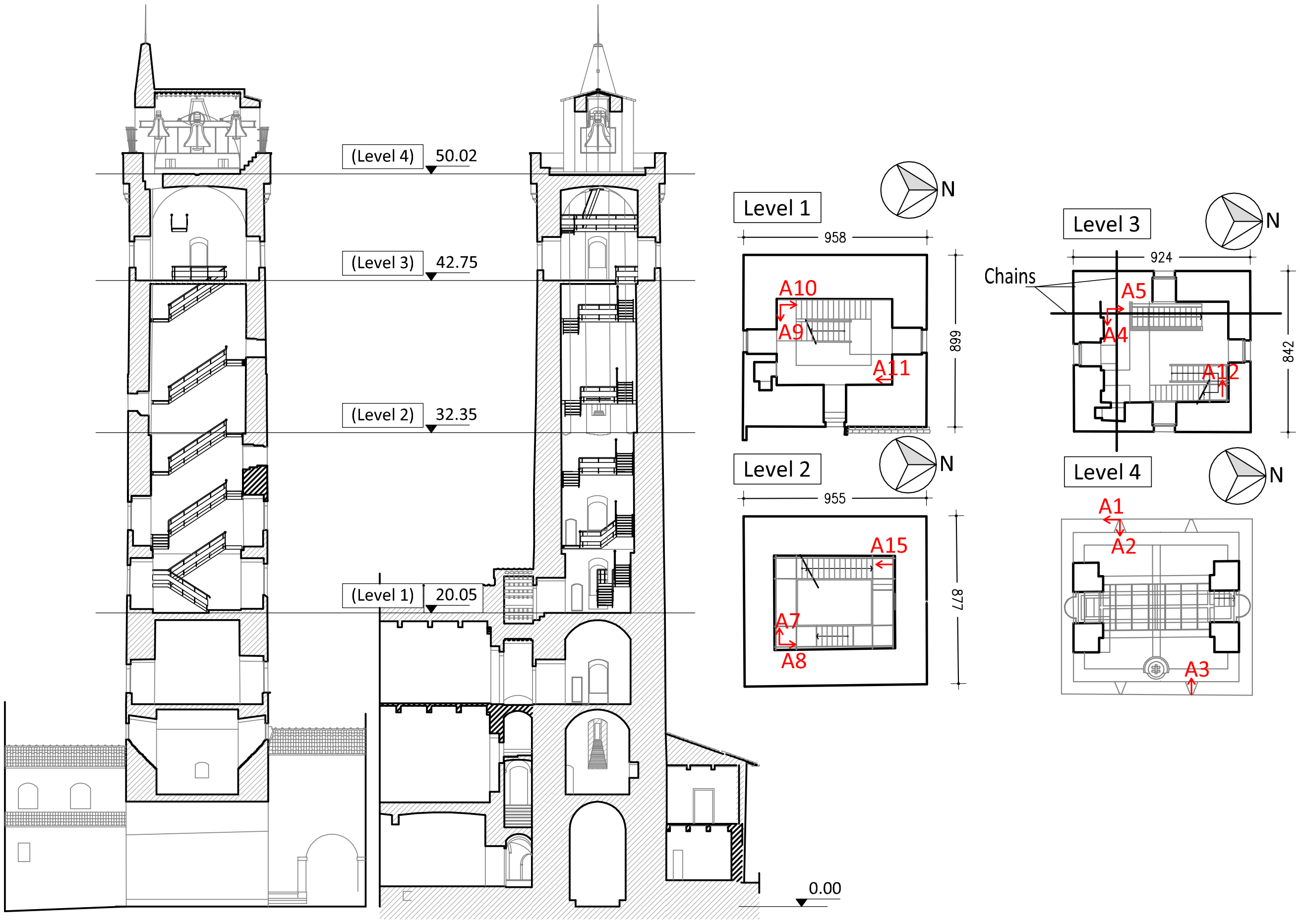

Figure 4-XXIII The experimental layout during the tests: (a)N-S cross section (b)E-W cross section (c) The planimetric distribution of the accelerometers, represented by the red arrows.

The experimental tests were developed between the 29th-30th of March 2017 by the DICEA-UNIFI Lab, employing 12 piezoelectric accelerometers: eight PCB-393C (A1,A2,A3,A4,A5,A7,A8,A15) with a range of 2,5 g and a sensitivity of 1V/g and four PCB-393B31 (A9,A10,A11,A12) with a range of 0,5 g and a sensitivity of 10V/g. The sampling frequency was of 400 Hz and the length of all the time series was about 2400 s. All the signals are filtered with a bandpass filter between 0.3-10 Hz, and the signal is resampled at 25 Hz to have a good frequency resolution and a limited quantity of data points. The position of the accelerometers is shown in Figure 4-XXIII (c). Each level has three accelerometers for identifying the torsional mode shape. The N-S direction is the X axis and the E-W direction (directed to the Town Hall) is the Y axis.

Table 4-VI The acquisitions made during the dynamic testing campaign (#DC 1) and the supposed dynamic loads.

Dynamic tests (#DC 1)					
Test number #TG	*Length [s]*	*Sampling rate [Hz]*	*Loads*	*Day*	*Time*
1	2400	400	wind+microtremors	02/04/19	18:02
2	2400	400	wind+microtremors	29/03/17	19:06
3	2400	400	wind+microtremors	29/03/17	20:10
4	2400	400	wind+microtremors	29/03/17	21:13
5	2400	400	wind+microtremors	29/03/17	22:17
6	2400	400	wind+microtremors	29/03/17	23:20

7	2400	400	wind+microtremors	30/03/17	0:24
8	2400	400	wind+microtremors	30/03/17	1:28
9	2400	400	wind+microtremors	30/03/17	2:31
10	2400	400	wind+microtremors	30/03/17	3:35
11	2400	400	wind+microtremors	30/03/17	4:38
12	2400	400	wind+microtremors	30/03/17	5:42
13	2400	400	wind+microtremors	30/03/17	6:46
14	2400	400	wind+microtremors	30/03/17	7:49

The dynamic tests campaign was developed acquiring 40 minutes every hour with a sampling frequency equal to 400 Hz from the 6:00 PM until the 8:00 AM, when the Tower is closed to the tourists. The wind was very low 1,2-1,3 m/s of average speed and the maximum values which reach 6,3-7,5 m/s (meteorological station of Scorgiano (SI), from *http://www.sir.toscana.it/*). Considering that the city centre of San Gimignano, where the tower is located, is restricted to the ordinary vehicular traffic, the main dynamic excitation should be some unknown random vibrations.

This is confirmed by a preliminary analysis of the signals in terms of rms and Kurtosis allowing the selection of the inputs with the higher signal content avoiding spikes and dropouts. In Figure 4-XXIV it is shown how both the outliers in the kurtosis and in rms can identify the anomalies in the signals. With that low energy signals, the modal identification become challenging and almost a low level of noise can compromise the results of the modal identification. This make the case study interesting for understanding the incidence of the low signal intensities and the capability of the MEX algorithm to identify the modes.

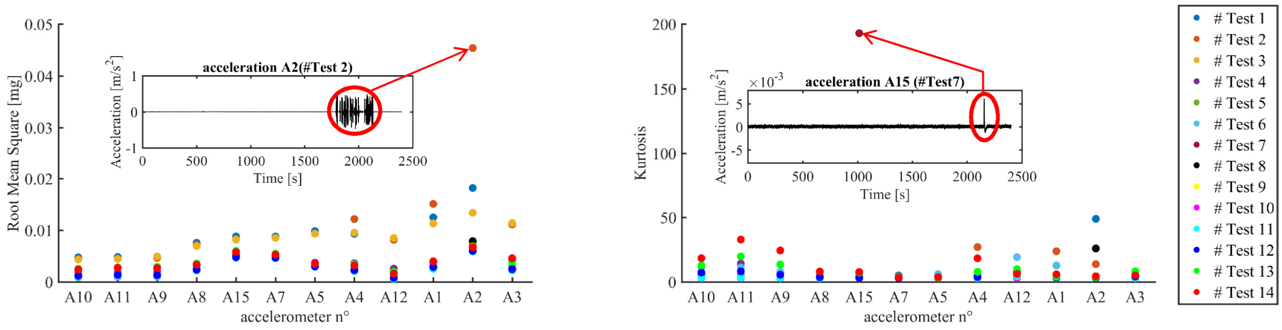

(a) (b)

Figure 4-XXIV (a) The RMS and (b) the Kurtosis of each filtered and resampled signal recorded by the accelerometers in every session. Abrupt changes in RMS or Kurtosis means some malfunctioning of the system as shown into the bounding box.

The aims of this tests are:

- Testing the effectiveness of the MEX algorithm for a real case of study
- Analyse the influence of the energy in the signals and of the random signal pdf
- Analyse the effect of the outliers in the signals (spike, dropout, etc.)
- Analyse the effect of a higher sampling rating and of the signal lengths

The first point is tackled comparing the results of all the sessions with the FDD technique and the automated SSI procedures proposed by the Authors in the last years. The focus will be on the setting parameters needed both in the setup phase and in the validation phase. Regarding the setup phase it will be also studied the influence of that in the modal identification.

The second and the third points are faced discussing the results obtained in the tests focusing on those which exhibiting higher level of rms and kurtosis. Indeed, the signals recorded during the #TEST 3 and #TEST 11 are analysed which are the boundaries of the testing session regarding the rms. The #TEST 1 which exhibit outliers in terms of rms (Figure 4-XXIV a) will be studied to understand how they can influence the modal identification results. The effects of higher values of Kurtosis (spread in all the signals) will be investigated through the analysis of #TEST 14 (Figure 4-XXIV b) and the #TEST 7 will give an indication of the effects of large kurtosis deviations.

The last point is tackled with the analysis of the results of another test performed the 2nd of April 2019 with a sampling frequency of 1200 Hz for understanding the influence on the dynamic identification of a sampling ratio 3 times higher.

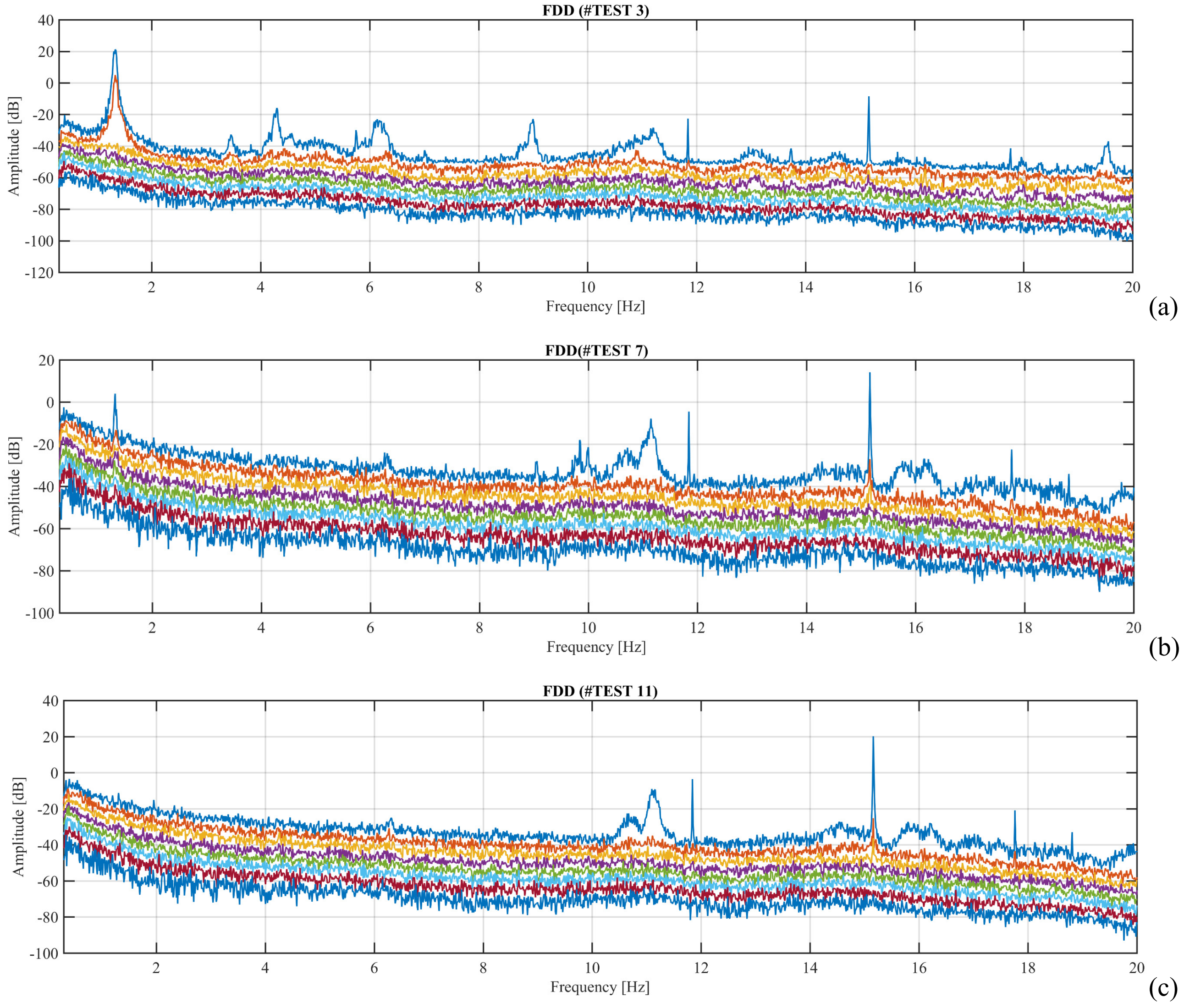

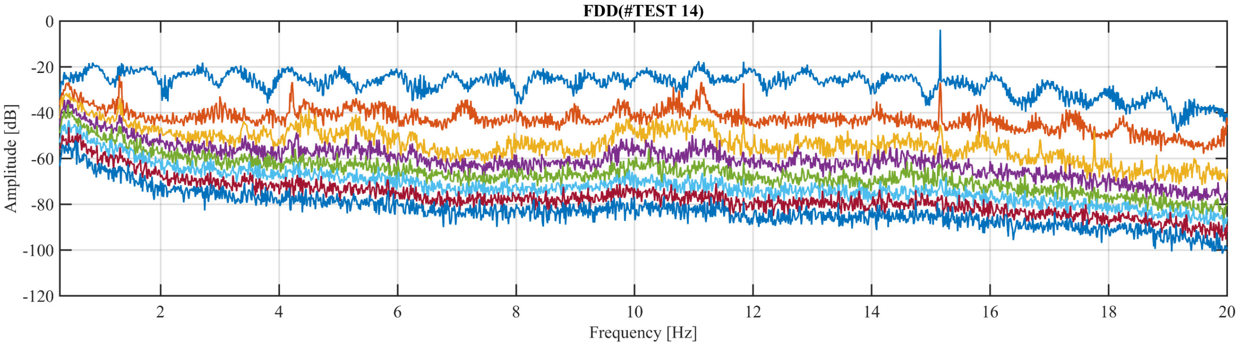

(d)

Figure 4-XXV The first eight normalized Singular values plot obtained with the FDD technique, (a) #TEST 3 (b) #TEST 7 (c) #TEST 11 (d) #TEST 14.

In Figure 4-XXV it is shown the frequency content of the signals through the FDD techniques for the selected tests that represent the variability of the signal energy and the effects of the noises that can be identified analysing the kurtosis values. For signals with too low energy (#TEST 11) the number of visible candidate modes is reduced than the higher energy signals (#TEST 3). In that case, the first two bending modes are clearly visible in the frequency band from 1-2 Hz and others five peaks can be observed in the frequency range from 2-10 Hz. Some doubts about the nature of the two peaks in the frequency band from 10-12 Hz that are clearly visible in the low content energy signals (# TEST 11). It can be that the low energy of the random input is bounded in that frequency range, exciting only that modes and not the first two bending modes. Some narrow bands process can be clearly distinguished at 11-15-18 Hz in all the signals. The SNR analysis confirms the obtained results exhibiting higher values (about 60 dB) in # TEST 3 and lower values (about 20 dB) in #TEST 11. Hence, both the SNR and the RMS are correlated to the number of identified modes and to their quality in the modal dentification. This can be clarified looking at Figure 4-XXV (b) the first two modes are visible and can be identified in terms of frequencies but the damping values are completely different in comparison with Figure 4-XXV (a).

In Figure 4-XXV (d) the wide-spread higher values of the kurtosis are confirmed by the noise represented by the first singular value that is dominating the others. Anyway, the largest kurtosis value recorded by the sensor A15 (Figure 4-XXIV b) does not affect too much the frequency content represented by the singular values.

The MEX setup procedure described in Section 4.3.1 is tested for the boundary values of the signals energy intensity aiming to correlate the selection of the setup parameters with the variance of the obtained results. Another key point that is investigated deals with the adequateness of performing the sensitivity analysis only once. Then the other modal identifications are performed with the same parameters and they should exhibit a satisfactory level of accuracy. If the that aim is achieved the computational procedure will lead to a reduced computational cost.

Table 4-VII The settings used in the Setup phase.

Parameters selection in the Setup phase

	Parameter		*Range of variation*	*Selected value*	*Phase*
SU1	Over-modelling coefficient to adjust the number of modes identifiable in the signals	k_1	[1-1,3]	1,15	Setup Phase
SU2	Over-modelling coefficient for the maximum model order	k_2	[5-15]	10	Setup Phase
SU3	Over-modelling coefficient for the maximum number of block rows	k_3	-	9	Setup Phase
SU4	Number of cycles of the lowest frequency	n_c	[1-11]	[1,31-11,84]	Setup Phase
SU5	Variation in the modal order	Δord	-	20	Setup Phase
SU6	Variation in the number of block rows	Δi	-	20	Setup Phase

From a visual inspection of the condition number surface (Figure 4-XXVI), it is possible to recognize a zone from where the condition number is still constant wherever is the selected modal order. That provides a preliminary indication of the optimal number of block rows in the Henkel matrix. The two surfaces plotted for the two extreme values of the signal energy, provide approximatively the same optimal values exhibiting a similar shape. The asymptotic value of the condition number is quite different, that can be explained analysing the Figure 4-XXVI: the value at the denominator, representing the low contribution to describe the system is almost the same, but the maximum values indicating the information contained in the covariances is definitively different.

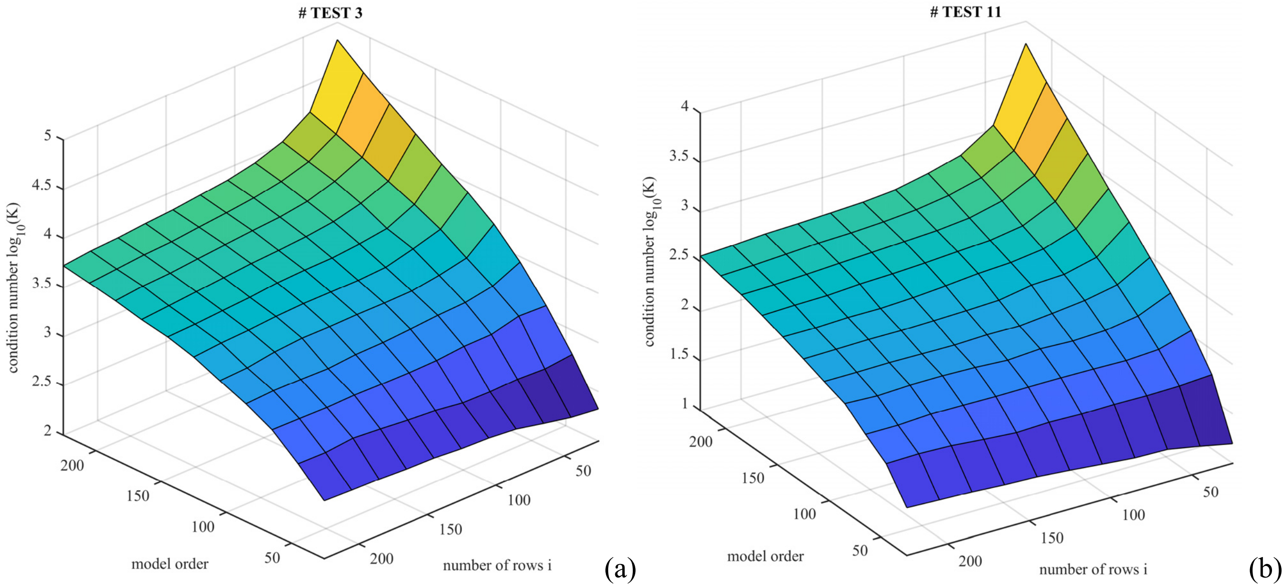

Figure 4-XXVI The plot of the condition number of the weighted projection matrix as a function of the subspace dimension; (a) #TEST 3 and (b) #TEST 11

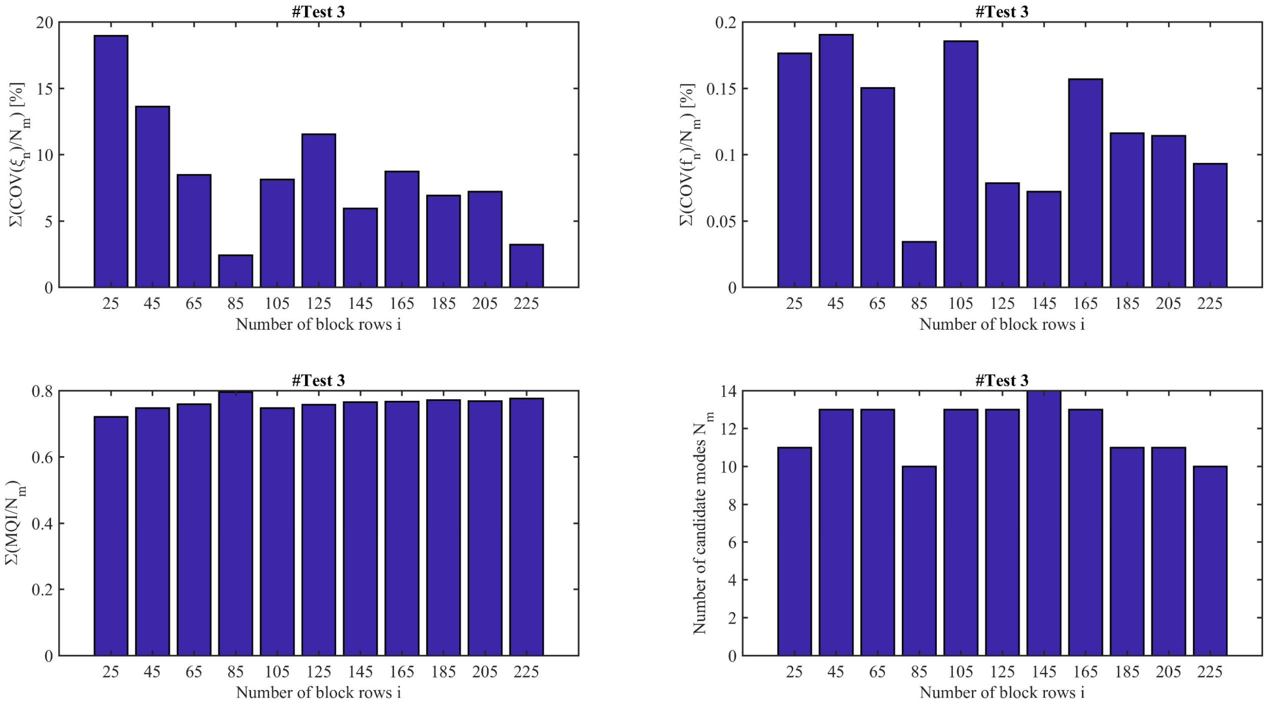

Figure 4-XXVII Variability in the estimation of the modal parameters due to the bias in the model for the #TEST 3.

A further investigation is performed (Figure 4-XXVII) comparing the obtained results from the modal identification for each value of *i* and the coefficient of variation of the modal parameters.

In the case of the higher signal quality an optimal value of *i* can be chosen equal to 85, providing mean values of the COV below the 3% and the 0,05% respectively for the damping ratio and the frequency. Moreover, it exhibits the highest level of the MQI encouraging the use of such indicator for selecting the identified modal properties.

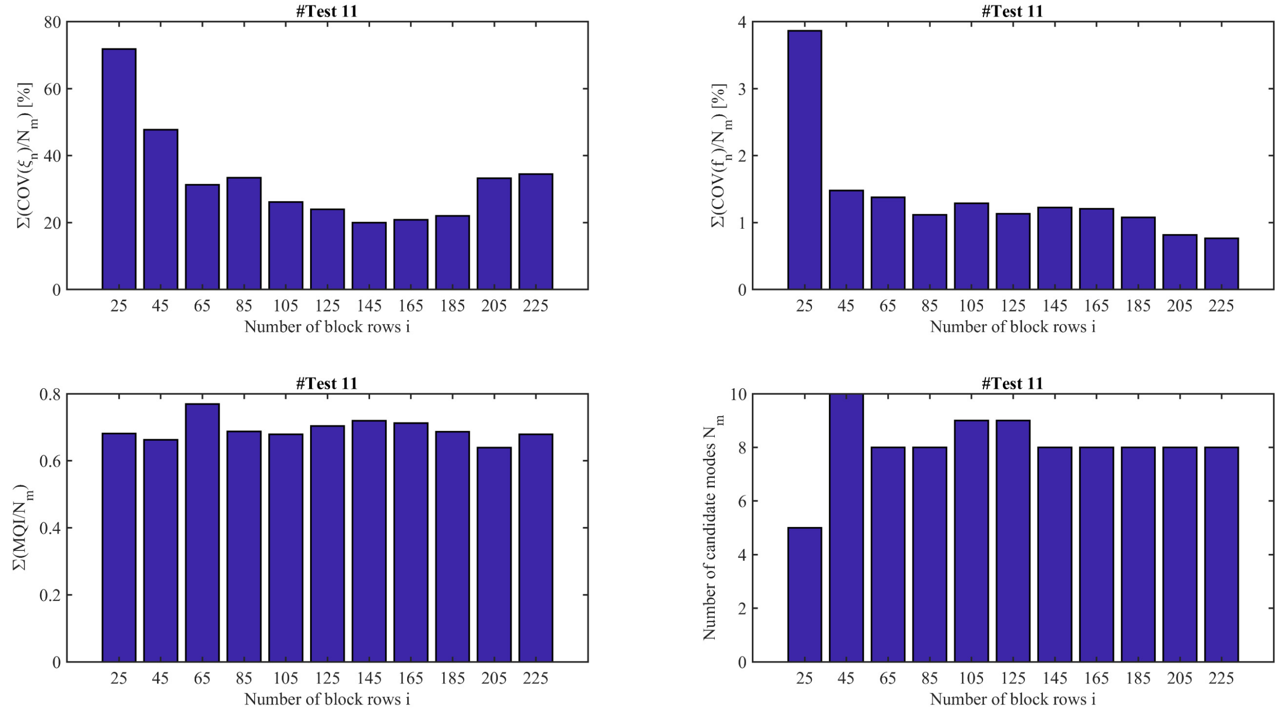

Figure 4-XXVIII Variability in the estimation of the modal parameters due to the bias in the model for the #TEST 11.

For poor quality signals (Figure 4-XXVIII), the mean values of the COVs stand in any case above the 20% and the 1% respectively for the modal damping and the natural frequency. The mean values of the MQI stand below the 0,7 (except for *i=65*) confirming the poor quality of the identified modal parameters.

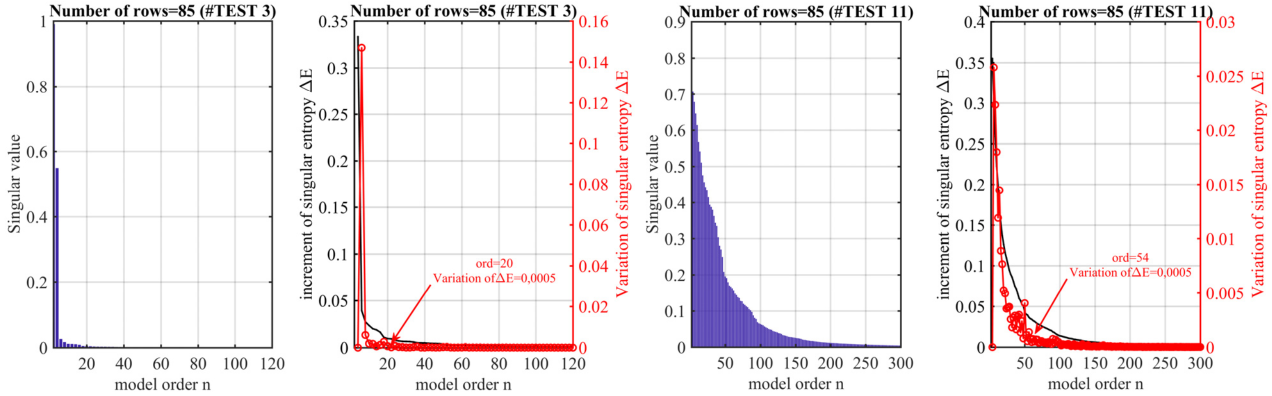

Figure 4-XXIX The normalized singular value of the weighted projection matrix, the singular value entropy and its first order perturbation values, respectively for the (a) #TEST 3 and (b) #TEST 11.

Once the optimum value of *i* is determined, the maximum value of the modal order is investigated through the analysis of the first order variation of the singular entropy values (Figure 4-XXIX). As it was expected two different model order are required in the two cases to reach the same values of first order variation of the singular entropy value. The poor quality of the signals implies the risk of modelling noise instead of the physical structural modes. That is confirmed by the singular value plot showing clearly that a model order equal to 20, corresponding to 10 modes, is enough for modelling the structural dynamics. On the other hand, decreasing the quality of the signals are needed more values to describe the covariances.

Table 4-VIII The settings of the parameters in the MEX algorithm used to perform the modal identification of the Torre Grossa.

Parameters in the MEX algorithm					
Parameter			*Range of variation*	*Selected value*	*Phase*
S1	SC in terms of frequency	df	[0-0,01]	0,01	Stabilization Phase
S2	SC in terms of damping	$d\xi$	[0-0,05]	0,05	Stabilization Phase
S3	SC in terms of mode shapes	$d\phi$	[0-0,02]	0,02	Stabilization Phase
H1	HC on the damping range	$\Delta\xi$	-	[0,002-0,1]	Stabilization Phase
H2	HC on the nature of the modes (complex conjugate)	-	-	-	Stabilization Phase
C2	Minimum number of elements for cluster	k_{cl}	[0-0,5]	0,25	Clustering Phase
V1	Weighting coefficients on the frequency variance	α_f	[0,75-1]	1	Validation Phase
V2	Weighting coefficients on the damping variance	α_ξ	[0-0,6]	0,75	Validation Phase

V3	Weighting coefficients on the Modal Transfer Norm	α_{MTN}	[0,75-1]	0,75	Validation Phase
V4	Weighting coefficients on the Modal Phase Collinearity	α_{MPC}	[0,75-1]	1	Validation Phase
V5	Weighting coefficients on the Mean Phase Deviation	α_{MPD}	[0,75-1]	1	Validation Phase
V6	Weighting coefficients on the Mean Frequency Rating	α_{FR}	[0-0,3]	0,1	Validation Phase

The settings parameters used in the MEX algorithm are resumed in Table 4-VIII, the results of the modal identification for every phase (cfr. Figure 4-V) are reported in Figure 4-XXX (*Stabilization phase*) Figure 4-XXXI (*Clustering phase*) Figure 4-XXXII (*Validation phase*).

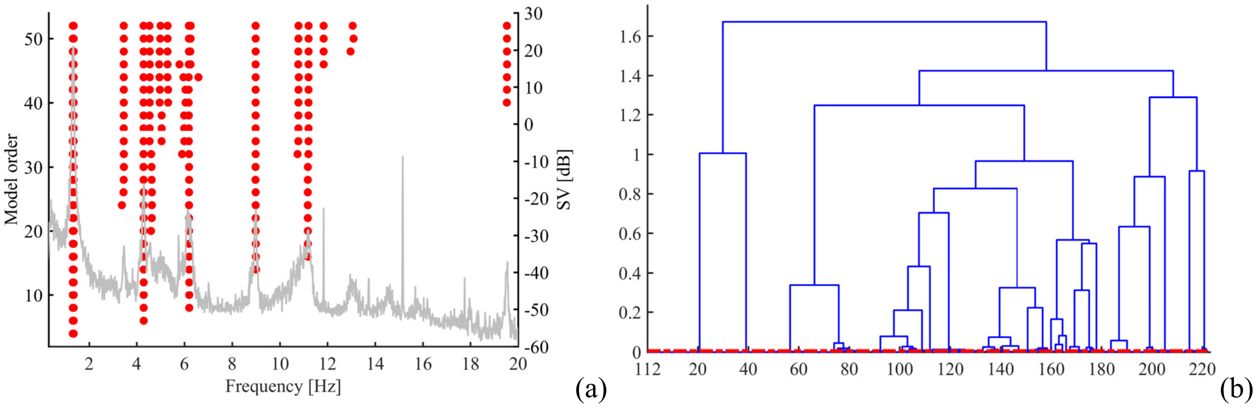

Figure 4-XXX (a) The stabilization chart for the #TEST 3 (b) The dendrogram of the hierarchical clustering performed with MEX algorithm; each branch represents the distance among the elements that are numbered progressively and the red line is the clustering threshold automatically defined by the algorithm.

In Figure 4-XXX (a) the stabilization chart is plotted; it is an output of the algorithm to have a check of the automated operations performed through the clustering phase. In Figure 4-XXX (b) the dendrogram represents the distances among each stable pole; then the red line id the threshold learned by the automated reading of the stabilization chart. In that case the threshold is quite low because of the small distances among the distinct poles (vertical lines in the stabilization chart).

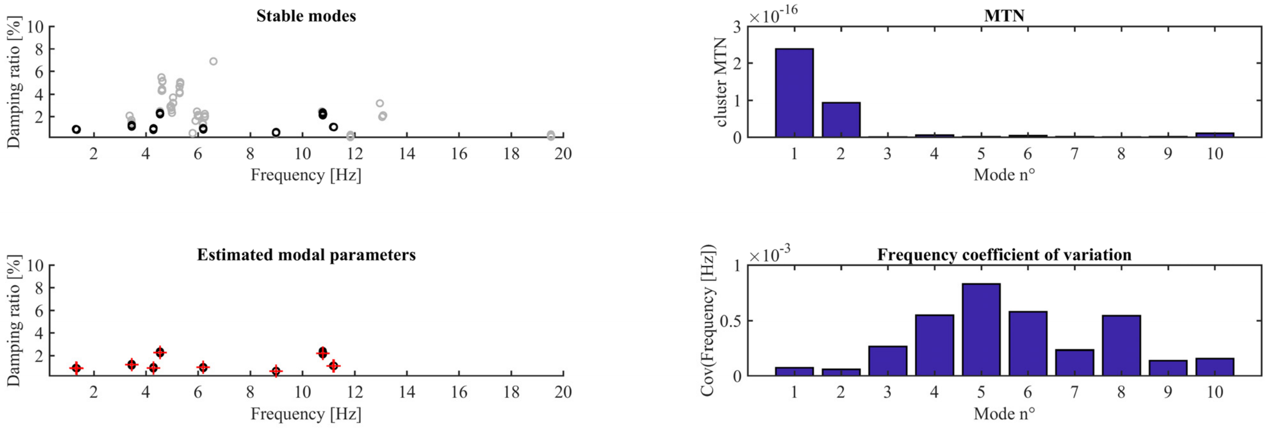

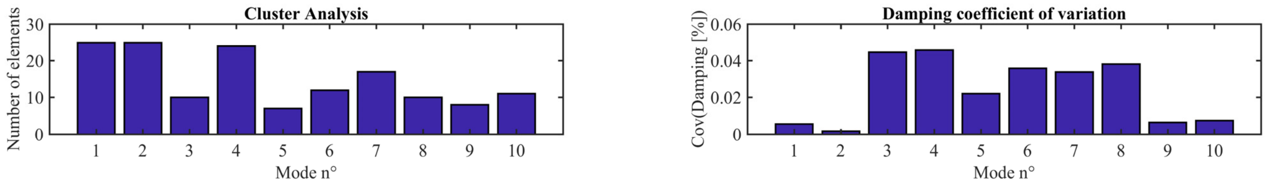

Figure 4-XXXI The operations performed by the algorithm during the clustering phase for the extraction of the modal parameters.

In Figure 4-XXXI are shown the automated operation developed in the clustering phase from all the stable modes (grey circles) are grouped together the elements that stand within the threshold (black circles). Then is cluster representing a candidate mode is represented through the mean values in terms of frequency and damping ratio (red cross). The properties of each cluster are represented to be successively analysed in the validation phase of the extracted modal parameters.

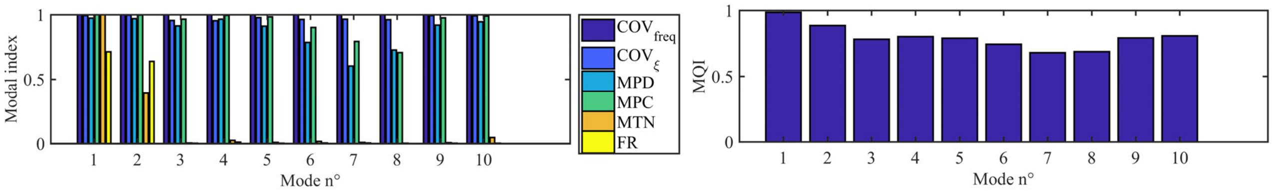

Figure 4-XXXII The results of the validation phase for each single mode validation criteria and the derived MQI index.

The validation phase resumes all the single mode validation criteria in the MQI. For instance, the weighting values can be adjusted after the observation of the results over a longer period.

Table 4-IX Results of the modal identification of the #TEST 3

Estimated Modal Parameters (#TEST 3)						
Mode n°	$\mu(f_n)$ $[Hz]$	$\mu(\xi_n)$ [%]	$cov(f_n)$ [%]	$cov(\xi_n)$ [%]	N_{cl}	MQI
1	1,315	0,879	0,007	0,562	25	0,98
2	1,348	0,856	0,006	0,173	25	0,88
3	3,453	1,180	0,026	4,471	10	0,78
4	4,284	0,876	0,055	4,573	24	0,80
5	4,540	2,263	0,083	2,198	7	0,79
6	6,195	0,945	0,058	3,597	12	0,74
7	8,987	0,603	0,023	3,386	17	0,68
8	10,782	2,193	0,054	3,824	10	0,68
9	11,1763	1,073	0,014	0,639	8	0,79
10	11,2058	1,068	0,016	0,749	11	0,80

As it was introduced before, the incidence of the sampling frequency in the modal identification is tackled comparing the obtained results with another test (#DC 2). The dynamic conditions are similar with an average wind speed recorded at the same meteorological station of 1,1 m/s. The monitored sections with accelerometers are the same of the previous dynamic campaign (#DC 1) and the devices are still the same.

Table 4-X The dynamic tests performed the 2nd of April 2019.

Dynamic tests (#DC 2)					
Test number #TG	*Length [s]*	*Sampling rate [Hz]*	*Loads*	*Day*	*Time*
15	970	1200	wind+microtremors	02/04/19	12:59
16	3600	1200	wind+microtremors	02/04/19	13:15
17	2257	1200	wind+microtremors	02/04/19	14:17
18	1805	1200	wind+microtremors	02/04/19	14:56
19	2138	1200	wind+microtremors	02/04/19	15:26
20	3151	1200	wind+microtremors	02/04/19	16:17
21	2223	1200	wind+microtremors	02/04/19	17:20

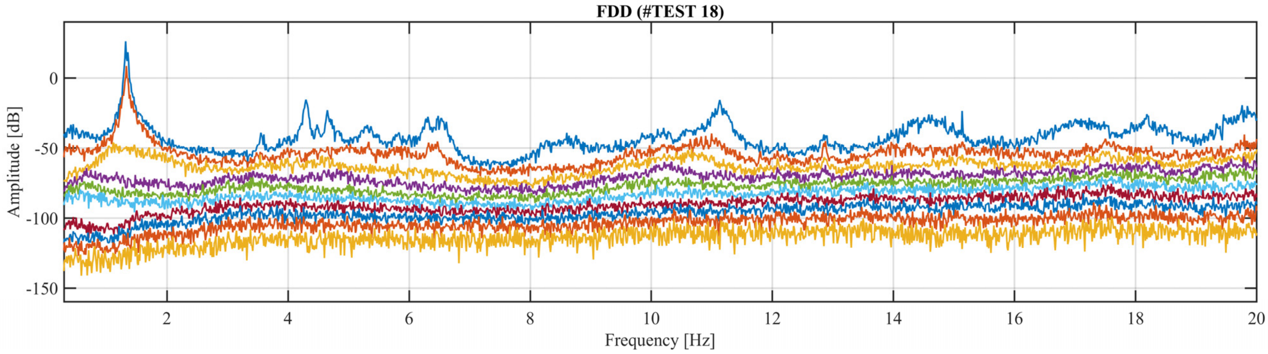

Figure 4-XXXIII The first eight normalized Singular values plot obtained with the FDD technique for the #TEST 18.

From a visual inspection of the SV plot (Figure 4-XXXIII) the peaks are clearer, and the SNR increases up to 115 dB, guaranteeing an easier modal identification.

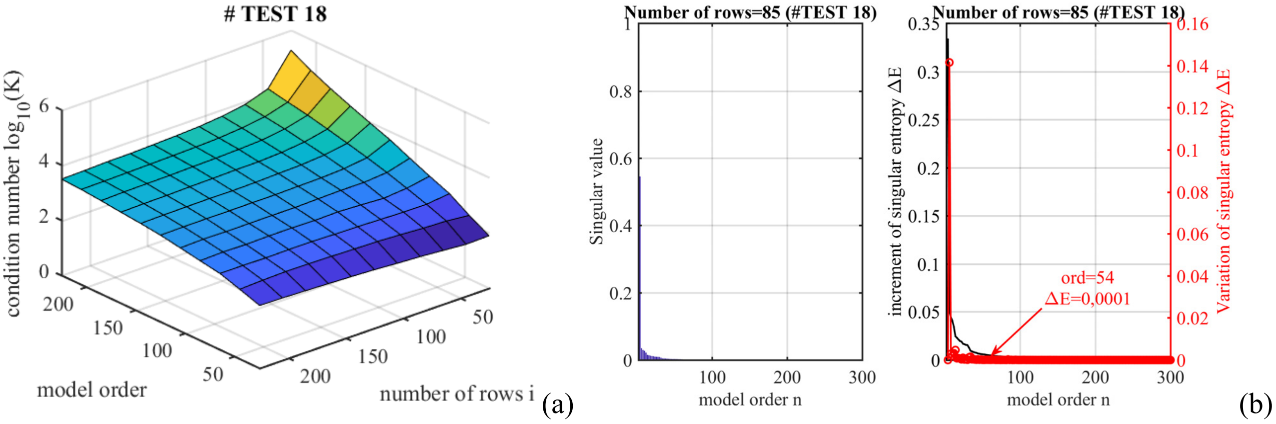

Figure 4-XXXIV (a) sensitivity analysis curve and (b) Normalized singular values and first order variation of the entropy for the #TEST 18.

The sensitivity analysis results encourage the use of the same settings in the MEX algorithm, even if the maximum model order can be set at lower levels. This is a good result confirming that the setup phase procedures can be done once if the inputs exhibit a good quality.

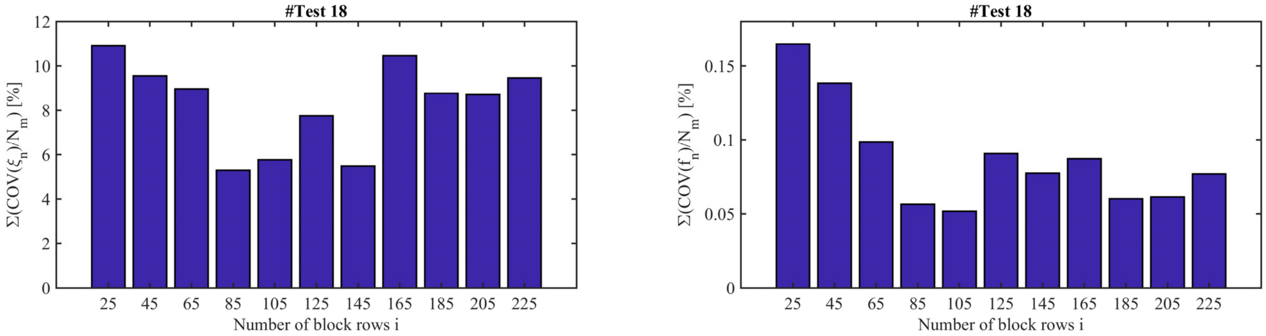

Figure 4-XXXV The average value of the Coefficient of variation [%] for the damping ratio and the frequency for every number of block row in the Hankel matrix in the #TEST 18.

The bias introduced with a blind selection of the block rows in the Hankel matrix can lead to a variance in the estimated modal parameters that is the doubled than the optimal value (Figure 4-XXXV). That result can be also found in [4], where it is highlighted the importance of the right choice of *i* for reducing the damping variance.

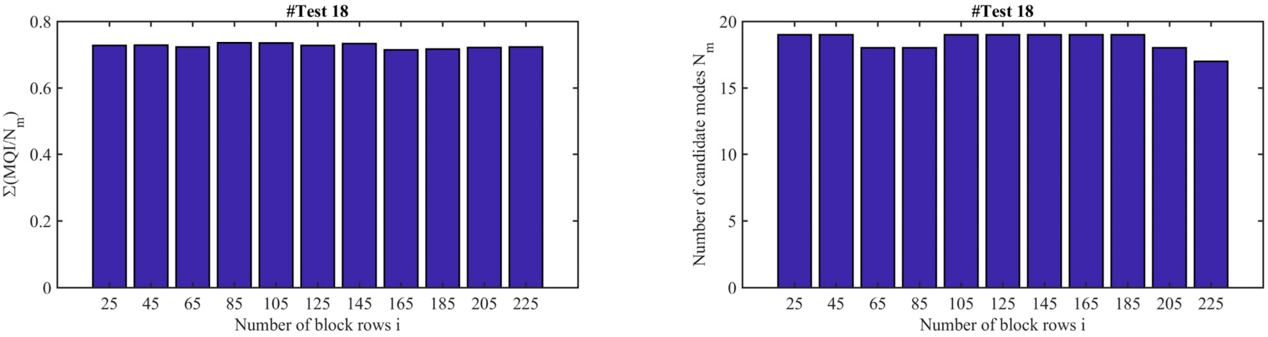

Figure 4-XXXVI The average values of the MQI index and the number of identified modes with the MEX algorithm in the #TEST 18.

The average value of the MQI (Figure 4-XXXVI) exhibit slightly higher values for the optimal value but the average values are definitively higher than the #TEST 3.In Figure 4-XXXVII are shown the results of the clustering phase of the #TEST 18 and a total of 18 candidate modes can be found (Table 4-XI).

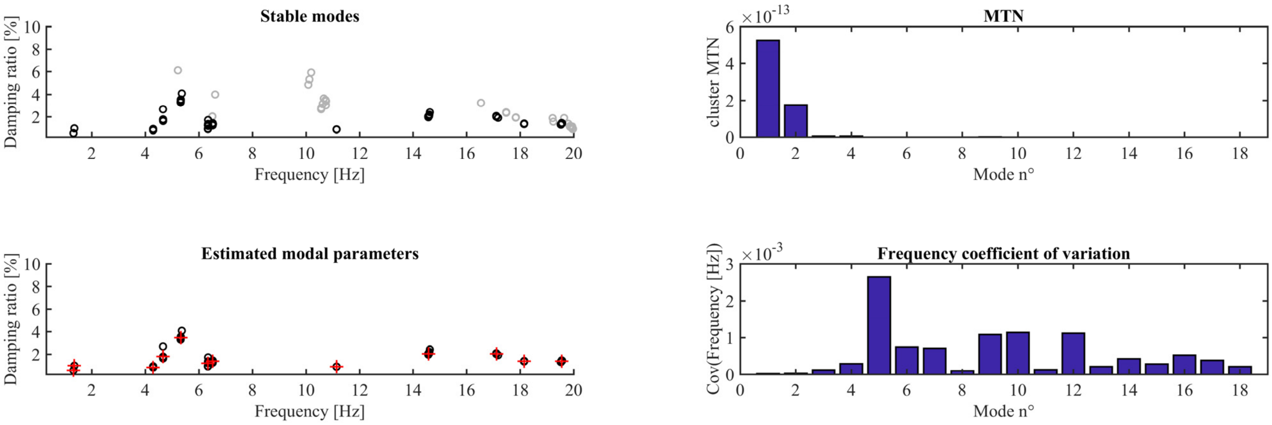

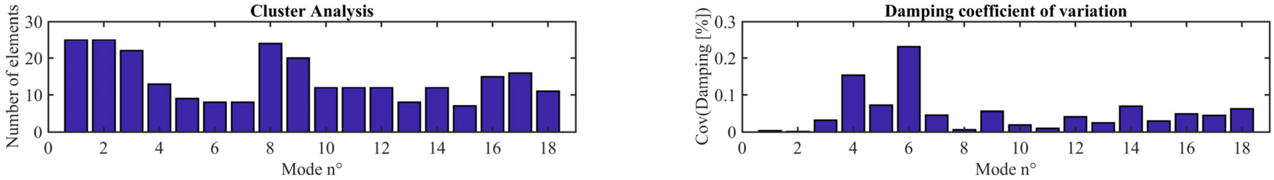

Figure 4-XXXVII The candidate modes after the clustering phase of the MEX algorithm for the #TEST 18.

In Figure 4-XXXVIII the results of the validation phase are introduced for all the modes both in terms of each single mode validation criteria both in terms of the global index MQI. In that way each mode can be labelled with a value that can be useful to set a threshold in an automated procedure.

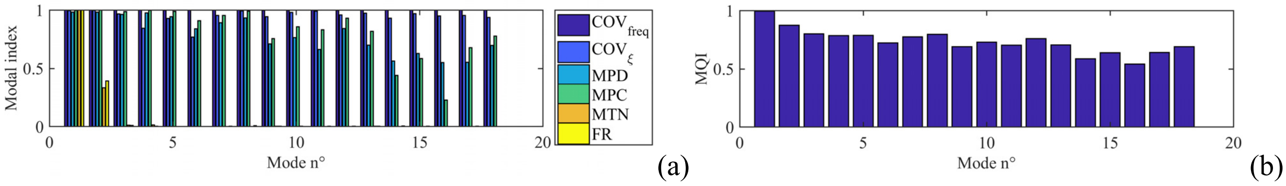

(a) (b)

Figure 4-XXXVIII The results of the validation phase for each mode validation criteria (a) and of the MQI index for the #TEST 18.

Table 4-XI Estimated modal parameters through the #TEST 18.

Estimated Modal Parameters (#TEST 18)						
Mode n°	$\mu(f_n)$ $[Hz]$	$\mu(\xi_n)$ [%]	$cov(f_n)$ [%]	$cov(\xi_n)$ [%]	N_{cl}	*MQI*
1	1,318	0,542	0,002	0,327	25	1,00
2	1,350	0,967	0,002	0,141	25	0,87
3	4,292	0,808	0,012	3,226	22	0,80
4	4,664	1,780	0,029	15,448	13	0,79
5	5,326	3,452	0,265	7,217	9	0,79
6	6,342	1,185	0,075	23,072	8	0,72
7	6,518	1,361	0,071	4,571	8	0,77
8	11,144	0,876	0,010	0,602	24	0,80
9	14,581	2,025	0,109	5,579	20	0,69
10	17,117	2,016	0,114	1,946	12	0,73
11	18,147	1,361	0,013	0,967	12	0,70
12	19,550	1,379	0,112	4,153	12	0,76
13	20,033	0,726	0,021	2,524	8	0,71
14	20,863	0,643	0,042	6,943	12	0,59
15	21,116	0,293	0,029	3,016	7	0,64
16	21,524	0,799	0,053	4,928	15	0,54
17	22,637	0,484	0,038	4,491	16	0,64
18	23,592	0,577	0,021	6,225	11	0,69

The first six modes exhibiting higher values of the MQI are plotted in Figure 4-XXXIX, the results seem reasonable for the tested structure.

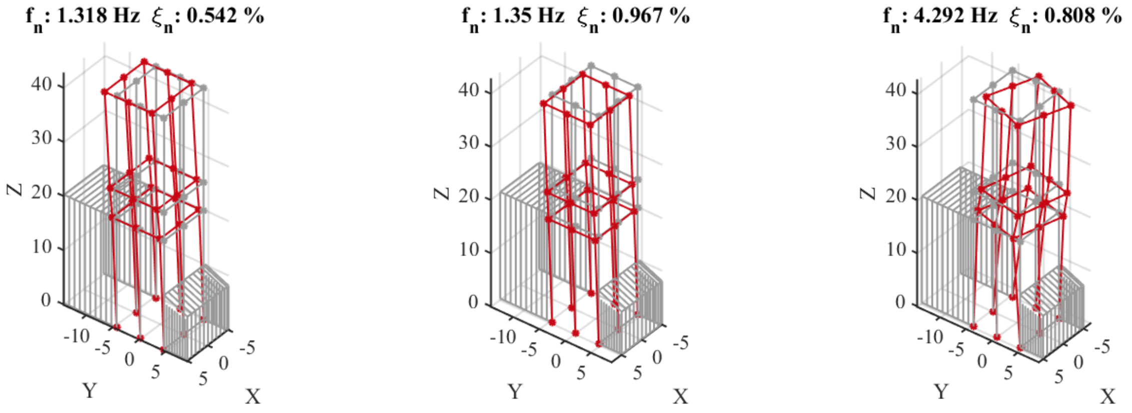
f_n: 1.318 Hz ξ_n: 0.542 % f_n: 1.35 Hz ξ_n: 0.967 % f_n: 4.292 Hz ξ_n: 0.808 %

First bending y-y   First bending x-x   First torsional

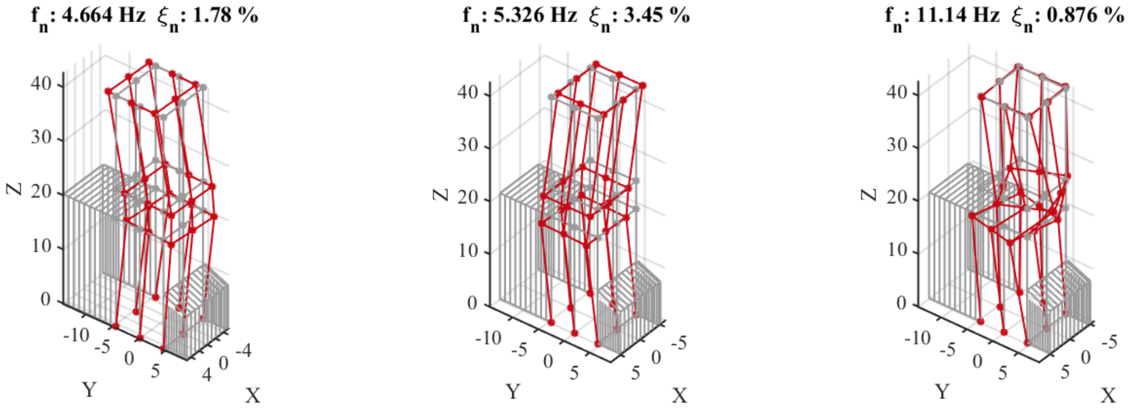
f_n: 4.664 Hz ξ_n: 1.78 % f_n: 5.326 Hz ξ_n: 3.45 % f_n: 11.14 Hz ξ_n: 0.876 %

Second bending y-y   Second bending x-x   Second torsional

Figure 4-XXXIX The first six modes that exhibit the higher MQI values (#TEST 18).

4.2.3 The Medici bridge

This case of study is a masonry arch bridge with two spans supported by the lateral abutments and by a masonry pier in the middle of the Sieve river. The bridge was Built in the middle of the XVI century on commission by Cosimo I de' Medici; after the ruin of the bridge during the flood of the Sieve river. The bridge was probably built by Stefano from San Piero a Ponti and his son Tommaso on the design project of the famous renaissance architect Ammannati. In the 1788 the bridge was restored by the archduke Peter Leopold of the Lorena's family for improving the route between Florence and the Casentino hills. The bridge was severely damaged during the second world war and one of the two arches was destroyed during the bombing.

(a) (b)

Figure 4-XL (a) The Medici bridge shot from the Pelago (a)and Pontassieve (b) side.

After the war the demolished arch was rebuilt with bricks keeping the same architectural features from the past and strengthened with concrete.

Nowadays the bridge appears as a red bricks double arch bridge with two asymmetric spans one of 29 meters and the other with length of 24 meters with a width of about 6 m. The longer span is restored and strengthened with concrete, instead the second is still the original with a red brick arch of 90 cm width and an incoherent infill above.

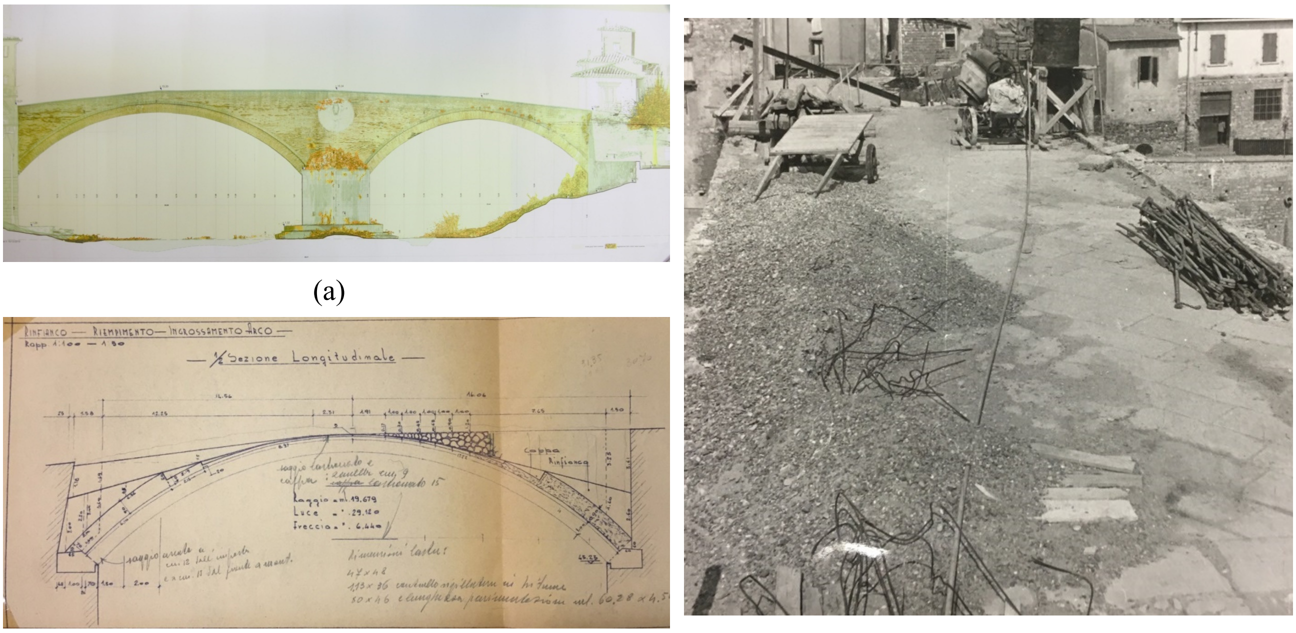

(a)

(b)

(c)

Figure 4-XLI (a) Frontal view of the bridge (*courtesy of Prof. Grazia Tucci*). (b) Design draw of the retrofitting works after the second world war (*courtesy: archivio di stato di Firenze*). (c) The reconstruction works of the bridge after the second world war.

The dynamic tests were performed with monoaxial piezo-electric accelerometers: three PCB 393 C (a6, a7, a8) with a range of 2,5g and a sensitivity of 1 V/g, three PCB 393 B31(a1, a2, a5) and one PCB 393 B12 (a3) with a range of 0,5g and a sensitivity of 10 V/g.

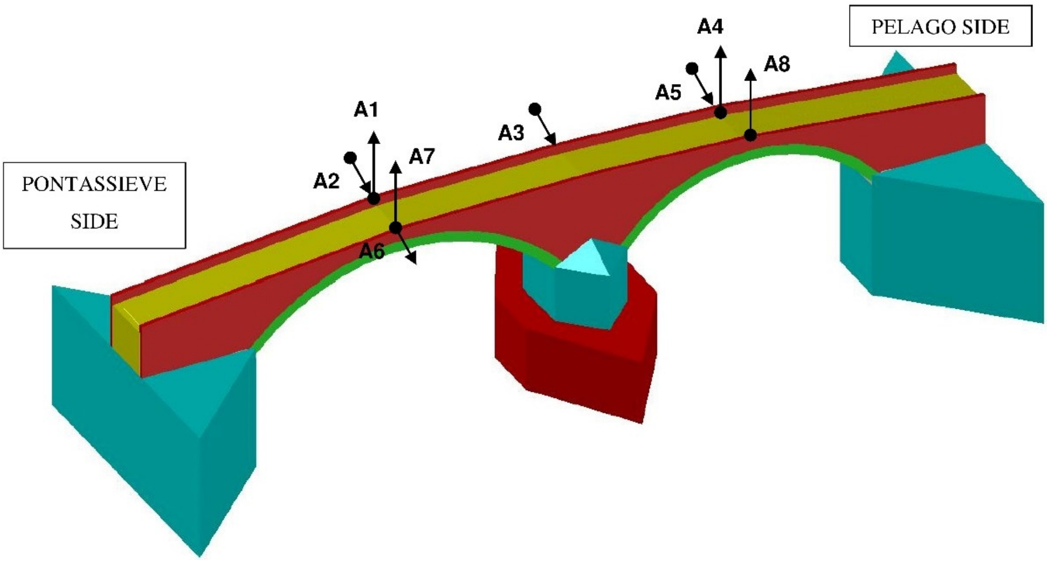

Figure 4-XLII Position of the accelerometers during the dynamic tests.

The tests were performed under different conditions: one is under operative conditions with excitations that are due mainly to the pedestrian because the bridge was closed to the vehicular traffic and the other consists in some impulsive tests performed with the drop of the mass of a truck from a step.


(a)

(b)

(c)

Figure 4-XLIII (a)-(b) The installation of the accelerometers to the bridge. (c) The truck falling down a step from the front wheels to simulate an impulsive force acting on the masonry arch on the Pelago side.

In the Ambient Vibration Tests (AVT) the raw signals were digitally filtered with a Butterworth filter of order three, in the frequency band 0.3-20 Hz, then the signal is resampled at a frequency of 50 Hz. In the Impulsive Tests (IT) the signals are just filtered in the same frequency band.

Table 4-XII Dynamic tests performed during the experimental campaign of the 6/11/2017.

Dynamic tests			
Test number #PS	*Length [s]*	*Sampling rate [Hz]*	*Loads*
1	1818	400	Pedestrian+wind+microtremors
2	2246	400	Pedestrian+wind+microtremors
3	1901	400	Pedestrian+wind+microtremors
4	375	1200	Impulsive on Pontassieve side span
5	412	400	Impulsive on Pelago side span

A first idea of the frequency content in all the signals can be obtained through the ANPSD plot in each direction (Figure 4-XLIV). Several peaks can be identified in the analysed frequency band allowing a first identification of the direction of motion.

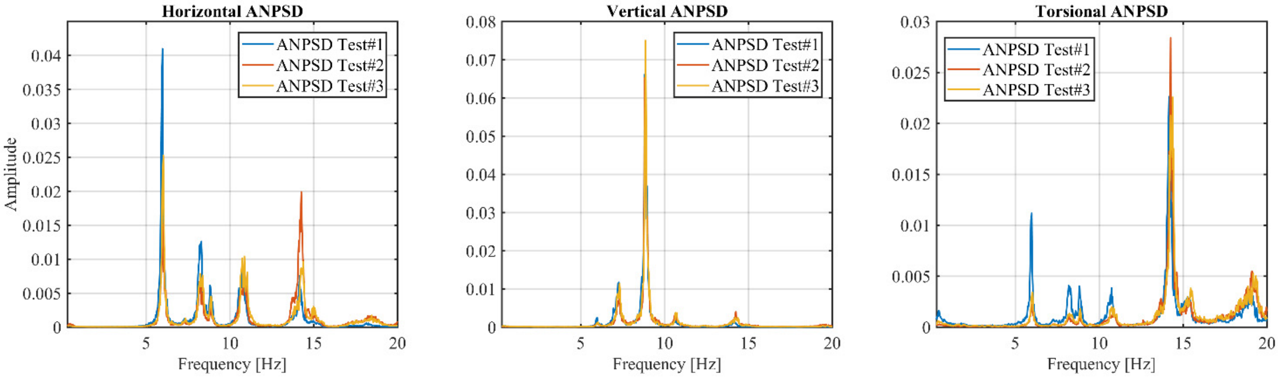

Figure 4-XLIV The Average Normalized Power Spectral density for each direction of motion during the ambient vibration tests

The analysis in the frequency domain is performed by the FDD technique, clearly detecting six peaks in the singular values plot (Figure 4-XLV) for every test under ambient vibrations.

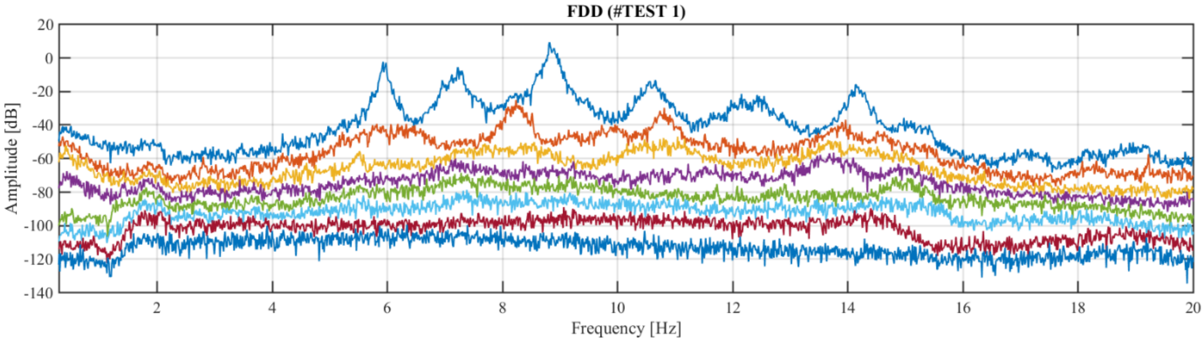

(a)

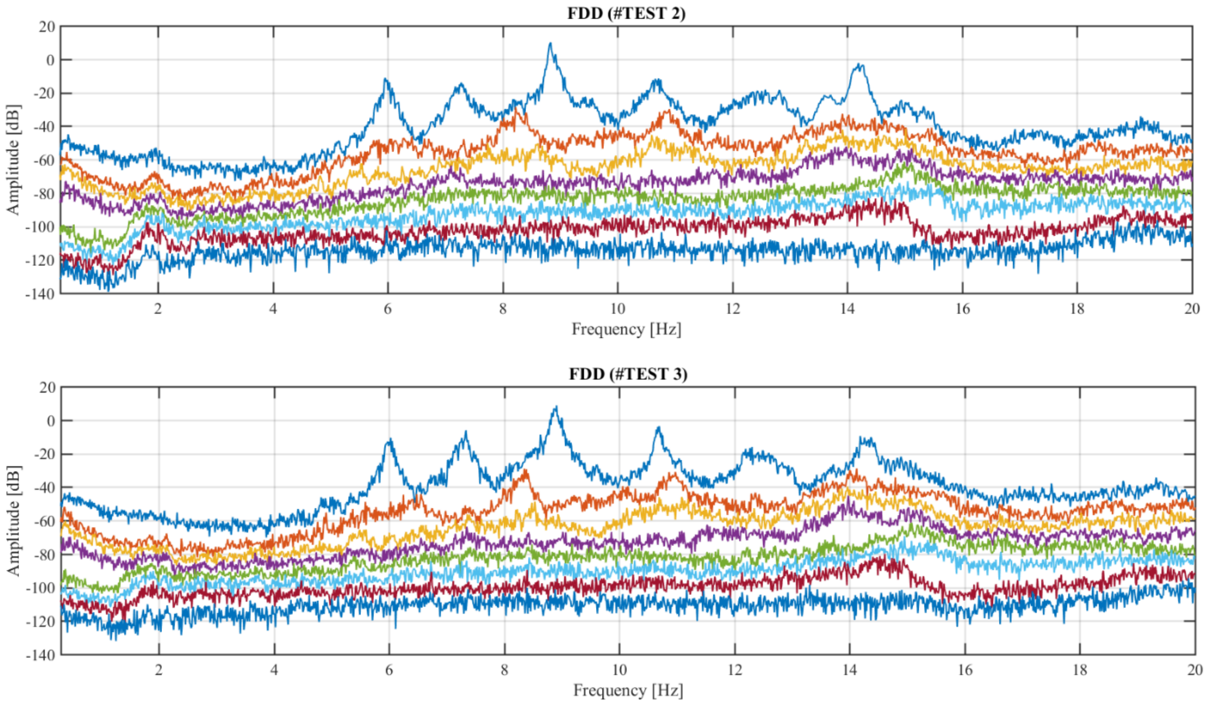

Figure 4-XLV Singular values of the PSD matrix plot in the #TEST 1 (a) #TEST 2 (b) and #TEST 3 (c)

The #TEST 1 is used for testing the MEX algorithm, because of the higher frequency content in the major part of the identified peaks (Figure 4-XLIV).

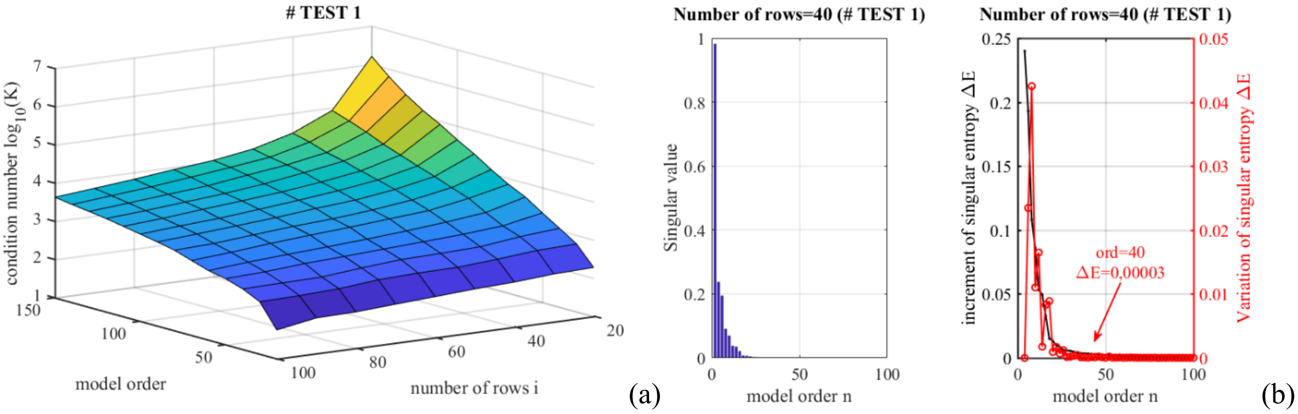

Figure 4-XLVI (a) Sensitivity surface for the #TEST 1 (b) Normalized singular values and entropy plot of the #TEST 1

The results of the setup phase using the same values of the coefficients introduced in Table 4-VII, confirm the selection of the block rows in the Hankel matrix as the first values where the condition number is stable (Figure 4-XLVI (a)). The high number of modes in the signals and the low level of noise lead to the selection of the modal order by the analysis of the first order variation of the entropy (Figure 4-XLVI (b)).

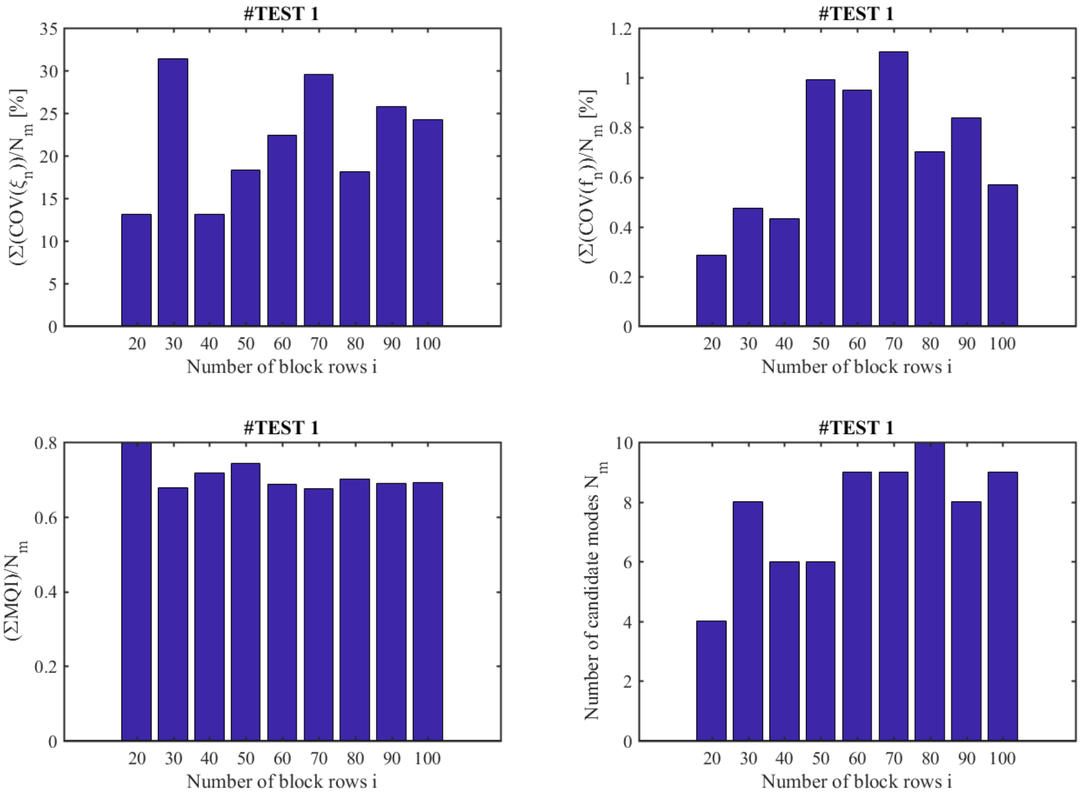

Figure 4-XLVII Sensitivity analysis in terms of average variances of the identified modal parameters in the #TEST 1

That result is confirmed analysing the variance of the identified modal parameters in the selected domain (Figure 4-XLVII). By increasing too much the number of rows the average variance of the modal parameters increases. On the other hand, the number of modes identified increases with a lower level of consistence respect to the MQI.

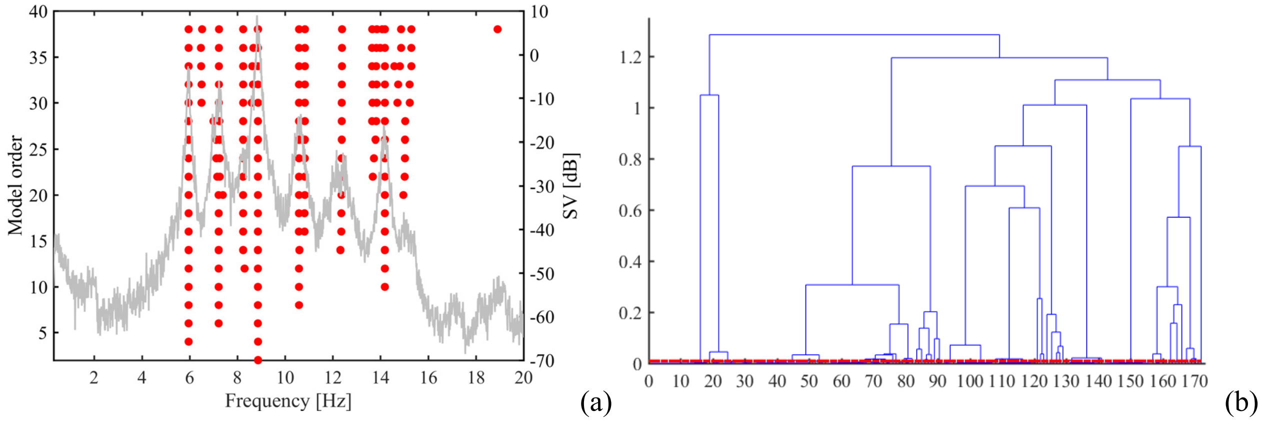

Figure 4-XLVIII (a) The stabilization chart plot (b) Dendrogram plot for the #TEST 1

The results of the clustering stage trough the automated definition of the threshold lead (Figure 4-XLVIII) to the identification of clear modes with a number of elements at least equal to half of the maximum value (Figure 4-XLIX).

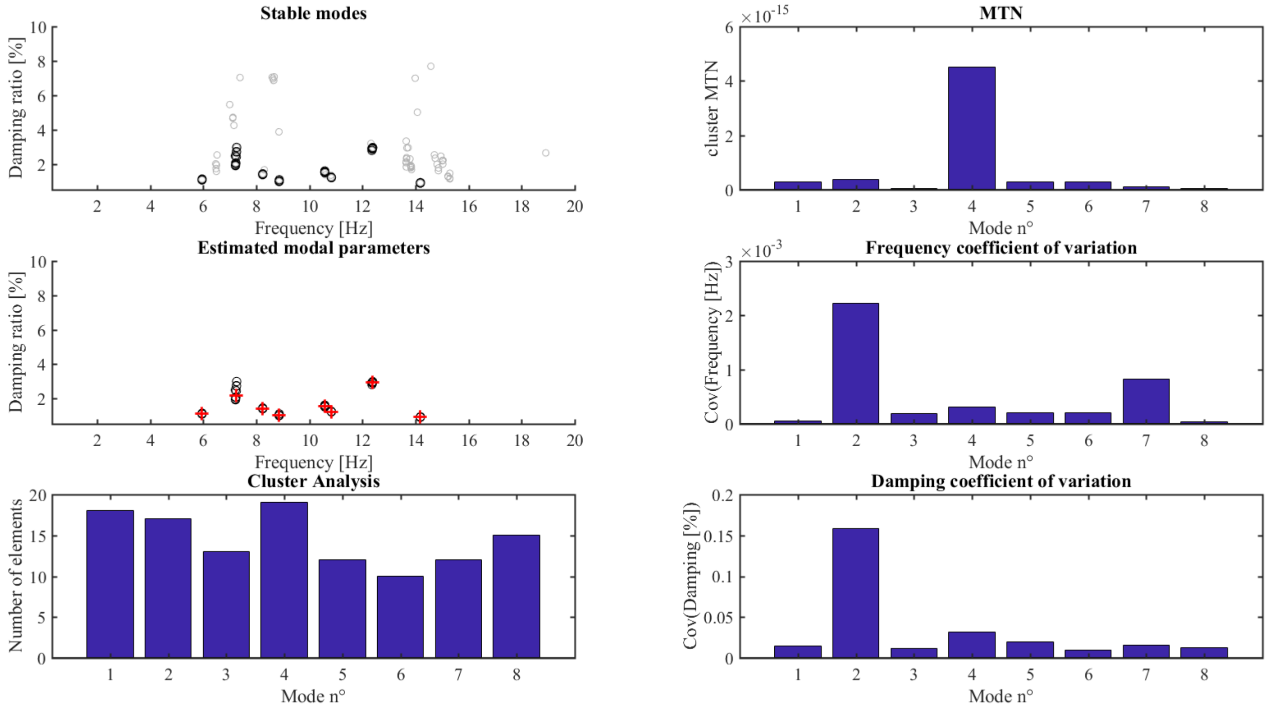

Figure 4-XLIX Graphic output of the clustering phase in the MEX algorithm for the #TEST 1

The results of the validation phase (Figure 4-L) confirm that all the candidate modes can be considered as physical, exhibiting MQI values major than 0,79 (Table 4-XIII).

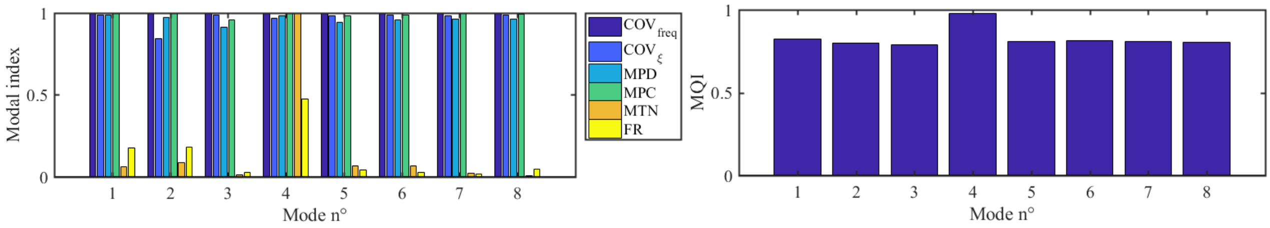

Figure 4-L Graphic output of the validation phase in the MEX algorithm for the #TEST 1

Except for the second identified the variance in terms of frequency and damping ratio are below the 0,03 % and the 3 %. The second mode should be retained but some further investigation is needed to obtained others information.

Table 4-XIII Estimated modal parameters through the MEX algorithm in #TEST 1

Estimated Modal Parameters (#TEST 1)						
Mode n°	$\mu(f_n)$ $[Hz]$	$\mu(\xi_n)$ [%]	$cov(f_n)$ [%]	$cov(\xi_n)$ [%]	N_{cl}	MQI
1	5,956	1,105	0,006	1,488	18	0,82
2	7,228	2,171	0,222	15,852	17	0,80
3	8,243	1,402	0,019	1,192	13	0,79
4	8,863	0,993	0,031	3,197	19	0,98
5	10,583	1,511	0,021	1,929	12	0,81
6	10,829	1,210	0,021	1,001	10	0,81
7	12,374	2,894	0,082	1,594	12	0,81

8	14,183	0,895	0,004	1,238	15	0,81

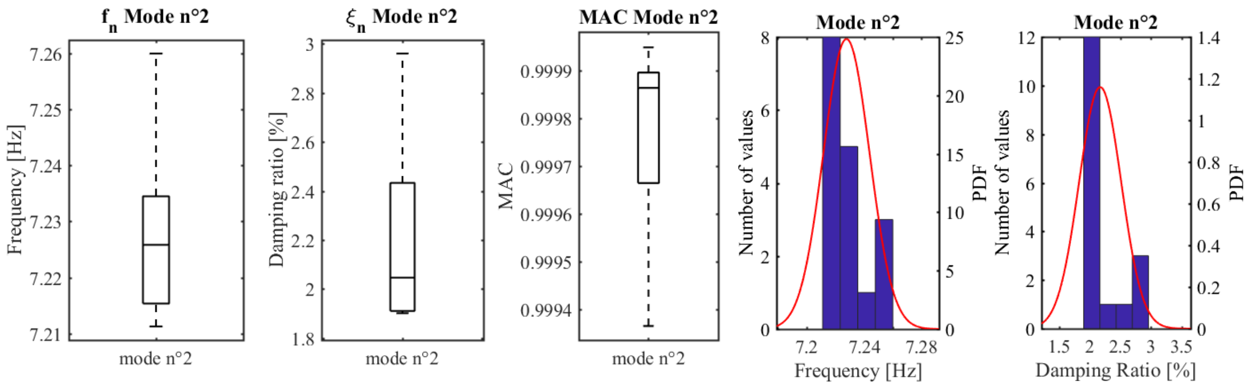

Figure 4-LI Outlier analysis for the second mode and the histogram of the identified values in terms of damping and frequency.

Some further investigations can be carried out with an outlier analysis of each cluster, excluding the values outside 1,5 times the interquartile range, to reduce the variability of the MP. In the case of the second identified mode which exhibits the highest variance of the identified parameters, are not detected any outliers. Meaning that the variability is not depending on the choice of the settings parameters.

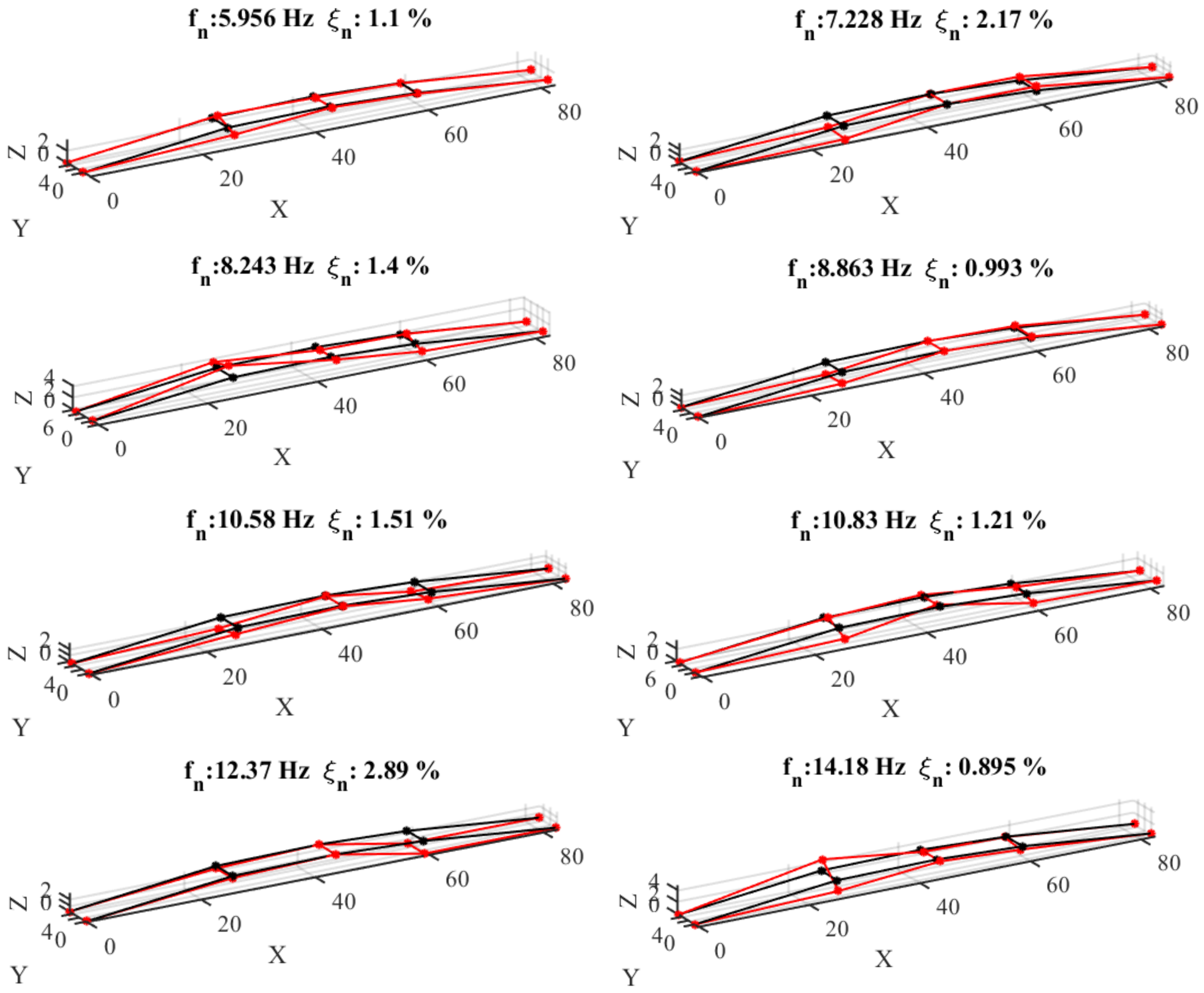

Figure 4-LII The eight mode shapes identified through the MEX algorithm for the #TEST 1

The complex dynamics of the structure is also investigated through two impulsive tests: #TEST 4 with the impulsive force applied on the concrete span on the Pontassieve side and the #TEST 5 with the impulsive force applied in the masonry arch span on the Pelago side. The response to the impulsive forces is the convolution in the time domain of the Impulsive Response Functions (IRF) function for each mode. Indeed, the Fourier transform is directly proportional to the Frequency Response Function (FRF).

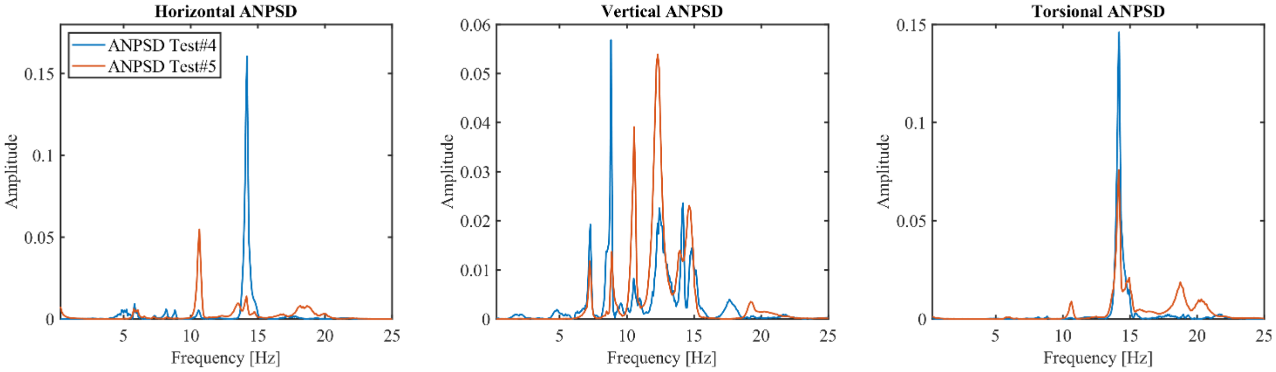

Figure 4-LIII The ANPSD for the two impulsive tests (#TEST 4 and #TEST 5)

The higher amplitude in the frequency domain (Figure 4-LIII) of the second, fourth and eight mode while the impulsive excitation is on the Pontassieve side(#TEST 4) confirms that these modes mainly involve the concrete span. That is confirmed by the response of the seventh mode that is more excited when the impulsive force is applied to the Pelago side (#TEST 5). Some further investigations should be performed to understand the nature of the third, fifth and sixth mode.

4.3 Comparison with other techniques

The MEX algorithm follows the main steps introduced by the Authors in the last decades (Figure 4-I). One of the novelties introduced is the automated selection of the cut-off threshold in the clustering phase from an automated interpretation of the distances among the poles in the stabilization chart (*cfr. Section 4.3.3*).

In order to compare the distances obtained with those proposed in literature that have been fixed in the range of 0,02-0,04 the histograms of the distances among each pole are plotted in Figure 4-LIV for the four cases of study that have been presented in this chapter.

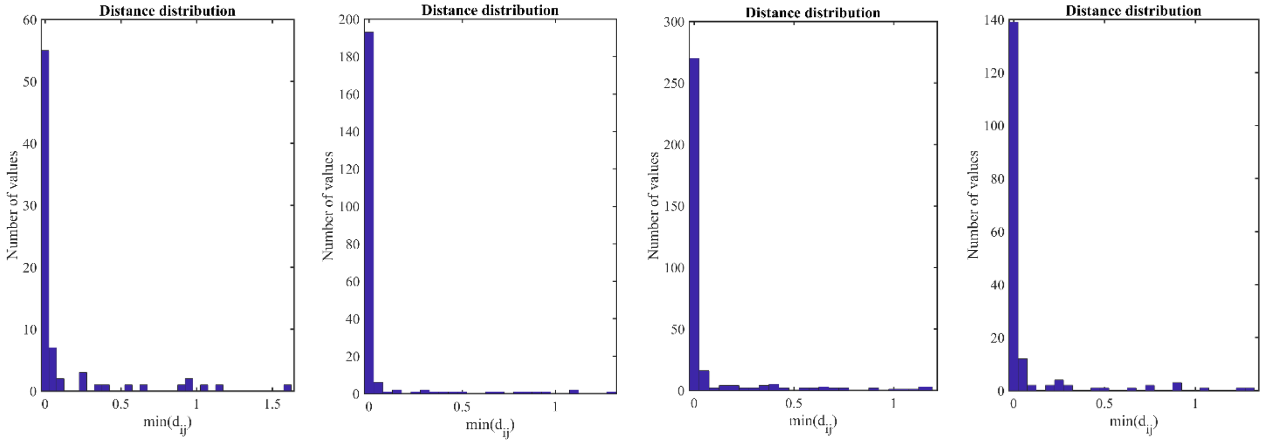

(a) #MM 02 **(b) #TG 02** **(c) #TG 18** **(d) #PS 2**

Figure 4-LIV The distribution of the distances in the stabilization chart calculated by the MEX algorithm.

From the observed data it is clear that they cannot be considered as a normal distributed (Figure 4-LIV). Hence the values of their statistical properties can be calculated as shown in Table 4-XIV.

Table 4-XIV The statistical properties of the selected four cases of study.

Hierarchical clustering threshold with MEX algorithm					
$TEST\ \#$	$median(d)$	d_{25}	d_{75}	$\mu(d)$	$cov(d)$
TG 02	0,00048	0,00002	0,0044	0,0549	3,6107
TG 18	0,00030	0,00002	0,0094	0,0721	2,8816
PS02	0,00048	0,00007	0,0090	0,0727	3,0715
MM 02	0,00140	0,00027	0,0338	0,1289	2,4624

The values are definitively lower than the used common range and they are dependent on the stabilization chart shape. Indeed, a slightly threshold can be selected based on the physical information buried in the analysed signals. Therefore, a value equal to the second or the third quartile of the distribution can be assumed to be suitable value to take out the spurious poles from the clusters representing physical modes,

4.4 Long-term monitoring application to the CH

The proposed procedure based on a C-SHM approach with a selection both of the input both of the extracted modal parameters is tested on a dynamic long-term monitoring system installed on CH buildings. The sensors are developed by the partners of the MOSCARDO project (a project funded by the Tuscany Region aiming at developing advanced techniques for the long-term monitoring of the CH). All the devices are wireless, and the accelerometers are assembled using MEMS sensors [22].

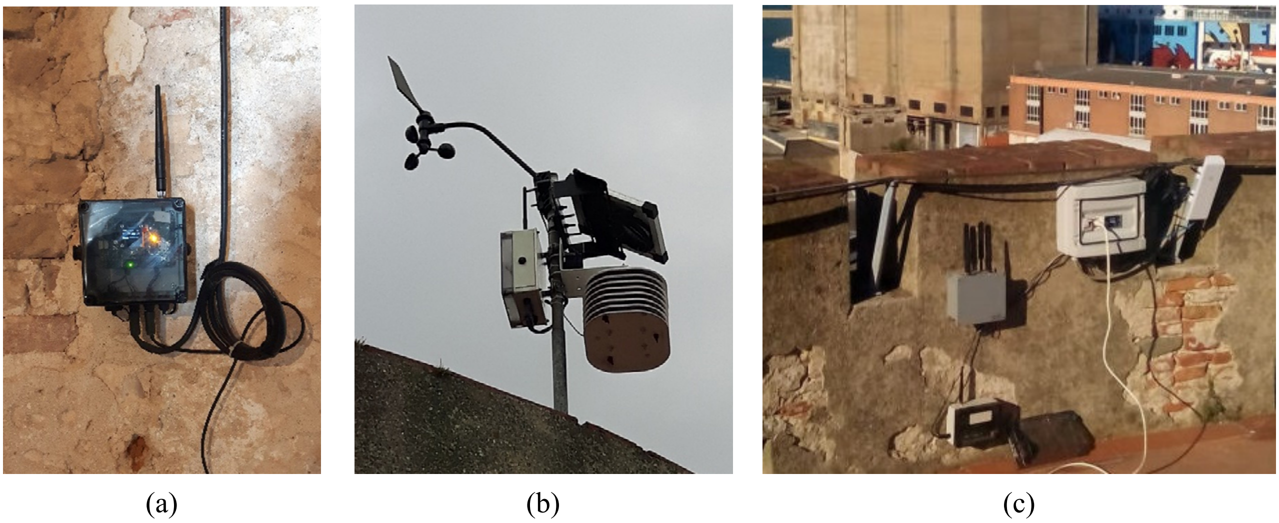

(a) (b) (c)

Figure 4-LV (a) Biaxial MEMS sensors accelerometer (b) anemometer and meteorological station (c) The gateway collecting all the signals

One of the goals was design and testing a robust long-term monitoring system suitable for the CH using some relevant cases of study. The devices are built to exhibit the lowest visual impact with a reasonable cost, on the other hand all the collected data must be processed with a robust automated procedure for the damage detection purposes.

Among all the monitored structures the case of the Matilde Tower is presented herein. The monitoring system is built with seven accelerometers (red arrows in Figure 4-LVI) at two different levels, two meteorological station that measures the temperature and the humidity (blue squares in Figure 4-LVI) and one anemometer (yellow circle in Figure 4-LVI) capable to measure the average wind speed and the direction. The signals recorded by the accelerometers are sampled with a frequency of 50 Hz for a length of acquisition of 10 minutes every hour. The environmental effects are recorded by the devices put both indoor and outdoor, furnishing an average value for every hour. The data collected every session are transmitted to the gateways and then to the server and the results can be visualized on the website (*http://www.moscardo.it/*).

The information collected during the preliminary identification campaign (Section 4.2.1) enables to increase the knowledge about the structural dynamics and something about the common operative conditions. In that case the structural dynamics seems simple, but the level of the disturbances can lead to misleading indications using in a blind way the automated procedure for the modal identification. All the information gathered together allows to design the monitoring system and the automated procedure for the feature extraction.

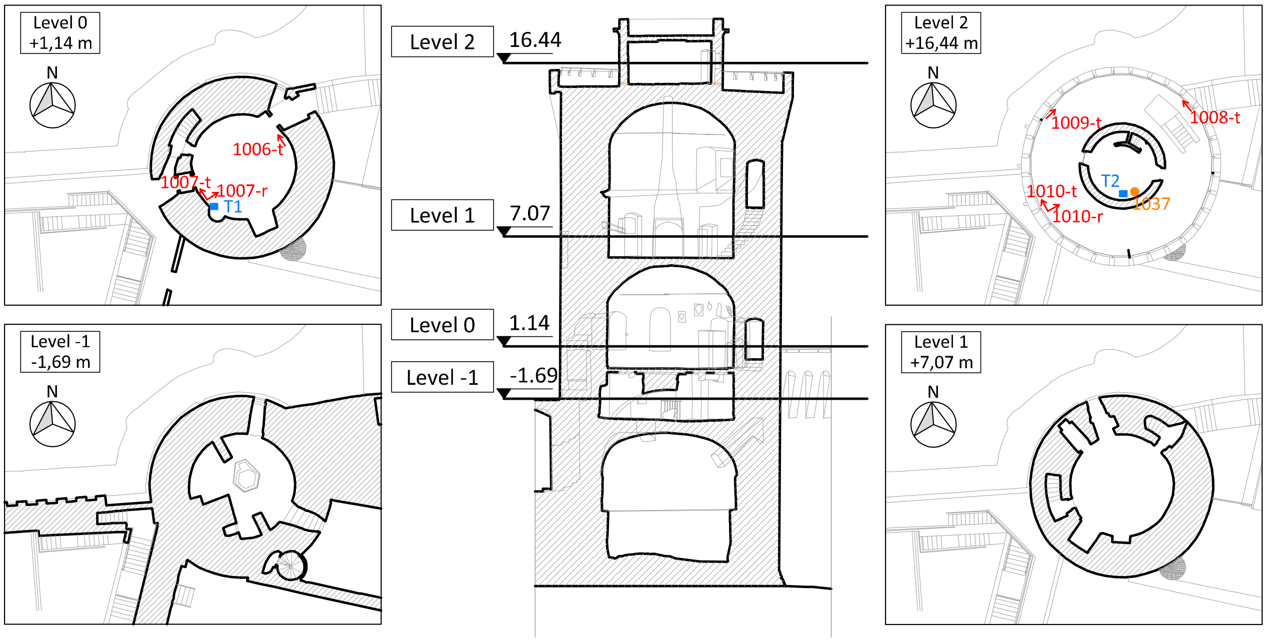

Figure 4-LVI Installed monitoring in the Matilde Tower: the red arrows represent the accelerometers and their directions, the blue square the meteorological stations and the yellow circle the anemometer.

4.4.1 Calibration phase

As shown in the previous sections the quality of the input data is crucial to obtain good results in the dynamic identification. From the acquired knowledge of the structure dynamics in operational conditions, two distinct periods of one week are chosen to calibrate the selection of the input that feed the automated procedure.

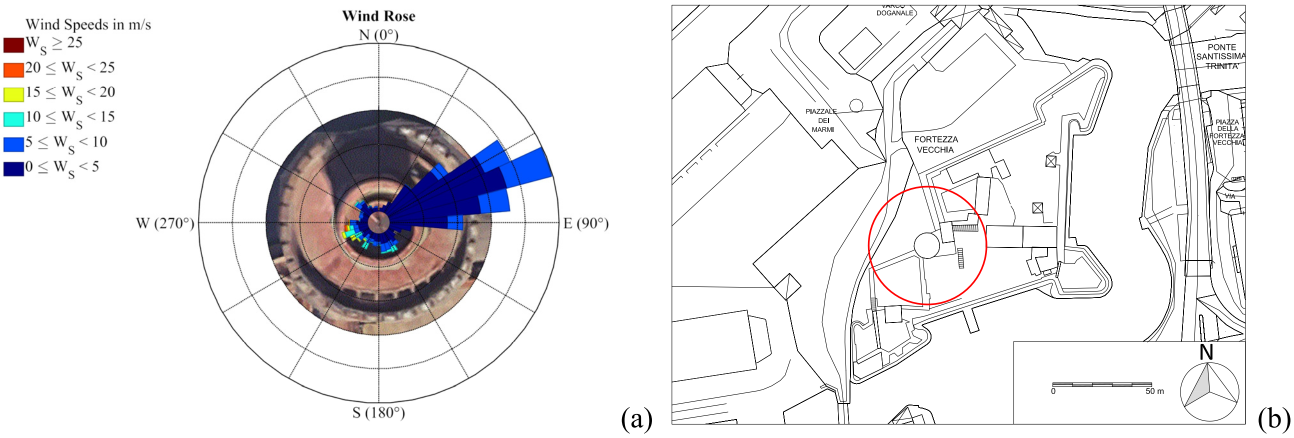

Figure 4-LVII (a) Wind directions and intensity in the monitored period on the Matilde Tower (b) CTR map of the Old fortress and the Matilde Tower in the red circle (*source http://www502.regione.toscana.it/geoscopio/cartoteca.html#*).

The first calibration period (#P1) goes from the 3rd to the 10th of December when the highest average wind speed is recorded (25 m/s). The second calibration period (#P2) is chosen when the recorded average wind speed is minimum (0,25 m/s). Considering the wind as the main excitation source for the Tower, the selected calibration periods represent two limit situations. Indeed, the boundary values for the selection of the inputs can be defined from the analysis of that periods. As shown in the previous sections the quality of the performed modal identification depends on several factors starting from the consistence of the unknown dynamic inputs. In Figure 4-LVIII and Figure 4-LIX are showed the results for both the calibration periods in terms of rms, average wind speed and SNR.

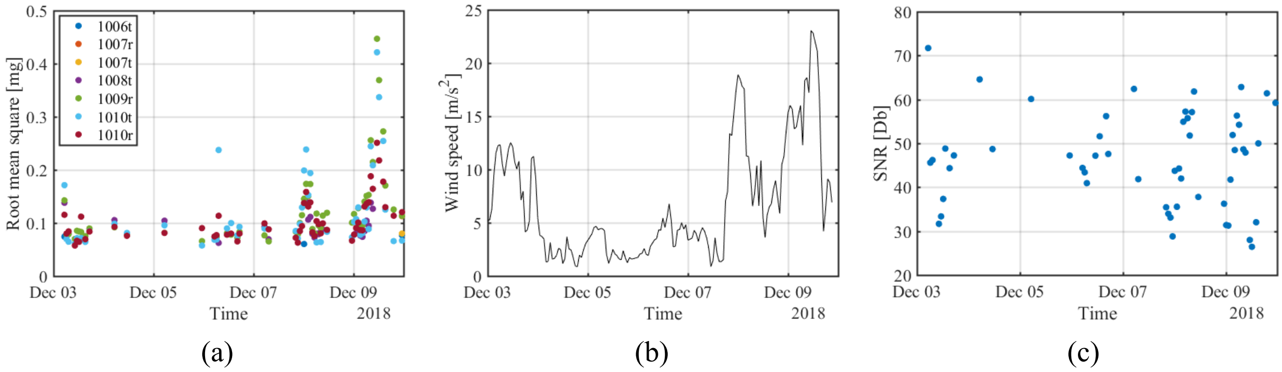

(a) (b) (c)

Figure 4-LVIII Calibration Period P1: (a) RMS (b) average wind speed (c) SNR the red lines represents the 25th percentile value

During the period P1 (Figure 4-LVIII) are recorded higher values of the RMS in the sensors at the last level; particularly the 1009r, 1010t and 1010r that seems to be directly stressed by the wind action. Unfortunately, the measurements at the level 0 are not available for a malfunctioning in the monitoring system. In the second period P2 when the wind speed reaches value at least equal to zero, the RMS recorded by the signals at the last level are three times lower than those measured in the period P1.

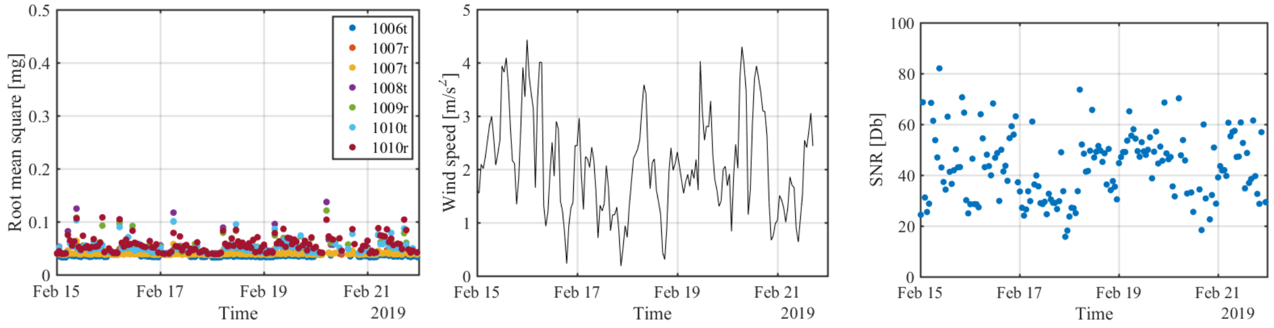

(a) (b) (c)

Figure 4-LIX Calibration Period P2: (a) RMS (b) average wind speed (c) SNR the red lines represents the 25th percentile value

As it was stated in the previous sections higher SNR values leads to more accurate identification of the modal parameters. Indeed, a lower bound is needed to exclude the signals that are dominated by the ground noise. On the other hand, it has been shown that higher values of the RMS and Kurtosis can arise from some electrical disturbances. At the same time a lower limit of the RMS should be fixed to reject signals without any physical content and also a threshold for the Kurtosis should be fixed to avoid twinkling signals (K=1,5 represents the pdf of a harmonic function).

From that considerations the system is calibrated to exclude the values outside the interquartile range.

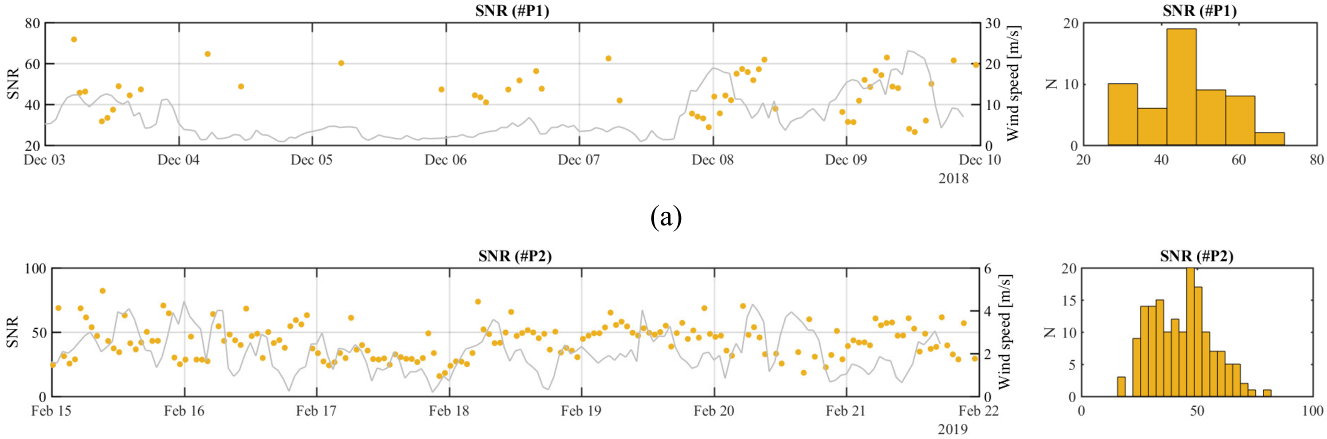

(a)

(b)

Figure 4-LX Histogram of the SNR values of each acquisition, for the P1 (a) and P2 (b).

Considering the two analysed periods as the boundary conditions in the operative range the thresholds are chosen to ensure the analysis of all the situation that stand between. For the sake of simplicity one threshold is fixed for all the signals, hence the minimum or maximum value of each interquartile range is selected.

Table 4-XV The thresholds of the input selection phase through the two calibration periods.

	SNR [dB]	**RMS [mg]**		**Kurtosis**	
		min	*max*	*min*	*max*
#P1	39,06	0,0063	0,14	3,28	8,58
#P2	34,72	0,0034	0,0063	2,99	3,73
Threshold	**34,72**	**0,0034**	**0,14**	**2,99**	**8,58**

The calibration phase gives also information about the settings in the system identification phase (number of block rows in the Henkel matrix, maximum model order) and it aids to understand the degree of complexity of the identified modes. That results are crucial to set the weighting parameters in the MQI (Figure 4-LXI) and to define a suitable threshold to exclude the non-physical or low excited modes.

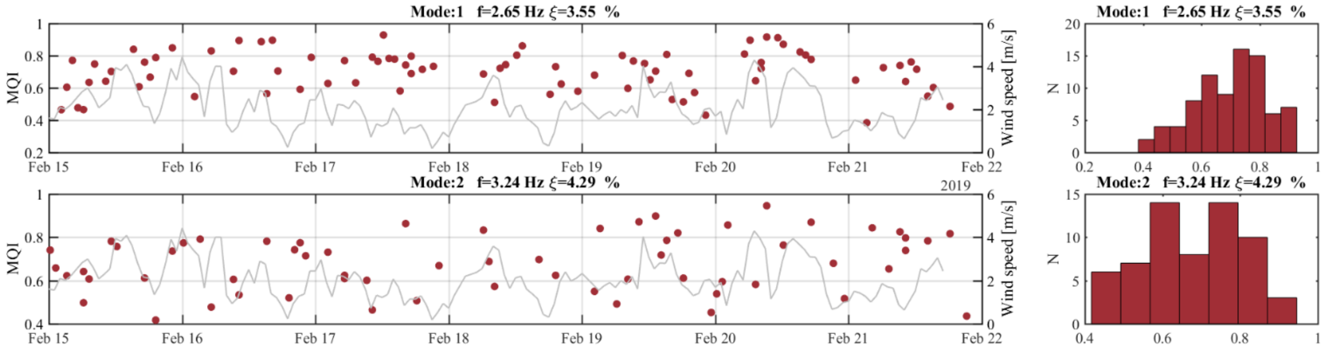

Figure 4-LXI The MQI for the first two modes in the calibration period #P2.

For instance, the frequency trend during the #P2 seems to be dependent on the temperature (Figure 4-LXII). Despite some outliers recorded during the night and the early mornings, that should be deepen with more accurate analysis.

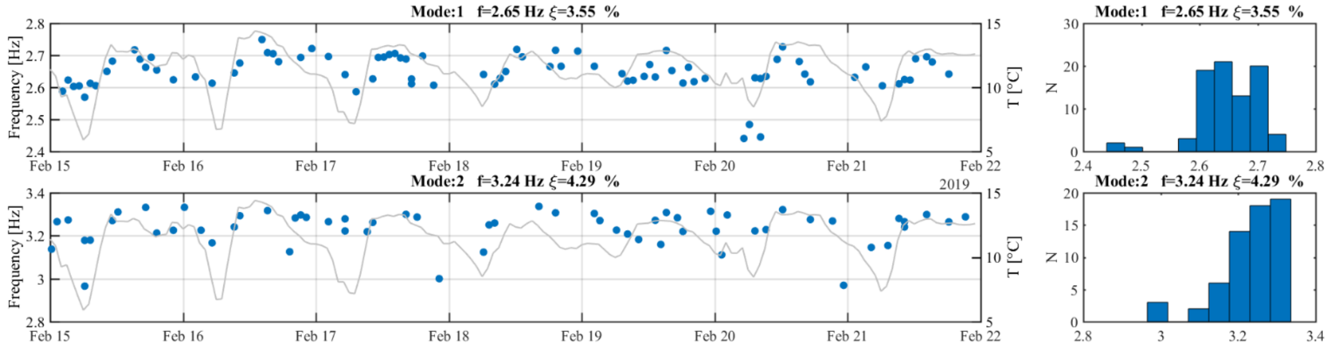

Figure 4-LXII The frequency values of the first two modes in the calibration period #P2.

The daily fluctuations in the damping ratio seems to be consistent but they correlation with temperature seems to be weaker.

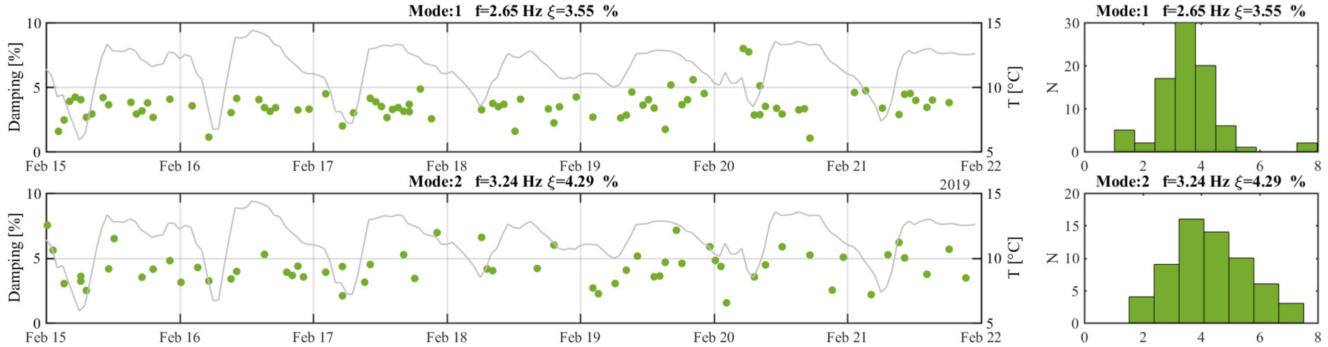

Figure 4-LXIII The damping values of the first two modes in the calibration period #P2.

Moreover, the analysis of the two calibration periods gives some information about the mode complexity that could depend on several factors [23]. Nonetheless, several authors have observed that the physical modes usually exhibit low value of complexity and have used both the MPD and the MPC as two strong indicators for distinguishing among the physical and spurious mode [12,13]. Thus, the analysis of the mode complexity in the two periods allows to set a proper weight coefficient (cfr. Section 4.3.4) for that parameters and a deeper investigation about the factors that paly the major role. Above all, the effects of the wind speed and the SNR in order to realize their influence on the established procedure for the long-term monitoring.

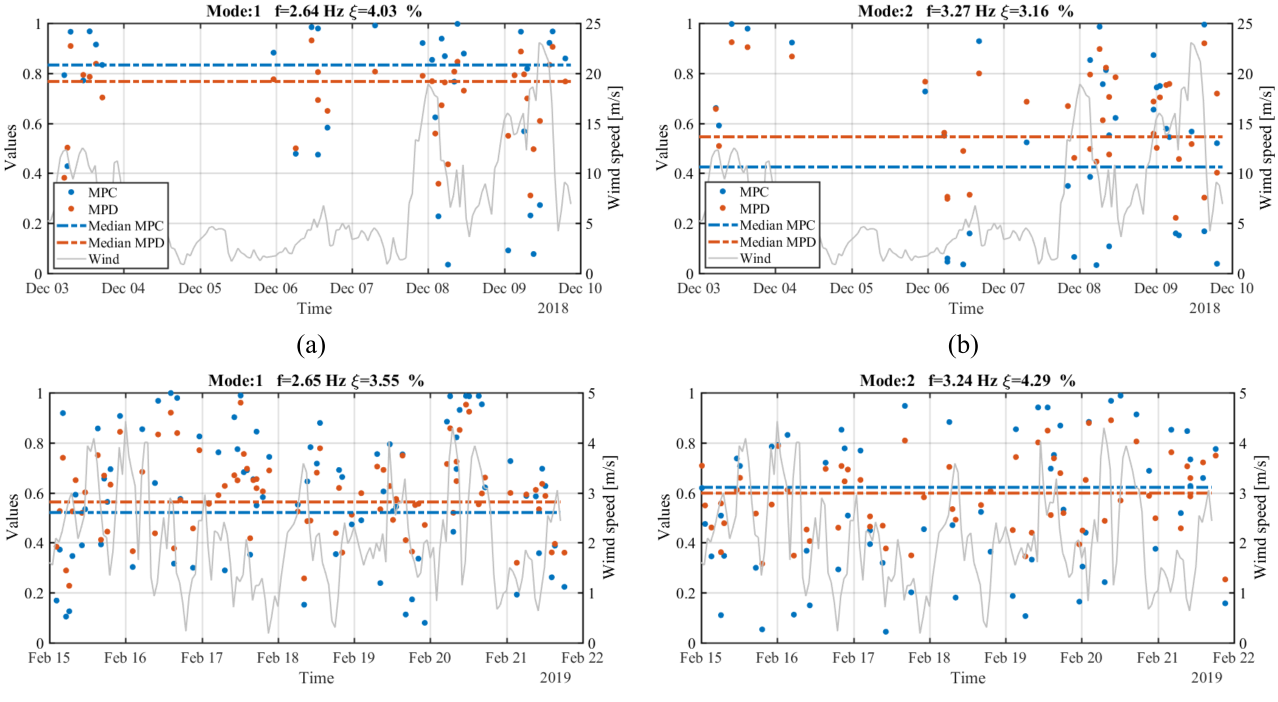

(a) (b)

(c) (d)

Figure 4-LXIV The MPD and the MPC for (a) the first mode identified in the #P1 (b) the second mode identified in the #P1 (c) the first mode identified in the #P2 (d) the second mode identified in the #P2.

At a first glance, it is clear that the MPC are more scattered than the MPD, but the median values are very close except for the second mode in the period #P1. In addition, when the mean wind speed reaches the highest peaks the degree of complexity of the first and particularly of the second mode increases. Consequently, a certain degree of complexity seems to arise from the interaction between the wind and the structure especially for the second mode.

In absence of wind (e.g. #P2) the level of complexity behaves like a random variable for the first and second modes. Thus, the median values of the distribution reach approximatively the same median values (approximatively 0,6). As a result, this value is quite less than the values obtained for the case of study presented before. That fact can be explained from the level of ground noise that is not minimized with a sampling frequency of 50 Hz and partially with the interaction with the wind for very high wind speed. Therefore, it is confirmed that is useless to fix defined threshold that can exclude some important information about the structural dynamics.

Table 4-XVI The median values of the MPC and MPD for the calibration periods and the first quartile value for the MQI, the thresholds have been selected with the same criterion introduced before.

	1st Mode			2nd Mode			3rd Mode		
	MPC	*MPD*	*MQI*	*MPC*	*MPD*	*MQI*	*MPC*	*MPD*	*MQI*
#P1	0,83	0,76	0,68	0,42	0,54	0,57	0,84	0,80	0,62
#P2	0,58	0,57	0,68	0,62	0,60	0,71	-	-	-
Threshold		**0,68**			**0,57**			**0,62**	

The minimum of the first quartile value (Table 4-XV) calculated for each mode along the calibration periods, has been chosen as a filter on the extracted parameters to improve the results of the automated procedure for the feature extraction in the long-term monitoring system.

4.4.2 Modal tracking

Once the results of the modal identification are available it is possible to track the modes through a hierarchical clustering algorithm. At the beginning, each identified mode is a seed then the elements that stands behind a threshold are joined for forming a cluster. The considered thresholds are two:

- Frequency relative distance
- Mode shape distance $\left(\Delta\phi_{ij} = 1 - MAC_{ij}\right)$

Starting from the assumption that the considered calibration periods are just one week, the seasonal fluctuations of the environmental effects can be neglected. The distances limits are fixed and are the 5% in terms of frequency (considering the daily fluctuations) and 0,3 in terms of mode shapes (Table 4-XII)From the analysis of the statistical properties of each cluster it is possible to define the MT thresholds for each mode based on the results obtained under extreme operative conditions.

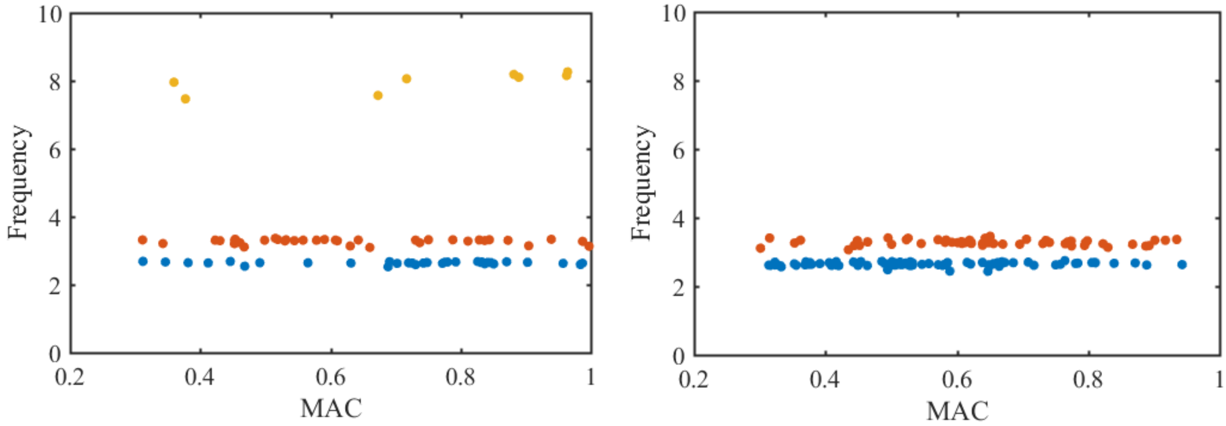

(a) (b)

Figure 4-LXV The MAC values for the identified mode shapes in the two calibration periods: (a)# P1 and (b) #P2.

During the period #P1 three modes are identified with higher MAC values (Figure 4-LXV). Instead during the period #P2 only the first two modes can be identified in the major part of the records. They exhibit lower MAC values confirming that is more difficult to match the same mode if the vibration level is very low (Figure 4-LXV).

Consequently, the thresholds for tracking the modes should be carefully selected to avoid the loss of information. Therefore, it seems that the mode shapes are sensitive to the excitation level, increasing their level of complexity.

Table 4-XVII The thresholds of the MAC values.

	1st Mode	**2nd Mode**	**3rd Mode**
#P1	0,84	0,80	0,95
#P2	0,78	0,79	-
Threshold	**0,78**	**0,79**	**0,95**

Moreover, the reference mode shapes value are chosen for each candidate mode selecting the higher MQI among every identification. That is needed because of the slightly different sensor positions between the preliminary dynamic test and the permanent long-term monitoring system. Indeed, for each mode has been chosen as reference values for the modal tracking those identified in different sessions exhibiting the highest value of the MQI (Table 4-XVIII).

Table 4-XVIII The reference sessions of three modes and their MQI.

	Reference MQI		
Date	*1st Mode*	*2nd Mode*	*3rd Mode*
14/06/2019 08:15	0,945	0,690	-
31/05/2019 16:15	0,875	0,965	0,870
02/10/2018 23:15	-	-	0,954

4.4.3 Correlation analysis

The correlation analysis of the modal properties with the environmental parameters is a crucial step in the damage assessment. Many Authors [19–21,24,25] underline how the temperature plays an important role modifying the frequency of the CH buildings. This phenomenon is related to the thermal expansion of the masonry blocks that close the microcracks in the mortar layers generating a stiffening on the masonry panels. For increasing temperature above the 0° C this effect is almost linear even though for the higher modes the correlations coefficients are usually below 0,5 [19,21] that can depend on some non-linear correlation among the data [20].

Below the 0°C in the freezing conditions, the linear effect is inverted with an increase of the frequency when the temperature goes down [19]. This phenomenon depends on the ice formation of the absorbed water leading to a rapid increase of the natural frequencies [18–20].

Some linear correlation effects between frequency and humidity have been found in [25] during strong rain events due to the absorption of water by the walls that leads to a slight decrease of the frequencies. But this effect was not detected in other cases of study proposed by the authors in the recent years. The correlation with the wind speed is not investigated for the CH buildings and only in [24] is highlighted a decrease of the frequencies in high wind speed condition.

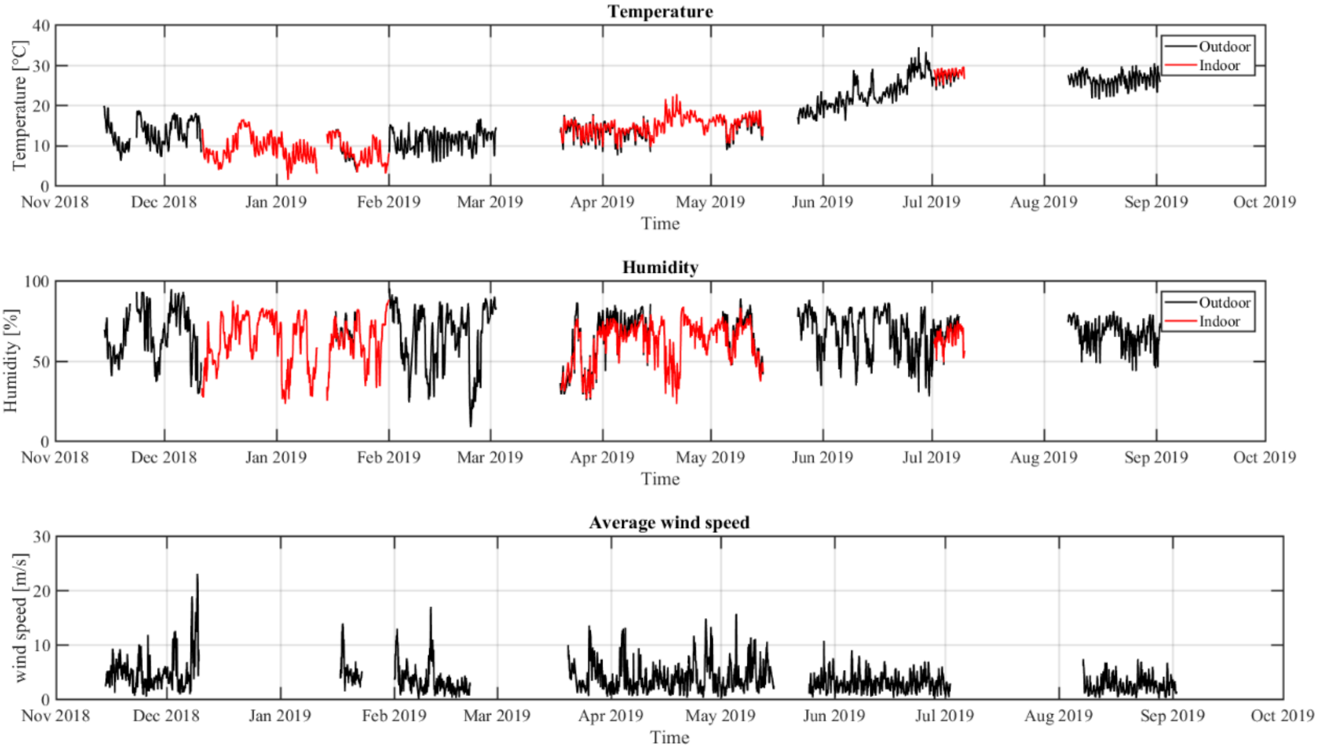

Figure 4-LXVI Changing of the environmental effects during the long-term monitoring period of the Tower Matilde.

The results of the first nine months of long-term monitoring are presented herein, tracking the identified natural frequencies for each mode. Considering some offline periods both of some sensor a minimum number of active channels to perform the analysis is selected. In that case a minimum number equal to 3 sensors is selected to perform the analysis. That variable number depending on the functioning of the whole system leads to add some adjustment both in terms of the calibration in the system identification both in the modal tracking. Therefore, the algorithm processes the distances in terms of mode shapes only in the common active channels during the MT.

The results of the proposed procedure are shown in Figure 4-LXVII where three modes of the tower have been tracked along the first nine months of monitoring.

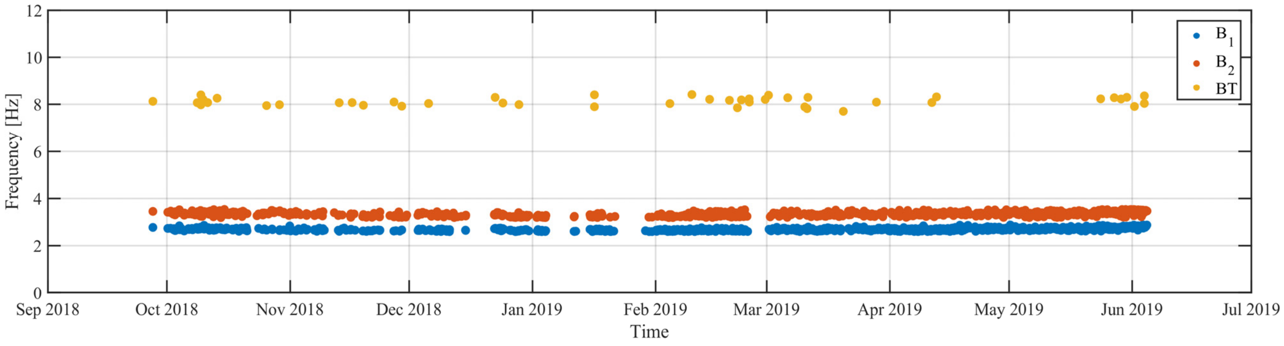

Figure 4-LXVII The Modal Tracking of the first nine months of long-term monitoring.

Once the identified modes are grouped in homogeneous clusters representing the structural modes tracked during the monitoring period, the correlation with the measured environmental parameters has been deepened.

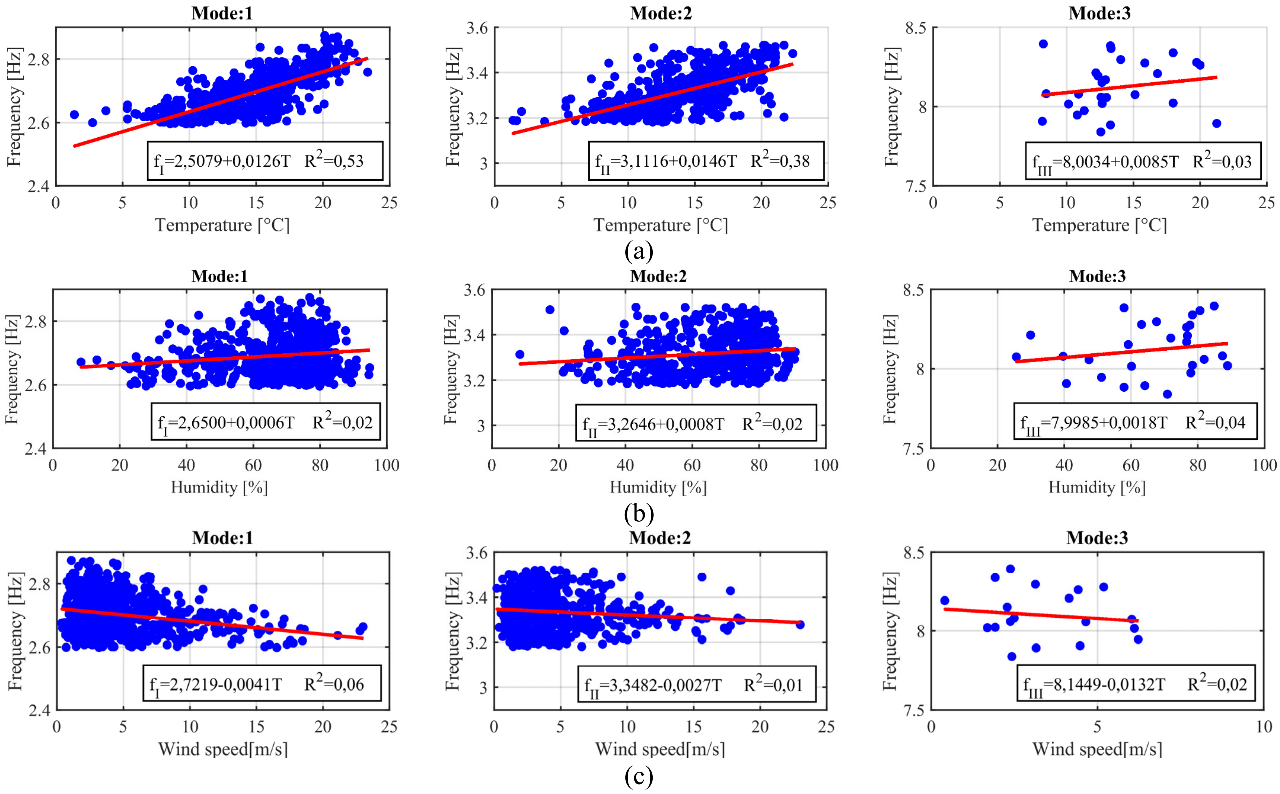

Figure 4-LXVIII The correlation of the tracked modes with the measured environmental parameters; (a) Temperature (b) Humidity (c) Wind speed

The number of tracked value for the first two identified modes is comparable (1170 for the first mode, 923 for the second mode), while the third one can be identified only on a limited number of session (46). This can be attributable to the higher level of energy needed to excite that mode.

Although a year of data has not yet been collected, some preliminary observations can still be done: the first two modes clearly exhibit an increase of the frequency with the temperature (Figure 4-LXVIII), while for the third mode the positive correlation is not so evident. The latter can be attributable to the current dataset that cannot still allow to establish the nature of the correlation.

4.5 Discussion of the results

The benefits adduced by the input selection and their effects have been just introduced in the previous sections for the CH buildings identified in a single dynamic test campaign. In order to check the effects for the introduced automatic procedure the minimum and maximum values recorded during the two calibration periods are fully analysed.

For instance, the records which exhibit the higher values of the Kurtosis during the #P1 (Figure 4-LXIX) can lead to satisfying results in the modal identification (Figure 4-LXX). Thus, the SNR and the RMS plays a more relevant role in the identification of the modal parameters.

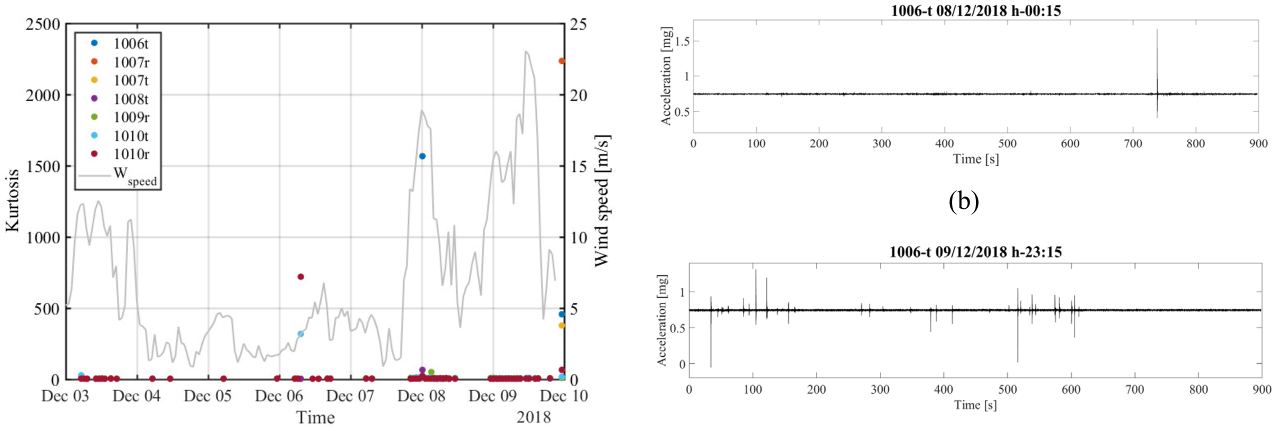

(b)

(a) (c)

Figure 4-LXIX (a) Kurtosis plot during the period #P1 (b) (c) the records corresponding to high Kurtosis values.

In Figure 4-LXX (a) it is possible to see the clear peaks relative to the first two modes and some other cluster around 5 Hz. Nonetheless, during the sessions with the highest Kurtosis (Figure 4-LXX (b)) exhibits one clear peak in the second mode, but the first mode is hidden by the noise level.

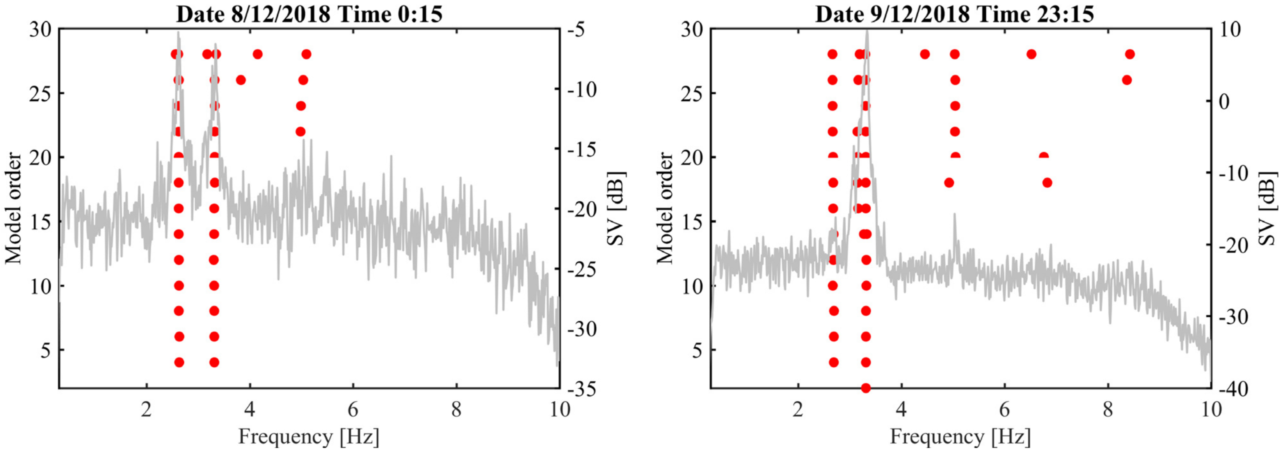

(a) (b)

Figure 4-LXX The Stabilization charts of the acquisition with the highest Kurtosis recorded during #P1 (a) 8/12/2018 0:15 (b) 9/12/2018 23:15

In both cases the SNR is quite good, so the modal identification gives adequate results and a clear stabilization chart can be obtained. As well as the SNR, the RMS (Table 4-XIX) reach values that can be considered satisfactory (for instance 10 times higher than the minimum value reached during the #P2).

Table 4-XIX The average properties of the signals exhibiting the highest Kurtosis.

Session	RMS [mg]	SNR [dB]	Kurtosis
8/12/2018 0:15	$1{,}356 \cdot 10^{-1}$	43	335
9/12/2018 23:15	$9{,}512 \cdot 10^{-2}$	59	527

While the Kurtosis value is out of the fixed range, the automated procedure presented herein, for the two sessions (Table 4-XX and Table 4-XXI) allows the identification of the first two modes with high MQI, approaching to the maximum values of elements for each cluster.

Table 4-XX The results of the modal identification in the session of the 8th of December 2018 at the 0:15.

Date 8/12/2018 Time 0:15						
Mode n°	*f_n [Hz]*	*ξ_n [%]*	*MPC*	*MPD*	*MQI*	*N_{cl}*
1	2,622	3,461	0,795	0,837	0,855	13
2	3,315	4,186	0,798	0,914	0,875	13

Table 4-XXI The results of the modal identification in the session of the 9th of December 2018 at the 23:15.

Date 9/12/2018 Time 23:15						
Mode n°	*f_n [Hz]*	*ξ_n [%]*	*MPC*	*MPD*	*MQI*	*N_{cl}*
1	2,671	4,849	0,439	0,351	0,607	10
2	3,159	1,778	0,792	0,880	0,767	6
3	3,310	1,396	0,835	0,950	0,883	14
4	5,040	1,973	0,516	0,360	0,572	5

However, the selection of the input based on the SNR and RMS values are is necessary to avoid the identification of low-quality modes and to speed up the whole procedure. Thus, two sessions exhibiting low value of SNR and RMS have been analysed from the calibration period #P2 (Table 4-XXII).

Table 4-XXII Lower SNR and RMS recorded in the period #P2

Session	**RMS [mg]**	**SNR [dB]**	**Kurtosis**
17/02/2019 22:15	$3{,}850\cdot 10^{-2}$	16	2,98
17/02/2019 23:15	$3{,}840\cdot 10^{-2}$	18	3,01

The stabilization chart plots in Figure 4-LXXI confirms that the information available are dominated by the noise level and the obtained results should be rejected.

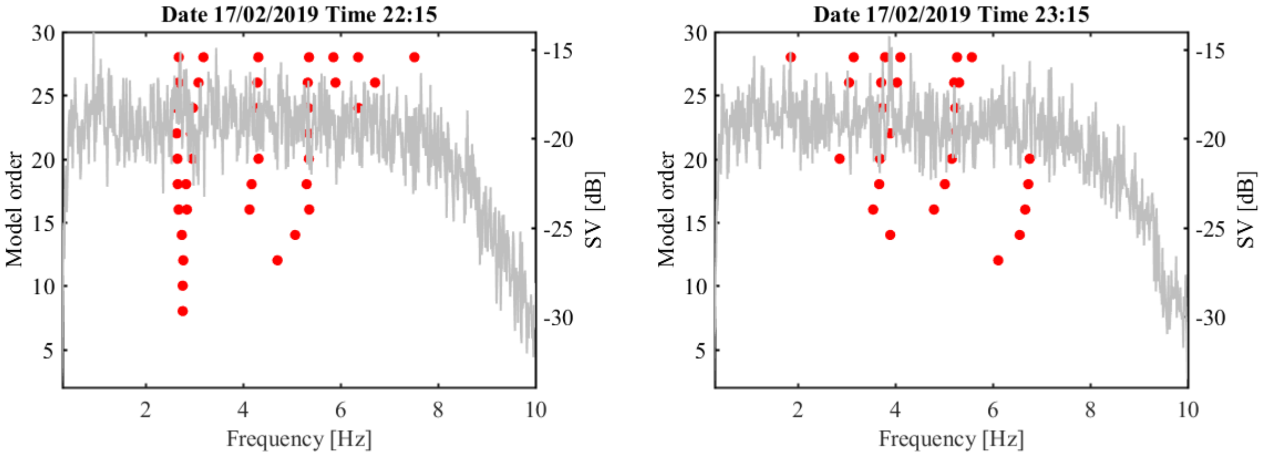

(a) (b)

Figure 4-LXXI The stabilization charts obtained for the lower SNR and RMS: (a) 17/02/2019 22:15 (b) 17/02/2019 23:15.

That fact has been confirmed by all the indicators dealing with the input quality (SNR,RMS) but the MQI values well behave in the first case (Table 4-XX), while for the second case (Table 4-XXIV) a possible false positive in the fourth mode can be detected.

Table 4-XXIII The results of the modal identification in the session of the 17th of February 2019 at the 23:15.

Date 17/02/2019 Time 23:15						
Mode n°	f_n *[Hz]*	ξ_n *[%]*	*MPC*	*MPD*	*MQI*	N_{cl}
1	3,725	4,765	0,469	0,527	0,601	7
2	4,995	4,824	0,630	0,555	0,604	11

Table 4-XXIV The results of the modal identification in the session of the 17th of February 2019 at the 22:15.

Date 17/02/2018 Time 22:15						
Mode n°	f_n *[Hz]*	ξ_n *[%]*	*MPC*	*MPD*	*MQI*	N_{cl}
1	2,664	4,257	0,391	0,560	0,646	6
2	3,000	6,949	0,582	0,454	0,669	6
3	4,288	3,009	0,368	0,243	0,514	6
4	5,244	2,929	0,701	0,819	0,721	9

Anyway, the MQI indicator seems to work well to identify some forced response due to harmonic components. For instance, the identified session of the 13th of October 2018 satisfies all the requirements in terms of signals properties (Figure 4-LXXII (b)) but some clear narrow bands process in the frequency band from 2-3 Hz are clearly visible (Figure 4-LXXII (a)).

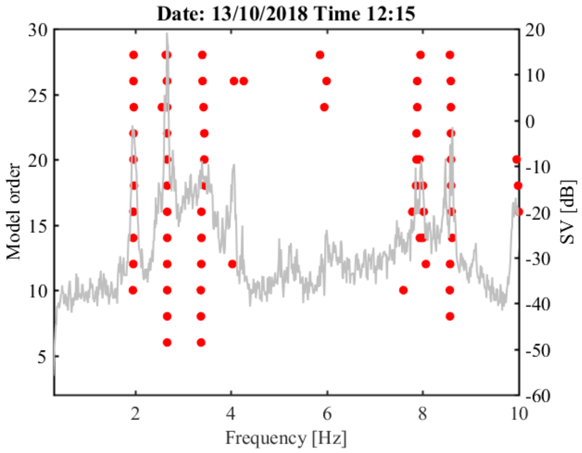

Session	**RMS [mg]**	**SNR [dB]**	**Kurtosis**
13/10/2018 12:15	$1{,}003 \cdot 10^{-1}$	72	3,76

(a) (b)

Figure 4-LXXII (a) The stabilization charts obtained in the 13/10/2018 and (b) The input signals properties for the session.

In that case the MQI values have been able to detect that processes even if they are close to a resonant frequency exhibiting very low values (Table 4-XXV).

Table 4-XXV The results of the modal identification in the session of the 13th of October 2018 at the 12:15.

Date 13/10/2018 Time 12:15						
Mode n°	f_n *[Hz]*	ξ_n *[%]*	*MPC*	*MPD*	*MQI*	N_{cl}
1	1,963	0,866	0,537	0,402	0,469	10
2	2,667	0,647	0,456	0,366	0,411	12
3	3,401	6,519	0,762	0,719	0,741	12
4	8,583	1,066	0,427	0,497	0,462	11

4.6 Conclusions

Some preliminary conclusions on the application of the proposed procedure to real cases of study can be drawn. For instance, the whole procedure aims to reach the following purposes:

- Define a fully automated procedure limiting the arbitrary tuning parameters
- Control the results of every step to reduce the variance of the MP

The first point has been tackled with the introduction of a smart algorithm capable to learn from the processed data. Selecting a small calibration period, it is possible to observe the structural dynamics under operative conditions obtaining some feedback on the adopted choices. Furthermore, as it is shown in the previous sections the parameters can be adjusted to fit with the structural dynamics of the monitored structure.

The second point is achieved firstly by the control of the whole process, starting from the input signals until the labelling of the extracted MP with a quality index. On the top of all that, a proper calibration of the weighting coefficients should be done to obtain more reliable information about the structure dynamics.

The procedure allows also a proper calibration of the modal tracking phase that in many cases has not been considered by the authors, but as it was shown previously can be very important to avoid misleading results. Along with all these operations introduced in the previous sections, it has been defined a method to fill the lack of information due to some malfunctioning in the system, that can be very frequent in the case of open structures subjected to harsh environmental conditions.

Despite that results some drawbacks should be underlined:

- The setup operation in the system identification phase should be done for each acquisition
- The reduction of the model bias could not be enough to perform a suitable reduction of the MP variance
- There are still some parameters that should be carefully set, and a judicious approach is needed
- The correlation with the environmental effects and the cleansing technique should be carefully selected

4.7 References

[1] E. Reynders, R. Pintelon, G. De Roeck, Uncertainty bounds on modal parameters obtained from stochastic subspace identification, Mech. Syst. Signal Process. 22 (2008) 948–969.

[2] S. Qin, J. Kang, Q. Wang, Operational Modal Analysis Based on Subspace Algorithm with an Improved Stabilization Diagram Method, Shock Vib. (2016).

[3] J.M.W. Brownjohn, F. Magalhaes, E. Caetano, A. Cunha, Ambient vibration re-testing and operational

modal analysis of the Humber Bridge, Eng. Struct. 32 (2010) 2003–2018.

[4] C. Rainieri, G. Fabbrocino, Influence of model order and number of block rows on accuracy and precision of modal parameter estimates in stochastic subspace identification, Int. J. Lifecycle Perform. Eng. 1 (2014) 317.

[5] B. Peeters, G. De Roeck, Reference-based stochastic subspace identification for output-only modal analysis, Mech. Syst. Signal Process. 13 (1999) 855–878.

[6] F. Magalhães, Á. Cunha, E. Caetano, Online automatic identification of the modal parameters of a long span arch bridge, Mech. Syst. Signal Process. 23 (2009) 316–329.

[7] F. Ubertini, C. Gentile, A.L. Materazzi, Automated modal identification in operational conditions and its application to bridges, Eng. Struct. 46 (2013) 264–278.

[8] B. Peeters, System Identification and Damage Detection in Civil Engineering, KU Leuven, 2000.

[9] M. Döhler, F. Hille, L. Mevel, W. Rücker, Structural health monitoring with statistical methods during progressive damage test of S101 Bridge, Eng. Struct. 69 (2014) 183–193.

[10] R. Pintelon, P. Guillaume, J. Schoukens, Uncertainty calculation in (operational) modal analysis, Mech. Syst. Signal Process. 21 (2007) 2359–2373.

[11] C. Rainieri, G. Fabbrocino, Development and validation of an automated operational modal analysis algorithm for vibration-based monitoring and tensile load estimation, Mech. Syst. Signal Process. 60 (2015) 512–534.

[12] A. Cabboi, F. Magalhães, C. Gentile, Á. Cunha, Automated modal identification and tracking: Application to an iron arch bridge, Struct. Control Heal. Monit. 24 (2017).

[13] E. Reynders, J. Houbrechts, G. De Roeck, Fully automated (operational) modal analysis, Mech. Syst. Signal Process. 29 (2012) 228–250.

[14] R.S. Pappa, K.B. Elliott, A. Schenk, Consistent-mode indicator for the eigensystem realization algorithm, J. Guid. Control. Dyn. 16 (1993) 852–858.

[15] R. Brincker, C.E. Ventura, Introduction to Operational Modal Analysis, 2015.

[16] A. Zucchini, P.B. Lourenço, A micro-mechanical model for the homogenisation of masonry, Int. J. Solids Struct. 39 (2002) 3233–3255.

[17] L.F. Lourenco, Paulo B and Ramos, Dynamic Identification and Monitoring of Cultural Heritage Buildings, (2011) 55–78.

[18] C. Gentile, M. Guidobaldi, A. Saisi, One-year dynamic monitoring of a historic tower: damage detection under changing environment, Meccanica. 51 (2016) 2873–2889.

[19] F. Ubertini, G. Comanducci, N. Cavalagli, A. Laura Pisello, A. Luigi Materazzi, F. Cotana, Environmental effects on natural frequencies of the San Pietro bell tower in Perugia, Italy, and their removal for structural performance assessment, Mech. Syst. Signal Process. 82 (2017) 307–322.

[20] A. Kita, N. Cavalagli, F. Ubertini, Temperature effects on static and dynamic behavior of Consoli Palace in Gubbio, Italy, Mech. Syst. Signal Process. 120 (2019) 180–202.

[21] R.M. Azzara, G. De Roeck, M. Girardi, C. Padovani, D. Pellegrini, E. Reynders, The influence of

environmental parameters on the dynamic behaviour of the San Frediano bell tower in Lucca, Eng. Struct. 156 (2018) 175–187.

[22] P. Barsocchi, P. Cassara, F. Mavilia, D. Pellegrini, Sensing a City's State of Health: Structural Monitoring System by Internet-of-Things Wireless Sensing Devices, IEEE Consum. Electron. Mag. 7 (2018) 22–31.

[23] M. Imregun, D.J. Ewins, Complex modes-origins and limits, Proc. 13th Int. Modal Anal. Conf. (1995) 496–506.

[24] R. Cantieni, One-Year Monitoring of a Historic Bell Tower, Key Eng. Mater. 628 (2014) 73–78.

[25] L.F. Ramos, L. Marques, P.B. Lourenço, G. De Roeck, A. Campos-Costa, J. Roque, Monitoring historical masonry structures with operational modal analysis: Two case studies, Mech. Syst. Signal Process. 24 (2010) 1291–1305.

Chapter 5

Damage Simulations

5.1 Introduction-5.2 Global damage mechanisms-5.3 Local damage mechanisms-5.4 Numerical analysis of a simplified model-5.5 Numerical analysis of a 3-D model -5.6 Discussion of the results- 5.7 Conclusive Remarks

5.1 Introduction

This chapter aims to investigate the damage occurred to the CH buildings during strong earthquake motions. In *Section 5.2* the global damage mechanisms are investigating focusing on the old masonry towers that are a very common kind of structure in all the EU countries. From the survey of the data available in literature is confirmed that the towers are very sensitive to damages, especially in the urban aggregate (Figure 5-I). In *Section 5.3* a brief overview of the local damage mechanisms occurred during the earthquakes are cited. In conclusion, the global damage mechanisms involving the main body of the tower are considered to analyse the performances of the adopted procedure for the damage detection. Then a simplified numerical model representing a bounded masonry tower is defined (*Section 5.4*). The results of that preliminary analysis give the indications about the quantities that should be measured to identify and assess the damage.

Hence a more refined 3-D model of a historic masonry tower is introduced in *Section 5.5* and the capability to detect and even localize a simulated pattern damage is evaluated. Finally, the results of the numerical analysis are discussed in *Section 5.6* and some conclusion about the introduced SHM framework are drawn in *Section 5.7*.

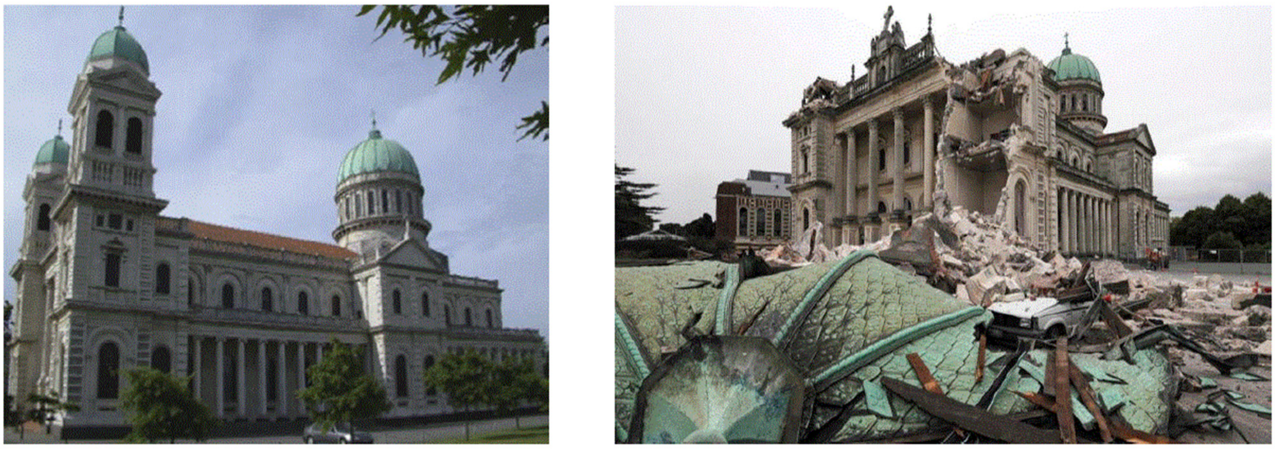

Figure 5-I The failure of the Christchurch cathedral after the Canterbury earthquake in the 2011 (*courtesy of A. Preciado*).

5.2 Global damage mechanisms

The global damage on masonry structures is represented by the total collapse of the structure due to the high tensile stress reached in the masonry walls. In addition, the CH buildings can be represented as an aggregate of blocks with a high compressive strength, but with a near zero tensile resistance of the mortar joints. That approximation is called “no-tension” model for the masonry [1] and the bearing capacity of the structures can be obtained with simple equilibrium equations.

Depending on the slenderness of the analysed structure the collapse can be obtained with a flexural or a shear mechanism. The distribution of the openings and the effect of the adjacent buildings [2] plays also an important role in the possible global damage mechanism. Moreover, the manufacturing properties of the walls and the presence of some change in the stiffness distribution can be some very important aspects that can lead to a specific collapse mechanism [3].

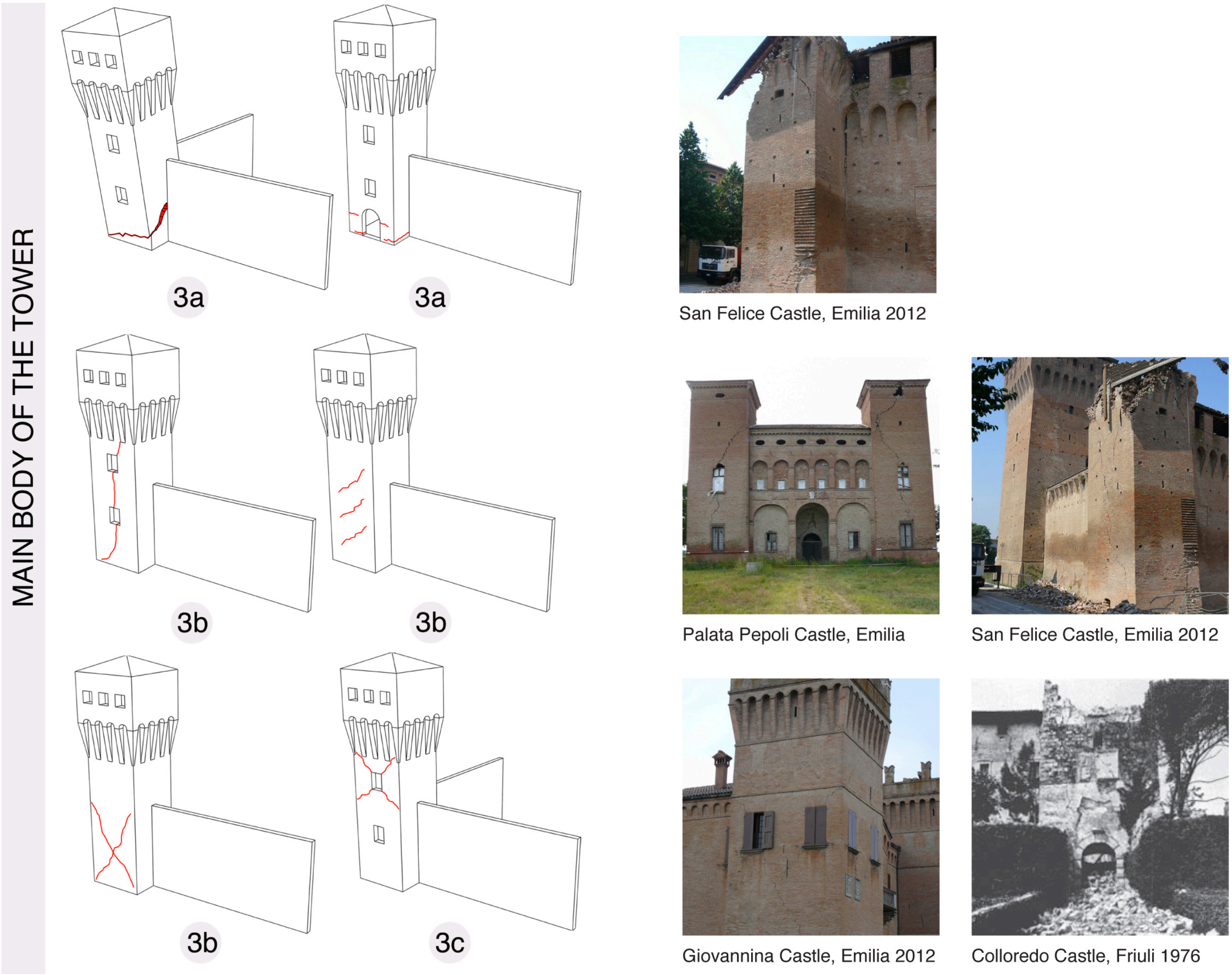

San Felice Castle, Emilia 2012

Palata Pepoli Castle, Emilia

San Felice Castle, Emilia 2012

Giovannina Castle, Emilia 2012

Colloredo Castle, Friuli 1976

Figure 5-II Global failure mechanism of the confined towers identified by Ferretti [4] through a survey of the post-earthquake damages on the historic castles in Italy.

Ferretti [4] identifies three global failure mechanism for the towers of the castles (Figure 5-II), analysing the earthquake of the last fifty years that occurred in Italy:

- Damage at the base of the tower, due to combined compressive and bending cracks or to soft storey (3a);
- Shear cracks in the main body of the tower (3b), with possible torsional effects if the tower is asymmetrically connected to the walls;
- Shear cracks in the upper part of the tower (3c), standing out from the fortress or walls;

Among all the failure mechanism analysed the ones involving the main body of the tower (group 3) are the most probable in all the analysed castles (Figure 5-II). The others representative mechanisms are the group 7 regarding the local failure of wooden floors or vaults and the category 4b involving the overturning of the merlons and the group 2c about the overturning of the perimetral walls. Then the sum of all the other mechanisms represent almost the fifty percent of the possible failure modes.

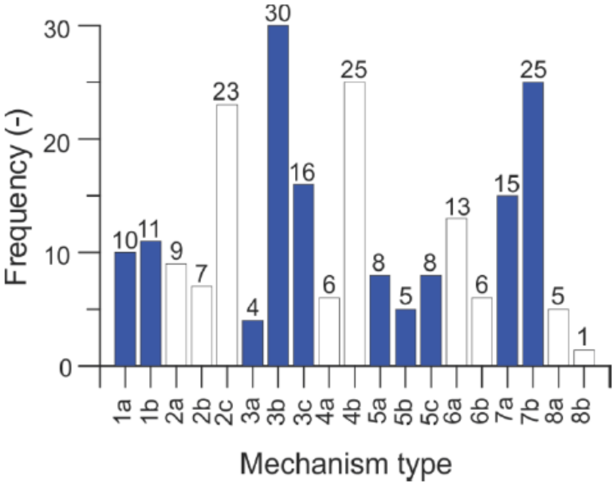

Figure 5-III Frequency of the global mechanism failures revealed in the study of Ferretti [4].

Hence the masonry tower is one of the weakest structural system in the masonry fortress. At the same time this typology is widespread in all the old towns and is usually bounded by other buildings built in different stages. Furthermore, the other local mechanism that are representative in the case of the masonry fortresses, but they cannot be faced in every masonry tower.

5.3 Local damage mechanisms

The local damage mechanisms regard the collapse of some structural parts that are not well connected to the others or presents some weak resistant mechanism. In [3] a complete review of all the possible local mechanisms that can be activated by the ground shaking. The acceleration that leads to the activation of a possible local failure can be easily found by the equilibrium conditions of different chains of rigid blocks. The hinge number and positions depend on the investigated mechanism. As a result, the different local failures depend structure by structure. For instance, masonry structures with arches, vaults or roofs with inclined beams that generate a consistent thrust are prone to the overturning of the façades or of the corners.

Despite the high number of local collapses in the old masonry houses [5] during the earthquakes, the CH structures (in particular the masonry towers) seems to be less sensitive to this failure (Figure 5-II). According to [4], the damage due to the local collapses that involve the structural part of the old masonry towers are the classes 4b, 5b, 6a, 6b that are about the 50 % of the total collapses. But the group 4b representing the 50% of the local collapses is the overturning of the merlons that is not common to the all existing masonry towers. In [6] is showed that the cusp and the belfry are structural parts that can be damaged severely during the earthquakes. As a result in all the old masonry bell-towers that part should be investigated and in some cases the cracks due to damages are still not visible after the earthquakes [7].

In conclusion, it is not possible to identify which are all the kind of collapses that can occur during strong ground motions. As it was underlined from the beginning of this thesis the masonry structures especially the CH buildings should be observed case by case. Despite the lack of generality, the global collapses of the towers due to shear or bending stresses (3a, 3b, 3c in Figure 5-III) seems to be common to a wide typology of existing masonry towers.

5.4 Numerical analysis of a simplified model

In this section are analysed the damage indices proposed in the last years for each of the damage sensitive properties. The analyses are performed on a simplified FE models of a cantilever beam bounded by elastic restraints. As was stated in the previous sections this is one of the most common situations of the old masonry towers.

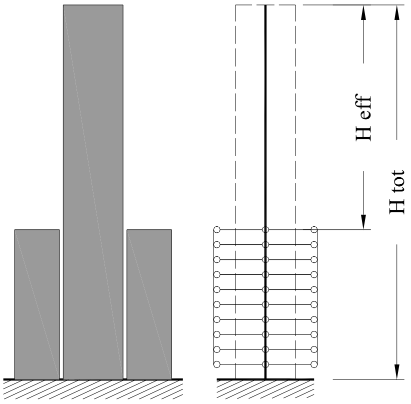

Figure 5-IV Structural scheme of the bounded masonry tower.

Figure 5-V The bounded masonry examples in the city centre of San Gimignano (SI).

The whole methodology aims to simulate a possible damage scenario after a seismic event, investigated how it is possible detect or even localize and quantify the damage (respectively Level 1, Level 2, Level 3 in the *Rytter's scale*). Finally, the capability of detecting the damage is investigated with a limited number of measures available. Both considering the classical translational components of the mode shapes that can be derived by the accelerometer records or the strain that might be measured through fibre optic sensors [8]. Clearly that simulation will not consider the environmental effects that can be correlated with the dynamic properties of the system. Anyway, it is fundamental that preliminary step to realize if the dynamic features without any source of external noise can be capable of detect a seismic induced damage on a no tension masonry model.

To fix the ideas that preliminary investigation can be subdivided in four stages (Figure 5-VI):

- Damage Simulation
- Damage identification
- Sensor grid influence
- Sensor position and influence

Each of that phase will be explained in the next paragraphs

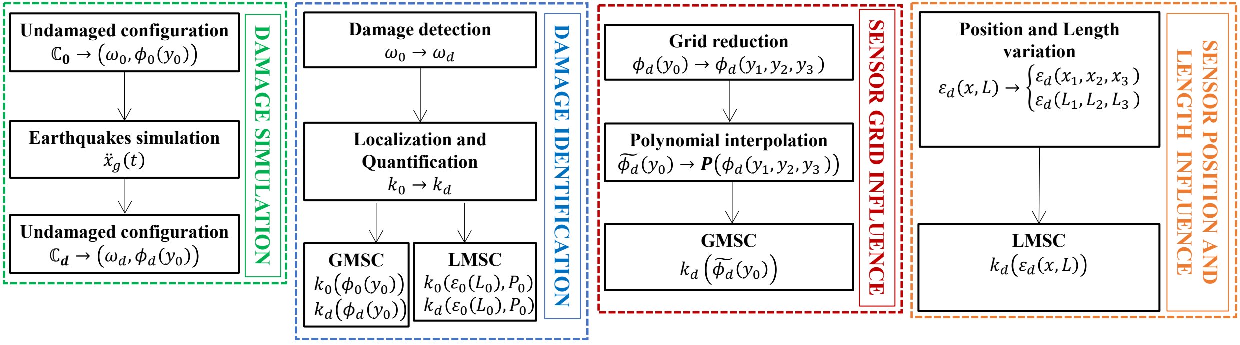

Figure 5-VI The preliminary numerical analysis flow chart.

5.4.1 FE model

The cases of study are cantilever restrained with translational springs, having different total heights and a square base 9.5 m x 9.5 m. All the models are developed with the FE software MADY [9] [10] elements with the nodes spaced of a distance between 1 and 0,5 m, using a Euler-Bernoulli beam where a standard nonlocal averaging approach has been used in the damage procedure, to avoid mesh sensitivity and convergence to incorrect solutions.. The numerical models have respectively 50, 60 and 70 nodes along the height for the T2, T5 and T8 models. The mass is constant along the height with a density of 1800 Kg/m^3 and the damping ratio is fixed at the 2%.

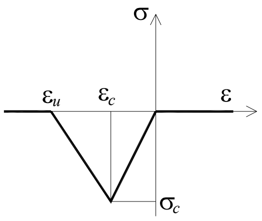

Figure 5-VII Masonry behaviour under uniaxial stress state.

Table 5-I The geometrical and material properties of the analysed models.

Numerical models properties			
#Model	**T2**	**T5**	**T8**
Base (B [m])	9,5	9,5	9,5
Total height (H_{tot} [m])	40	50	60
Effective height (H_{eff} [m])	20	30	40
Limit compressive strength ($\boldsymbol{\sigma_c}$ [MPa])	5	5	5
Young's elastic modulus (E [MPa])	3000	3000	3000
Strain Ductility ($\boldsymbol{\mu_\varepsilon}$)	3	3	3

The material's behaviour is described by non-linear constitutive equations, which assumes masonry to have null tensile strength and limited compressive strength (Table 5-I) [11]. According to the assumed behavior, a damage function has been determined to define the constitutive law for the beam section [12], where damage is represented by a reduction of the initial mechanical properties (Young's elastic modulus and compressive strength). The limit value of the compressive deformability ε_u, has been chosen to have a strain ductility $\mu_\varepsilon = \varepsilon_u / \varepsilon_c = 3$ (Figure 5-VII).

A procedure for solving the eigenvalues problem at each step of a loading process has been introduced into the code. When the structure behaves elastically, the modal properties can be found through the equation:

$$\phi_n[\boldsymbol{K} - \omega_n^2 \boldsymbol{M}] = 0 \tag{1}$$

Where ϕ_n is the n-th mode shape and ω_n is the natural circular frequency of vibration that is related with the natural frequency of vibration f_n dividing for 2π.

Conversely, when the structure undergoes a nonlinear behavior, i.e. cracking and/or crushing, the equation that provides the modal properties (of the nonlinear model) is:

$$\widetilde{\phi_n}[\widetilde{\boldsymbol{K}} - \widetilde{\omega_n^2} \boldsymbol{M}] = 0 \tag{2}$$

Where $\widetilde{\phi_n}$ is the n-th mode shape and $\widetilde{\omega_n}$ is the natural circular frequency and $\widetilde{\boldsymbol{K}}$ is the tangent stiffness matrix. It is worth noting that, due to the no-tension model used and in view of equations. (1) and (2), when cracking occurs under the loading process, the modal properties change with respect to the unloaded case; however, if cracks are re-closed in the final configuration, the evaluated modal properties are equal to the initial ones. Conversely, if the structure undergoes crushing and the softening branch is attained, a damage process occurs that leads to a permanent variation of the modal properties.

By the modal properties calculated both for the reference or undamaged configuration C_u and the damaged configuration C_d it is possible to have an idea of the most sensitive damage indexes for an earthquake induced damage on the simplified model.

5.4.2 Damage Simulation

The damage is introduced as a result of a dynamic non-linear analysis based on earthquake accelerograms recorded in the past (Table 5-II). Every model exhibits different slenderness ratio, consequently the natural frequency changes in every case of study. As a result, the spectral ordinates of the seismic actin will be different for each mode in each tower model (Figure 5-VIII).

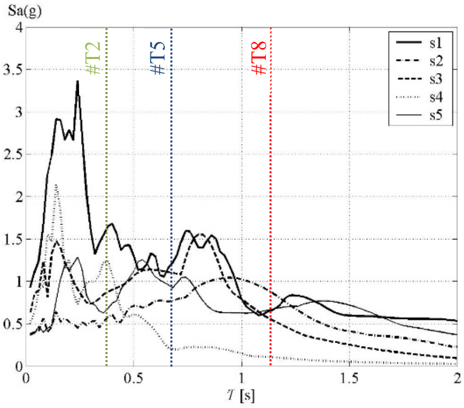

Figure 5-VIII Spectral content of each accelerogram.

Table 5-II Properties of each accelerogram applied to the model

Accelerogram properties

#Acc	Date	Mw	Length [s]	PGA [g]
s1	Tabas	7,4	63,40	0,925
s2	Montenegro (1)	6,9	47,80	0,374
s3	Friuli (1)	6,4	9,35	0,602
s4	Friuli (2)	6	9,98	0,505
s5	Montenegro (2)	6,9	47,80	0,362

In Figure 5-IX are represented the damage values for each model after the simulated seismic events. The zone corresponding to the end of the restrains (H=20) for al length of about 5 m is the most damaged zone. Because of the pounding effect between the freestanding part of the tower and the adjacent buildings represented by the elastic restraints.

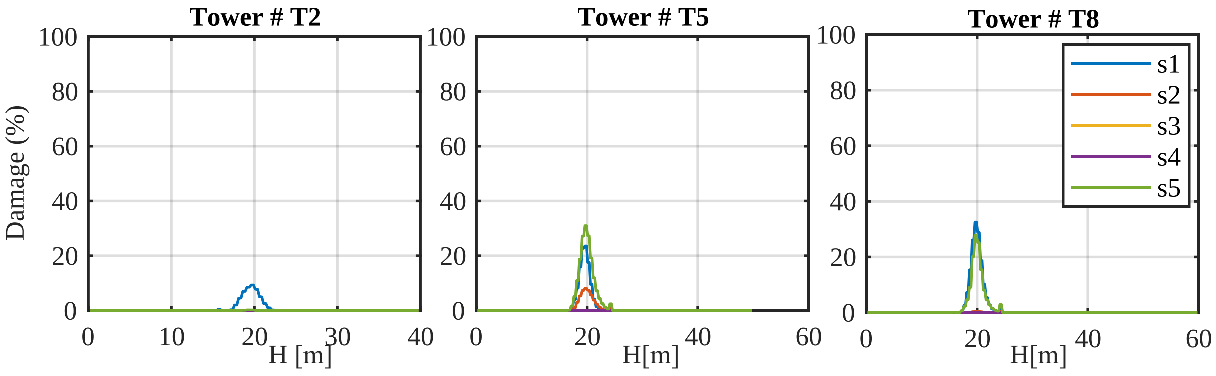

(a) (b) (c)

Figure 5-IX The damage indexes for each simulated seismic event for the three models: (a) #T2 (b) #T5 (c) #T8

Whilst the code allows to calculate, by using Hermite shape functions, the transverse displacements and their derivatives (required to draw mode shapes, rotations and modal curvatures), only displacement of the mode shape have been considered. They are assumed as reference values and employed in the next section to independently calculate the modal curvature and to assess the effect of the sensor grid.

5.4.3 Damage Identification

This phase aims to investigate the capability of detect or even localize (and quantify) the damage for the considered structures. Considering only the horizontal displacements of the mode shapes ϕ_u,ϕ_d and the natural frequencies ω_u, ω_d respectively in the configuration C_u and C_d. At this stage the mode shapes are defined considering all the available results in the nodes (reference grid y_0) and the damage sensitive features are calculated from the input data mentioned above.

The first considered parameter is the natural frequency to achieve the goal of detecting the damage itself on the structure.

Table 5-III The frequency shift results for the model #T2 for each imposed seismic action at the base.

Frequency shift model #T2							
	First mode shape		*Third mode shape*		*Fifth mode shape*		DI [%]
	f [Hz]	Δf [%]	f [Hz]	Δf [%]	f [Hz]	Δf [%]	
und	2,55	-	12,08	-	27,22	-	-
s1	**2,53**	**0,49 %**	**12,04**	**0,32 %**	**27,21**	**0,03 %**	**10**
s2	2,55	0,00 %	12,08	0,00 %	27,22	0,00 %	0
s3	2,55	0,00 %	12,08	0,00 %	27,22	0,00 %	0
s4	2,55	0,00 %	12,08	0,00 %	27,22	0,00 %	0
s5	2,55	0,00 %	12,08	0,00 %	27,22	0,00 %	0

Table 5-IV The frequency shift results for the model #T5 for each imposed seismic action at the base.

Frequency shift model #T5							
	First mode shape		*Third mode shape*		*Fifth mode shape*		DI [%]
	f [Hz]	Δf [%]	f [Hz]	Δf [%]	f [Hz]	Δf [%]	
und	1,46	-	7,93	-	18,51	-	-
s1	**1,44**	**1,41 %**	**7,92**	**0,13 %**	**18,40**	**0,62 %**	**24**
s2	**1,45**	**0,52 %**	**7,93**	**0,07 %**	**18,47**	**0,22 %**	**8**
s3	1,46	0,00 %	7,93	0,00 %	18,51	0,00 %	0
s4	1,46	0,00 %	7,93	0,00 %	18,51	0,00 %	0
s5	**1,43**	**2,27 %**	**7,91**	**0,30 %**	**18,34**	**0,95 %**	**30**

Table 5-V The frequency shift results for the model #T8 for each imposed seismic action at the base.

Frequency shift model #T8							
	First mode shape		*Third mode shape*		*Fifth mode shape*		DI [%]
	f [Hz]	Δf [%]	f [Hz]	Δf [%]	f [Hz]	Δf [%]	
und	0,94	-	5,44	-	13,48	-	-
s1	**0,92**	**2,05 %**	**5,44**	**0,01 %**	**13,37**	**0,86 %**	**32**
s2	**0,94**	**0,02 %**	**5,44**	**0,00 %**	**13,48**	**0,01 %**	**1**
s3	0,94	0,00 %	5,44	0,00 %	13,48	0,00 %	0
s4	0,94	0,00 %	5,44	0,00 %	13,48	0,00 %	0

s5	**0,93**	**1,60 %**	**5,44**	**0,02 %**	**13,39**	**0,68 %**	**29**

The resonant frequencies () can be an indicator of the damage occurrence but requires a very good accuracy in the measurement. Furthermore, the environmental effects might be very important causing frequency shift higher than those due to the damage (maximum 2%). That result is close to the results obtained by previous researchers as it was introduced in the Chapter 3.

In terms of mode shapes there is some slightly difference in the damage zone (Figure 5-X) that is more clear in the higher modes but it does not seem so consistent.

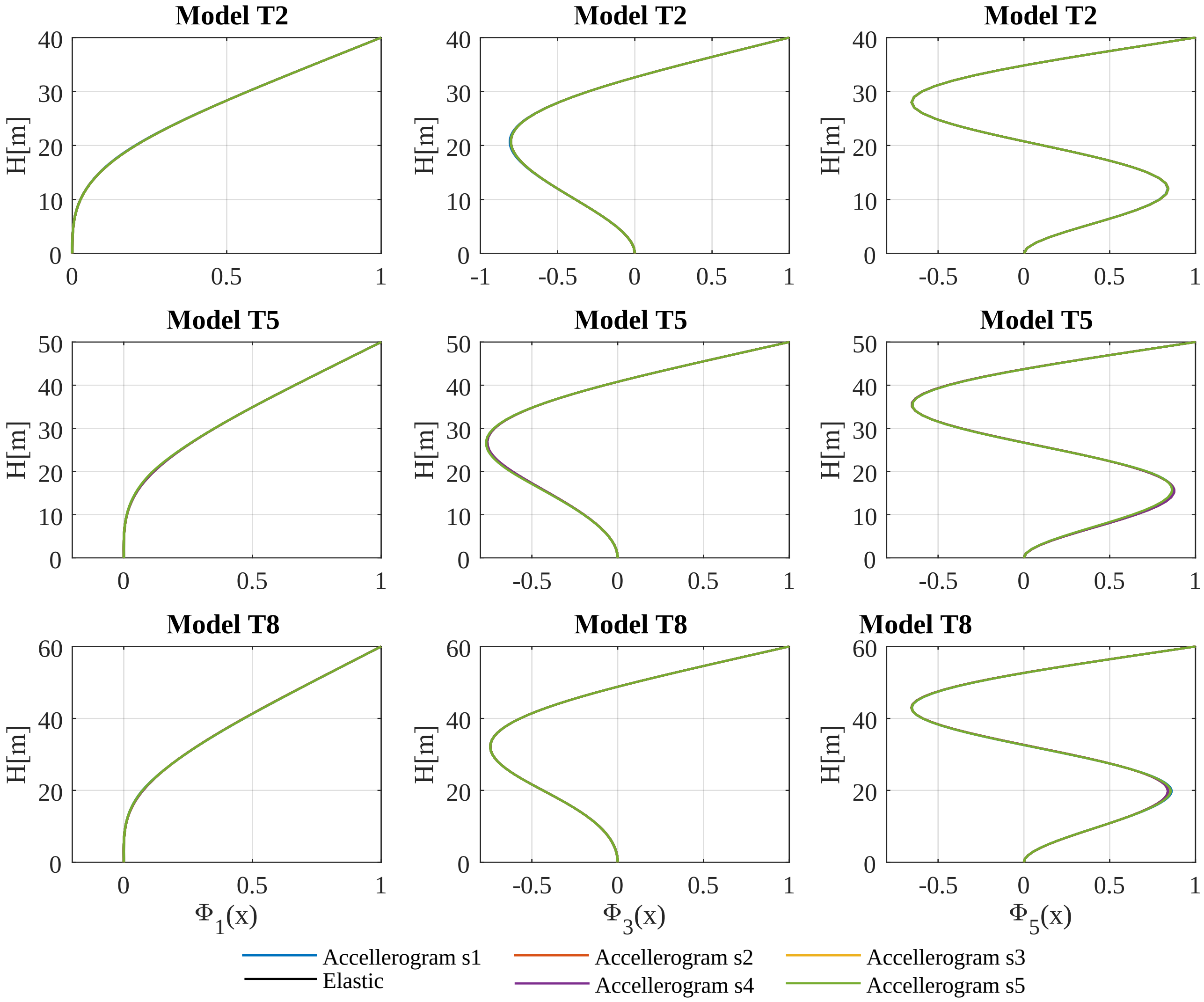

Figure 5-X The plot of the first three translational mode shapes for each model considering the damage state after the applied accelerograms.

The shape curvature confirms the results obtained by the researchers [13] [14] [15] during the last decades and it appears as the most sensitive damage properties. From a first view of the results (Figure 5-XI), it is possible to capture a larger difference in the curvature than in the mode shape.

In particular, the mode shape curvature of the first modes seems to be more sensitive to damage than the higher mode shapes. This is very important because usually the more excited mode shapes are the first, requiring less energy to be activated.

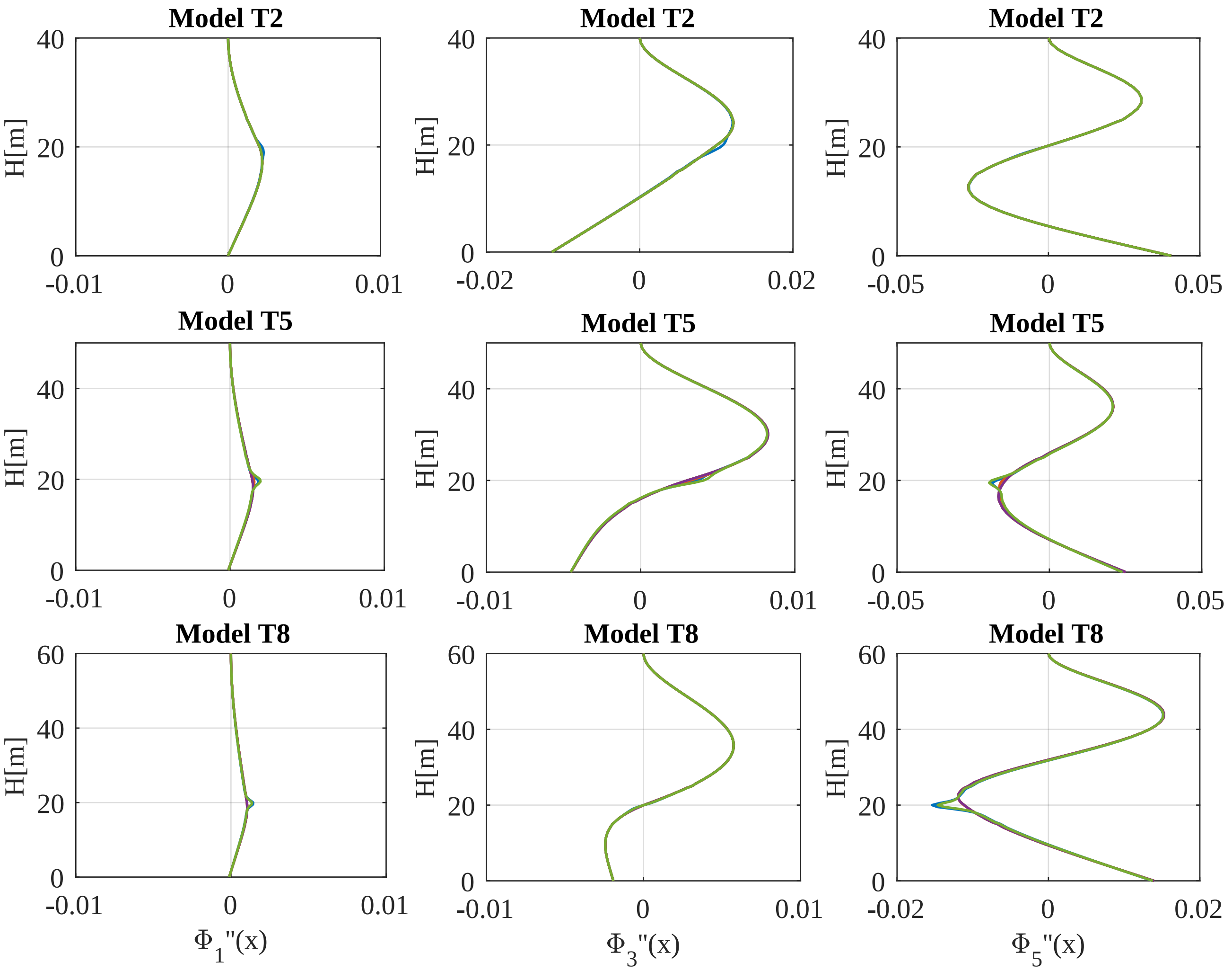

Figure 5-XI The plot of the first three translational mode shape curvatures for each model considering the damage state after the applied accelerograms (for the legend see Figure 5-VIII).

From the analysis results is clear how the frequency can be used for the damage detection if the procedure used for the extraction minimize the noise effects (electrical, environmental, model, etc.) and the mode shape curvature can be a suitable parameter for the localization and quantification of damage.

The problem is how these values can be calculated with a good precision. In Chapter 4 is introduced the MEX algorithm that can process automatically a large number of data minimizing the variance due to the errors that can be arise in the modal identification. Regarding the Modal Shape Curvature (MSC) are adopted two indexes the Curvature Damage Factor (CFD) introduced in [16] and the direct measures of the pure bending stresses due to each mode shape. Then a damage index is introduced as the algebraic mean of the difference between C_u and C_d. Both the indexes operate in the same way but the MSC itself is calculated with two procedures: the first from the mode shapes through the central difference method and the second from the local measurement of the strain. In this context to distinguish between these two methods, the first is called Global Mode Shape Curvature (GMSC) and the second Local Mode Shape Curvature (LMSC).

From that observations two problems arise, one for each method:

- Which is the minimum number of sensors needed to calculate with a good accuracy the GMSC?
- Which is the best position for measuring the strains and which is the required base length to obtain a good accuracy in the LMSC?

5.4.4 *Sensor grid influence*

In the case of the reference grid the obtained value of the GMSC and LMSC are equal confirming that the two different approach lead to the same value that is the CDF as it was introduced above.

Then in the case of the GMSC the number of points in the measurement grid are progressively decreased and it is investigated how is possible to obtain acceptable values of the damage index. In that case is considered only the horizontal component of the mode shapes measured in the specified grid points. The idea behind is to simulate a set of information that can be calculated from the data recorded by a horizontal accelerometer. Hence the mode shape component in the unmeasured points are estimated through a polynomial interpolation.

$$\phi''(x_i) = \alpha\phi(x_i) + \beta\phi(x_{i+1}) + \gamma\phi(x_{i-1}) \tag{3}$$

Then the second derivative of the mode shape that is directly related to the MSC is calculated with the central difference method adjusted for three points $(x_{i-1}, \phi(x_{i-1}); x_0, \phi(x_0); x_{i+1}, \phi(x_{i+1}))$non-equally spaced.

$$\phi''(x_i) = \alpha\phi(x_i) + \beta\phi(x_{i+1}) + \gamma\phi(x_{i-1}) \tag{4}$$

Where α, β, γ are the calculated weighting coefficients truncating the Taylor's series at the second order.

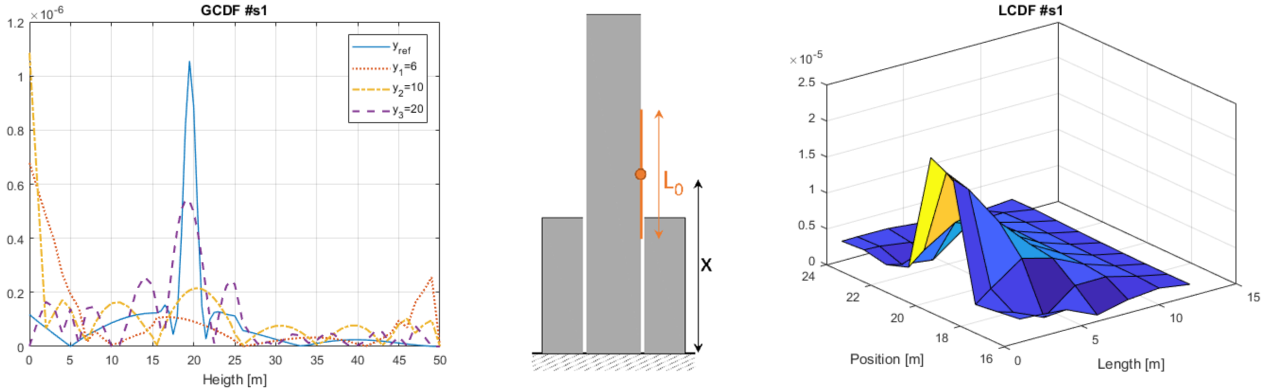

(a) (b) (c)

Figure 5-XII Model #T5:(a) The sensitivity of the GCDF to the reduction of the measuring points (b) The scheme of the position and length of the measurement base to calculate the strain (c) The sensitivity of the LCDF to the position and length of the measurement base.

For the sake of simplicity is considered the model #T5 under the seismic event s1 that lead to a damage index of the 24 %. In Figure 5-XII (a) is showed how the GCDF changes at varying the number of measuring points: the blue line is the reference value and the other lines represent other three measurement grid (y_1, y_2, y_3). At least 20 measurement points are needed to localize the damage. Conversely the LCDF works fine if the position of the chord centroid (distance x in Figure 5-XII-b) is positioned in a zone between 18 and 22 m, reaching a maximum length of the measurement base of 10 m (length L_0 in Figure 5-XII-c).

Summing up the results of that simplified analysis in the following points:

- The frequency shift due to damage is not so high but is more consistent in the first mode shape
- The MSC is confirmed to be the most sensitive modal property respect to the damage and the CDF works well for the localization and quantification of damage.
- The GCDF (the CDF evaluated through the central difference method after the polynomial interpolation) can localize the damage, but a consistent number of measuring points is needed.

- The LCDF (the CDF evaluated through the local measure of the strain) gives a good indication if the position is near the damaged zone and the base length is not selected too much high.

5.5 Numerical analysis of a 3-D model

Considering the results presented in Section 5.4 a more accurate analysis has been performed on a FE model built with solid elements. That simulations aims to investigate which is the level of damage that can be revealed by a classical monitoring system mounting several accelerometers. While in the simplified model (cfr. Section 5.4) the damage scenarios are a consequence of a simulated earthquake; in this case they have been imposed (cfr. Section 5.5.2) by a reduction of the Young's moduli on a limited zone of the tower simulating the formation of a crack on the masonry walls. Hence both the global and the local damages can be replicated according to sections 5.2-5.3.
Thus the workflow of the simulations is similar to those shown in Figure 5-VI where the reference or healthy conditions C_0 has been identified by the MEX algorithm on a set of simulated responses after the application of a white noise at the base both in x and y directions. The adopted signals are the #Test 1 in Table 3-IX (signals length 1400 s with a sampling rate of 50 Hz); consequently, the results of the modal identification can be found in Appendix II. Then the damage has been imposed (Figure 5-XIII) and the configuration C_d has been available. Then the MEX algorithm has been applied on simulated response under random vibrations on the damaged state and the modal quantities have been identified again. Lastly a comparison between the two configurations has been performed to detect the presence of damage (cfr. section 5.5.2).

5.5.1 FE model

The adopted model is the same that has been used for the validation of the MEX algorithm and further information can be found in section 3.5. The horizontal accelerations are measured on five sections of the towers in two points along the internal face of the masonry walls (Figure 3-VII). Therefore, that kind of simulated response under a Gaussian white noise aims to simulate the acquisition that could be made by a biaxial accelerometer.
In order to check the influence of the computational error that could arise from the direct step integration, the modal analysis have been performed also for the damaged configurations C_d and the distances with the identified modal parameters have been computed.

5.5.2 Damage Simulations

From the analysis of the most frequent damage scenarios after an earthquake in Sections 5.2 and 5.3 two feasible local damages cracking pattern for the isolated masonry tower have been selected. The first deals with the possible formation of a crack along a line of openings that are a weak element in the masonry walls (Figure 5-XIII (a)) and the second is referred to a possible cracking pattern of an incipient overturning of the façade (Figure 5-XIII(b)). Lastly, has been imposed a possible damage due to a flexural global mechanism (Figure 5-XIII (c)).

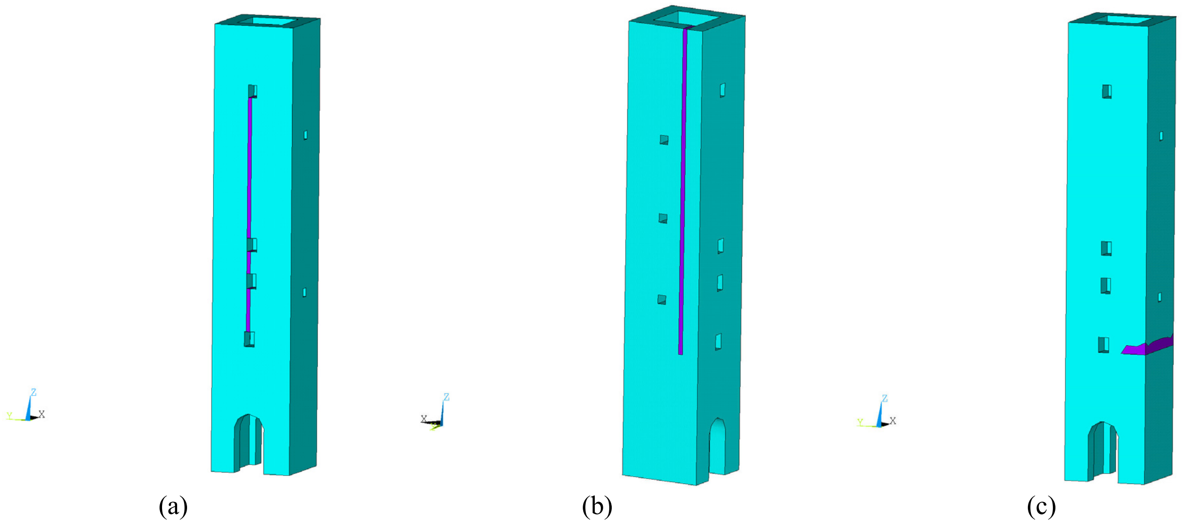

Figure 5-XIII The three damage scenarios: (a) Damage Scenario 1 (#DS 1) (b) Damage Scenario 2 (#DS 2) (c) Damage Scenario 3 (#DS 3)

Two different level of damages defined a priori have been investigated, corresponding to a 90 % reduction of the elastic modulus (#LV 1) up to the 98% for the second level (#LV2). Hence, the second level simulates a complete opened crack and the second a little residual capacity (Table 5-VI).

Table 5-VI The simulated damages on the FE model

Damage Scenarios			
Damage #	*Level (#LV1)*	*Level (#LV2)*	*Description of the cracking pattern*
D1	10% E	2% E	Crack corresponding to a possible overturning of the façades
D2	10% E	2% E	Vertical crack along the openings
D3	10% E	2% E	Global flexural damage

5.5.3 Damage Identification

Following the damage simulation procedure described in section 5.5 the results from the comparison of each damage scenario have been evaluated in terms of frequency relative distance Δf and in terms of mode shapes Δϕ.

$$\Delta f = \frac{|f_u - f_d|}{f_u} \cdot 100 \tag{5}$$

$$\Delta\phi = (1 - MAC_{ud}) \cdot 100 \tag{6}$$

Where f_u and f_d are the identified resonant frequencies respectively of the undamaged and the damaged case and MAC_{ud} is calculated between the healthy and the damaged configurations.

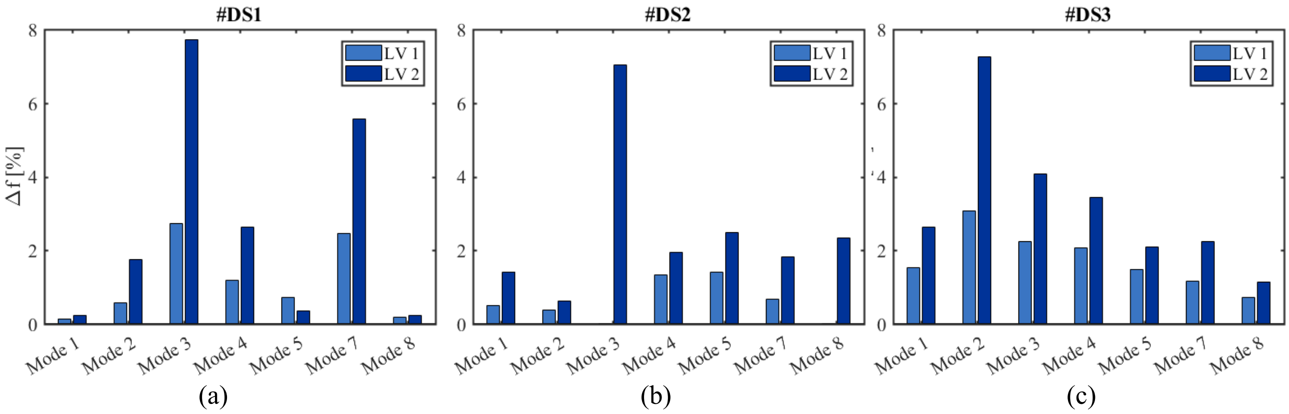

Figure 5-XIV The relative distance in terms of frequency for each damage scenarios: (a) #DS1 (b) #DS2 (c) #DS3

The results in terms of frequencies (Figure 5-XIV) show how the range of variation is between some percentage point up to the 8%. For the simulated local damage scenarios (#DS1 and #DS2) the torsional mode seems to be more sensitive to damage. While for the global damage mechanism the second resonant frequency exhibits the highest value, but some consistent differences can be recognized also in the other modes.

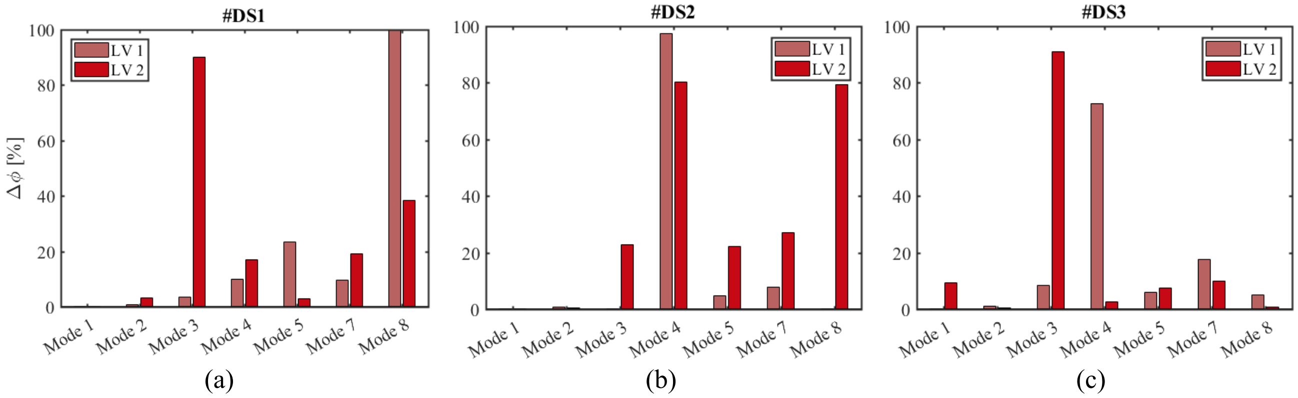

Figure 5-XV The relative distance in terms of mode shapes for each damage scenarios: (a) #DS1 (b) #DS2 (c) #DS3

Regarding the mode shapes (Figure 5-XV) the results are not so satisfactory; in particular, some huge difference can be detected in several modes but some unexpected situation in the quantification of damage suddenly appears. That fact can depend on some bias introduced by the time step integration especially for the modes higher than the first two. Thus, a verification of the correspondence between the identified damaged modes and those obtained by the modal analysis in the FE software have been performed.

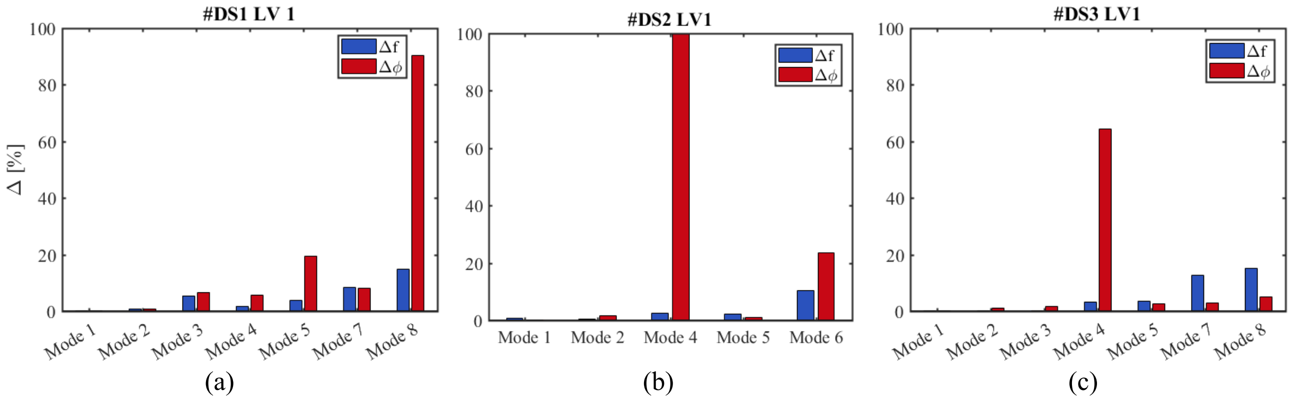

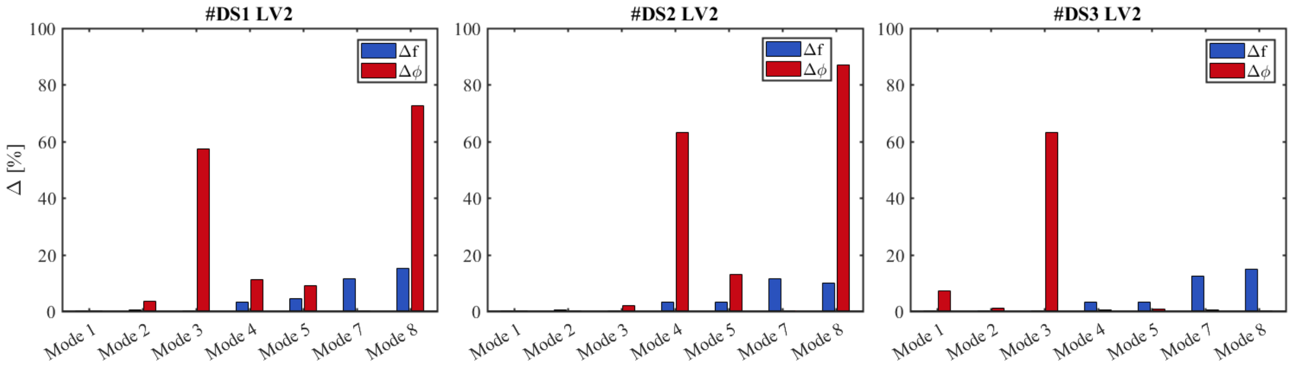

(d) (e) (f)

Figure 5-XVI The comparison between the mode shape from the FE model and those identified by the MEX algorithm for each damage scenario with different levels of damage: (a) Damage scenario 1 with the #LV 1 (b) Damage scenario 2 with the #LV 1 (c) Damage scenario 3 with the #LV 1 (d) Damage scenario 1 with the #LV 2 (e) Damage scenario 2 with the #LV 2 (f) Damage scenario 3 with the #LV 2.

As a consequence, the biased modes should be excluded from the comparison between the healthy and the damage states. All the modes that exhibit a good agreement with the FE model have been retained (maximum a distance of the 5%) and the other have been discarded.

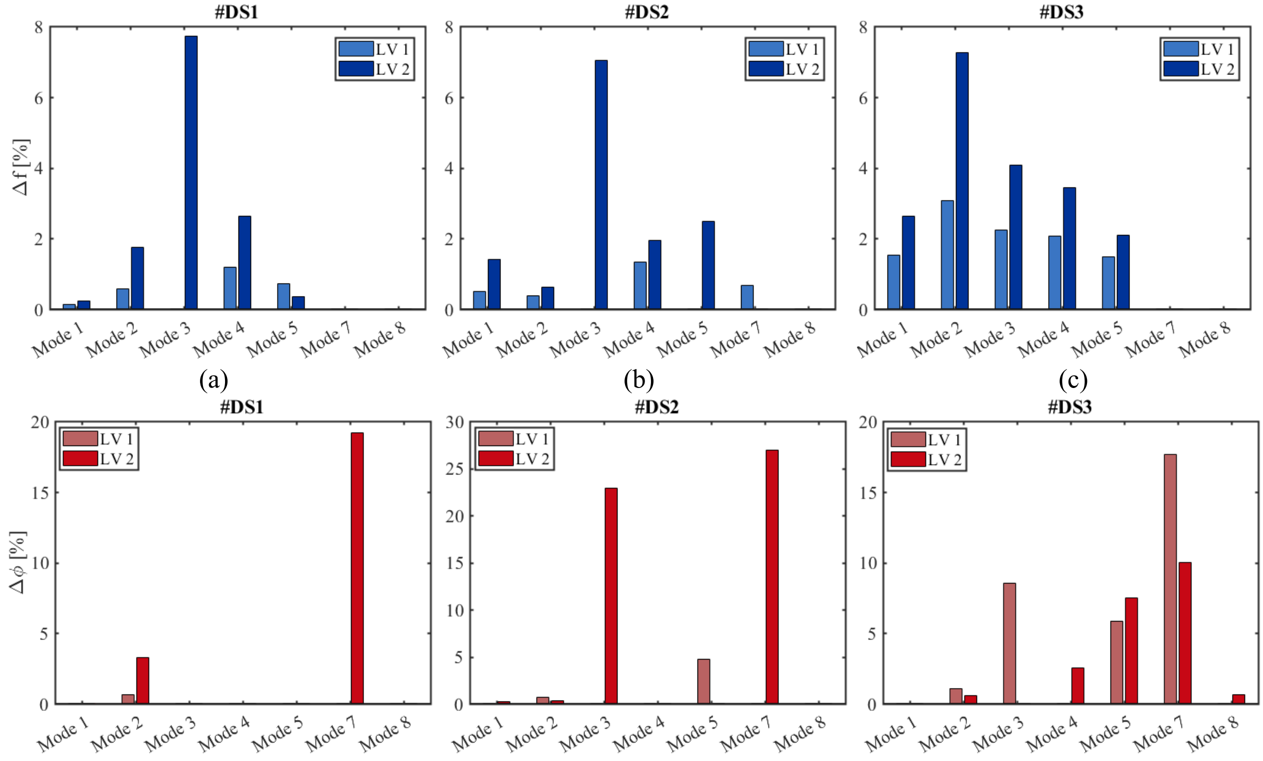

(a) (b) (c)

(d) (e) (f)

Figure 5-XVII The comparison in terms of frequency and mode shape considering only the values with a distance within the 5% between the FE model and the identified modes: (a) Damage scenario 1 with the #LV 1 (b) Damage scenario 2 with the #LV 1 (c) Damage scenario 3 with the #LV 1 (d) Damage scenario 1 with the #LV 2 (e) Damage scenario 2 with the #LV 2 (f) Damage scenario 3 with the #LV 2.

From the results obtained shown in Figure 5-XVII the mode shape seems to be most sensitive to damage (up to a 30%) even if it is more difficult to identify the mode that seems to be most sensitive to bias.

5.6 Discussion of the results

From an Engineering point of view the simulated damages scenario should be correlated with the quantification of the reduction of the structure's bearing capacity. Furthermore, that reduction can be substantial toward a certain external action but not for other. For example, horizontal cracks on masonry panels reduce the capacity toward horizontal forces but there is no reduction if the force is considered vertical. In the case of masonry structures the main problems are related to the seismic actions (*cfr. Chapter 1*). Indeed, the reduction of the capacity should be evaluated with seismic criteria. Therefore, the tested damage scenarios have been studied also in terms of capacity reduction considering acting a set of horizontal forces. The approach used is the pushover analysis reducing the dynamic system in an equivalent system that describes the motion. Hence the capacity can be described in terms of pushover curves.

In order to perform the static non-linear analysis a failure criterion should be selected and the combination of the Drucker Prager plasticity model with the Willam-Warnke failure criterion has been extensively used to modelling the masonry in the code ANSYS [17]. The selected parameters for the non-linear behaviour of the material have been chosen based on the results available in literature.

Table 5-VII The Non-linear parameters set for the pushover analysis performed with the FE model

Non-linear properties of the material						
c [MPa]	ϕ [°]	δ [°]	β_t [-]	β_c [-]	f_t [MPa]	f_c [MPa]
0,32	40	20	0,25	0,75	0,298	8

For instance the case of the damage scenario #DS3 has been analysed herein (Figure 5-XVIII) with the different level of damage (Figure 5-VI). The reduction of the capacity of the tower is visible both in terms of base shear and in terms of drift at the last level of the structure.

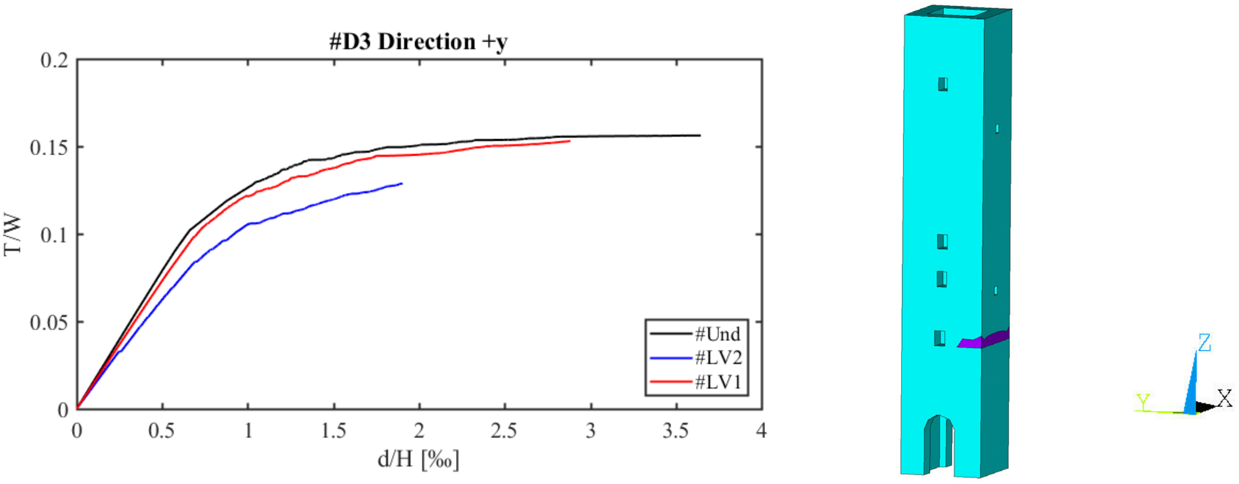

(a) (b)

Figure 5-XVIII (a) The pushover curve in the +y direction for the undamaged configuration and for the two level of damage (#LV1,#LV2) applied to the damage scenario #DS 3 (b)

Avoiding the full description of the numerical procedure that is beyond the aim of this analysis, the reduction in term of capacity at each level of damage can be found in Table 5-VIII.

Clearly both the reduction of the total base shear and the ultimate drift decrease with the levels of damage, exhibiting a decreasing stiffness in the elastic branch due to the Young's moduli reduction performed in the different damage scenarios.

Table 5-VIII The Reduction of capacity in term of base shear and ultimate drift.

Capacity reduction					
#Und		*#LV 1*		*#LV 2*	
V/W [-]	d/H [‰]	ΔV [%]	$\Delta \delta$ [%]	ΔV [%]	$\Delta \delta$ [%]
0,156	3,645	-3	-20	-18	-48

5.7 Conclusive Remarks

In this chapter some application to the damage identification in some FE model representing an idealized model of a masonry tower. Then the damage has been applied and both the damaged and undamaged configurations are identified with simulated responses under random vibrations.

Under the hypothesis of total absence of external noise, the shift in terms of frequency can be quantified about the 8% for the #LV2 and about the 4% for the LV1. Meanwhile, the mode shapes seem to be more sensitive to the induced damage up to the 20% but are more sensitive to the numerical errors induced by the direct integration procedure. On the other hand, the damage intensity cannot be known a-priori and it could be investigated only by posterior analysis. Thus, some pushover analyses have been performed to quantify the capacity reduction of the system under horizontal forces. Consequently, the levels of damage correspond to a reduction in terms of shear base of about the 18 % in the first case and the 3% in the second case, while the ultimate drift decrease respectively of the 20 and 48 %. That analyses aimed to focus with some reduced model on the correlation between the detectable level of damage with the reduction of the capacity to give an idea of the levels of damage applied to the considered structure.

On the other hand, that simple way has the advantages of minimizing the computational effort avoiding the use of complex damage criteria that should be carefully tuned. Considering that facts, the results should be considered as a preliminary indication of what measure in a masonry tower to design a long-term monitoring system for SHM purposes.

5.8 References

[1] J. Heyman, The stone skeleton, Int. J. Solids Struct. 2 (1966) 249–279.

[2] G. Bartoli, M. Betti, L. Galano, G. Zini, Numerical insights on the seismic risk of confined masonry towers, Eng. Struct. (2019). doi:10.1016/j.engstruct.2018.10.001.

[3] D. D’Ayala, E. Speranza, Definition of Collapse Mechanisms and Seismic Vulnerability of Historic Masonry Buildings, Earthq. Spectra. 19 (2003) 479–509. doi:10.1193/1.1599896.

[4] E. Coïsson, D. Ferretti, E. Lenticchia, Analysis of damage mechanisms suffered by Italian fortified buildings hit by earthquakes in the last 40 years, Bull. Earthq. Eng. 15 (2017) 5139–5166. doi:10.1007/s10518-017-0172-0.

[5] A. Preciado, Analysis of Behavior and Failure of Old URM Constructions During Strong, (2019).

[6] N. Cavalagli, G. Comanducci, F. Ubertini, Earthquake-Induced Damage Detection in a Monumental Masonry Bell-Tower Using Long-Term Dynamic Monitoring Data, J. Earthq. Eng. 22 (2018) 96–119. doi:10.1080/13632469.2017.1323048.

[7] N. Cavalagli, G. Comanducci, C. Gentile, M. Guidobaldi, A. Saisi, F. Ubertini, Detecting earthquake-induced damage in historic masonry towers using continuously monitored dynamic response-only data, Procedia Eng. 199 (2017) 3416–3421. doi:10.1016/j.proeng.2017.09.581.

[8] C. Rodrigues, D. Inaudi, B. Glišić, Long-gauge fibre optic sensors: performance comparison and applications, Int. J. Lifecycle Perform. Eng. 1 (2013) 209. doi:10.1504/ijlcpe.2013.058196.

[9] G. Bartoli, M. Betti, P. Biagini, A. Borghini, A. Ciavattone, M. Girardi, G. Lancioni, A.M. Marra, B. Ortolani, B. Pintucchi, L. Salvatori, Epistemic Uncertainties in Structural Modeling: A Blind Benchmark for Seismic Assessment of Slender Masonry Towers, J. Perform. Constr. Facil. 31 (2017) 1–18. doi:10.1061/(ASCE)CF.1943-5509.0001049.

[10] M. Lucchesi, B. Pintucchi, A numerical model for non-linear dynamic analysis of slender masonry structures, Eur. J. Mech. A/Solids. 26 (2007) 88–105. doi:10.1016/j.euromechsol.2006.02.005.

[11] M. Lucchesi, B. Pintucchi, M. Šilhavý, N. Zani, On the dynamics of viscous masonry beams, Contin. Mech. Thermodyn. 27 (2015) 349–365. doi:10.1007/s00161-014-0352-y.

[12] B. Pintucchi, N. Zani, A simple model for performing nonlinear static and dynamic analyses of unreinforced and FRP-strengthened masonry arches, Eur. J. Mech. A/Solids. 59 (2016) 210–231. doi:10.1016/j.euromechsol.2016.03.013.

[13] J. Ciambella, F. Vestroni, The use of modal curvatures for damage localizationin beam-type structures, J. Sound Vib. 340 (2015) 126–137. doi:10.1016/j.jsv.2014.11.037.

[14] M.M. Abdel Wahab, G. De Roeck, Damage detection in bridges using modal curvatures: Application to a real damage scenario, J. Sound Vib. 226 (1999) 217–235. doi:10.1006/jsvi.1999.2295.

[15] A.K. Pandey, M. Biswas, M.M. Samman, Damage detection from changes in curvature mode shapes, J. Sound Vib. 145 (1991) 321–332. doi:10.1016/0022-460X(91)90595-B.

[16] S. Rucevskis, M. Wesolowski, Identification of damage in a beam structure by using mode shape curvature squares, Shock Vib. 17 (2010) 601–610.

[17] G. Bartoli, M. Betti, S. Monchetti, Seismic Risk Assessment of Historic Masonry Towers: Comparison of Four Case Studies, J. Perform. Constr. Facil. (2017).

Chapter 6

Conclusions

6.1- Conclusions-6.2 Drawbacks and limitations-6.3 Future outlooks

6.1 Conclusions

The thesis aims to develop a framework to manage large dataset from the long-term monitoring system with Structural Health Monitoring (SHM) purposes. The investigated class of structures are the CH buildings with a focus on the historic masonry towers both with analysis of simulated response and real long-term monitoring data.

The method follows the frameworks introduced by the researchers in the last years, but it tries to improve the results obtained, proposing some innovations that can be useful in the application to the CH. Above all, a robust automated procedure for the extraction of the modal parameters has been set; then it has been employed as the core of a wide workflow that uses as inputs the raw data and giving back as outputs the properties relative to each mode over the monitoring period. Lastly, some numerical simulations both of a mono dimensional and a 3-D model have been performed to investigate the capability of the damage detection or even localization both using global and local measures.

As a result, the achievements reached can be divided in two groups: the first dealing with the definition and application of the proposed automated procedure and the second relative to the numerical simulations. To the first group belong the following results:

- *Definition of a robust fully automated procedure for the dynamic identification minimizing the model bias*
- *Definition of a more complex framework that automatically process the monitoring data and tracks the identified modes minimizing the variance of the obtained parameters*

Regarding the second group some results obtained can be resumed in the following points:

- *Some earthquakes feasible damage scenario can be well detected by the measure of the Mode Shape Curvature*
- *The direct measure of the curvature is more efficient than those derived by the algebraic derivation of the identified mode shapes*

The first part that can be applied in all the structures is particularly efficient for the CH; the reason why is not so immediate, but it can be found on the requirements that a suitable long-term should exhibit. In the first place, the architectonical features should be preserved, and the devices of the measurement chain should have a small visual impact. Hence, the wireless monitoring systems should be considered preferable than the traditional cabled piezoelectric accelerometers. Meanwhile the cost-effectiveness and the reliability should also be as relevant but not crucial aspects for this kind of monitoring system. As a consequence, a feasible solution has been found, within the MOSCARDO project as the Continuous SHM, using small wireless MEMS accelerometers with a limited resolution. Thus, the proposed method aims to manage automatically large dataset that in some cases are not necessarily containing suitable information about the structure dynamics.

On the other hand, the second part has been showed how the direct measurement of the mode shape curvature is an effective solution for the localization and quantification of a possible flexural global damage after an earthquake simulation. In that case, the damaged configuration can be simulated only by FE numerical model introducing some others epistemic uncertainties to the results as it has been remarked in section 5. In the meantime, that is still the only available method to investigate on that particular aspect.

6.2 Drawbacks and limitations

The entire work does not investigate about the environmental effects that have been considered by the researchers as one of the most important effect that affect the structural dynamics. Hence, the method aims to minimize the variance in the identified modal parameters due to noisy signals and modelling errors in the modal identification phase. Moreover, the thresholds for the input selection, the system identification and the modal tracking phases are derived from the observation of the structural dynamics under operational conditions to exclude those values that can be corrupted by noise. Hence, the definition of a suitable observation period should be deepened, also considering the selection of a representative observation period for the definition of the healthy conditions in the data driven proposed method.

In addition, the results of the numerical models should be carefully analysed as it has been explained in section 5.7 and only some qualitative information should be kept. On account of the errors that can arise from: numerical bias introduced with the direct integration of the equation of motion, the way of modelling the damaged sections and lastly, the way of calculating the reduced capacity of the structural system after the damage. But also, the representativeness of the selected damage scenarios and the simplifications in the 3D FE model derived by considering a stand-alone structure, neglecting the effects of the boundary conditions imposed by the adjacent buildings.

So, the results obtained should be interpreted in the light of all the circumstances that have been described herein and that must be clear for the readers.

6.3 Future outlooks

Starting from the goals reached in that works that have been described in section 6.1 some aspects should be faced. For instance, the cleansing phase of the damage sensitive features from the environmental effects should be investigated with one of the methods described in section 2 and the obtained results should be compared.

Then the damage detection using the control chart can be enabled and implemented to the automated procedure. Then some efforts should be spent on direct measuring the curvature with some high precision devices; such as the fibre-optic systems and tests the capability in detecting and localizing the damage on a real masonry panel or a scaled model where the length of the device is comparable with the dimensions of the blocks.

That further studies can be useful for defining a hybrid monitoring system where the damage detection can be accomplished by a limited number of accelerometers, for instance three at the last level, and on or more critic section can be locally monitoring using a proper measuring device, based on the possible damages mechanisms. Thus, the selection of the proper damage scenarios should be made with a judicious approach based on the observation of the existing cracking pattern and analysing the possible structural weakness.

Last but not least, the proposed method is mainly a data driven approach and the future developments can use some statistical model based of the past observations to assess the structural health. Nevertheless, from the automated extracted modal properties it is possible to adapt a FE model that is current update with the new information of each record. In the author opinion a data driven approach is preferable to avoid all the epistemic uncertainties connected with the FE modelling of the historic masonry.

Appendix I

MATLAB scripts

A1.I MEX - A1.II MEX_AUT - A1.III MOD_TRACK

A1.I MEX

The flow chart of the MATLAB code for the MEX algorithm is shown in that session and it has been described in the chapter 3. The input data are the raw signals converted in acceleration assembled on a matrix $\mathbf{A}\,\epsilon\,\mathcal{R}^{n_{dat}\times n_{sig}}$, after the filtering process including a high (f_{high} is the cut-off frequency) and a low-pass (f_{low} is the cut-off frequency) Butterworth filter of degree n_{Butt} to remove the frequency outside the band of interest; then the signals have been down-sampled to a frequency approximatively equal to $f_c = 2{,}4 \cdot f_{low}$. At the end of that phase the filtered signals are rearranged in the matrix $\mathbf{A}_{rf}\,\epsilon\,\mathcal{R}^{\overline{n_{dat}}\times n_{sig}}$; where $\overline{n_{dat}}$ is the number of data after the down-sampling procedure depending on the value of f_c.

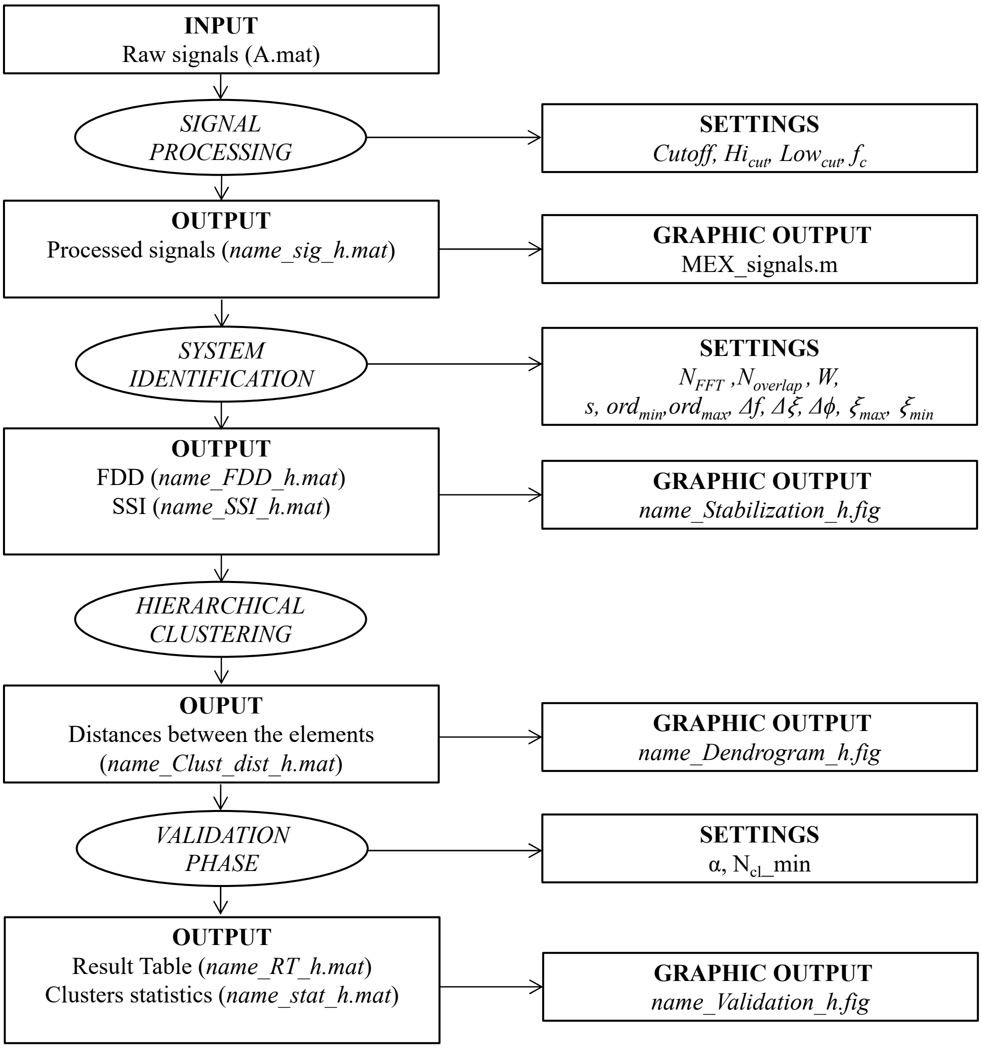

Figure A1-I The MEX algorithm workflow split in every phase. The output can be disabled if the user is not interested to plot all the graphs.

According to the process described in section 3.4 all the settings and the outputs have been shown for each phase. At the end of each phase a .mat file is created, and a graphic output is saved to check the results of the identification procedure. The obtained results are resumed in the result table that save for each identified mode the mean, the median and the standard deviation values, the relative MQI and the population of the cluster (N_{cl}).

A1.II MEX_AUT

This script is created for the automated processing of the collected data through the MEX algorithm (*cfr. Section 3.3*). The input database must be structured with different folders for each monitoring day. Each folder will contain the raw signals matrix $\mathbf{A}\ \epsilon\ \mathcal{R}^{n_{dat}\times n_{sig}}$ of the acquisitions performed each hour. All the monitoring days will be stored in the date vector, which length will equal to the total number of monitoring days N_d.

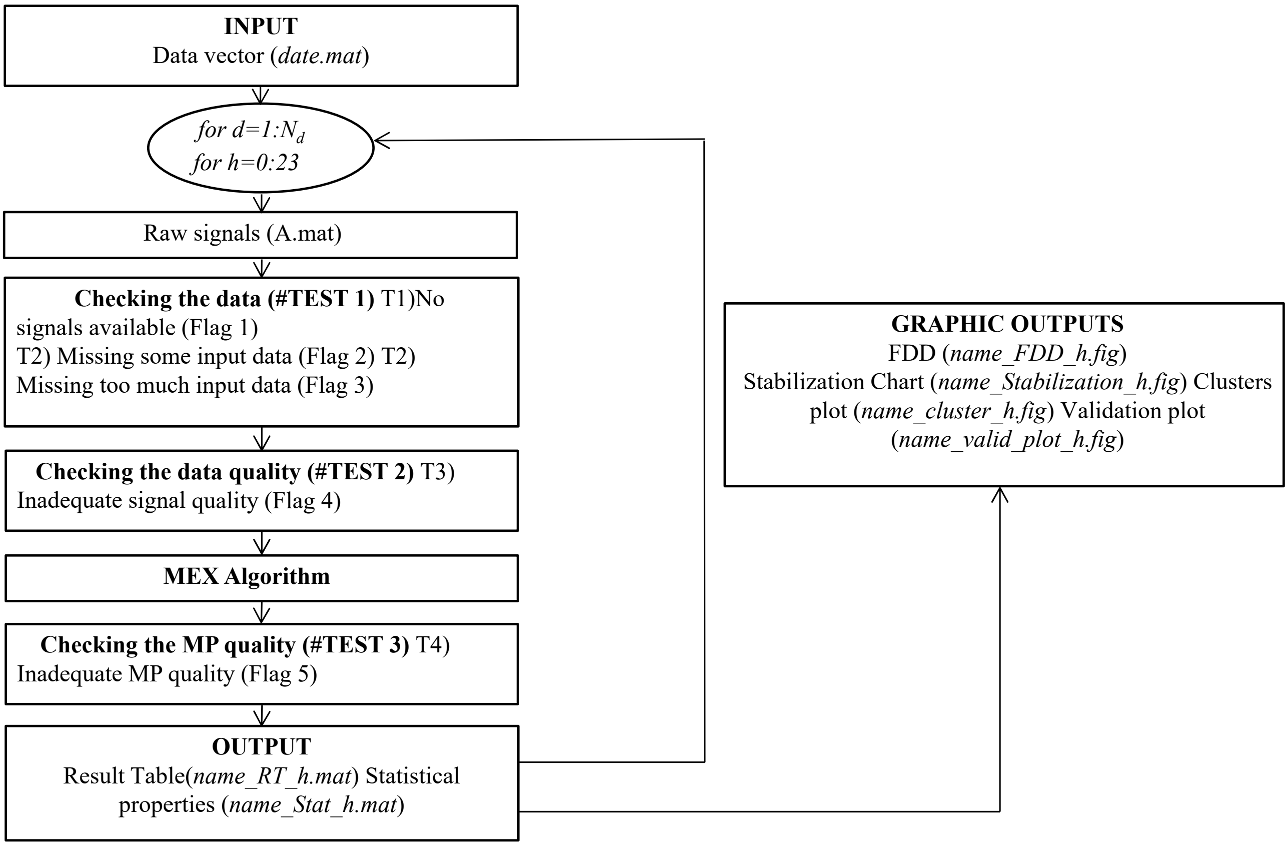

Figure A1-II The flowchart of the MEX_AUT algorithm

The procedure firstly checks the consistence of the data with a series of test (#TEST 1) that if are not satisfied will return a flag file in the examined folder. Hence a minimum number of active channels will be fixed to perform the modal identification. Then the tests on the signal quality (#TEST 2) and on the identified modal parameters (#TEST 3) will be performed to increase the accuracy of the estimations.

The outputs are the result table, collecting the mean values of each identified MP and their MQI value, and the statistical properties of each identified cluster.

It is worth to notice that the user can select which of the available graphic outputs would like to save during the MEX algorithm. By default, only the structure of the MEX algorithm is a little bit slimmer than the one used for a single modal identification. Indeed, some outputs are buried but they can be enabled again on the needs of the users.

A1.III MOD_TRACK

The script deals with the automated track of each mode once the reference sessions are fixed and the frequency and mode shapes thresholds are derived from the calibration phase (cfr. section 3.6.1).

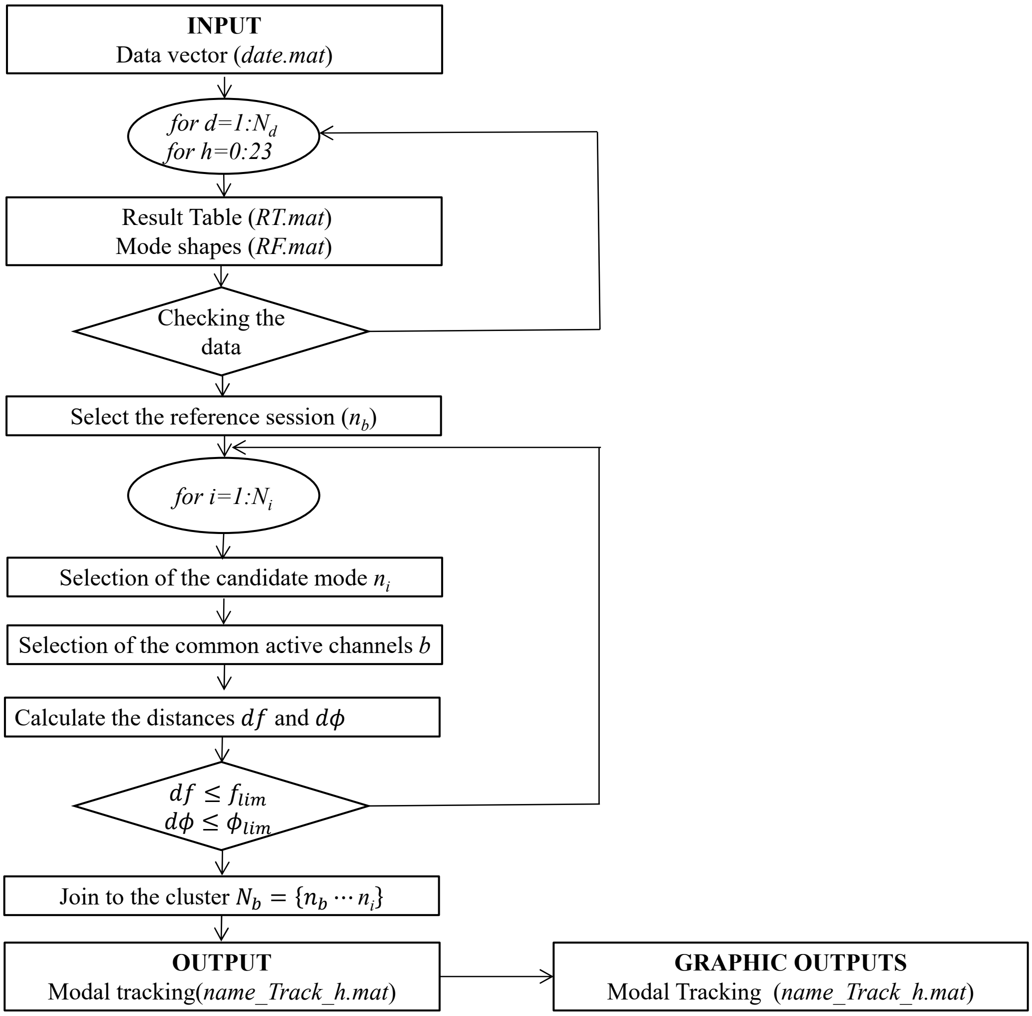

Figure A1-III The flowchart of the proposed algorithm for the modal tracking.

First of all, the algorithm verifies the presence of the data joining them together in several matrices containing the modal parameters of interest. Hence the number of identified sessions N_i can be found. Then from the reference modes selected by the user (cfr. Section 4.4.2) the reference values are compared with all the identified parameters during each session measuring the distances in terms of frequency and mode shapes.

The thresholds are defined through the observation of the structural dynamics for a certain time span (cfr. Section 4.4.1) under operational loads.

.

Appendix II

Tables

A2.I 3D FE model results for the MEX algorithm validation - A2.II Damage identification

A2.I 3D FE model results for the MEX algorithm validation

The Results of each identified modes through the MEX algorithm from the simulated response on the FE 3D model presented in section 3.5. All the tests performed are listed as it was introduced in table 3-IX.

Table A2-I The results of the tests performed during the validation phase in terms of damping ratio and frequency

Test number #TEST	f_1 [Hz]	ξ_1 [%]	f_2 [Hz]	ξ_2 [%]	f_3 [Hz]	ξ_3 [%]	f_4 [Hz]	ξ_4 [%]	f_5 [Hz]	ξ_5 [%]	f_6 [Hz]	ξ_6 [%]	f_7 [Hz]	ξ_7 [%]	f_8 [Hz]	ξ_8 [%]
Ref.	0,972	4	1,067	4	4,511	4	5,062	4	5,377	4	7,715	4	11,445	4	12,730	4
1	0,972	2,720	1,060	2,240	4,505	2,660	4,930	3,580	5,179	3,240	-	-	9,996	4,750	10,780	4,830
2a	0,969	2,876	1,061	1,929	4,528	0,888	4,885	2,748	5,179	2,908	-	-	10,030	4,650	10,810	4,310
2b	0,973	2,156	1,070	2,534	4,553	2,247	5,025	2,603	5,371	2,968	-	-	10,923	6,415	12,461	3,560
3	0,971	3,020	1,059	1,830	-	-	4,900	2,940	5,183	1,950	-	-	10,050	4,890	10,800	5
4	0,970	2,280	1,067	1,830	-	-	5,018	2,070	5,286	2,800	-	-	10,070	1,050	10,780	4,960
5	0,975	2,170	1,073	2,590	4,544	3,120	5,030	2,490	5,346	3,050	-	-	11,550	3.350	12,670	5,060
6	0,973	2,160	1,070	2,530	4,539	1,940	5,025	2,600	5,371	2,970	-	-	11,190	5,910	12,460	2,740
7	0,973	2,030	1,070	2,460	4,843	3,050	5,042	2,640	5,335	3,370	-	-	11,020	5,850	12,260	4,170
8	0,975	1,950	1,072	2,470	-	-	5,028	2,650	5,370	2,470	-	-	-	-	-	-
9	0,941	3,200	1,057	3,210	-	-	5,043	2,190	5,351	3,400	-	-	-	-	-	-
10	0,973	2,150	1,070	2,540	4,544	2,190	5,023	2,600	5,366	3,130	-	-	10,990	6,730	12,650	3,210
11	0,974	2,230	1,071	2,540	4,475	3,240	5,020	2,680	5,375	2,530	-	-	11,250	5,780	12,270	6,920
12	0,971	2,300	1,070	2,790	-	-	5,034	2,610	5,417	1,670	-	-	11,460	5,790	-	-
13	0,985	3,030	1,087	3,980	-	-	5,031	2,380	5,359	2,810	-	-	-	-	-	-
14	1,040	9,150	1,092	2,760	4,591	1,220	4,908	3,170	5,202	2,710	-	-	9,962	4,210	10,790	4,520

Table A2-II The results of the tests performed during the validation phase in terms of MAC and MQI

Test number	1st Mode		2nd Mode		3rd Mode		4th Mode		5th Mode		6th Mode		7th Mode		8th Mode	
#TEST	MAC	MQI	MAC	MQI	MAC	MQI	MAC	MQI	MAC	MQI	MAC	MQI	MAC	MQI	MAC	MQI
Ref.	-	-	-	-	-	-	-	-	-	-	-	-	-	-	-	-
1	1,000	0,904	1,000	0,991	0,861	0,812	0,993	0,800	0,998	0,829	-	-	0,928	0,831	0,992	0,821
2a	1,000	0,888	0,935	0,981	0,308	0,551	0,999	0,832	0,933	0,860	-	-	0,998	0,824	0,982	0,798
2b	1,000	0,935	0,901	0,988	0,383	0,705	0,999	0,940	0,998	0,930	-	-	0,893	0,882	0,671	0,834
3	1,000	0,920	0,952	0,981	-	-	0,959	0,841	0,806	0,789	-	-	0,814	0,803	0,968	0,813
4	0,999	0,965	0,670	0,972	-	-	0,976	0,795	0,918	0,807	-	-	0,945	0,782	0,806	0,918
5	0,999	0,984	0,976	0,881	0,954	0,746	0,999	0,921	1,000	0,933	-	-	0,921	0,831	0,858	0,779
6	0,999	0,807	0,942	0,910	0,341	0,549	0,999	0,962	0,984	0,747	-	-	0,893	0,740	0,560	0,601
7	0,999	0,793	0,965	0,902	0,090	0,470	0,991	0,781	0,991	0,756	-	-	0.889	0,675	0,340	0,572
8	0,998	0,796	0,987	0,979	-	-	0,749	0,763	0,969	0,722	-	-	-	-	-	-
9	0,780	0,707	0,890	0,796	-	-	0,873	0,799	0,695	0,722	-	-	-	-	-	-
10	1,000	0,844	0,924	0,983	0,531	0,556	0,972	0,780	0,993	0,751	-	-	0,880	0,729	0,945	0,825
11	0,998	0,807	0,958	0,977	0,436	0,516	0,998	0,791	0,999	0,751	-	-	0,972	0,730	0,370	0,725
12	1,000	0,801	0,901	0,974	-	-	0,994	0,770	0,925	0,726	-	-	0,966	0,388	-	-
13	0,905	0,800	0,997	0,880	-	-	0,682	0,631	0,951	0,857	-	-	-	-	-	-
14	0,101	0,629	0,965	0,854	0,725	0,546	0,999	0,914	0,997	0,965	-	-	0,996	0,896	0,984	0,768

A2.II Damage identification

Table A2-III The identified modal parameters for the undamaged state #D0

	Estimated Modal Parameters (#D0)					
Mode n°	$\mu(f_n)$ $[Hz]$	$\mu(\xi_n)$ [%]	$cov(f_n)$ [%]	$cov(\xi_n)$ [%]	N_{cl}	MQI
1	0,972	2,720	0,025	1,798	15	0,919
2	1,060	2,240	0,013	1,608	15	0,995
3	4,505	2,660	0,077	6,135	7	0,837

4	4,930	3,580	0,153	6,597	15	0,822
5	5,197	3,240	0,304	6,516	8	0,852
6	9,996	4,750	0,341	6,464	12	0,855
7	10,780	4,832	0,166	3,957	10	0,847

Table A2-IV The identified modal parameters for the damage scenario #D1-LV1

Estimated Modal Parameters (#D1-LV1)						
Mode n°	$\mu(f_n)$ $[Hz]$	$\mu(\xi_n)$ [%]	$cov(f_n)$ [%]	$cov(\xi_n)$ [%]	N_{cl}	MQI
1	0,972	2,706	0,023	2,210	15	0,982
2	1,055	2,138	0,020	1,751	15	0,986
3	4,381	2,721	0,084	3,543	8	0,899
4	4,874	3,508	0,198	3,028	15	0,893
5	5,155	3,233	0,342	5,886	15	0,888
6	9,916	4,842	0,204	8,156	7	0,905
7	10,791	4,914	0,226	5,088	10	0,815

Table A2-V The identified modal parameters for the damage scenario #D1-LV2

Estimated Modal Parameters (#D1-LV2)						
Mode n°	$\mu(f_n)$ $[Hz]$	$\mu(\xi_n)$ [%]	$cov(f_n)$ [%]	$cov(\xi_n)$ [%]	N_{cl}	MQI
1	0,971	2,606	0,033	3,833	15	0,944
2	1,042	1,915	0,046	2,466	15	0,930
3	4,156	2,600	0,081	3,293	9	0,852
4	4,803	2,925	0,058	4,269	15	0,924
5	5,173	2,867	0,025	2,718	4	0,916
6	9,438	4,768	0,467	13,581	8	0,980
7	10,747	4,863	0,122	4,479	11	0,881

Table A2-VI The identified modal parameters for the damage scenario #D2-LV1

Estimated Modal Parameters (#D2-LV1)						
Mode n°	$\mu(f_n)$ $[Hz]$	$\mu(\xi_n)$ [%]	$cov(f_n)$ [%]	$cov(\xi_n)$ [%]	N_{cl}	MQI
1	0,968	2,720	0,022	1,829	15	0,984
2	1,057	2,165	0,014	1,576	15	0,956
3	-	-	-	-	-	-
4	4,867	3,445	0,114	2,641	15	0,894
5	5,119	2,855	0,237	1,942	15	0,929
6	9,928	4,792	0,091	0,592	9	0,863
7	-	-	-	-	-	-

Table A2-VII The identified modal parameters for the damage scenario #D2-LV2

Estimated Modal Parameters (#D2-LV2)

Mode n°	$\mu(f_n)$ $[Hz]$	$\mu(\xi_n)$ [%]	$cov(f_n)$ [%]	$cov(\xi_n)$ [%]	N_{cl}	MQI
1	0,959	2,751	0,018	2,217	15	0,940
2	1,054	2,129	0,017	1,860	15	0,991
3	4,187	2,418	0,035	0,733	12	0,924
4	4,836	3,118	0,055	0,777	15	0,924
5	5,063	2,410	0,037	4,079	15	0,863
6	9,814	5,088	0,120	7,173	4	0,890
7	10,521	4,506	0,128	1,483	6	0,901

Table A2-VIII The identified modal parameters for the damage scenario #D3-LV1

Estimated Modal Parameters (#D3-LV1)

Mode n°	$\mu(f_n)$ $[Hz]$	$\mu(\xi_n)$ [%]	$cov(f_n)$ [%]	$cov(\xi_n)$ [%]	N_{cl}	MQI
1	0,958	2,515	0,080	2,819	15	0,935
2	1,028	1,933	0,091	1,580	15	0,980
3	4,403	2,746	0,097	5,802	9	0,918
4	4,831	3,196	0,091	1,900	14	0,914
5	5,114	2,697	0,168	4,559	15	0,916
6	9,880	4,746	0,358	4,026	11	0,910
7	10,694	4,685	0,135	2,983	9	0,907

Table A2-IX The identified modal parameters for the damage scenario #D3-LV2

Estimated Modal Parameters (#D3-LV2)

Mode n°	$\mu(f_n)$ $[Hz]$	$\mu(\xi_n)$ [%]	$cov(f_n)$ [%]	$cov(\xi_n)$ [%]	N_{cl}	MQI
1	0,947	2,627	0,089	4,090	15	0,924
2	0,984	2,328	0,084	5,660	15	0,979
3	4,321	2,506	0,039	1,848	8	0,871
4	4,763	2,581	0,099	2,308	15	0,974
5	5,083	2,292	0,211	8,790	15	0,900
6	9,771	4,660	0,487	7,268	11	0,905
7	10,649	4,686	0,202	3,107	11	0,937

References

Abdel Wahab M.M., De Roeck G., Damage detection in bridges using modal curvatures: Application to a real damage scenario, J. Sound Vib. 226 (1999) 217–235.

Acito M., Bocciarelli M., Chesi C., Milani G., Collapse of the clock tower in Finale Emilia after the May 2012 Emilia Romagna earthquake sequence: Numerical insight, Eng. Struct. 72 (2014) 70–91.

American National Standards Institute (ANSI), "Vibration of buildings—Guidelines for the measurement of vibrations and evaluation of their effects on buildings." ANSI S2.47-1990, (1990).

Andersen P., Identification of Civil Engineering Structures using Vector ARMA Models, Engineering. 37 (1997) 14–21.

Azzara R.M., De Roeck G., Girardi M., Padovani C., Pellegrini D., Reynders E., The influence of environmental parameters on the dynamic behaviour of the San Frediano bell tower in Lucca, Eng. Struct. 156 (2018) 175–187.

Barrias A., Casas J.R., Villalba S., A review of distributed optical fibre sensors for civil engineering applications, Sensors (Switzerland). 16 (2016).

Barsocchi P., Cassara P., Mavilia F., Pellegrini D., Sensing a City's State of Health: Structural Monitoring System by Internet-of-Things Wireless Sensing Devices, IEEE Consum. Electron. Mag. 7 (2018) 22–31.

Bartoli G., Betti M., Biagini P., Borghini A., Ciavattone A., Girardi M., Lancioni G., Marra A.M., Ortolani B., Pintucchi B., Salvatori L., Epistemic Uncertainties in Structural Modeling: A Blind Benchmark for Seismic Assessment of Slender Masonry Towers, J. Perform. Constr. Facil. 31 (2017) 1–18.

Bartoli G., Betti M., Galano L., Zini G., Numerical insights on the seismic risk of confined masonry towers, Eng. Struct. (2019).

Bartoli G., Betti M., Monchetti S., Seismic Risk Assessment of Historic Masonry Towers: Comparison of Four Case Studies, J. Perform. Constr. Facil. (2017).

Bassoli E., Vincenzi L., D'Altri A.M., S. de Miranda, M. Forghieri, G. Castellazzi, Ambient vibration-based finite element model updating of an earthquake-damaged masonry tower, Struct. Control Heal. Monit. 25 (2018) 1–15.

Bendat J.S., Piersol A.G., Engineering applications of correlation and spectral analysis, New York, Wiley-Interscience, 1980. 315 P. (1980).

Bendat J.S., Piersol A.G., Random Data: Analysis and Measurement Procedures: Fourth Edition, 2012.

Bernal D., Gunes B., Flexibility Based Approach for Damage Characterization: Benchmark Application, J. Eng. Mech. 130 (2003) 61–70.

Binda L., Anzani A., Saisi A., Failures due to long-term behaviour of heavy structures: the Pavia Civic Tower and the Noto Cathedral, Struct. Stud. Repairs, Maint. Herit. Archit. VIII. 66 (2003) 99–108.

Binda L., Learning from Failure Masonry Structures, WITpress, Southampton, n.d.

Box G.E.P., Jenkins G.M., Reinsel G.C., Time series analysis: Forecasting and control: Fourth edition, 2013.

Brandt A., Noise and Vibration Analysis: Signal Analysis and Experimental Procedures, 2011.

Brincker R., Ventura C.E., Andersen P., Damping estimation by frequency domain decomposition, Time. 1 (2001) 698–703.

Brincker R., Ventura C.E., Introduction to Operational Modal Analysis, 2015.

Brincker R., Zhang L., Andersen P., Modal identification of output-only systems using frequency domain decomposition, Smart Mater. Struct. 10 (2001) 441–445.

Brownjohn J.M.W., Magalhaes F., Caetano E., Cunha A., Ambient vibration re-testing and operational modal analysis of the Humber Bridge, Eng. Struct. 32 (2010) 2003–2018.

Cabboi A., Magalhães F., Gentile C., Cunha A., Automated modal identification and tracking: Application to an iron arch bridge, Struct. Control Heal. Monit. 24 (2017).

Calvi G.M., Moratti M., O'Reilly G.J., Scattarreggia N., Malomo D., Monteiro R., Pinho R., Once upon a time in Italy: the tale of the Morandi bridge, Submitt. to Struct. Eng. Int. 8664 (2018).

Cantieni R., One-Year Monitoring of a Historic Bell Tower, Key Eng. Mater. 628 (2014) 73–78.

Castellazzi G., D'Altri A.M., de Miranda S., Ubertini F., An innovative numerical modeling strategy for the structural analysis of historical monumental buildings, Eng. Struct. 132 (2017) 229–248.

Caughey T.K., O'Kelly M.E.J., General theory of vibration of damped linear dynamic systems, (1963).

Cavalagli N., Comanducci G., Gentile C., Guidobaldi M., Saisi A., Ubertini F., Detecting earthquake-induced damage in historic masonry towers using continuously monitored dynamic response-only data, Procedia Eng. 199 (2017) 3416–3421.

Cavalagli N., Comanducci G., Ubertini F., Earthquake-Induced Damage Detection in a Monumental Masonry Bell-Tower Using Long-Term Dynamic Monitoring Data, J. Earthq. Eng. 22 (2018) 96–119.

Cawley P., Adams R.D., The Location of Defects in Structures from Measurements of Natural Frequencies The Journal of Strain Analysis for Engineering Design, J. Strain Anal. Eng. Des. 14 (1979) 49–57.

Ceravolo R., De Lucia G., Pecorelli M.L., Issues on the modal characterization of large monumental structures with complex dynamic interactions, Procedia Eng. 199 (2017) 3344–3349.

Chopra A.K., Dynamics of structures : theory and applications to earthquake engineering, Pearson Educ. (2007) 874.

Ciambella J., Vestroni F., The use of modal curvatures for damage localization in beam-type structures, J. Sound Vib. 340 (2015) 126–137.

Clough R.W; Penzien J., Dynamics of Structures,2nd York, 2003.

Coïsson E., Ferretti D., Lenticchia E., Analysis of damage mechanisms suffered by Italian fortified buildings hit by earthquakes in the last 40 years, Bull. Earthq. Eng. 15 (2017) 5139–5166.

Cooley J.W., Lewis P.A.W., Welch P.D., The Fast Fourier Transform and its Applications, IEEE Trans. Educ. (1969).

Cross E.J., Koo K.Y., Brownjohn J.M.W., Worden K., Long-term monitoring and data analysis of the Tamar Bridge, Mech. Syst. Signal Process. 35 (2013) 16–34.

D'Ayala D., Speranza E., Definition of Collapse Mechanisms and Seismic Vulnerability of Historic Masonry Buildings, Earthq. Spectra. 19 (2003) 479–509.

Deraemaeker A., Worden K., New trends in vibration based structural health monitoring, Springer Science & Business Media, 2012.

Dessi D., Camerlengo G., Damage identification techniques via modal curvature analysis: Overview and comparison, Mech. Syst. Signal Process. 52–53 (2015) 181–205.

Doebling S.W., Farrar C.R., Prime M.B., A summary review of vibration-based damage identification methods, Shock Vib. Dig. (1998).

Döhler M., Hille F., Mevel L., Rücker W., Structural health monitoring with statistical methods during progressive damage test of S101 Bridge, Eng. Struct. 69 (2014) 183–193.

Ewins D.J., Modal Testing: Theory, Practice and Application, 2000.

Farrar C. R., Warden K., Structural Health Monitoring: A Machine Learning Perspective, New York, 2013.

Farrar C.R., Doebling S.W., Cornwell P.J., Straser E.G., Variability of modal parameters measured on the Alamosa Canyon Bridge, 15th Int. Modal Anal. Conf. (1997) 8.

Gentile C., Guidobaldi M., Saisi A., One-year dynamic monitoring of a historic tower: damage detection under changing environment, Meccanica. 51 (2016) 2873–2889.

Glišić B., Inaudi D., Fibre Optic Methods for Structural Health Monitoring, 2007.

Gudmundson P., Eigenfrequency changes of structures due to cracks, notches or other geometrical changes, J. Mech. Phys. Solids. 30 (1982) 339–353.

Heylen W., Sas P., Modal analysis theory and testing, Katholieke Universteit Leuven, Departement Werktuigkunde; Leuven, 2006.

Heyman J., The stone skeleton, Int. J. Solids Struct. 2 (1966) 249–279.

Imregun M., Ewins D.J., Complex modes-origins and limits, Proc. 13th Int. Modal Anal. Conf. (1995) 496–506.

James G.H. III, Carne T.G., Lauffer J.P., The Natural Excitation Technique (NExT) for Modal Parameter Extraction From Operating Wind Turbines, Int. J. Anal. Exp. Modal Anal. 10 (1993) 260–277.

Joshi V.M., Historic Earthquake-Resilient Structures in Nepal and Other Himalayan Regions and Their Seismic Restoration, 33 (2017) 299–319.

Juang J.-N., R.S. Pappa, An eigensystem realization algorithm for modal parameter identification and model reduction, J. Guid. Control. Dyn. 8 (1985) 620–627.

Kambhatla N., Leen T., Dimension Reduction by Local PCA, Neural Comput. 9 (1997) 1493.

Kim J.-T., Stubbs N., Crack Detection in Beam-Type Structures Using Frequency Data, J. Sound Vib. 259 (2003) 145–160.

Kita A., Cavalagli N., Ubertini F., Temperature effects on static and dynamic behavior of Consoli Palace in Gubbio, Italy, Mech. Syst. Signal Process. 120 (2019) 180–202.

Kullaa J., Damage detection of the Z24 bridge using control charts, Mech. Syst. Signal Process. 17 (2003) 163–170.

Ljung L., System Identification Theory for User.pdf, PTR Prentice Hall Up. Saddle River NJ. (1987).

Lourenco P.B., Karanikoloudis G., Seismic behavior and assessment of masonry heritage structures. Needs in engineering judgement and education, RILEM Tech. Lett. 3 (2019) 114–120.

Lourenco P.B., Ramos L.F., Dynamic Identification and Monitoring of Cultural Heritage Buildings, (2011) 55–78.

Lucchesi M., Pintucchi B., A numerical model for non-linear dynamic analysis of slender masonry structures, Eur. J. Mech. A/Solids. 26 (2007) 88–105.

Lucchesi M., Pintucchi B., Šilhavý M., Zani N., On the dynamics of viscous masonry beams, Contin. Mech. Thermodyn. 27 (2015) 349–365.

M.M. Abdel Wahab, G. De Roeck, Damage Detection in Bridges Using Modal Curvatures: Application To a Real Damage Scenario, J. Sound Vib. 226 (1999) 217–235.

Magalhães F., Cunha A., Caetano E, Online automatic identification of the modal parameters of a long span arch bridge, Mech. Syst. Signal Process. 23 (2009) 316–329.

Magalhães F., Cunha A., Caetano E., Vibration based structural health monitoring of an arch bridge: From automated OMA to damage detection, Mech. Syst. Signal Process. 28 (2012) 212–228.

Masciotta M.G., Roque J.C.A., Ramos L.F., Lourenço P.B., A multidisciplinary approach to assess the health state of heritage structures: The case study of the Church of Monastery of Jerónimos in Lisbon, Constr. Build. Mater. 116 (2016) 169–187.

Meruane V., Heylen W., Structural damage assessment under varying temperature conditions, Struct. Heal. Monit. 11 (2012) 345–357.

Monchetti S., on the Role of Uncertainties in the seismic assessment of historic masonry towers, Florence/ TU Braunschweig, 2018.

Mottershead J., Friswell M., Finite element model updating in structural dynamics, Springer N, Dordrecht, 1995.

Ndambi J.M., Vantomme J., Harri K., Damage assessment in reinforced concrete beams using eigenfrequencies and mode shape derivatives, Eng. Struct. 24 (2002) 501–515.

Neu E., Janser F., Khatibi A.A., Orifici A.C., Fully Automated Operational Modal Analysis using multi-stage clustering, Mech. Syst. Signal Process. 84 (2017) 308–323.

Newland D.E., Random Vibration, in: Handb. Noise Vib. Control, 2008.

Oppenheim A. V., Schafer R.W., Discrete Time Signal Processing (2nd version), Book. (2009).

Pandey A.K., Biswas M., Samman M.M., Damage detection from changes in curvature mode shapes, J. Sound Vib. 145 (1991) 321–332.

Papoulis A., Pillai S.-U., Probabilities, Random Variables, and Stochastic Processes, 1991.

Pappa R.S., Elliott K.B., Schenk A., Consistent-mode indicator for the eigensystem realization algorithm, J. Guid. Control. Dyn. 16 (1993) 852–858.

Peeters B., De Roeck G., Reference-based stochastic subspace identification for output-only modal analysis, Mech. Syst. Signal Process. 13 (1999) 855–878.

Peeters B., System Identification and Damage Detection in Civil Engineering, KU Leuven, 2000.

Pintelon R., Guillaume P., Schoukens J., Uncertainty calculation in (operational) modal analysis, Mech. Syst. Signal Process. 21 (2007) 2359–2373.

Pintucchi B., Zani N., A simple model for performing nonlinear static and dynamic analyses of unreinforced and FRP-strengthened masonry arches, Eur. J. Mech. A/Solids. 59 (2016) 210–231.

Preciado A., Analysis of Behavior and Failure of Old URM Constructions During Strong earthquakes, Vol. 1, 1-25. Masonry: Design, Materials and Techniques, Nova Science Publishers (2019).

Preciado A., Sperbeck S.T., Ramírez-Gaytán A., Seismic vulnerability enhancement of medieval and masonry bell towers externally prestressed with unbonded smart tendons, Eng. Struct. 122 (2016) 50–61.

Qin S., Kang J., Wang Q., Operational Modal Analysis Based on Subspace Algorithm with an Improved Stabilization Diagram Method, Shock Vib. (2016).

Rainieri C., Fabbrocino G., Development and validation of an automated operational modal analysis algorithm for vibration-based monitoring and tensile load estimation, Mech. Syst. Signal Process. 60 (2015) 512–534.

Rainieri C., Fabbrocino G., Influence of model order and number of block rows on accuracy and precision of modal parameter estimates in stochastic subspace identification, Int. J. Lifecycle Perform. Eng. 1 (2014) 317.

Ramos L.F., Damage identification on masonry structures based on vibration signatures, PhD Thesis. (2007).

Ramos L.F., Marques L., Lourenço P.B., De Roeck G., Campos-Costa A., Roque J., Monitoring historical masonry structures with operational modal analysis: Two case studies, Mech. Syst. Signal Process. 24 (2010) 1291–1305.

Reynders E., Houbrechts J., De Roeck G., Fully automated (operational) modal analysis, Mech. Syst. Signal Process. 29 (2012) 228–250.

Reynders E., Pintelon R., De Roeck G., Uncertainty bounds on modal parameters obtained from stochastic subspace identification, Mech. Syst. Signal Process. 22 (2008) 948–969.

Reynders E., System Identification Methods for (Operational) Modal Analysis: Review and Comparison, Arch. Comput. Methods Eng. 19 (2012) 51–124.

Reynders E., Wursten G., de Roeck G., Output-only structural health monitoring in changing environmental conditions by means of nonlinear system identification, Struct. Heal. Monit. 13 (2014) 82–93.

Rodrigues C., Inaudi D., Glišić B., Long-gauge fibre optic sensors: performance comparison and applications, Int. J. Lifecycle Perform. Eng. 1 (2013) 209.

Roy K., Ray-Chaudhuri S., Fundamental mode shape and its derivatives in structural damage localization, J. Sound Vib. 332 (2013) 5584–5593.

Rucevskis S., Wesolowski M., Identification of damage in a beam structure by using mode shape curvature squares, Shock Vib. 17 (2010) 601–610.

Rytter A., Aalborg Universitet Vibrational Based Inspection of Civil Engineering Structures Rytter , Anders, Aalborg Universitet, 1993.

Sabia D., Aoki T., Cosentini R.M., Lancellotta R., Model Updating to Forecast the Dynamic Behavior of the Ghirlandina Tower in Modena, Italy, J. Earthq. Eng. 19 (2015) 1–24.

Sinou J., A review of damage detection and health monitoring of mechanical systems from changes in the measurement of linear and non-linear vibrations, 2013.

Sohn H., Farrar C.R., Hemez F.M., Czarnecki J.J., A Review of Structural Health Monitoring Literature : 1996-2001, 2003.

Sohn H., Worden K., Farrar C.R., Novelty detection under changing environmental condition, Smart Struct. Mater. 2001 Smart Syst. Bridg. Struct. Highw. 4330 (2003) 108–118.

Tabachnick B.G., Fidell L.S., Osterlind S.J., Using multivariate statistics, 5th edition New York,NY: Harper and Row 2001.

Theodossopoulos D., Sinha B., A review of analytical methods in the current design processes and assessment of performance of masonry structures, Constr. Build. Mater. 41 (2013) 990–1001.

Tinsley H.E.A., Brown S.D., Multivariate Statistics and Mathematical Modeling, in: Handb. Appl. Multivar. Stat. Math. Model., 2007.

Ubertini F., Cavalagli N., Comanducci G., Materazzi A.L., Pisello A.L., Cotana F., Automated post-earthquake damage detection in a monumental bell tower by continuous dynamic monitoring, in: Struct. Anal. Hist. Constr. Anamn. Diagnosis, Ther. Control. - Proc. 10th Int. Conf. Struct. Anal. Hist. Constr. SAHC 2016, 2016.

Ubertini F., Comanducci G., Cavalagli N., Pisello A. L., Materazzi A. L., Cotana F., Environmental effects on natural frequencies of the San Pietro bell tower in Perugia, Italy, and their removal for structural performance assessment, Mech. Syst. Signal Process. 82 (2017) 307–322.

Ubertini F., Gentile C., Materazzi A.L., Automated modal identification in operational conditions and its application to bridges, Eng. Struct. 46 (2013) 264–278.

Van Overschee P., De Moor B., Subspace Identification for Linear Systems, Holanda: Kluwer Academic Publishers, Dordrecht, 1996.

Wah W.S.L., Chen Y.T., Roberts G.W., Elamin A., Damage Detection of Structures Subject to Nonlinear Effects of Changing Environmental Conditions, Procedia Eng. 188 (2017) 248–255.

Worden K., Farrar C.R., Manson G., Park G., The fundamental axioms of structural health monitoring, Proc. R. Soc. A Math. Phys. Eng. Sci. 463 (2007) 1639–1664.

Wu W.H., Wang S.W., Chen C.C., Lai G., Assessment of environmental and non-destructive earthquake effects on modal parameters of an office building based on long-term vibration measurements, Smart Mater. Struct. 26 (2017).

Xiong W., Kong B., Tang P., Ye J., Vibration-Based Identification for the Presence of Scouring of Cable-Stayed Bridges, J. Aerosp. Eng. 31 (2018) 04018007.

Yan A.M., Kerschen G., De Boe P., Golinval J.C., Structural damage diagnosis under varying environmental conditions - Part II: Local PCA for non-linear cases, Mech. Syst. Signal Process. 19 (2005) 865–880.

Zanotti Fragonara L., Boscato G., Ceravolo R., Russo S., Ientile S., Pecorelli M.L., Quattrone A., Dynamic investigation on the Mirandola bell tower in post-earthquake scenarios, Bull. Earthq. Eng. 15 (2017) 313–337.

Zhang K., Yan X., Multi-cracks identification method for cantilever beam structure with variable cross-sections based on measured natural frequency changes, J. Sound Vib. 387 (2017) 53–65.

Zhang L., Wang T., Tamura Y., A frequency-spatial domain decomposition (FSDD) method for operational modal analysis, Mech. Syst. Signal Process. 24 (2010) 1227–1239.

Zucchini A., Lourenço P.B., A micro-mechanical model for the homogenisation of masonry, Int. J. Solids Struct. 39 (2002) 3233–3255.